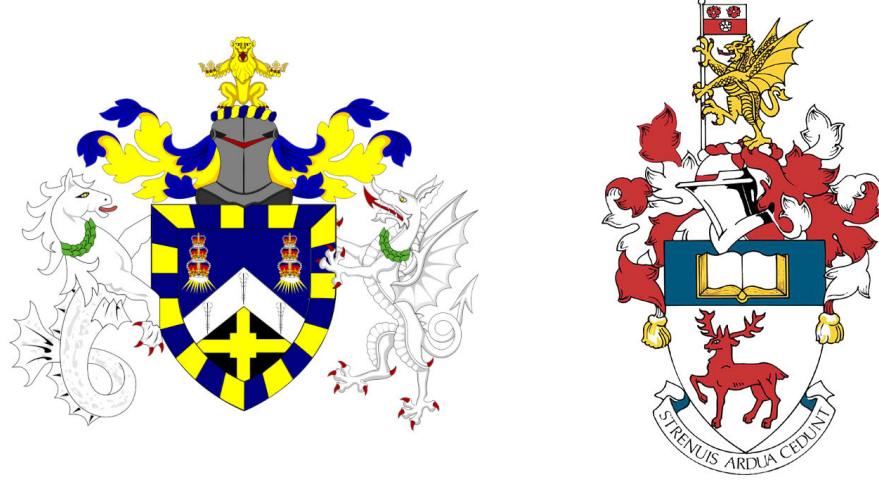


¹ ADVANCING NEUTRINO
² DETECTION AND TRIGGERING IN
³ DUNE

⁴



⁵

Francisco Martínez López

⁶

Submitted in partial fulfillment of the requirements

of the Degree of Doctor of Philosophy

⁸

School of Physical and Chemical Sciences

⁹

Queen Mary University of London

¹⁰

School of Physics and Astronomy

¹¹

University of Southampton

¹²

December 2024

Statement of originality

- 14 I, Francisco Martínez López, confirm that the research included within this thesis is my
15 own work or that where it has been carried out in collaboration with, or supported by
16 others, that this is duly acknowledged below and my contribution indicated. Previously
17 published material is also acknowledged below.
- 18 I attest that I have exercised reasonable care to ensure that the work is original, and
19 does not to the best of my knowledge break any UK law, infringe any third party's
20 copyright or other Intellectual Property Right, or contain any confidential material.
- 21 I accept that the University has the right to use plagiarism detection software to check
22 the electronic version of the thesis.
- 23 I confirm that this thesis has not been previously submitted for the award of a degree
24 by this or any other university.
- 25 The copyright of this thesis rests with the author and no quotation from it or information
26 derived from it may be published without the prior written consent of the author.
- 27 Signature: [can be digital signature]
- 28 Date:
- 29 Details of collaboration and publications:
30 [insert details here if applicable]

Abstract

31

32 Work in progress ...

¡Oh memoria, enemiga mortal de mi descanso!

El ingenioso hidalgo don Quijote de la Mancha

MIGUEL DE CERVANTES SAAVEDRA

Acknowledgements

34 Work in progress ...

Contents

35

36	Statement of originality	3
37	Abstract	5
38	Acknowledgements	9
39	List of Figures	15
40	List of Tables	31
41	List of Abbreviations	33
42	1 Introduction	35
43	2 Neutrino physics	37
44	2.1 Neutrinos in the SM	37
45	2.2 Trouble in the neutrino sector	41
46	2.2.1 The solar neutrino problem	41
47	2.2.2 The atmospheric neutrino problem	43
48	2.3 Massive neutrinos	45
49	2.4 Neutrino oscillation formalism	47
50	2.4.1 Oscillations in vacuum	49
51	2.4.2 Oscillations in matter	52
52	2.4.3 Current status of neutrino oscillations	54
53	2.5 Open questions in the neutrino sector	55
54	2.6 Neutrino interactions	56

CONTENTS

55	3 The Deep Underground Neutrino Experiment	59
56	3.1 Overview	59
57	3.2 Physics goals of DUNE	61
58	3.3 LBNF beamline	63
59	3.4 Near Detector	64
60	3.4.1 ND-LAr	67
61	3.4.2 TMS/ND-GAr	68
62	3.4.3 PRISM	69
63	3.4.4 SAND	70
64	3.5 A More Capable Near Detector	70
65	3.5.1 Requirements	71
66	3.5.2 Reference design	71
67	3.5.3 R&D efforts	74
68	3.6 Far Detector	77
69	3.6.1 Horizontal Drift	78
70	3.6.2 Vertical Drift	80
71	3.6.3 FD Data Acquisition System	82
72	4 Matched Filter approach to Trigger Primitives	85
73	4.1 Motivation	85
74	4.2 Signal-to-noise ratio definition	87
75	4.3 Low-pass FIR filter design	89
76	4.4 Matched filters	92
77	4.5 Using simulated samples	98
78	4.5.1 Angular dependence	104
79	4.5.2 Distortion and peak asymmetry	106
80	4.5.3 Hit sensitivity	109
81	5 DM searches with neutrinos from the Sun	119
82	5.1 Motivation	119

CONTENTS

83	5.2 Gravitational capture of DM by the Sun	119
84	5.3 Neutrino flux from DM annihilations	126
85	5.4 Computing limits from solar neutrino fluxes	127
86	5.5 Example: Kaluza-Klein Dark Matter	131
87	5.6 High energy DM neutrino signals	134
88	5.6.1 DIS events	137
89	5.6.2 Single proton QEL events	141
90	5.6.3 Results	145
91	5.7 Example: Leptophilic Dark Matter	147
92	6 Particle ID in GArSoft	153
93	6.1 GArSoft	154
94	6.1.1 Event generation	154
95	6.1.2 Detector simulation	155
96	6.1.3 Reconstruction	156
97	6.2 dE/dx measurement in the TPC	158
98	6.2.1 Energy calibration	160
99	6.2.2 Truncated dE/dx mean	170
100	6.2.3 Mean dE/dx parametrisation	173
101	6.2.4 Particle identification	177
102	6.3 Muon and pion separation in the ECal and MuID	177
103	6.3.1 Track-ECal matching	180
104	6.3.2 Classification strategy	185
105	6.3.3 Feature selection and importance	188
106	6.3.4 Hyperparameter optimisation	200
107	6.3.5 Probability calibration	203
108	6.3.6 Performance	205
109	6.4 ECal time-of-flight	205
110	6.4.1 Arrival time estimations	207

CONTENTS

111	6.4.2 Proton and pion separation	209
112	6.5 Charged pion decay in flight	210
113	6.5.1 Track breakpoints	212
114	6.6 Neutral particle identification	219
115	6.6.1 ECal clustering	219
116	6.6.2 π^0 reconstruction	222
117	7 Event selection in ND-GAr	225
118	7.1 CAFs and CAFAna	225
119	7.2 Event selection	225
120	7.2.1 ν_μ CC selection	225
121	7.2.2 Charged pion multiplicity	225
122	8 Conclusions	227
123	A An appendix	229
124	Bibliography	231

List of Figures

125

126	2.1 Solar neutrino fluxes for the solar model BS05(OP).	42
127	2.2 Zenith angle distributions for the selected ν_e and ν_μ events in the SK	
128	detector.	44
129	2.3 $K^0 \rightleftharpoons \bar{K}^0$ mixing through W^\pm exchange.	48
130	2.4 Feynman diagrams of the four most relevant CC interactions to long	
131	baseline neutrino oscillation experiments.	57
132	2.5 Schematic representation of a ν_μ CCQE interaction with a neutron inside	
133	a nucleus.	58
134	3.1 Schematic diagram of the DUNE experiment and the LBNF beamline. .	60
135	3.2 Schematic longitudinal section of the LBNF beamline at Fermilab. . .	63
136	3.3 Predicted neutrino fluxes at the FD in FHC mode and RHC mode. . .	64
137	3.4 Representation of the ND hall in Phase II, showing the different subcomponents.	65
138	3.5 Schematic representation of the external components of ND-LAr, including	
139	the cryostat and the PRISM movable system and detailed drawing of one	
140	ArgonCube module.	66
141	3.6 Schematic view of the TMS detector, highlighting its main parts. . . .	67
142	3.7 Cross section of the ND-GAr geometry, showing the HPgTPC, ECal and	
143	magnet.	68
144	3.8 Predicted beam muon neutrino flux at the ND location for different off-axis	
145	positions.	69
146	3.9 Diagram of the ALICE TPC, showing the two drift chambers, inner and	
147	outer field cages and readout chambers.	72

LIST OF FIGURES

148	3.10 Diagram of the ALICE TPC, showing the two drift chambers, inner and outer field cages and readout chambers.	73
149		
150	3.11 Photographs of the TOAD pressure vessel at RHUL.	75
151		
152	3.12 Electron microscope image and schematic diagram of a GEM electrode.	76
153		
154	3.13 Schematic diagram showing the operating principle of a LArTPC with wire readout.	77
155		
156	3.14 Proposed design for the FD-1 and FD-2 modules following the HD principle.	78
157		
158	3.15 Schematic representation of an APA frames showing the U, V, X and G wires.	79
159		
160	3.16 A PDS module containing 24 X-ARAPUCAs and the location of the modules on the APAs.	80
161		
162	3.17 Proposed design for the FD-3 module following the VD principle.	81
163		
164	3.18 Schematic representation of the electrode strip configuration for a top and bottom CRU.	82
165		
166	3.19 Detailed diagram of the DUNE FD DAQ system.	83
167		
168	<i>4.1 Schematic representation of an APA. The black lines represent the APA steel frame. The green and magenta lines correspond to the direction of the U and V induction wires respectively. The blue lines indicate the direction of the X collection wires and the wire shielding G.</i>	86
169		
170	<i>4.2 Left panel: Zoomed unfiltered waveform corresponding to channel 7840 from the ProtoDUNE-SP raw data capture <i>felix-2020-07-17-21:31:44</i> (blue line). The green dashed lines mark the region $\pm 3\sigma_{raw}$. The resulting noise waveform is also shown (red line). Top right panel: ADC distribution for channel 7840, where the green shaded region represents $\pm \sigma_{raw}$. Bottom right panel: noise ADC distribution for channel 7840, where the green shaded region represents $\pm \sigma_{noise}$.</i>	87
171		
172		
173		

LIST OF FIGURES

174	4.3 <i>Left panel:</i> Zoomed filtered waveform corresponding to channel 7840 from the ProtoDUNE-SP raw data capture <i>felix-2020-07-17-21:31:44</i> (blue line). The filter used was the current implementation of the low-pass FIR filter in <i>dtp-firmware</i> . The green dashed lines mark the region $\pm 3\sigma_{\text{raw}}$. The resulting noise waveform is also shown (red line). <i>Top right panel:</i> ADC distribution for channel 7840 after filtering, where the green shaded region represents $\pm \sigma_{\text{raw}}$. <i>Bottom right panel:</i> noise ADC distribution for channel 7840 after filtering, where the green shaded region represents $\pm \sigma_{\text{noise}}$	89
181		
182		
183	4.4 Power spectrum in decibels for the current implementation of the low-pass FIR filter in <i>dtp-firmware</i> (blue line), compared to the response of an optimal filter obtained using the Parks-McClellan algorithm for the same pass-band (red line). Also for comparison I include the spectrum of the optimal filter when taking only the integer part of the coefficients (red dashed line).	90
187		
188		
189	4.5 Relative change in the S/N for the ProtoDUNE-SP raw data capture <i>felix-2020-07-17-21:31:44</i> , using different values of the cutoff frequency f_c and the transition width δf . The optimal Chebyshev filters were applied using just the integer part of the coefficients given by the Parks-McClellan algorithm.	91
191		
192		
193		
194	4.6 Distribution of the relative change of the S/N on the different wire planes from the ProtoDUNE-SP raw data capture <i>felix-2020-07-17-21:31:44</i> after the optimal Chebyshev filter was applied. The filter was computed with the Parks-McClellan algorithm using a cutoff of $f_c = 0.068 \text{ ticks}^{-1}$ and a transition width $\delta f = 0.010 \text{ ticks}^{-1}$.	92
195		
196		
197		

LIST OF FIGURES

198	4.7 Left panel: Zoomed match filtered waveform corresponding to channel 7840 from the ProtoDUNE-SP raw data capture <i>felix-2020-07-17-21:31:44</i> (blue line). The filter used was directly extracted from the data, being the 32 values around the first peak in the original waveform. The green dashed lines mark the region $\pm 3\sigma_{\text{raw}}$. The resulting noise waveform is also shown (red line). Top right panel: ADC distribution for channel 7840 after match filtering, where the green shaded region represents $\pm \sigma_{\text{raw}}$. Bottom right panel: noise ADC distribution for channel 7840 after match filtering, where the green shaded region represents $\pm \sigma_{\text{noise}}$	93
207	4.8 Relative improvement in the S/N for the raw data capture <i>felix-2020-07-17-21:31:44</i> , using the matched filter following the parametrisation in Eq. (4.17). The black crosses in both panels denote the location of the maximum ratio value.	96
210	4.9 Left panel: Optimal matched filter coefficients for the U (blue line) and V (red line) planes. The filters were computed with our parametrisation in Eq. (4.17) for the parameter values $\delta = 0.035$, $\sigma = 0.191$ and $\delta = 0.018$, $\sigma = 0.191$ respectively. Right panel: Distribution of the relative change of the S/N on the two induction wire planes from the ProtoDUNE-SP raw data capture <i>felix-2020-07-17-21:31:44</i> after their respective optimal matched filters were applied.	99
217	4.10 Left panel: distributions of the particles track length in the liquid argon for the generated $E_k = 100$ MeV monoenergetic samples, electrons (blue), muons (red), protons (green) and neutral pions (purple). Right panel: distribution of the length of the longest photon in the neutral pion sample after the decay process $\pi^0 \rightarrow \gamma\gamma$	100

LIST OF FIGURES

LIST OF FIGURES

247	4.15 Selected consecutive waveforms corresponding to two monoenergetic $E_k =$	
248	100 MeV muon events, one is parallel to the APA and to the wires in	
249	the U plane (left panel) and the other is normal to the APA plane and	
250	perpendicular to the U plane wires (right panel). The solid lines represent	
251	the raw waveforms whereas the dashed lines correspond to the waveforms	
252	after the matched filter was applied. The waveforms on the left panel have	
253	been scaled by a factor of 0.15 to have similar amplitude to the ones on	
254	the right panel.	107
255	4.16 Left panel: peak asymmetry distribution for the case of the monoenergetic	
256	$E_k = 100$ MeV muon sample. Each value corresponds to a single bipolar	
257	signal peak from a channel in any event. The blue distribution represents	
258	the peaks on U plane channels, whereas the red corresponds to signal peaks	
259	in V wires. Right panel: relation between the mean peak asymmetry per	
260	event with the S/N for U channel waveforms from the $E_k = 100$ MeV	
261	muon sample. The top subplot shows the decimal logarithm of the mean	
262	S/N for the raw (red) and the matched filtered (blue) waveforms. The	
263	bottom subplot contains the mean S/N improvement ratio after the matched	
264	filter was applied.	108
265	4.17 Raw data display in the plane time (in firmware ticks) vs. offline channel	
266	number for an $E_k = 100$ MeV electron event. The produced true hits are	
267	superimposed (black boxes) as well as the hits comming from the standard	
268	hit finder chain (blue circles) and the hit finder using the matched filter	
269	(green triangles).	110

LIST OF FIGURES

- 270 4.18 *Dependence of the precision (blue), sensitivity (red) and F_1 (green) scores*
271 *on the threshold values used in the hit finder, for the FIR (left panel)*
272 *and matched filter (right panel) cases. The results were obtained after*
273 *matching the hits to the true hits in the case of the isotropic muon sample*
274 *with kinetic energy in the range 5 to 100 MeV, taking only into account*
275 *the induction plane channels. The points represent the mean value while*
276 *the error bars indicate one standard deviation around that mean value.* . . 112
- 277 4.19 *Dependence of the averaged hit sensitivity on the kinetic energy of the*
278 *events for the matched filter (blue) and standard (red) hits, for the case of*
279 *the muon (left panel) and electron (right panel) samples, separated between*
280 *U (top plots) and V (bottom plots) induction wire planes. The top subplots*
281 *contain the hit sensitivities for the two hit finder alternatives, while the*
282 *bottom subplots show the ratio between the two. The horizontal lines sit at*
283 *the mean value and represent the size of the energy bins, while the vertical*
284 *error bars indicate one standard deviation around that mean value.* . . . 114
- 285 4.20 *Distributions of the hit sensitivity in the U (top panels) and V (bottom*
286 *panels) planes versus the hit sensitivity in the X plane, both for the*
287 *standard hits (left panels) and the matched filter hits (right panels), in the*
288 *case of the electron sample and a threshold of 30 ADC.* 115
- 289 4.21 *Top panels: standard residual plots of the hit sensitivities between the X*
290 *and U planes. Bottom panels: quantile-quantile plots of the hit sensitivity*
291 *standard residuals between the X and U planes. In all cases, the left*
292 *panel corresponds to the standard hits while the right panel represents the*
293 *matched filter case, all from the electron sample with a 30 ADC threshold.* 116

LIST OF FIGURES

294	5.1	<i>Input solar parameters used in our capture rate computation as functions of the Sun's radius, from left to right: temperature (with respect to the temperature at the core), mass (in solar masses) and electron number density (with respect to the electron density at the core). All quantities shown correspond to the standard solar model BS2005-OP [1].</i>	122
299	5.2	<i>Capture rates as a function of the DM mass for the DM-electron interactions (red lines), SD DM-nucleons interactions (green lines) and SI DM-nucleons interactions (blue lines). Solid lines represent the values computed in this work while the dashed lines are the one given in Ref. [2]. All the rates are shown for a choice of scattering cross section of $\sigma_i = 10^{-40} \text{ cm}^2$. . .</i>	124
304	5.3	<i>NuWro computed $\nu_\mu - {}^{40}\text{Ar}$ charged-current scattering cross section as a function of the neutrino energy E_μ. The black line shows to the total cross section, whereas the others correspond to the different contributions (in red quasi-elastic scattering, in green resonant pion exchange, in blue deep inelastic scattering and in purple meson exchange current).</i>	128
309	5.4	<i>Expected atmospheric neutrino flux as a function of the neutrino energy E_ν at Homestake at solar minimum, taken from Ref. [3]. The blue solid (dashed) line correspond to muon neutrinos (antineutrinos) and the red solid (dashed) line correspond to electron neutrinos (antineutrinos). . . .</i>	130
313	5.5	<i>Feynman diagrams for B^1B^1 annihilation into SM fermions.</i>	131
314	5.6	<i>Feynman diagrams for B^1B^1 annihilation into a Higgs boson pair. . . .</i>	132
315	5.7	<i>Computed spectra of muon neutrinos at the DUNE FD site from B^1 annihilations in the Sun for three different values of M_{LKP}, plotted in relative energy units for legibility.</i>	133

LIST OF FIGURES

<p>318 5.8 <i>Projected 90% confidence level upper limit for DUNE (400 kT yr) on the</i> 319 <i>spin-dependent B^1-proton scattering cross section as a function of M_{LKP}</i> 320 <i>(green dots). I also show the previous limits from IceCube [4] (blue line)</i> 321 <i>and Antares [5] (red line) on the LKP cross section. The shaded area</i> 322 <i>represents the disfavoured region (at 95% confidence level) on the mass of</i> 323 <i>the LKP from LHC data [6].</i></p> <p>324 5.9 <i>Computed spectra of muon neutrinos at the DUNE FD site from $\tau^+\tau^-$</i> 325 <i>(left panel) and $b\bar{b}$ (right panel) annihilations in the Sun for the DM</i> 326 <i>masses $m_{\text{DM}} = 10 \text{ GeV}$ (red line), 50 GeV (green line) and 100 GeV</i> 327 <i>(blue line), plotted in relative energy units.</i></p> <p>328 5.10 <i>Distribution of the muon neutrino energies from the $\tau^+\tau^-$ (left panel)</i> 329 <i>and $b\bar{b}$ (right panel) annihilation channels, for $m_{\text{DM}} = 10 \text{ GeV}$, separated</i> 330 <i>by CC interaction type: QEL (blue), MEC (orange), RES (green) and</i> 331 <i>DIS (red).</i></p> <p>332 5.11 <i>Distributions of θ_μ (left panel), θ_j (central panel) and θ_{plane} (right panel)</i> 333 <i>for the $b\bar{b}$ sample with $m_{\text{DM}} = 10 \text{ GeV}$ (blue) and the atmospheric</i> 334 <i>background (red).</i></p> <p>335 5.12 <i>Left panel: signal efficiencies (blue lines) and background rejections (red</i> 336 <i>lines) for events passing the cuts $\theta < \theta_{\text{cut}}$ for the jet (solid lines) and</i> 337 <i>muon (dashed lines) angles. Right panel: signal efficiency (blue line) and</i> 338 <i>background rejection (red line) for events passing the cut $\theta_{\text{plane}} < \theta_{\text{cut}}$ for</i> 339 <i>the momentum conservation plane deviation.</i></p> <p>340 5.13 <i>Signal efficiencies for the $\tau^+\tau^-$ (blue line) and $b\bar{b}$ (red line) DIS samples</i> 341 <i>as functions of the DM mass, m_{DM}, obtained by applying the optimal</i> 342 <i>angular cuts $\theta_\mu < 27^\circ$, $4^\circ < \theta_j < 26^\circ$ and $\theta_{\text{plane}} < 3.5^\circ$.</i></p> <p>343 5.14 <i>Distributions of $\cos \theta_\mu$ (left panel), $\cos \theta_p$ (central panel) and $\cos \theta_N$</i> 344 <i>(right panel) for the $\tau^+\tau^-$ QEL sample with $m_{\text{DM}} = 5 \text{ GeV}$ (blue) and</i> 345 <i>the atmospheric background (red).</i></p>	<p>134</p> <p>135</p> <p>136</p> <p>137</p> <p>139</p> <p>140</p> <p>141</p>
--	--

LIST OF FIGURES

346	5.15 Left panel: value of the loss function for the training sample (blue line) and accuracy for the validation sample (red line) versus the number of iterations for the MLP classifier training. Right panel: distributions of the predicted probabilities assigned by the MLP classifier to the test sample for the $\tau^+\tau^-$ QEL signal with $m_{\text{DM}} = 5$ GeV (blue) and the atmospheric background (red).	142
352	5.16 Signal efficiencies for the $\tau^+\tau^-$ (blue line) and $b\bar{b}$ (red line) single proton QEL samples as functions of the DM mass, m_{DM} , obtained by requiring a minimum predicted probability from the MLP classifier of 0.97 in order to achieve a background rejection greater than 99.8%.	144
356	5.17 Projected 90% confidence level upper limit for DUNE (400 kT yr) on the spin-dependent DM-nucleon scattering cross section as a function of m_{DM} , for the annihilation channels $\tau^+\tau^-$ (blue) and $b\bar{b}$ (red) separated by interaction type (up triangles denote DIS interactions whereas down triangles represent QEL interactions). I also show the previous limits from IceCube [7] (solid lines) and the projected sensitivities for Pingu [8] (dashed lines) and Hyper-Kamiokande [9] (dash-dotted lines), as well as the direct detection limits from PICASSO [10] (solid green line) and PICO-60 C ₃ F ₈ [11] (dashed green line).	145
365	5.18 Left panel: Projected 90% confidence level sensitivity of DUNE (400 kT yr) to the scale Λ of an EFT containing only leptophilic DM axial-axial interactions (blue line). Right panel: . In both cases the corresponding limits from DarkSide-50 [12] (dotted green line) and XENON1T [13] (dashed red line) are also shown, together with the configurations for which the correct relic density is achieved (black line), all for the coupling values $c_A^e = 10^3$ and $c_A^\nu = 10^{-2}$	150

LIST OF FIGURES

<p>372 6.1 Distribution of the fraction of energy deposits with residual range less 373 than 20% of the total track length, and distribution of the ionisation per 374 unit length after removing the tracks with less than 30% of their energy 375 deposits in the last 20% of the track.</p> <p>376 6.2 Distribution of the reconstructed ionisation charge per unit length for 377 different reclustering values, and distribution of the median change in 378 dQ/dx per track for the $N_{group} = 4$ reclustering.</p> <p>379 6.3 Distribution of the Geant4-simulated energy losses per unit length versus 380 residual range for the stopping proton sample.</p> <p>381 6.4 Fitted most probable dQ/dx values for each dE/dx bin, together with 382 best fit to the logarithmic calibration function.</p> <p>383 6.5 Fitted most probable dQ/dx values for each dE/dx bin for three different 384 ADC bit limits.</p> <p>385 6.6 Area normalised dE/dx distributions for the true and the reconstructed 386 energy deposits in the stopping proton sample, both after applying the 387 calibration and the calibration and the normalisation correction.</p> <p>388 6.7 Fractional residuals between the true and the corrected dE/dx means 389 and the 60% truncated means, and fractional residuals between the true 390 and the uncorrected, corrected and uncalibrated dE/dx 60% truncated 391 means.</p> <p>392 6.8 Estimated values of the mean dE/dx bias and resolution for the stopping 393 proton sample at different values of the truncation factor.</p> <p>394 6.9 Examples of the truncated mean dE/dx LanGauss fits for various $\beta\gamma$ 395 bins, from a simulated FHC neutrino sample.</p> <p>396 6.10 Resulting one and two dimensional projections of the posterior probability 397 distributions of the ALEPH $\langle dE/dx \rangle$ parameters obtained by fitting the 398 60% truncated mean dE/dx values from a FHC neutrino sample.</p>	<p>162</p> <p>163</p> <p>164</p> <p>165</p> <p>167</p> <p>168</p> <p>170</p> <p>171</p> <p>174</p> <p>175</p>
---	---

LIST OF FIGURES

399	6.11 Truncated mean dE/dx obtained for the FHC neutrino sample as a function of the $\beta\gamma$ product, together with the fitted most probable values for each $\beta\gamma$ bin and the best fit obtained using the ALEPH parametrisation.	176
400		
401		
402	6.12 Distribution of the 60% truncated mean dE/dx versus reconstructed momentum for the FHC neutrino sample.	177
403		
404	6.13 Estimated values of the mean dE/dx bias and resolution obtained for the true protons in a FHC neutrino sample.	178
405		
406	6.14 True momentum distribution for the primary muon in ν_μ CC $N\pi^\pm$ interactions inside the fiducial volume of ND-GAr, compared to the post FSI charged pion spectrum.	179
407		
408		
409	6.15 Distributions of energy deposits in the ECal for a muon and a charged pion with similar momenta.	180
410		
411	6.16 Left panel: comparison between the precision (blue), sensitivity (yellow) and F_1 score (red) obtained for the default (horizontal lines) and new algorithms, both with the χ^2 -based direction estimator (squares) and cheating the directions (circles), for different values of the χ^2 cut. Right panel: comparison of the performance of the new algorithm when applying the cluster t_0 correction (squares) and when (circles).	182
412		
413		
414		
415		
416		
417	6.17 Schematics of a possible option to deal with track-ECal associations in non-zero t_0 neutrino interaction events, trying to correct for the drift direction uncertainty in a cluster-by-cluster basis using the cluster time, $t_{cluster}$	184
418		
419		
420		
421	6.18 Momentum distribution for the reconstructed muons (top panel) and charged pions (bottom panel) in a FHC neutrino sample, together with the fraction of them reaching the ECal (red) and MuID (blue). Each entry corresponds to a reconstructed track, backtracked to a true muon or pion which has not produced any other reconstructed track.	185
422		
423		
424		
425		

LIST OF FIGURES

<p>426 6.19 Predicted truncated mean dE/dx versus momentum, for electrons, muons, 427 charged pions and protons, obtained using the ALEPH parametrisation. 428 The vertical dashed lines represent the boundaries of the six regions used 429 for the muon and pion classification training.</p> <p>430 6.20 Example ECal feature distributions for muons and charged pions in the 431 five different momentum ranges considered.</p> <p>432 6.21 Example MuID feature distributions for muons and charged pions in the 433 three different momentum ranges considered.</p> <p>434 6.22 Left panel: cumulative explained variance for the first three principal 435 components (top panel) and contribution of the different features to the 436 principal axes in feature space (bottom panel). Right panel: Shapley 437 (blue) and Gini (red) feature importances for the different input features. 438 Both figures correspond to the samples in the momentum range $0.3 \leq$ 439 $p < 0.8 \text{ GeV}/c$.</p> <p>440 6.23 Left panel: cumulative explained variance for the first three principal 441 components (top panel) and contribution of the different features to the 442 principal axes in feature space (bottom panel). Right panel: Shapley 443 (blue) and Gini (red) feature importances for the different input features. 444 Both figures correspond to the samples in the momentum range $0.8 \leq$ 445 $p < 1.5 \text{ GeV}/c$.</p> <p>446 6.24 Evolution of the SHAP importance for the top six most important features 447 across all five momentum ranges.</p> <p>448 6.25 Permutation importances for the ten most important features in the 449 different momentum ranges (from left to right, top to bottom, in increasing 450 momentum order). The bars indicate the effect that permutations of 451 each feature have on the purity (blue) and the sensitivity (yellow), the 452 translucent regions representing one standard deviation around the central 453 value.</p>	<p style="margin-right: 20px;">186</p> <p style="margin-right: 20px;">190</p> <p style="margin-right: 20px;">191</p> <p style="margin-right: 20px;">193</p> <p style="margin-right: 20px;">194</p> <p style="margin-right: 20px;">197</p> <p style="margin-right: 20px;">198</p>
---	--

LIST OF FIGURES

454	6.26 Values of the precision and sensitivity obtained for 10000 BDT hyperparameter configurations, for the momentum regions I, III and V.	201
455		
456	6.27 Reliability diagrams for the BDT classifier used in the momentum range	
457	$0.3 \leq p < 0.8 \text{ GeV}/c$, both for the original (blue circles) and calibrated	
458	(yellow squares) responses. For reference, the response of a perfectly	
459	calibrated classifier is also shown (black dashed line).	204
460		
461	6.28 Uncalibrated (left panel) and calibrated (right panel) predicted probabilities assigned by the BDT classifiers for true muons (blue) and charged pions	
462	(red) in the momentum range $0.3 \leq p < 0.8 \text{ GeV}/c$	205
463		
464	6.29 Schematic of the hit selection used for the ToF measurement. The grid represents the layers of the inner ECal, with coloured squares indicating	
465	the tiles with hits. Green squares indicate the selected hits.	206
466		
467	6.30 Particle velocity versus momentum measured with different ECal arrival time estimations. From left to right: earliest hit time, average hit time,	
468	and fitted hit time. In all cases the time resolution is $\Delta\tau = 0.1 \text{ ns}$	208
469		
470	6.31 Mass spectra for p (blue) and π^\pm (yellow) particles, using different ECal time resolution values (from top to bottom, in ascending order), and	
471	arrival time estimates. From left to right: earliest hit time, average hit time,	
472	and fitted hit time. The dashed lines indicate the true masses of	
473	the particles.	210
474		
475	6.32 Efficiency (top panel) and purity (bottom panel) for the proton selection as a function of the momentum, for $\Delta\tau = 0.10 \text{ ns}$	211
476		
477	6.33 Distributions of the velocities measured by ToF with the inner ECal, for different momentum bins, in a FHC neutrino interaction sample. The	
478	Gaussian fits are performed around the maxima for each particle species.	212

LIST OF FIGURES

479	6.34 Left panel: number of non-decaying, decaying and decaying in the fiducial volume pions for a MC sample of 100000, $p = 500$ MeV/ c isotropic positively charged pions inside the TPC. Right panel: event display for a positive pion decaying inside the fiducial volume, with a single reconstructed track for the pion and muon system.	213
484	6.35 Values of $\chi_k^2(FB)$ (top left panel), F_k (top right panel), $D_k^{1/R}$ (bottom left panel) and D_k^ϕ (bottom right panel) versus position along the drift direction for a reconstructed track in a positive pion decay event. The vertical red dashed line indicates the true location of the decay point. . .	214
488	6.36 Fractional residual distributions of the true and reconstructed decay position along the drift coordinate, using the position of the maximum of $\chi_k^2(FB)$ (left panel) and F_k (right panel) as estimates of the decay position. Also shown are double Gaussian fits to these points (red lines).	215
492	6.37 Distributions of the extreme values of $\chi_k^2(FB)$ (top left panel), F_k (top right panel), $D_k^{1/R}$ (bottom left panel) and D_k^ϕ (bottom right panel) for non-decaying reconstructed pion tracks (blue) and tracks which include the decay inside the fiducial volume (red).	217
496	6.38 Left panel: distributions of the predicted probabilities assigned by the BDT classifier to a test sample of decaying pion+muon tracks (blue) and non-decaying pion tracks (red). Left: signal efficiency versus background acceptance (ROC curve) obtained from the BDT for the test sample. . .	218
500	6.39 Left panel: dependence of the decay position finding resolution on the true value of the decay angle for the $\chi_k^2(FB)$ (red) and F_k (blue) methods. Right panel: signal efficiency (blue line) and background rejection (red line) from the BDT classifier versus true decay angle.	218

LIST OF FIGURES

504	6.40 Mean values of the F_1 -score marginal distributions for the different	
505	free parameters of the new clustering algorithm, with the error bars	
506	representing one standard deviation around the mean. The F_1 -score	
507	values were computed for the 6561 possible parameter configurations	
508	using 1000 ν_μ CC interaction events.	221
509	6.41 Left panel: distributions of the number of ECal clusters per photon from	
510	π^0 decays for the standard (red) and new (blue) clustering algorithms.	
511	Right panel: reconstructed invariant mass distributions for photon pairs	
512	from single π^0 events using the standard (red) and new (blue) ECal	
513	clustering algorithms.	223

List of Tables

514

515	2.1	Values of T_3 and $Y/2$ assigned to the first generation of fermions.	39
516	2.2	Neutral current couplings.	40
517	2.3	Summary of neutrino oscillation parameters determined in the Neutrino	
518		Global Fit of 2020 [14].	55
519	3.1	Summary of the two-phased plan for DUNE.	61
520	3.2	Exposure and time required to achieve the different physics milestones of	
521		the two phases.	61
522	4.1	<i>Characteristic parameters of the two monoenergetic muon events selected, relative to the U plane: projected angles in the xz' and $y'z'$ planes, S/N values for the raw and filtered waveforms, mean improvement of the S/N and peak asymmetry.</i>	107
526	6.1	Calibration parameters obtained from the fit of the ND-GAr simulated	
527		stopping proton sample to the calibration function, for different ADC limits.	167
528	6.2	Momentum ranges and description of the PID approach assumed for the	
529		muon and pion classification task.	187
530	6.3	Optimal values of the hyperparameters used by the BDT, for each	
531		momentum range.	202
532	6.4	Performance metrics of the BDTs with optimal hyperparameters, for the	
533		different momentum ranges.	203
534	6.5	Summary of parameters and sampled values used in the optimisation of	
535		the clustering algorithm.	221

LIST OF TABLES

536

List of Abbreviations

ADC	Analog to Digital Converter.
ALEPH	Apparatus for LEP PHysics.
ALICE	A Large Ion Collider Experiment.
BDT	Boosted Decision Tree.
CC	Charged Current.
DM	Dark Matter.
DUNE	Deep Underground Neutrino Experiment.
ECal	Electromagnetic Calorimeter.
FD	Far Detector.
FHC	Forward Horn Current.
HPgTPC	High Pressure gaseous Time Projection Chamber.
LBL	Long BaseLine.
MuID	Muon IDentification system.
NC	Neutral Current.
ND	Near Detector.
ND-GAr	Near Detector Gaseous Argon.
ND-LAr	Near Detector Liquid Argon.
PDG	Particle Data Group.
RHC	Reverse Horn Current.

1

538

Introduction

539

2

540

541

Neutrino physics

542 *Little particles of inspiration sleet through the universe all the time traveling
543 through the densest matter in the same way that a neutrino passes through a
544 candyfloss haystack, and most of them miss.*

545

– Terry Pratchett, *Sourcery*

546 Ever since they were postulated in 1930 by Wolfgang Pauli to explain the continuous
547 β decay spectrum [15] and later found by F. Reines and C. Cowan at the Savannah
548 River reactor in 1953 [16], neutrinos have had a special place among all other elementary
549 particles. They provide a unique way to probe a wide range of quite different physics,
550 from nuclear physics to cosmology, from astrophysics to colliders. Moreover, there is
551 compelling evidence to believe that the study of neutrinos may be key to unveil different
552 aspects of physics beyond the SM, difficult to test elsewhere.

553 In this Chapter, I will review the basics of neutrino physics, from its role within the
554 SM to the main open questions related to the neutrino sector, paying special attention
555 to the phenomenology of neutrino oscillations.

556 2.1 Neutrinos in the SM

557 The SM of fundamental interactions was initially proposed in 1967 by S. Glashow, S.
558 Weinberg and A. Salam[17–19]. This theoretical framework describes the dynamics
559 of leptons and quarks, by introducing a collection of mediating gauge vector bosons
560 and one scalar particle, known as the Higgs boson. It assumes that the local $SU(3) \times$

CHAPTER 2. NEUTRINO PHYSICS

561 $SU(2)_L \times U(1)_Y$ gauge symmetry is an internal symmetry of the system, with $SU(3)$
562 describing quantum chromodynamics, and $SU(2)_L \times U(1)_Y$ being the gauge groups of
563 the electroweak sector. For a detailed overview of the SM of electroweak interactions,
564 see Ref. [20].

565 In the SM, neutrinos appear in three flavours, namely ν_e , ν_μ , and ν_τ . These are
566 associated with the corresponding charged leptons, e , μ , and τ . Neutrinos exist only
567 as left-handed particles, grouped in doublets with the charged leptons, while the later
568 come in both chirality states:

$$\begin{pmatrix} \nu_e \\ e_L^- \end{pmatrix}, \quad \begin{pmatrix} \nu_\mu \\ \mu_L^- \end{pmatrix}, \quad \begin{pmatrix} \nu_\tau \\ \tau_L^- \end{pmatrix}, \quad e_R^-, \quad \mu_R^-, \quad \tau_R^-. \quad (2.1)$$

569 Similarly, quarks also exist in both chirality states, and are grouped as:

$$\begin{pmatrix} u_L \\ d_L \end{pmatrix}, \quad \begin{pmatrix} s_L \\ c_L \end{pmatrix}, \quad \begin{pmatrix} t_L \\ b_L \end{pmatrix}, \quad u_R, \quad d_R, \quad s_R, \quad c_R, \quad t_R, \quad b_R. \quad (2.2)$$

570 The fact that there are no right-handed neutrino fields implies that neutrinos are
571 strictly massless within the SM. This restriction follows from the experimental observation
572 that all neutrinos produced via weak interactions are pure left-handed helicity states
573 (and similarly antineutrinos are pure right-handed states). The hypothetical existence
574 of right-handed neutrinos could be indirectly inferred from the observation of non-zero
575 neutrino masses, nevertheless the existence of neutrino masses is not a sufficient condition
576 for the existence of such fields.

577 Left and right-handed fermions transform differently under $SU(2)_L \times U(1)_Y$ rotations,
578 as the right-handed particles are singlets under $SU(2)_L$. Applying a local transformation,
579 they change as:

$$\begin{aligned} \psi_L &\longrightarrow e^{-iY\beta(x)/2} e^{-iT_a\alpha_a(x)} \psi_L, \\ \psi_R &\longrightarrow e^{-iY\beta(x)/2} \psi_R, \end{aligned} \quad (2.3)$$

580 where $Y/2$ and T_a are the generators of $SU(2)_L$ and $U(1)_Y$, respectively, and $\beta(x)$ and

2.1. NEUTRINOS IN THE SM

Table 2.1: Values of T_3 and $Y/2$ assigned to the first generation of fermions.

	e_L	ν_e	e_R	u_L	d_L	u_R	d_R
T_3	-1/2	1/2	0	1/2	-1/2	0	0
$Y/2$	-1/2	-1/2	-1	1/6	1/6	2/3	-1/3

581 $\alpha_a(x)$ are the parameters of the rotation.

582 The values of the quantum numbers $Y/2$ and T_3 , the third component of the weak
 583 isospin, have to be assigned to the different particles. The values of T_3 follow from the
 584 commutation relations of the generators of $SU(2)$. After the spontaneous symmetry
 585 breaking $SU(2)_L \times U(1)_Y \rightarrow U(1)_{EM}$, one finds the relation which determines the electric
 586 charge:

$$Q = T_3 + \frac{Y}{2}, \quad (2.4)$$

587 Setting the electric charge to -1 for electrons, we can find the values of the hypercharge
 588 for the rest of the fermions. The resulting values for the first generation of leptons and
 589 quarks are shown in Tab. 2.1.

590 It is clear that the free Lagrangian of the theory is not be invariant under the gauge
 591 transformations, as the kinetic terms contain derivatives. Therefore, to make it invariant,
 592 one needs to introduce a set of gauge bosons. They appear in the so-called covariant
 593 derivative, which replaces the common derivative and transforms in the same way as the
 594 fermion fields under local rotations. This constrain fixes completely the transformations
 595 of the spin-1 fields. For left and right-handed particles, the covariant derivatives are
 596 given by:

$$\begin{aligned} D_\mu \psi_L &= \left(\partial_\mu + ig' \frac{Y}{2} B_\mu + ig T_a W_\mu^a \right) \psi_L, \\ D_\mu \psi_R &= \left(\partial_\mu + ig' \frac{Y}{2} B_\mu \right) \psi_R, \end{aligned} \quad (2.5)$$

597 where W_μ^i , $i = 1, 2, 3$ and B_μ are the gauge bosons for the $SU(2)_L$ and $U(1)_Y$ factors,
 598 respectively, and g and g' are the corresponding gauge couplings. It can be shown that
 599 these fields transform in the adjoint representation of the gauge group.

CHAPTER 2. NEUTRINO PHYSICS

Table 2.2: Neutral current couplings.

	u	d	ν_e	e
$2v_f$	$1 - \frac{8}{3}\sin^2\theta_W$	$-1 + \frac{4}{3}\sin^2\theta_W$	1	$-1 + 4\sin^2\theta_W$
$2a_f$	1	-1	1	-1

So far, the theory only contains massless particles, as adding bare mass terms to the Lagrangian would spoil the gauge symmetry. Therefore, the mass terms need to be induced by a spontaneous violation of the symmetries. In the SM, the responsible for this is the Higgs mechanism. The Higgs doublet is coupled to the gauge bosons through the covariant derivative, and to the fermions through the Yukawa couplings. Upon spontaneous symmetry breaking, the vacuum expectation value of the Higgs field generate the mass terms of the particles.

In order to obtain the physical intermediate vector boson states, we need to perform the following redefinitions:

$$\begin{aligned} A_\mu &= \sin \theta_W W_\mu^3 + \cos \theta_W B_\mu, \\ Z_\mu &= \cos \theta_W W_\mu^3 - \sin \theta_W B_\mu, \\ W_\mu^\pm &= \frac{1}{\sqrt{2}} (W_\mu^1 \mp i W_\mu^2), \end{aligned} \tag{2.6}$$

where A_μ is the photon field, and Z_μ and W_μ^\pm are the neutral and the charged weak boson fields, respectively. The Weinberg angle, θ_W , relates the weak coupling constants and the electric charge:

$$e = g' \cos \theta_W = g \sin \theta_W. \tag{2.7}$$

At this point, the interacting part of the electroweak Lagrangian can be re-written as the sum of three contributions: the electromagnetic (EM), charged-current (CC) and neutral-current (NC) components:

$$\begin{aligned} \mathcal{L}_{\text{EW}}^{\text{int}} &= \mathcal{L}_{\text{EM}} + \mathcal{L}_{\text{CC}} + \mathcal{L}_{\text{NC}} \\ &= -e A_\mu J_{\text{EM}}^\mu - \frac{g}{2\sqrt{2}} (W_\mu^+ J_{\text{CC}}^\mu + \text{h.c.}) - \frac{g}{2\cos\theta_W} Z_\mu J_{\text{NC}}^\mu, \end{aligned} \tag{2.8}$$

2.2. TROUBLE IN THE NEUTRINO SECTOR

615 with the currents defined as:

$$\begin{aligned} J_{\text{EM}}^\mu &= \sum_f Q_f \bar{f} \gamma^\mu f, \\ J_{\text{CC}}^\mu &= \sum_\ell \bar{\nu}_\ell \gamma^\mu (1 - \gamma_5) \ell + \sum_f \bar{u}_f \gamma^\mu (1 - \gamma_5) d_f, \\ J_{\text{NC}}^\mu &= \sum_f \bar{f} \gamma^\mu (v_f - a_f \gamma_5) f, \end{aligned} \quad (2.9)$$

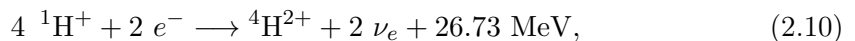
616 where f denotes any SM fermion, ℓ and ν_ℓ a charged lepton and a neutrino of any flavour,
617 and u_f and d_f an up-like and a down-like quarks of any flavour. For the NC case, the
618 values of the v_f and a_f couplings are given in Tab. 2.2.

619 As seen in Eq. (5.8), in the electroweak theory neutrinos are coupled to the Z boson
620 in a universal way. Therefore, by measuring the so-called invisible decay width of the Z
621 boson we have an estimate of the number of light (i.e. lighter than the Z boson) neutrino
622 flavours. This number was measured by LEP in a combined analysis of $e^+ e^- \rightarrow \mu^+ \mu^-$
623 and $e^+ e^- \rightarrow$ hadrons to be $N_\nu = 2.9840 \pm 0.0082$ [21].

624 2.2 Trouble in the neutrino sector

625 2.2.1 The solar neutrino problem

626 Neutrinos are produced everywhere in vast amounts. One of the most prominent sources
627 of neutrinos in our vicinity is our Sun. The Sun is powered mainly by two nuclear fusion
628 reactions, the p – p chain and the CNO cycle. In both cases, the overall reaction is:



629 where part of the released energy is lost to the neutrinos. The electron neutrinos
630 produced are often labelled after the processes that generate them. Figure 2.1 shows the
631 solar neutrino flux as a function of the neutrino energy, broken down by the production
632 process.

CHAPTER 2. NEUTRINO PHYSICS

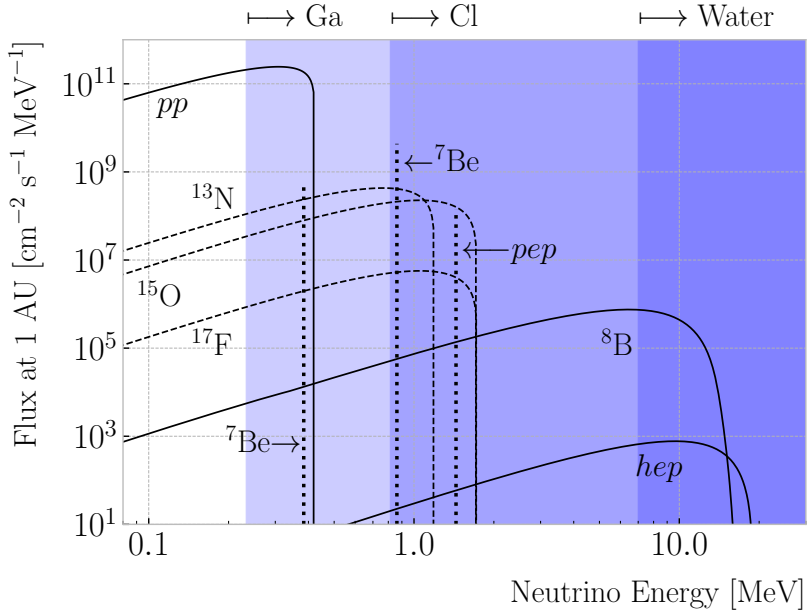


Figure 2.1: Solar neutrino fluxes for the solar model BS05(OP). The detection thresholds for Gallium, Chlorine and water-based experiments are also shown. Figure adapted from Ref. [1].

633 In the late 1960s, the Brookhaven Solar Neutrino Experiment, led by R. Davis, started

634 data taking with the goal of measuring the solar neutrino flux [22]. The experiment

635 used a tank containing 380 m^3 of tetrachloroethene (C_2Cl_4), a liquid commonly used

636 in dry-cleaning, located 1.5 km underground in the Homestake mine, in Lead, South

637 Dakota. The incoming neutrinos would get captured following the reaction:



638 therefore allowing to measure the neutrino flux by counting the ${}^{37}\text{Ar}$ isotopes. The

639 threshold for this reaction is 0.814 MeV, just below the 0.862 MeV line from the ${}^7\text{Be}$

640 ground state transition.

641 The results of the experiment were compared to the theoretical predictions made by

642 J. Bahcall [23]. During its operation from 1968 to 2002, the experiment observed a solar

643 ν_e flux that was approximately a third of the total prediction [24].

644 In the early 1990s, the SAGE [25] and GALLEX [26] experiments started operations.

2.2. TROUBLE IN THE NEUTRINO SECTOR

645 The detection principle used for both experiments was similar to that of the Homestake
 646 experiment, but using ^{71}Ga instead of C_2Cl_4 . With a detection threshold of 0.233 MeV,
 647 the Gallium-based experiments were able to observe the pp neutrino flux. Both
 648 experiments measured a solar electron neutrino flux that was a factor of two lower
 649 than the predictions, demonstrating that this deficit was energy-dependent.

650 In the early 2000s, the SNO experiment put an end to the solar neutrino puzzle
 651 [27, 28]. Thanks to its directionality capabilities, being a Cherenkov light detector, as
 652 well as to its heavy water target, SNO measured the total solar neutrino flux through
 653 the NC process:

$$\nu_\alpha + d \longrightarrow n + p + \nu_\alpha, \quad (2.12)$$

654 where $\alpha = e, \mu, \tau$. This measurement agreed with the solar model predictions. Then,
 655 measuring the CC reaction:

$$\nu_e + d \longrightarrow p + p + e^-, \quad (2.13)$$

656 they were able to establish that the ν_μ and ν_τ solar fluxes are in fact non-zero, revealing
 657 that electron neutrinos were transitioning into different flavours.

658 2.2.2 The atmospheric neutrino problem

659 When cosmic-rays interact with the atoms in the upper atmosphere, a plethora of
 660 hadrons, mainly π and K mesons, are produced. In particular, for the charged pions,
 661 we have the following decay chain dominates:

$$\begin{aligned} \pi^+ &\longrightarrow \mu^+ + \nu_\mu, \\ \mu^+ &\longrightarrow e^+ + \bar{\nu}_\mu + \nu_e, \end{aligned} \quad (2.14)$$

662 and similar for the antiparticles. For neutrino energies < 1 GeV, the ratio:

$$\frac{N(\nu_\mu + \bar{\nu}_\mu)}{N(\nu_e + \bar{\nu}_e)}, \quad (2.15)$$

663 of produced neutrinos and antineutrinos is, in good approximation, equal to two [29].

CHAPTER 2. NEUTRINO PHYSICS

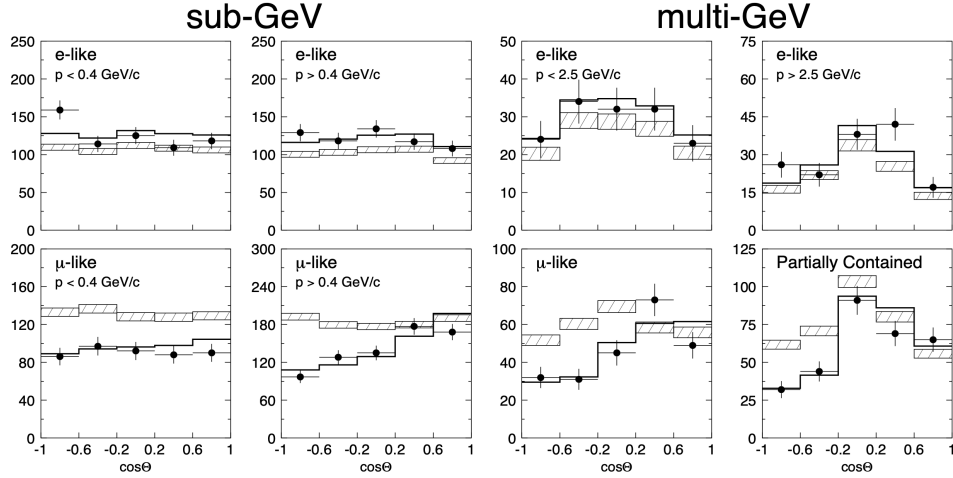


Figure 2.2: Zenith angle distributions for the selected ν_e (top row) and ν_μ (bottom row) events in the SK detector. The hatched region corresponds to the expectation in the case of no oscillations, whereas the solid line indicates the best-fit in the case of $\nu_\mu \rightarrow \nu_\tau$ oscillations. Figure taken from Ref. [34].

During the 1980s, several proton decay experiments, like Kamiokande [30], IMB [31],

MACRO [32], and Soudan-2 [33], measured the flux of atmospheric neutrinos. This was

an important part of their research programme, as the atmospheric neutrinos constitute

their main background. All these experiments reported an atmospheric neutrino ratio

lower than the predictions.

A few years before the SNO discovery, in 1998, Super-Kamiokande (SK) collaboration

measured the atmospheric ν_e and ν_μ spectra as a function of the zenith angle [34].

Upward-going particles have negative zenith angle, $\cos \Theta < 0$, indicating that they

entered from the bottom of the detector. These upward-going neutrinos had to travel

through the Earth in order to reach the detector, allowing SK to probe a broad range

of baselines. Figure 2.2 shows the reported distributions (black dots), compared to the

no oscillations prediction (hatched region). This measurement confirmed that muon

neutrinos transition to other flavours, and that this phenomenon depends both on the

energy and the path length of the neutrino.

The SK and SNO findings provided definitive evidence for the existence of neutrino

oscillations, and therefore non-zero neutrino masses. This constitutes one of the

groundbreaking discoveries of modern physics and has acted as driving force for beyond

2.3. MASSIVE NEUTRINOS

the Standard Model (BSM) physics. The minimal extension of the SM we can do to address these phenomena is introducing different masses for at least two of the neutrinos. This way, we are left with three neutrino mass eigenstates ν_1 , ν_2 , and ν_3 , with masses m_1 , m_2 , and m_3 respectively, which in general will not coincide with the flavour eigenstates, ν_e , ν_μ , and ν_τ .

2.3 Massive neutrinos

The existence of neutrino oscillations imply that neutrinos are massive particles. However, as we have seen before, within the SM neutrinos are massless, as they do not have a mass term in the Lagrangian. If one wants to give neutrinos a mass, the particle content of the SM needs to be expanded.

A way of generating massive neutrinos while maintaining gauge invariance is by introducing an arbitrary number of sterile neutrinos N_i , $i = 1, \dots, m$. These allow for two different types of neutrino mass terms:

$$-\mathcal{L}_{M_\nu} = \sum_{i=1}^m \sum_{j=1}^3 M_D^{ij} \bar{N}_i \nu_{Lj} + \frac{1}{2} \sum_{i=1}^m \sum_{j=1}^m M_N^{ij} \bar{N}_i N_j^c + \text{h.c.}, \quad (2.16)$$

where M_D is a complex $m \times 3$ matrix and M_N a complex and symmetric $m \times m$ matrix. The first term, often referred to as the Dirac mass term, arises from the corresponding Yukawa interaction after the spontaneous electroweak symmetry breaking, similar to the other fermions. The second term, called the Majorana mass term, is allowed in the Lagrangian, as it is a singlet of the gauge group. However, it violates lepton number conservation by two units.

If one imposes lepton number symmetry conservation, the Majorana term must banish, $M_N = 0$. In this case, if $m = 3$ we can identify the sterile neutrinos as the right-handed component of the neutrino field. The Dirac mass matrix can be diagonalised using two unitary matrices, V_R^ν and V_L^ν , as:

$$M_D = V_R^\nu \text{ diag}(m_1, m_2, m_3) V_L^{\nu\dagger}, \quad (2.17)$$

CHAPTER 2. NEUTRINO PHYSICS

704 where m_i , $i = 1, 2, 3$ are the masses of the three neutrino mass eigenstates.

705 The neutrino mass term can be written in term of the resulting eigenstates as:

$$-\mathcal{L}_{M_\nu} = \sum_{i=1}^3 m_i \bar{\nu}_{Di} \nu_{Di}, \quad (2.18)$$

706 with:

$$\nu_{Di} = \left(V_L^{\nu\dagger} \nu_L \right)_i + \left(V_R^{\nu\dagger} N \right)_i. \quad (2.19)$$

707 In this scenario, both the low energy particle budget and the symmetries of the SM
 708 have to be modified. Moreover, the masses of the neutrinos are generated exclusively
 709 through the Higgs mechanism, which does not explain why they are much smaller than
 710 those of the charged leptons.

711 Going back to the general case, we can re-write Eq. (2.16) in matrix form as:

$$-\mathcal{L}_{M_\nu} = \frac{1}{2} \left(\bar{\nu}_L^c, \bar{N} \right) \begin{pmatrix} 0 & M_D^T \\ M_D & M_N \end{pmatrix} \begin{pmatrix} \nu_L \\ N^c \end{pmatrix} + \text{h.c.} = \bar{\nu}^c M_\nu \nu + \text{h.c.}, \quad (2.20)$$

712 with $\nu = (\nu_L, N^c)^T$ being a $(3+m)$ -dimensional vector grouping the active and the
 713 sterile neutrinos. The matrix M_ν , which is a complex $(3+m) \times (3+m)$ symmetric
 714 matrix, can be diagonalised by means of a unitary matrix V^ν , yielding:

$$M_\nu = V^\nu \text{ diag}(m_1, m_2, \dots, m_{3+m}) V^{\nu T}. \quad (2.21)$$

715 Using this eigendecomposition, the neutrino mass term can be expressed as:

$$-\mathcal{L}_{M_\nu} = \frac{1}{2} \sum_{i=1}^{3+m} m_i \bar{\nu}_{Mi} \nu_{Mi}, \quad (2.22)$$

716 where the states ν_{Mi} , commonly referred to as Majorana neutrinos, are defined as:

$$\nu_{Mi} = \left(V^{\nu\dagger} \nu \right)_i + \left(V^{\nu\dagger} \nu \right)_i^c, \quad (2.23)$$

717 in such a way that the Majorana condition, $\nu_M^c = \nu_M$, holds true.

2.4. NEUTRINO OSCILLATION FORMALISM

718 As a consequence of the Majorana condition, the neutrino and the antineutrino states
 719 can be described in terms of a single field. As opposed to the charged leptons, which
 720 need to be represented by a four-component or Dirac spinor, the Majorana neutrino is
 721 described by a two-component or Weyl spinor.

722 If the eigenvalues of the Majorana mass matrix, M_N , are much larger than the
 723 electroweak symmetry breaking scale, the diagonalisation of M_ν leads to 3 light and m
 724 heavy neutrino states:

$$-\mathcal{L}_{M_\nu} = \frac{1}{2}\bar{\nu}_l M_l \nu_l + \frac{1}{2}\bar{\nu}_h M_h \nu_h, \quad (2.24)$$

725 where the two mass matrices are given by:

$$\begin{aligned} M_l &\simeq -V_l^T M_D^T M_N^{-1} M_D V_l, \\ M_h &\simeq V_h^T M_N V_h, \end{aligned} \quad (2.25)$$

726 with V_l and V_h two unitary matrices.

727 This scenario represents the so-called see-saw mechanism [35–39]. The name comes
 728 from the fact that the masses of the heavy states are proportional to M_N , whereas for
 729 the light states they are proportional to M_N^{-1} . While both the heavy and the light
 730 neutrinos are Majorana particles, it can be shown that the heavy states are mainly
 731 right-handed, whereas the light ones are mostly left-handed.

732 2.4 Neutrino oscillation formalism

733 Neutrino oscillations were first proposed in 1958 by B. Pontecorvo [40], inspired by the
 734 neutral kaon oscillation phenomenon [41]. Neutral kaons, K^0 and \bar{K}^0 , have opposite
 735 strangeness (± 1) and are produced in strong processes. It was observed that, when
 736 having a beam initially pure of neutral kaons of one type, these would transition into
 737 their antiparticles while propagating. Because the weak interaction does not conserve
 738 strangeness, neutral kaons can change their identity via the processes shown in Fig. 2.3.

739 The mixing considered initially by Pontecorvo was between the neutrino and the

CHAPTER 2. NEUTRINO PHYSICS

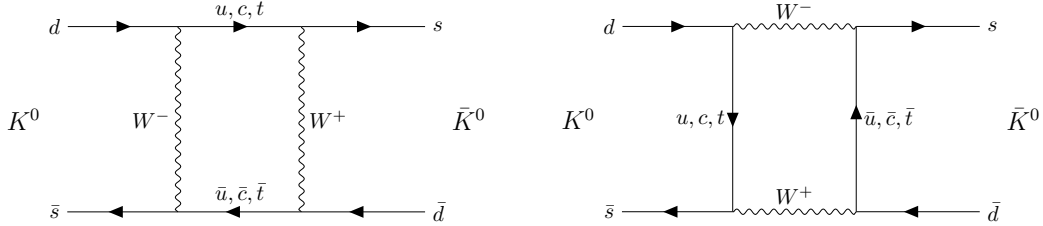


Figure 2.3: $K^0 \rightleftharpoons \bar{K}^0$ mixing through W^\pm exchange.

740 antineutrino states, as only one neutrino flavour was known at the time. After the
 741 discovery of the muon neutrino, the mixing between flavours was also explored [42].

742 In the general case, we have 3 active and m sterile neutrinos, resulting in $3 + m$
 743 neutrino mass eigenstates. Working in the mass basis, the leptonic charged-current
 744 Lagrangian can be written as:

$$-\mathcal{L}_{CC}^{lep} = \frac{g}{\sqrt{2}} (\bar{e}_L, \bar{\mu}_L, \bar{\tau}_L) \gamma^\mu U \begin{pmatrix} \nu_1 \\ \nu_2 \\ \vdots \\ \nu_{3+m} \end{pmatrix} W_\mu^+ + \text{h.c.}, \quad (2.26)$$

745 where U is a $3 \times (3 + m)$ matrix which obeys $UU^\dagger = I_{3 \times 3}$, but in general will not be
 746 unitary, $U^\dagger U \neq I_{(3+m) \times (3+m)}$.

747 The leptonic mixing matrix, U , establishes how the neutrino mass states couple to
 748 the charged leptons. In general, a complex $n \times n$ matrix can be fully specified by $2n^2$ real
 749 parameters. If the matrix is unitary, then the number of independent parameters reduces
 750 to n^2 , as one has to impose n normalisation and $n(n - 1)$ orthogonality constraints.
 751 In our case, we can further reduce the number of parameters by performing a phase
 752 redefinition of the charged lepton fields, without affecting the physics. This is not true
 753 for the neutrinos. As they may be their own antiparticles, one is not allowed to remove
 754 any physically relevant phases. If we consider n generations of leptons, the total number
 755 of parameters in the mixing matrix is $n^2 - n$. Out of these, half of them are mixing
 756 angles, while the other half are complex phase factors.

757 Considering the extended SM without any additional sterile neutrino states, the
 758 resulting 3×3 mixing matrix is unitary. This matrix, often called the Pontecorvo-Maki-

2.4. NEUTRINO OSCILLATION FORMALISM

759 Nakagawa-Sakata (PMNS) matrix [43, 44], relates the set of active neutrinos and the
760 three mass eigenstates as:

$$|\nu_\alpha\rangle = \sum_{i=1}^3 U_{\alpha i}^* |\nu_i\rangle, \quad (2.27)$$

761 where the Greek index α denotes the flavour $\{e, \mu, \tau\}$ and the Latin index i the mass state
762 $\{1, 2, 3\}$. This leptonic mixing matrix may be parametrized in terms of 6 parameters, 3
763 of which are mixing angles θ_{12} , θ_{13} and θ_{23} , one CP-violating phase δ_{CP} and 2 Majorana
764 phases α and β :

$$U = \begin{pmatrix} 1 & 0 & 0 \\ 0 & c_{23} & s_{23} \\ 0 & -s_{23} & c_{23} \end{pmatrix} \begin{pmatrix} c_{13} & 0 & s_{13} e^{-i\delta_{CP}} \\ 0 & 1 & 0 \\ -s_{13} e^{i\delta_{CP}} & 0 & c_{13} \end{pmatrix} \begin{pmatrix} c_{12} & s_{12} & 0 \\ -s_{12} & c_{12} & 0 \\ 0 & 0 & 1 \end{pmatrix} \begin{pmatrix} 1 & 0 & 0 \\ 0 & e^{i\alpha} & 0 \\ 0 & 0 & e^{i\beta} \end{pmatrix}, \quad (2.28)$$

765 where $c_{ij} \equiv \cos \theta_{ij}$ and $s_{ij} \equiv \sin \theta_{ij}$. This matrix is analogous to the Cabibbo-Kobayashi-
766 Maskawa (CKM) matrix in the quark sector. If neutrinos are Dirac fermions, we can
767 drop the Majorana phases in the PMNS matrix, as in this case we can perform the
768 phase redefinitions. However, these phases play no role on the neutrino oscillation
769 phenomenology.

770 In the case that additional sterile neutrinos states are present, the full leptonic mixing
771 matrix would not be unitary in general. For instance, in the see-saw scenario, the 3×3
772 submatrix for the three light Majorana neutrinos is not unitary. However, the deviations
773 from unitarity are of the order $\mathcal{O}(M_D/M_N)$, and therefore expected to be negligible.

774 2.4.1 Oscillations in vacuum

775 Consider the case where a neutrino of flavour α is produced at $t = 0$, and then it
776 propagates through vacuum. Such a state will evolve in time according to the relation:

$$|\nu_\alpha(\vec{x}, t)\rangle = \sum_{i=1}^3 U_{\alpha i}^* e^{-i(E_i t - \vec{p}_i \cdot \vec{x})} |\nu_i(\vec{x} = \vec{0}, t = 0)\rangle, \quad (2.29)$$

777 in the plane wave approximation, as the mass eigenstates are also eigenstates of the free
778 Hamiltonian.

CHAPTER 2. NEUTRINO PHYSICS

779 This way, the probability for the neutrino to transition from flavour α to flavour β

780 will be given by:

$$P(\nu_\alpha \rightarrow \nu_\beta) = |\langle \nu_\beta | \nu_\alpha(\vec{x}, t) \rangle|^2 = \left| \sum_{i=1}^3 \sum_{j=1}^3 U_{\alpha i}^* U_{\beta j} e^{-i(E_i t - \vec{p}_i \cdot \vec{x})} \langle \nu_j | \nu_i \rangle \right|^2 \\ = \left| \sum_{i=1}^3 U_{\alpha i}^* U_{\beta i} e^{-i(E_i t - \vec{p}_i \cdot \vec{x})} \right|^2, \quad (2.30)$$

781 where we have used the orthogonality relation $\langle \nu_i | \nu_j \rangle = \delta_{ij}$. A usual approximation to

782 take at this point is to consider ultra-relativistic neutrinos, i.e. $p_i \simeq E$, so we can write

783 the dispersion relations as:

$$E_i = \sqrt{p_i^2 + m_i^2} \approx E + \frac{m_i^2}{2E}. \quad (2.31)$$

784 In the end, assuming $t \approx L$ where L is the distance between the production and the

785 detection points, the probability for the $\nu_\alpha \rightarrow \nu_\beta$ transition becomes:

$$P(\nu_\alpha \rightarrow \nu_\beta) = \sum_{i,j} U_{\alpha i}^* U_{\beta i} U_{\alpha j} U_{\beta j} e^{-i \frac{\Delta m_{ij}^2}{2E} L} \\ = \delta_{\alpha\beta} - 4 \sum_{i < j} \Re [U_{\alpha i}^* U_{\beta i} U_{\alpha j} U_{\beta j}^*] \sin^2 \left(\frac{\Delta m_{ij}^2}{4E} L \right) \\ + 2 \sum_{i < j} \Im [U_{\alpha i}^* U_{\beta i} U_{\alpha j} U_{\beta j}^*] \sin \left(\frac{\Delta m_{ij}^2}{2E} L \right), \quad (2.32)$$

786 where Δm_{ij}^2 is the difference of the squared masses of the j th and i th neutrino mass

787 eigenvalues. At this point, it is usual to write the phase responsible for the oscillations

788 as:

$$\Delta_{ij} \equiv \frac{\Delta m_{ij}^2}{4E} L \simeq 1.27 \frac{\Delta m_{ij}^2}{(\text{eV}^2)} \frac{L}{(\text{km})} \frac{(\text{GeV})}{E}. \quad (2.33)$$

789 Notice that, in the case of antineutrinos, the only difference would be the sign of the

790 last term in the oscillation probability. As the process $\bar{\nu}_\alpha \rightarrow \bar{\nu}_\beta$ is the CP-mirror image

791 of $\nu_\alpha \rightarrow \nu_\beta$, the differences between their oscillation probabilities would be a measure of

2.4. NEUTRINO OSCILLATION FORMALISM

792 CP symmetry violation:

$$\begin{aligned} A_{CP}^{\alpha\beta} &= P(\nu_\alpha \rightarrow \nu_\beta) - P(\bar{\nu}_\alpha \rightarrow \bar{\nu}_\beta) \\ &= 4 \sum_{i<j} \Im \left[U_{\alpha i}^* U_{\beta i} U_{\alpha j} U_{\beta j}^* \right] \sin 2\Delta_{ij}. \end{aligned} \quad (2.34)$$

793 Assuming that CPT invariance holds, then the following relation must be true:

$$P(\nu_\alpha \rightarrow \nu_\beta) = P(\bar{\nu}_\beta \rightarrow \bar{\nu}_\alpha), \quad (2.35)$$

794 as these two process are related by the CPT symmetry. From the definition of probability,
795 we also must have:

$$\sum_{\beta} P(\nu_\alpha \rightarrow \nu_\beta) = \sum_{\beta} P(\bar{\nu}_\alpha \rightarrow \bar{\nu}_\beta) = 1, \quad (2.36)$$

796 where the sum includes all flavours, including α . From these two constraints, one can
797 probe that:

$$A_{CP}^{\alpha\beta} = -A_{CP}^{\beta\alpha}, \quad (2.37)$$

798 and in particular:

$$A_{CP}^{\alpha\alpha} = 0. \quad (2.38)$$

799 A direct consequence of this last relation is that there are no observable CP-violating
800 effects in the so-called disappearance experiments. One needs to perform appearance
801 experiments, where the flavour detected is different from the original flavour, in order
802 to measure the CP asymmetry. Neutrino experiments often report the amount of CP-
803 violation through the Jarlskog invariant. In terms of the parametrisation typically used
804 to write the PMNS matrix, it is given by:

$$J = \frac{1}{8} \cos \theta_{13} \sin 2\theta_{12} \sin 2\theta_{13} \sin 2\theta_{23} \sin \delta_{CP}. \quad (2.39)$$

805 The Jarlskog invariant can be used to compare the amount of CP-violation in the lepton
806 and the quark sectors, where $J = 3.12^{+0.13}_{-0.12} \times 10^{-5}$ in the latter [45].

CHAPTER 2. NEUTRINO PHYSICS

2.4.2 Oscillations in matter

When neutrinos propagate through matter, their oscillation can be affected in mainly two ways. First, neutrinos can inelastically scatter with nuclei, thus destroying the coherent propagation of their quantum state. Nevertheless, in most cases this effect is negligible (even in very dense mediums like the core of the Sun). Second, neutrinos can also experience coherent or forward scatterings, that can affect their oscillation but not lose the coherent propagation of the state.

The first proposed model to account for neutrino oscillations in matter was proposed by Mikhaev, Smirnov and Wolfenstein (MSW) [46]. It relies on the fact that, as the only charged lepton present in ordinary matter is the electron, electron neutrinos can undergo both charged and neutral-current interactions with matter whereas for muon and tau neutrinos just neutral currents are possible.

An illustrative way to introduce the MSW mechanism is by considering the two flavours case. It can be shown that the evolution of the two flavour eigenstates in vacuum is given by the following time-dependent Schrödinger equation:

$$i \frac{d}{dt} \begin{pmatrix} \nu_e \\ \nu_\mu \end{pmatrix} = H_V \begin{pmatrix} \nu_e \\ \nu_\mu \end{pmatrix}, \quad (2.40)$$

with a vacuum Hamiltonian given by:

$$H_V = \frac{\Delta m^2}{4E} \begin{pmatrix} -\cos 2\theta & \sin 2\theta \\ \sin 2\theta & \cos 2\theta \end{pmatrix}, \quad (2.41)$$

where Δm^2 is the mass splitting between the two neutrino states and θ the only mixing angle. For simplicity, I omit the terms of the Hamiltonian that are proportional to the identity, as they do not affect the oscillation phenomenology.

The NC contribution to the matter potential is identical for all the flavours, and has the form:

$$V_{NC} = -\frac{G_F}{\sqrt{2}} N_n(x), \quad (2.42)$$

2.4. NEUTRINO OSCILLATION FORMALISM

828 where G_F is the Fermi constant and $N_n(x)$ the local neutron density. Because it is
 829 common to all flavours, I do not take it into account in the effective Hamiltonian, as it
 830 would appear as a term proportional to the identity. The CC component only affects
 831 the electron neutrino (and antineutrino). It can be written as:

$$V_{\text{CC}} = \pm \sqrt{2} G_F N_e(x), \quad (2.43)$$

832 with $N_e(x)$ being the local electron density in the material. In the end, the effective
 833 Hamiltonian which describes the propagation of the flavour eigenstates in matter only
 834 contains an extra $\nu_e - \nu_e$ element:

$$H_M = H_V + \begin{pmatrix} V_{\text{CC}} & 0 \\ 0 & 0 \end{pmatrix}. \quad (2.44)$$

835 The solution to the Schrödinger equation greatly simplifies if one considers the case
 836 of a constant matter density. In that case, the effective Hamiltonian can be diagonalised,
 837 obtaining the effective neutrino mass eigenstates in matter. It can be re-written in the
 838 same form as the vacuum Hamiltonian:

$$H_M = \frac{\Delta m_m^2}{4E} \begin{pmatrix} -\cos 2\theta_m & \sin 2\theta_m \\ \sin 2\theta_m & \cos 2\theta_m \end{pmatrix}, \quad (2.45)$$

839 where the effective mass splitting and the effective mixing angle are given by:

$$\begin{aligned} \Delta m_m^2 &= \lambda \Delta m_m^2, \\ \sin 2\theta_m &= \frac{\sin 2\theta_m}{\lambda} \end{aligned} \quad (2.46)$$

840 with:

$$\begin{aligned} \lambda &= \sqrt{(\cos 2\theta - A)^2 + \sin^2 2\theta}, \\ A &= \pm \frac{2\sqrt{2} G_F N_e E}{\Delta m^2}. \end{aligned} \quad (2.47)$$

841 In terms of the effective matter oscillation parameters, the transition probability

CHAPTER 2. NEUTRINO PHYSICS

842 $\nu_e \rightarrow \nu_\mu$ (in the two flavour approximation) reads:

$$P(\nu_e \rightarrow \nu_\mu) = \sin^2 2\theta_m \sin^2 \left(\frac{\Delta m_m^2}{2E} L \right) \quad (2.48)$$

843 From this last equation one can see that, when $\cos 2\theta = A > 0$ the oscillations are
844 greatly enhanced. This effect is known as the MSW resonance. For the neutrinos, this
845 resonant condition is only satisfied if $\Delta m^2 > 0$ (the opposite is true for antineutrinos).
846 This is can be exploited by long baseline experiments, which can gain sensitivity to the
847 neutrino mass hierarchy through matter effects.

848 2.4.3 Current status of neutrino oscillations

849 A wide range of neutrino experiments provide experimental input to the neutrino
850 oscillation framework, both using natural or synthetic neutrino sources. The results
851 from one of the neutrino global fit analyses, shown in Tab. 2.3¹, summarise well our
852 current understanding of the different oscillation parameters.

853 **Solar neutrino experiments** detect neutrinos produced in thermonuclear reactions
854 inside the Sun, mainly from the so-called *pp* chain and the CNO cycle. These neutrinos
855 have a typical energy in the range from 0.1 to 20 MeV. These experiments (Homestake
856 [47], GALLEX [26], SAGE [25], Borexino [48], Super-Kamiokande [49] and SNO [50])
857 provide the best sensitivities to θ_{12} and Δm_{21}^2 .

858 **Atmospheric neutrino experiments** detect the neutrino flux produced when
859 cosmic rays scatter with particles in Earth's atmosphere. These collisions generate particle
860 showers that eventually produce electron and muon neutrinos (and antineutrinos). Their
861 energies range from few MeV to about 10^9 GeV. Experiments, like Super-Kamiokande
862 [51] and IceCube [52] use atmospheric neutrinos to measure oscillations and are specially
863 sensitive to θ_{23} and Δm_{32}^2 .

864 **Reactor neutrino experiments** look for the $\bar{\nu}_e$ spectrum produced by nuclear
865 reactors, with energies in the MeV scale. Depending on the distance to the source,

¹These are the results reported during M. Tórtola's talk at Neutrino 2024 (see this link). I need to keep an eye and see if they publish these or other updated results in the near future.

2.5. OPEN QUESTIONS IN THE NEUTRINO SECTOR

Table 2.3: Summary of neutrino oscillation parameters determined in the Neutrino Global Fit of 2020 [14].

Parameter	Best fit $\pm 1\sigma$	3σ range
Δm_{21}^2 [eV $^2 \times 10^{-5}$]	$7.55^{+0.22}_{-0.20}$	6.98 – 8.19
$ \Delta m_{31}^2 $ [eV $^2 \times 10^{-3}$] (NO)	$2.51^{+0.02}_{-0.03}$	2.43 – 2.58
$ \Delta m_{31}^2 $ [eV $^2 \times 10^{-3}$] (IO)	$2.41^{+0.03}_{-0.02}$	2.34 – 2.49
$\sin^2 \theta_{12}/10^{-1}$	3.04 ± 0.16	2.57 – 3.55
$\sin^2 \theta_{23}/10^{-1}$ (NO)	$5.64^{+0.15}_{-0.21}$	4.23 – 6.04
$\sin^2 \theta_{23}/10^{-1}$ (IO)	$5.64^{+0.15}_{-0.18}$	4.27 – 6.03
$\sin^2 \theta_{13}/10^{-2}$ (NO)	$2.20^{+0.05}_{-0.06}$	2.03 – 2.38
$\sin^2 \theta_{13}/10^{-2}$ (IO)	$2.20^{+0.07}_{-0.04}$	2.04 – 2.38
δ_{CP}/π (NO)	$1.12^{+0.16}_{-0.12}$	0.76 – 2.00
δ_{CP}/π (IO)	$1.50^{+0.13}_{-0.14}$	1.11 – 1.87

866 long-baseline experiments like KamLAND [53] are sensitive to the solar mass splitting
867 Δm_{21}^2 whereas much shorter baseline experiment such as RENO [54] or DayaBay [55]
868 measure θ_{13} and Δm_{31}^2 .

869 **Accelerator experiments** measure neutrino fluxes generated in particle accelerators.
870 Usually mesons are produced in the accelerator to be focused into a beam, then some
871 decay to muon neutrinos and the rest are absorbed by a target. Depending on the
872 configuration one can obtain a beam made of mostly neutrinos or antineutrinos. The
873 typical energies of these neutrinos are in the GeV range. Experiments such as NOvA
874 [56], T2K [57], MINOS [58], OPERA [59] and K2K [60] (and in the future DUNE [61])
875 are primarily sensitive to θ_{13} , θ_{23} and Δm_{32}^2 . Also, in the coming years DUNE [61] and
876 Hyper-Kamiokande [62] will be sensitive to δ_{CP} .

877 2.5 Open questions in the neutrino sector

878 A crucial question that remains open these days, and is of vital importance for oscillation
879 phenomena, is whether the mass eigenvalue ν_3 is the heaviest (what we call normal
880 ordering) or the lightest (referred to as inverted ordering) of the mass eigenstates. In

CHAPTER 2. NEUTRINO PHYSICS

other words, this means that we do not know the sign of Δm_{32}^2 , so we can either have $m_1 < m_2 < m_3$ (NO) or $m_3 < m_1 < m_2$ (IO).

Another big puzzle is related to the value of δ_{CP} . Nowadays it is poorly constrained, with all values between π and 2π being consistent with data. A prospective measurement different from $\delta_{CP} = 0, \pi$ will predict CP-violation in the leptonic sector, and thus contribute along with the one measured in the quark sector to the total amount of CP-violation. Although it is true that these two contributions by themselves are not enough to explain the matter anti-matter asymmetry in our universe, the amount of CP-violation in the leptonic sector can be key to explain such imbalance.

Both of these questions, because of their nature, could be understood thanks to future oscillation experiments.

Notwithstanding, there are other mysteries that can not be unveiled just by conducting oscillation experiments, as certain quantities do not influence these phenomena. Among these there is the question of the absolute values of the neutrino masses. Depending on the value of the lightest of the neutrino masses we can have different mass spectra, from hierarchical $m_1 \ll m_2 < m_3$ (NO) or $m_3 \ll m_1 < m_2$ (IO) to quasi-degenerate $m_1 \simeq m_2 \simeq m_3$.

Other open question concerns the nature itself of the neutrinos. If neutrinos are Dirac particles then their mass term can be generated through the usual Higgs mechanism by adding right-handed neutrino fields. However, if they are Majorana particles and therefore their own antiparticles, there is no need to add extra fields to have the mass term in the Lagrangian. Experiments like SuperNEMO [63], SNO+ [64] and NEXT [65], which search for neutrino-less double beta decay, will be able to determine whether neutrinos are Dirac or Majorana.

2.6 Neutrino interactions

The study of neutrino-nucleus interactions is of great importance for long baseline neutrino oscillation experiments. The interaction model provides a mapping between

2.6. NEUTRINO INTERACTIONS

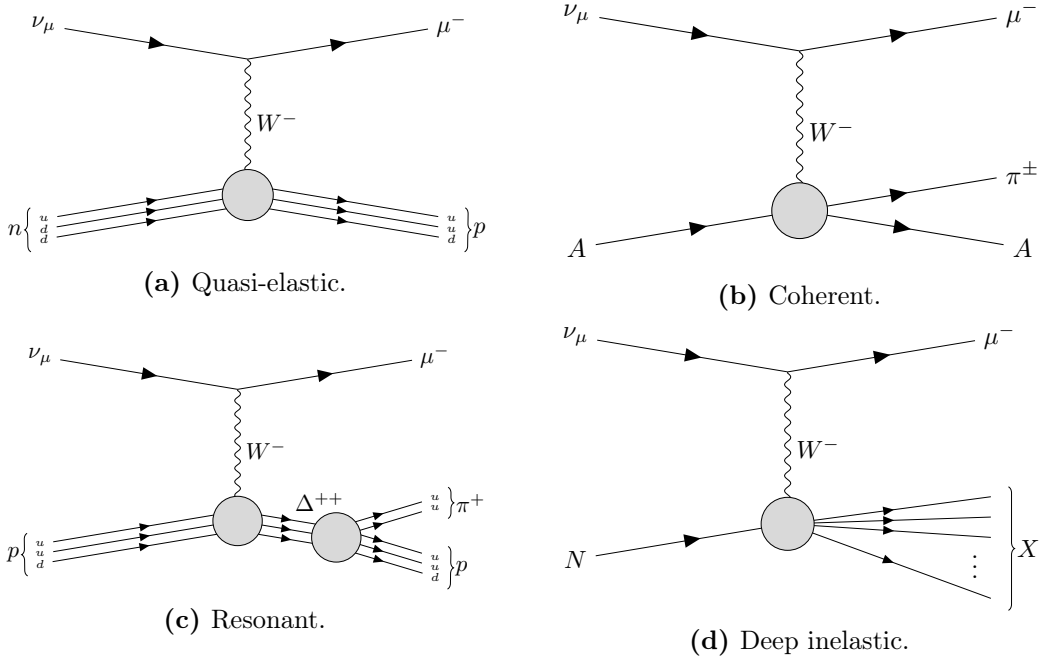


Figure 2.4: Feynman diagrams of the four most relevant CC interactions to long baseline neutrino oscillation experiments.

the energy of the incoming neutrino and the final state particles after the interaction.
 Because in this kind of experiments neutrinos are obtained as secondary decay products of mesons, typically charged pions and kaons, their energies are not known a priori. Not only that, but the kinematics of the interacting nucleon are also unknown. Therefore, we rely on the neutrino interaction models to provide this relation between the observables in the detector and the true kinematics of the neutrino. Interaction modelling is expected to be the one of the leading sources of systematic uncertainties in the next generation of long baseline experiments [66–68].

In the case of neutrino interactions with nuclei at the energies relevant for long baseline oscillation experiments, cross section for the neutrino-nucleon interaction. Figure 2.4 shows examples of the four most common neutrino CC interactions.

At low energies, below 1 GeV, quasi-elastic (QE) interactions dominate. In a CCQE interaction a neutrino (antineutrino) interacts with a neutron (proton), converting it into a proton (neutron) which is then ejected from the nucleus together with the resulting charged lepton. At energies above 1 GeV the neutrino is able to excite the nucleon

CHAPTER 2. NEUTRINO PHYSICS

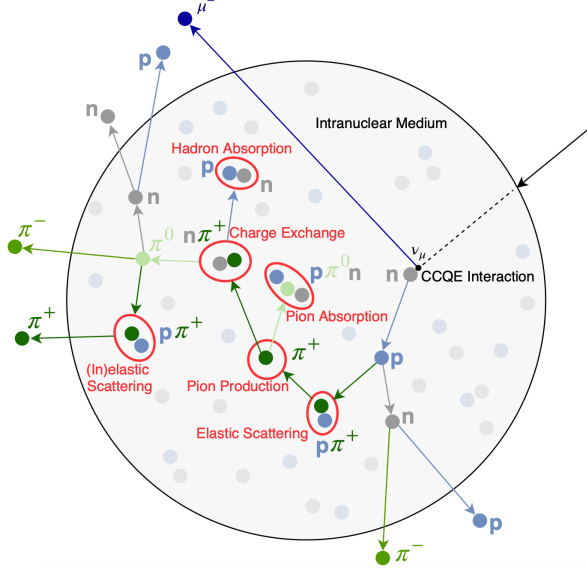


Figure 2.5: Schematic representation of a ν_μ CCQE interaction with a neutron inside a nucleus. The reaction produces a muon and a proton, which travel through the nuclear medium. The outgoing proton undergoes various kinds of hadronic FSIs on its way out. Figure taken from Ref. [69].

923 into a baryonic resonance, which promptly decays into a nucleon and a pion. These are
 924 the so-called resonant (RES) interactions. Neutrinos also interact with entire nucleus
 925 coherently, in the process known as coherent (COH) interaction. This kind of reactions
 926 also produce a single pion in the final state. At high neutrino energies, above 5 GeV,
 927 deep inelastic scattering (DIS) takes place. In these processes, the neutrino interacts
 928 with a single quark within the nucleon, breaking the nucleon and producing a hadronic
 929 shower.

930 Nuclear effects alter the neutrino cross section, as well as the final states particles.
 931 There are several models available to describe the initial state of the nucleus, like the
 932 relativistic Fermi gas model, spectral functions or the random phase approximation.
 933 Figure 2.5 illustrates the effects of FSI on the observable particle content in the detector
 934 after a ν_μ CCQE interaction.

3

The Deep Underground Neutrino Experiment

938 The Deep Underground Neutrino Experiment (DUNE) is a next generation long-baseline
939 neutrino experiment [70]. It will aim to address several questions in neutrino physics,
940 study neutrinos from astrophysical sources and search for beyond the standard model
941 physics.

This chapter reviews the main goals of the DUNE experiment, the design of the far detector modules and their data acquisition (DAQ) system, and the role that the near detector plays in the physics program of DUNE.

945 3.1 Overview

⁹⁴⁶ The main physics goals of DUNE are:

- measure the neutrino mass hierarchy, the amount of CP violation in the leptonic sector and the θ_{23} octant,
 - detect rare low energy neutrino events, like neutrinos from supernova bursts, and
 - search for proton decay and other beyond the standard model phenomena.

The design of DUNE has been tailored with these goals in mind. It will consist of two neutrino detectors. A near detector (ND) complex will be placed at Fermilab, 574 m downstream of the neutrino production point, whereas a larger far detector

CHAPTER 3. THE DEEP UNDERGROUND NEUTRINO EXPERIMENT

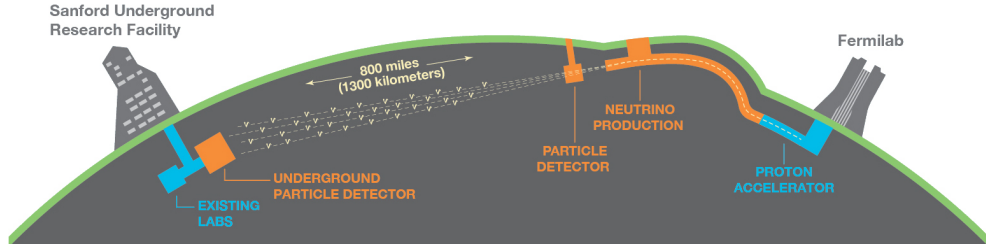


Figure 3.1: Schematic diagram of the DUNE experiment and the LBNF beamline [70].

954 (FD) will be built in the Sandford Underground Research Facility (SURF), South
 955 Dakota, approximately 1300 km away. Figure 3.1 shows a simplified view of the various
 956 components of DUNE (not to scale).

957 The beam neutrinos will be provided by the Long-Baseline Neutrino Facility (LBNF)
 958 beamline, the multi-megawatt wide-band neutrino beam planned for Fermilab. It will
 959 produce neutrinos travelling in the direction of SURF, with the capability to switch
 960 between neutrino and antineutrino mode.

961 Before arriving to the FD, the neutrino beam meets the ND complex, which serves
 962 as the experiment's control. The design of the DUNE ND is mainly driven by the
 963 needs of the oscillation physics program, as its main role is to measure the unoscillated
 964 neutrino energy spectra. From these we can predict the unoscillated spectra at the FD,
 965 which can be compared to the spectra measured at the FD to extract the oscillation
 966 parameters. Additionally, the ND has a physics programme of its own, including cross
 967 section measurements and BSM physics searches.

968 The technology chosen for the FD modules of DUNE is the liquid Argon time
 969 projection chamber (LArTPC). Its four modules will record neutrino interactions from
 970 the accelerator-produced beam arriving at predictable times. As it also aims at recording
 971 rare and low energy events, like supernovae and solar neutrinos, the FD requires trigger
 972 schemes which can deal with both kinds of physics, and also maximum uptime.

973 DUNE is planned to be built using a staged approach consisting on two phases,
 974 which are summarised in Tab. 3.1. Phase I consists of a FD with 50% of the total

3.2. PHYSICS GOALS OF DUNE

Table 3.1: Summary of the two-phased plan for DUNE. Adapted from Ref. [71].

Parameter	Phase I	Phase II	Benefit
FD mass	20 kt fiducial	40 kt fiducial	FD statistics
Beam power	up to 1.2 MW	2.4 MW	FD statistics
ND config.	ND-LAr, TMS, SAND	ND-LAr, ND-GAr, SAND	Systematic constraints

Table 3.2: Exposure and time required to achieve the different physics milestones of the two phases. The predictions assume a Phase II staging scenario where FD modules 3 and 4 are deployed in years 4 and 6 and both the beam and ND are upgraded after 6 years. Adapted from Ref. [71].

Stage	Physics milestone	Exposure (kt-MW-years)	Years (staged)
Phase I	5σ MO ($\delta_{CP} = -\pi/2$)	16	1-2
	5σ MO (100% of the δ_{CP} values)	66	3-5
	3σ CPV ($\delta_{CP} = -\pi/2$)	100	4-6
Phase II	5σ CPV ($\delta_{CP} = -\pi/2$)	334	7-8
	δ_{CP} resolution of 10 degrees ($\delta_{CP} = 0$)	400	8-9
	5σ CPV (50% of the δ_{CP} values)	646	11
	3σ CPV (75% of the δ_{CP} values)	936	14
	$\sin^2(2\theta_{13})$ resolution of 0.004	1079	16

975 fiducial mass, a reduced version of the ND complex and a 1.2 MW proton beam. It will
 976 be sufficient to achieve some early physics goals, like the determination of the neutrino
 977 mass ordering. For its Phase II, DUNE will feature the full four FD modules, a more
 978 capable ND and a 2.4 MW proton beam. The physics milestones for the two phases are
 979 given in Tab. 3.2, in a staging scenario which assumes that Phase II is completed after
 980 6 years of operation.

981 A summary of the DUNE science program can be found in the DUNE FD Technical
 982 Design Report (TDR) Volume I [70]. For a detailed discussion on the two-phased
 983 approach the reader is referred to the DUNE Snowmass 2021 report [71].

984 3.2 Physics goals of DUNE

985 As noted in the literature (see for instance Ref. [14] for a review), the parameter space of
 986 the neutrino oscillation phenomena within the three-flavour picture is quite constrained

CHAPTER 3. THE DEEP UNDERGROUND NEUTRINO EXPERIMENT

987 by current experimental data. However, there are still crucial open questions, like the
988 mass ordering, the value of δ_{CP} or the θ_{23} octant. One of the main goals of DUNE is to
989 determine precisely the values of these parameters [72].

990 To address these questions DUNE can look to the subdominant oscillation channel
991 $\nu_\mu \rightarrow \nu_e$ ($\bar{\nu}_\mu \rightarrow \bar{\nu}_e$) and study the energy dependence of the ν_e ($\bar{\nu}_e$) appearance probability.
992 When we focus on the antineutrino channel $\bar{\nu}_\mu \rightarrow \bar{\nu}_e$ there is a change in the sign of δ_{CP} ,
993 thus introducing CP-violation. Moreover, due to the fact that there are no positrons in
994 the composition of Earth, there is a sign difference for the matter effect contribution
995 when looking to the antineutrino channel. This asymmetry is proportional to the baseline
996 length L and is sensitive to the sign of Δm_{31}^2 , and thus to the neutrino mass ordering.

997 Another of the main physics goals of DUNE is the search for baryon-number violating
998 processes. Specifically, it will try to answer the question of whether protons are stable
999 or not. There is no symmetry argument that forbids protons from decaying, but its
1000 apparent stability seems to suggest that baryon number is conserved [73]. However,
1001 proton decay is a usual feature of grand-unified theories, where electromagnetic, weak
1002 and strong interactions are unified above a certain energy scale [74].

1003 As the energy deposition scale for this kind of searches is nearly the same as the one
1004 for long-baseline neutrino oscillations, DUNE will be able to look for them. It has several
1005 advantages over other experiments, such as excellent imaging and particle identification,
1006 which can be translated to lower backgrounds.

1007 The last of the main objectives of DUNE is the detection of neutrinos originated in
1008 supernovae explosions, what is called a supernova neutrino burst (SNB). These neutrinos
1009 carry with them information about the core-collapse process, from the progenitor to the
1010 explosion and the remnant; but also may have information about new exotic physics. So
1011 far, the only neutrino events ever recorded from such a process were a few dozens of $\bar{\nu}_e$
1012 events from the 1987A supernova located in the Magellanic Cloud, 50 kpc away from
1013 Earth [75, 76].

1014 DUNE aims to collect SNB events. Although these are quite rare, as the expected
1015 supernovae explosion events are about one every few decades for our galaxy and

3.3. LBNF BEAMLINE

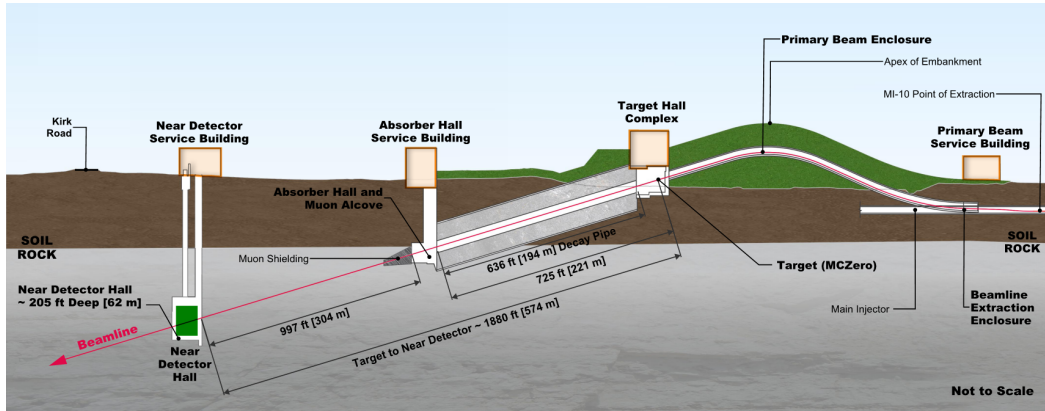


Figure 3.2: Schematic longitudinal section of the LBNF beamline at Fermilab (not to scale). Figure taken from Ref. [77].

1016 Andromeda, the long lifetime of the experiment (around a few decades as well) makes it
 1017 reasonable to expect some. Nowadays the main sensitivity to SNB of most experiments
 1018 is to the $\bar{\nu}_e$ through inverse beta decay. One of the advantages of DUNE is its expected
 1019 sensitivity to ν_e , since the dominant channel will be ν_e CC scattering.

1020 Moreover, due to the stringent requirements that the main physics goals set for
 1021 DUNE, it will allow also to perform searches for all kind of BSM physics. Among
 1022 others, DUNE will be able to look for: active-sterile neutrino mixing, non-unitarity of
 1023 the PMNS matrix, non-standard interactions, Lorentz and CPT violations, neutrino
 1024 trident production, light-mass DM, boosted DM and heavy neutral leptons. The reader
 1025 is referred to the DUNE FD TDR Volume II [72] for a full discussion of the physics
 1026 scope of DUNE.

1027 3.3 LBNF beamline

1028 The LBNF project is responsible for producing the neutrino beam for the DUNE detectors.
 1029 A detailed discussion of the LBNF program can be found in the DUNE/LBNF CDR
 1030 Volume III [77].

1031 A schematic diagram of the longitudinal section of the LBNF beamline is shown in
 1032 Fig. 3.2. First, a beam of 60 – 120 GeV protons is extracted from the Fermilab Main
 1033 Injector. This beam is aimed towards the target area, where it collides with a cylindrical

CHAPTER 3. THE DEEP UNDERGROUND NEUTRINO EXPERIMENT

graphite target to produce pions and kaons.

The diffuse, secondary beam of particles is focused by a pair of magnetic horns. These select the positively charged particles when operated in Forward Horn Current (FHC) mode, or the negatively charged ones when the current is reversed, also known as Reverse Horn Current (RHC) mode. The focused secondary beam then enters a 194 m decay pipe where the pions and kaons will predominantly produce $\mu^+\nu_\mu$ pairs when in FHC mode (or $\mu^-\bar{\nu}_\mu$ in RHC mode).

At the end of the decay pipe a hadron absorber removes the undecayed hadrons and muons from the beam, which reduces the ν_e ($\bar{\nu}_e$) and ν_μ ($\bar{\nu}_\mu$) contamination coming from the μ^+ (μ^-) decays. The resulting neutrino flux at the FD is shown in Fig. 3.3, both for FHC (left) and RHC (right) modes. These predictions show the intrinsic ν_e contamination and wrong sign component from wrong sign and neutral meson decays, as well as muons decaying before reaching the absorber.

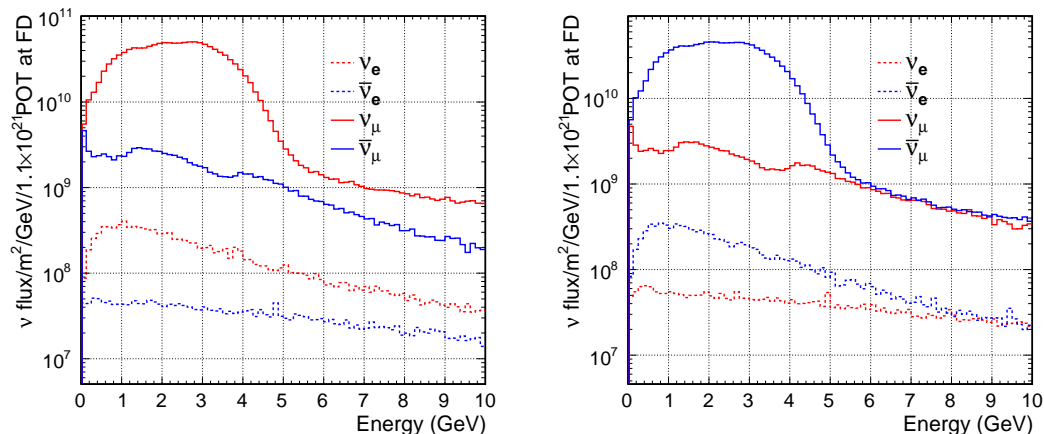


Figure 3.3: Predicted neutrino fluxes at the FD in FHC mode (left panel) and RHC mode (right panel). Figures taken from Ref. [72].

3.4 Near Detector

To estimate the oscillation parameters we measure the neutrino energy spectra at the FD. This reconstructed energy arises from a convolution of the neutrino flux, cross section, detector response and the oscillation probability. Using theoretical and empirical models

3.4. NEAR DETECTOR

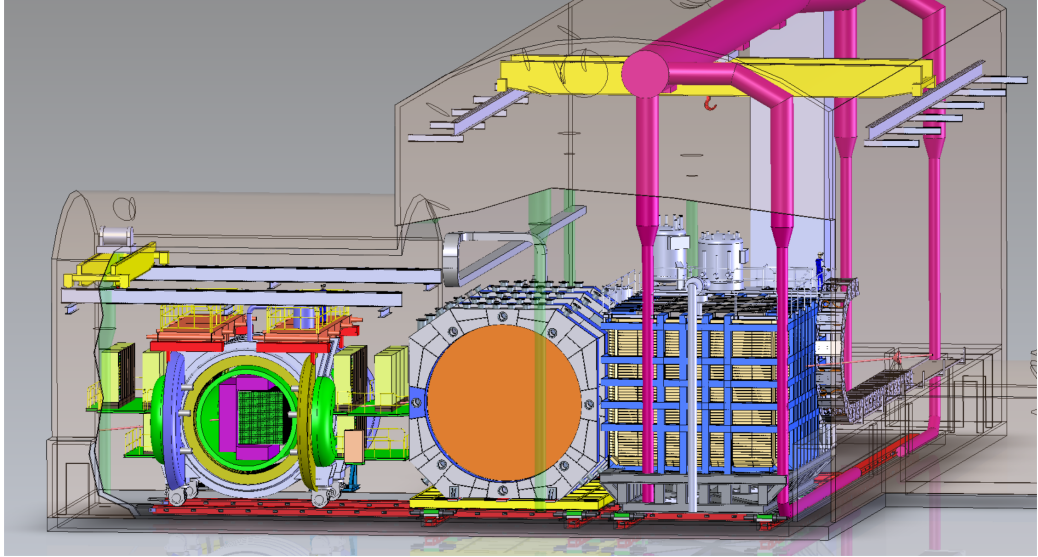


Figure 3.4: Representation of the ND hall in Phase II, showing the different subcomponents. From right to left, in the direction of the beam, we have ND-LAr, ND-GAr and SAND. Figure taken from Ref. [78].

1051 to account for the other effects, one can extract the oscillation probability using the
 1052 measurement. However, these models have associated a number of uncertainties that
 1053 are then propagated to the oscillation parameters.

1054 One of the main roles of the ND is to measure the neutrino interaction rates before
 1055 the oscillation effects become relevant, i.e. close to the production point. By measuring
 1056 the ν_μ and ν_e energy spectra, and that of their corresponding antineutrinos, at the ND
 1057 we can constrain the model uncertainties. A complete cancellation of the uncertainties
 1058 when taking the ratio between the FD and ND measurements is not possible, as that
 1059 would require both detectors to have identical designs and the neutrino fluxes to be
 1060 the same. Because of the distance, the flux probed by the FD will have a different
 1061 energy and flavour composition than that at the ND, as neutrinos oscillate and the beam
 1062 spreads. The differences in the flux also determine the design of the detectors, therefore
 1063 the ND is limited in its capability to match the FD design.

1064 Nevertheless, having a highly capable ND, DUNE can minimise the systematic
 1065 uncertainties affecting the observed neutrino energy. The ND data can be used to
 1066 tune the model parameters by comparison with the prediction. Then, one uses the

CHAPTER 3. THE DEEP UNDERGROUND NEUTRINO EXPERIMENT

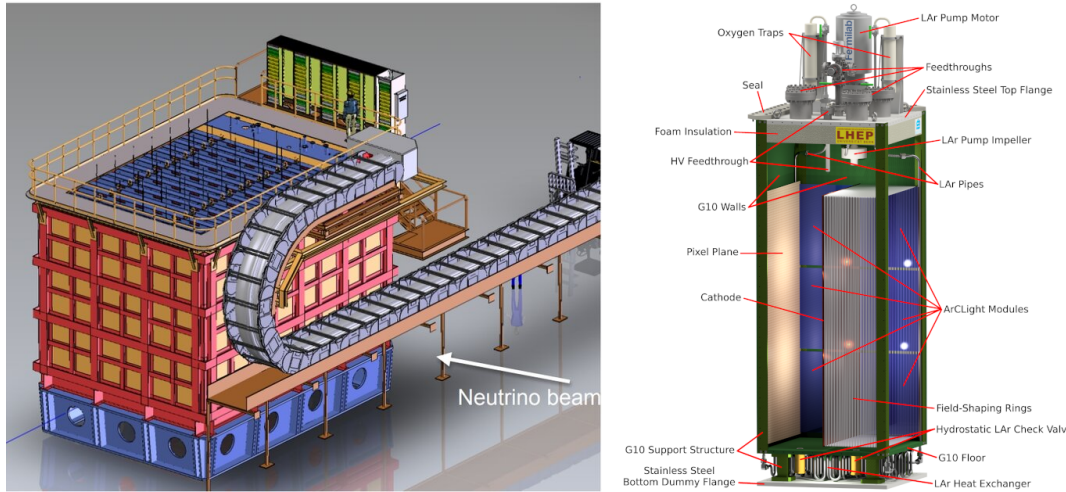


Figure 3.5: Schematic representation of the external components of ND-LAr, including the cryostat and the PRISM movable system (left) and detailed drawing of one ArgonCube module (right). Figure adapted from Ref. [70].

1067 tuned model to predict the unoscillated FD spectra. Comparing the prediction with the
 1068 measured spectra it is possible to extract the oscillation parameters.

1069 Additionally, the ND will have a physics program of its own. In particular, it will
 1070 measure neutrino cross sections that will then be used to constrain the model used in
 1071 the long-baseline oscillation analysis. It will also be used to search for BSM phenomena
 1072 such as heavy neutral leptons, dark photons, millicharged particles, etc.

1073 The DUNE ND can be divided in three main components, a LArTPC known as ND-
 1074 LAr, a magnetised muon spectrometer, which will be the Temporary Muon Spectrometer
 1075 (TMS) in Phase I and ND-GAr in Phase II, and the System for on-Axis Neutrino
 1076 Detection (SAND). The layout of the Phase II DUNE ND can be seen in Fig. 3.4. The
 1077 first two components of the ND will be able to move off-axis, in what is called the
 1078 Precision Reaction-Independent Spectrum Measurement (PRISM) concept. More details
 1079 on the purpose and design of the ND can be found in the DUNE ND Conceptual Design
 1080 Report (CDR) [78].

3.4. NEAR DETECTOR

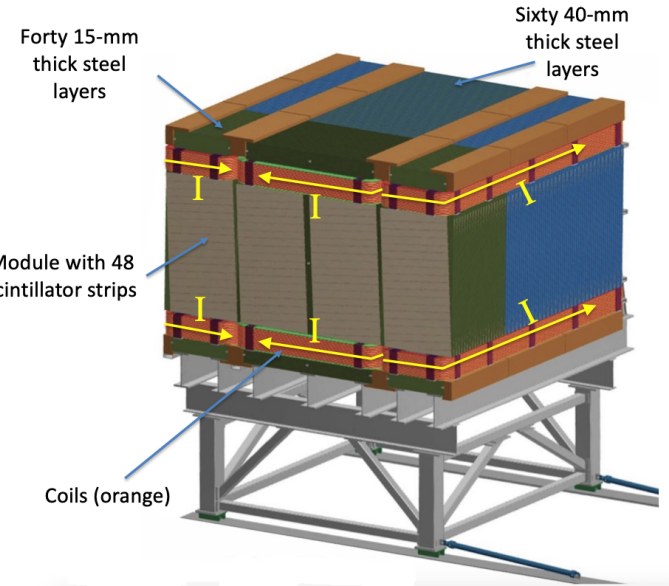


Figure 3.6: Schematic view of the TMS detector, highlighting its main parts. Figure adapted from Ref. [70].

1081 3.4.1 ND-LAr

1082 ND-LAr is a LArTPC, as the ND needs a LAr component to reduce cross section and
 1083 detector systematic uncertainties in the oscillation analysis. However, its design differs
 1084 significantly from those proposed for the FD modules. Because of the high event rates
 1085 at the ND, approximately 55 neutrino interaction events per $10 \mu\text{s}$ spill, ND-LAr will be
 1086 built in a modular way. Each of the modules, based on the ArgonCube technology, is a
 1087 fully instrumented, optically isolated TPC with a pixelated readout. The pixelisation
 1088 allows for a fully 3D reconstruction and the optical isolation reduces the problems due
 1089 to overlapping interactions. Figure 3.5 shows a representation of the external parts of
 1090 ND-LAr (left) and a detailed diagram of an ArgonCube module (right).

1091 With a fiducial mass of 67 t and dimensions $7 \text{ m} (\text{w}) \times 3 \text{ m} (\text{h}) \times 5 \text{ m} (\text{l})$, ND-LAr
 1092 will be able to provide high statistics and contain the hadronic systems from the beam
 1093 neutrino interactions, but muons with a momentum higher than 0.7 GeV will exit the
 1094 detector.

CHAPTER 3. THE DEEP UNDERGROUND NEUTRINO EXPERIMENT

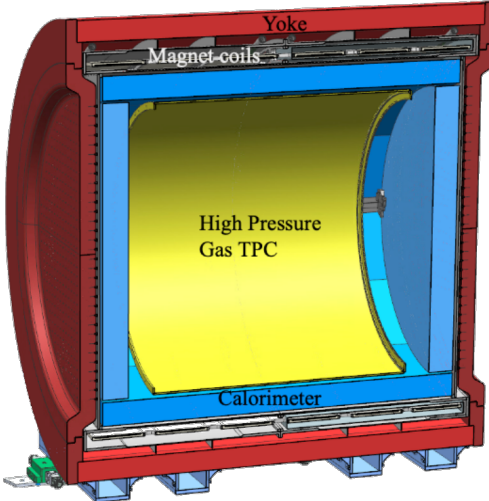


Figure 3.7: Cross section of the ND-GAr geometry, showing the HPgTPC, ECal and magnet. Figure adapted from Ref. [79].

1095 3.4.2 TMS/ND-GAr

1096 To accurately estimate the neutrino energy, the momentum of the outgoing muons needs
 1097 to be determined. That is the reason why a muon spectrometer is needed downstream
 1098 of ND-LAr.

1099 In Phase I that role will be fulfilled by TMS. It is a magnetised sampling calorimeter,
 1100 with alternating steel and plastic scintillator layers. Figure 3.6 shows a schematic view
 1101 of the TMS detector. The magnetic field allows a precise measurement of the sign of the
 1102 muon, so one can distinguish between neutrino and antineutrino interactions.

1103 After the Phase II upgrade, TMS will be replaced with a more capable near detector.
 1104 The current technology considered is ND-GAr. This detector is a magnetised, high-
 1105 pressure GAr TPC (often denoted as HPgTPC) surrounded by an electromagnetic
 1106 calorimeter (ECal) and a muon tagger. A cross section of its geometry can be seen
 1107 in Fig. 3.7. ND-GAr will be able to measure the momenta of the outgoing muons
 1108 while also detect neutrino interactions inside the GAr volume. This allows ND-GAr
 1109 to constrain the systematic uncertainties even further, as it will be able to accurately
 1110 measure neutrino interactions at low energies thanks to the lower tracking thresholds of
 1111 GAr.

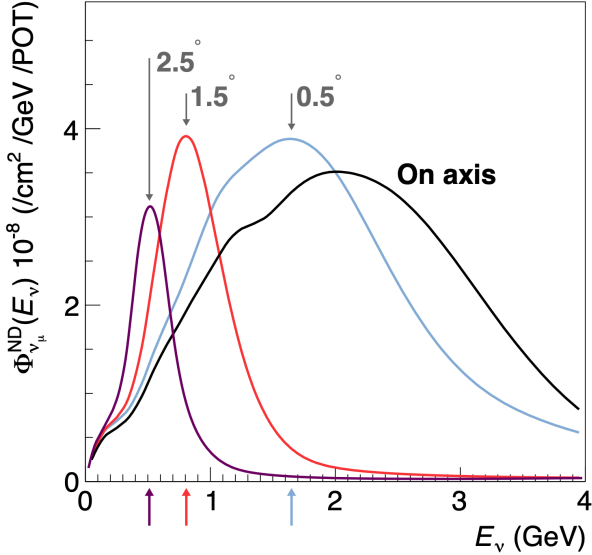


Figure 3.8: Predicted beam muon neutrino flux at the ND location for different off-axis positions. Figure taken from Ref. [78].

3.4.3 PRISM

In general, the observed peak neutrino energy of a neutrino beam decreases as the observation angle with respect to the beam direction increases. This feature has been used in other long-baseline neutrino experiments, like T2K (2.5° off-axis) and NOvA (0.8° off-axis), to achieve narrower energy distributions. The DUNE PRISM concept exploits this effect using a movable ND. Within PRISM both ND-LAr and the muon spectrometer (TMS in Phase I and ND-GAr in Phase II) can be moved up to 3.2° off-axis, equivalent to move the detectors 30.5 m laterally through the ND hall.

This allows to record additional data samples with different energy compositions. Figure 3.8 compares the on-axis muon neutrino flux at the ND with the fluxes at different off-axis positions. As the off-axis position increases the neutrino flux becomes closer to a monoenergetic beam with a lower peak energy. These samples can be used to perform a data-driven determination of the relation between true and reconstructed neutrino energy, to reduce the dependence on the interaction model. The off-axis samples are linearly combined to produce a narrow Gaussian energy distribution centered on a target true energy. From the combination coefficients one can build a sample of reconstructed

CHAPTER 3. THE DEEP UNDERGROUND NEUTRINO EXPERIMENT

1128 neutrino events that will determine the energy mapping.

1129 The PRISM samples will be used to form a flux at the ND location similar in shape
1130 to the oscillated flux measured by the FD. This method can be used to extract the
1131 oscillation parameters with minimal input from the neutrino interaction model.

1132 3.4.4 SAND

1133 The role of SAND is to monitor the beam stability by measuring the on-axis neutrino
1134 energy spectra. As the PRISM program requires that ND-LAr and its downstream
1135 muon spectrometer spend about half of the time in off-axis positions, it is not possible
1136 to monitor the stability with the movable detectors. Moreover, for the success of PRISM
1137 it is essential to have a stable beam configuration, or, at least, a quick assessment and
1138 modeling of the distortions.

1139 The SAND detector is magnetised, and features an inner low density tracker, a LAr
1140 target with optical readout and surrounding sampling calorimeter.

1141 3.5 A More Capable Near Detector

1142 In DUNE Phase II, a more capable near detector is needed to achieve the ultimate physics
1143 goals of the experiments. The current leading proposal for this detector is ND-GAr.
1144 As mentioned previously, it will fulfill the role of TMS, measuring the momentum and
1145 sign of the charged particles exiting ND-LAr. Additionally, it will be able to measure
1146 neutrino interactions inside the HPgTPC, achieving lower energy thresholds than those
1147 of the ND and FD LArTPCs. By doing so ND-GAr will allow to constrain the relevant
1148 systematic uncertainties for the LBL analysis even further. A detailed discussion on the
1149 requirements, design, performance and physics of ND-GAr can be found in the DUNE
1150 ND CDR [78] and the ND-GAr white paper [80].

3.5. A MORE CAPABLE NEAR DETECTOR

1151 3.5.1 Requirements

1152 The primary requirement for ND-GAr is to measure the momentum and charge of
1153 muons from ν_μ and $\bar{\nu}_\mu$ CC interactions in ND-LAr, in order to measure their energy
1154 spectrum. To achieve the sensitivity to the neutrino oscillation parameters described
1155 in the DUNE FD TDR Volume II [72], ND-GAr should be able to constrain the muon
1156 energy within a 1% uncertainty or better. The main constraint will come from the
1157 calibration of the magnetic field, which will be performed using neutral kaon decays in
1158 the HPgTPC.

1159 Another requirement for ND-GAr is the precise measurement of neutrino interactions
1160 on argon for the energies relevant to the neutrino oscillation program. The goal is to
1161 constrain the cross section systematic uncertainties in the regions of phase space that
1162 are not accessible to ND-LAr. This requires the kinematic acceptance for muons in
1163 ND-GAr to exceed that of ND-LAr, being comparable to the one observed in the FD.

1164 ND-GAr should also be able to help establishing the relationship between true and
1165 reconstructed energy from neutrino interactions on argon with low thresholds, being
1166 sensitive to particles that are not observed or may be misidentified in ND-LAr. In
1167 particular, ND-GAr needs to have low tracking thresholds in order to measure the
1168 spectrum of pions and protons produced in final-state interactions (FSI). It also must
1169 be able to accurately measure the pion multiplicity in 1, 2 and 3 pions final states, to
1170 inform the pion mass correction in the LArTPCs.

1171 3.5.2 Reference design

1172 The final design of ND-GAr is still under preparation. However, a preliminary baseline
1173 design was in place at the time of the ND CDR. This section summarises the main
1174 features of that design, as it is also the one used for the default geometry in our simulation.
1175 A DUNE Phase II white paper, discussing the different options under consideration for
1176 the ND-GAr design, is in progress.

CHAPTER 3. THE DEEP UNDERGROUND NEUTRINO EXPERIMENT

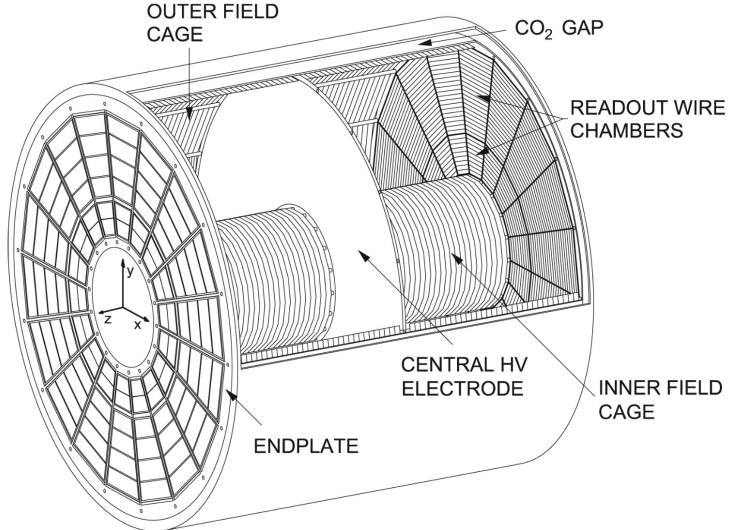


Figure 3.9: Diagram of the ALICE TPC, showing the two drift chambers, inner and outer field cages and readout chambers. Figure taken from Ref. [78].

1177 HPgTPC

1178 The reference design for the ND-GAr HPgTPC follow closely that of the ALICE TPC.
 1179 It is a cylinder with a central high-voltage cathode, generating the electric field for
 1180 the two drift volumes, with a maximum drift distance of 2.5 m each. The anodes will
 1181 be instrumented with charge readout chambers. The original design repurposed the
 1182 multi-wire proportional readout chambers (MWPCs) of ALICE, however some of the
 1183 current R&D efforts focus on a gas electron multiplier (GEM) [81] option instead. Figure
 1184 3.9 shows a schematic diagram of the ALICE TPC design. The basic ND-GAr geometry
 1185 will resemble this, except for the inner field cage.

1186 It will use a 90:10 molar fraction Ar: CH_4 mixture at 10 bar. With this baseline gas
 1187 mixture light collection is not possible, as the quenching gas absorbs most of the VUV
 1188 photons. Additional R&D efforts are underway, to understand if different mixtures allow
 1189 for the light signal to be used to provide a t_0 while maintaining stable charge gain.

3.5. A MORE CAPABLE NEAR DETECTOR

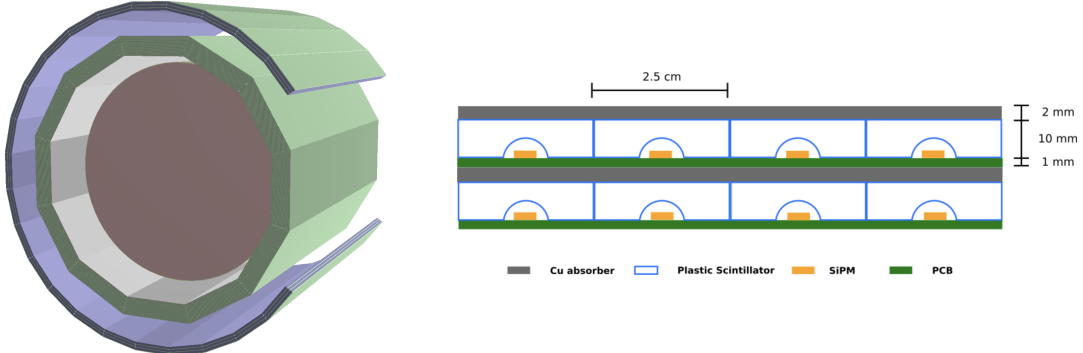


Figure 3.10: View of the 12-sided ECal barrel and outer muon tagger geometries (left) and layout of the ECal tile layers for the 2 mm Cu, 10 mm scintillator option (right). Figure adapted from Ref. [78].

1190 ECal

1191 The main role of the ND-GAr ECal is the calorimetric measurement of the electron
 1192 energies and the reconstruction of photons, in particular those from neutral pion decays.
 1193 Also, the ECal is able to provide a t_0 timestamp for neutrino interactions, by associating
 1194 its activity to the tracks in the HPgTPC. The ECal will also be able to perform
 1195 neutron reconstruction using time of flight and reject external backgrounds, thanks to
 1196 its sub-nanosecond time resolution.

1197 The ECal design features three independent subdetectors, two end caps at each side
 1198 and a barrel surrounding the HPgTPC. Each of the detectors is divided in modules,
 1199 which combine alternating layers of plastic scintillator and absorber material readout
 1200 by SiPMs. The inner scintillator layers consist of $2.5 \times 2.5 \text{ cm}^2$ high-granularity tiles,
 1201 whereas the outer ones are made out of 4 cm wide cross-strips spanning the whole
 1202 module length. The current barrel geometry consists of 8 tile layers and 34 strip layers,
 1203 while the end caps feature 6 and 36 respectively. The thickness of the scintillator layers
 1204 is 7 mm and 5 mm for the Pb absorber layers. The 12-sided geometry of the ECal barrel
 1205 (left) and the layout of the tile layers (left)¹ can be seen in Fig. 3.10.

¹The figure shows the layout of the tile layers for a previous design with 2 mm Cu absorber and 10 mm plastic scintillator, as mentioned in the text the current choice is 5 mm Pb absorber and 7 mm scintillator.

CHAPTER 3. THE DEEP UNDERGROUND NEUTRINO EXPERIMENT

1206 Magnet

1207 The ND-GAr magnet design, know as the Solenoid with Partial Yoke (SPY), consists of
1208 two coupled solenoids with an iron return yoke. The idea behind the design is to have a
1209 solenoid as thin as possible, as well as a return yoke mass distribution that minimises
1210 the material budget between ND-LAr and ND-GAr. The magnet needs to provide a
1211 0.5 T field in the direction perpendicular to the beam, parallel to the drift electric field.
1212 It needs to host the pressure vessel and the surrounding ECal, which points to a inner
1213 diameter of ~ 6.4 m.

1214 The solenoid is a single layer coil, based on niobium titanium superconducting
1215 Rutherford cable. The total length of the coil is 7.5 m. The bobbin will be split in four
1216 segments grouped in pairs with two identical cryostats, connected in series. The iron
1217 yoke features an aperture in the upstream side to allow the muons coming from ND-LAr.
1218 Still, its material will be enough to reduce the magnetic field reaching SAND, and also
1219 stop the charged pions produced inside the HPgTPC.

1220 Muon system

1221 The design of the ND-GAr muon system is still in a preliminary stage. Its role is to
1222 distinguish between muons and pions punching through the ECal. This is especially
1223 important for wrong-sign determination, to separate these from neutral current events.

1224 In its current form, the muon system consists of three layers of longitudinal sampling
1225 structures. It alternates 10 cm Fe absorber slabs with 2 cm plastic scintillator strips.
1226 The transverse granularity required is still under study.

1227 3.5.3 R&D efforts

1228 There are several ND-GAr-related prototypes, mostly focused on the TPC charge
1229 readout and electronics. The priority is to test the full readout chain, in a high-pressure
1230 environment, using a gas mixture with high argon fraction. A detailed summary of these
1231 can be found in the DUNE Phase II white paper [79].

3.5. A MORE CAPABLE NEAR DETECTOR

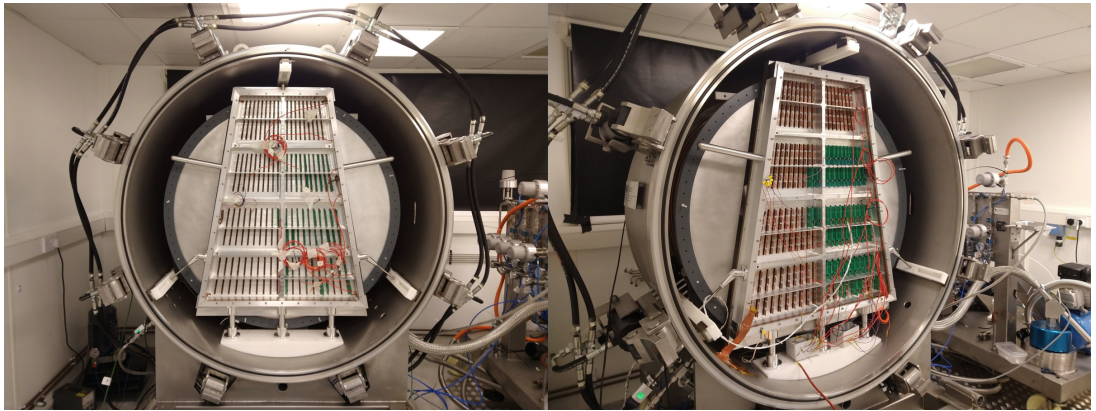


Figure 3.11: Photographs of the TOAD pressure vessel at RHUL. The TPC is mounted inside the vessel, and the OROC is supported by an aluminium frame. Figure taken from Ref. [82].

1232 Multi-Wire Proportional Chambers

1233 As mentioned before, the original ND-GAr design repurposes the MWPCs of the ALICE
1234 TPC, which became available after the recent upgrade [83]. These were operated using
1235 a 90:10:5 Ne:CO₂:N₂ gas mixture at 1 atm. Therefore, their performance needed to be
1236 studied in an argon gas environment at high pressure.

1237 The Gas-argon Operation of ALICE TPC (GOAT) test stand tested the ALICE
1238 readout chambers at high pressure. In particular, it used one of the previously operated
1239 ALICE inner MWPCs, also known as IROCs, in a pressure vessel rated to 10 atm. It
1240 measured the gas gain at various pressure points, voltages and gas mixtures.

1241 The Test stand of an Overpressure Argon Detector (TOAD) tested an ALICE outer
1242 MWPC, also known as OROC, up to 5 atm. During its time at RHUL, it was used to
1243 study the achievable gas gain of the OROC [82]. At the moment, it is being commissioned
1244 at Fermilab for a full detector test of the readout electronics and the DAQ.

1245 Figure 3.11 shows the interior of the TOAD pressure vessel. The TPC is mounted
1246 inside the vessel on three rails. The back of the OROC, supported by an aluminium
1247 frame, can be seen at the front.

CHAPTER 3. THE DEEP UNDERGROUND NEUTRINO EXPERIMENT

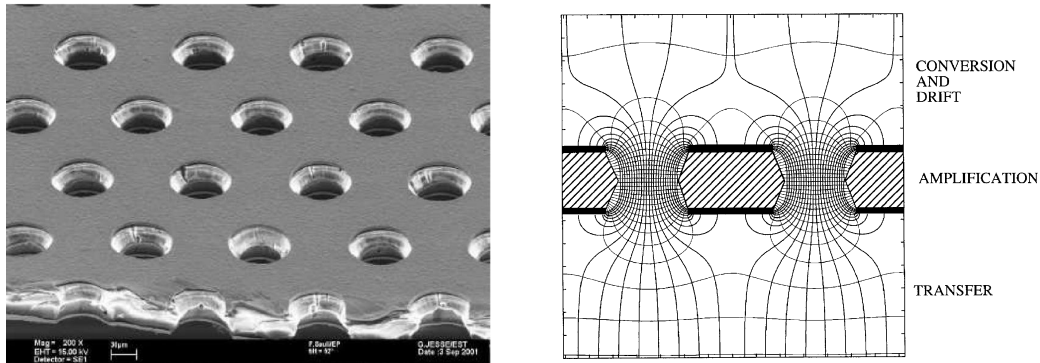


Figure 3.12: Left panel: electron microscope image of a 50 μm thick GEM electrode, with hole pitch and diameter of 140 and 70 μm , respectively. Right panel: Schematics of a GEM electrode cross section, showing the electric field lines around the holes. Figures taken from Ref. [84].

1248 Gas Electron Multiplier

1249 An alternative to the MWPC option is the use of GEMs. These are a type of micro-patter
 1250 detector, where the ionisation electrons passing through the holes in the GEM layers
 1251 are accelerated by a high intensity electric field. The acceleration causes the electrons
 1252 to ionise the medium, resulting in an avalanche which increase the signal exponentially
 1253 [81]. GEMs are used in numerous experiments that need a high spatial resolution, like
 1254 ALICE [85] and CMS [86] after their upgrades.

1255 Figure 3.12 (left panel) shows an electron microscope picture of a 50 μm thick GEM
 1256 electrode, with a pitch between neighbouring holes of 140 μm and a hole diameter of
 1257 70 μm . A schematic representation of the cross section of a GEM layer is shown in Fig.
 1258 3.12 (left panel).

1259 The Gaseous Argon T0 (GAT0²) prototype studies the use of thick GEMs made out
 1260 of glass to achieve optical imaging of the primary ionisation. Using a 10 atm pressure
 1261 vessel, the goal is to study different argon-based mixtures that allow for a precise t_0
 1262 determination.

1263 The GEM Over-pressurized with Reference Gases (GORG³) test stand is currently
 1264 testing a GEM-based charge readout, using a triple-GEM stack.

²Spanish for cat.

³Persian for wolf.

3.6. FAR DETECTOR

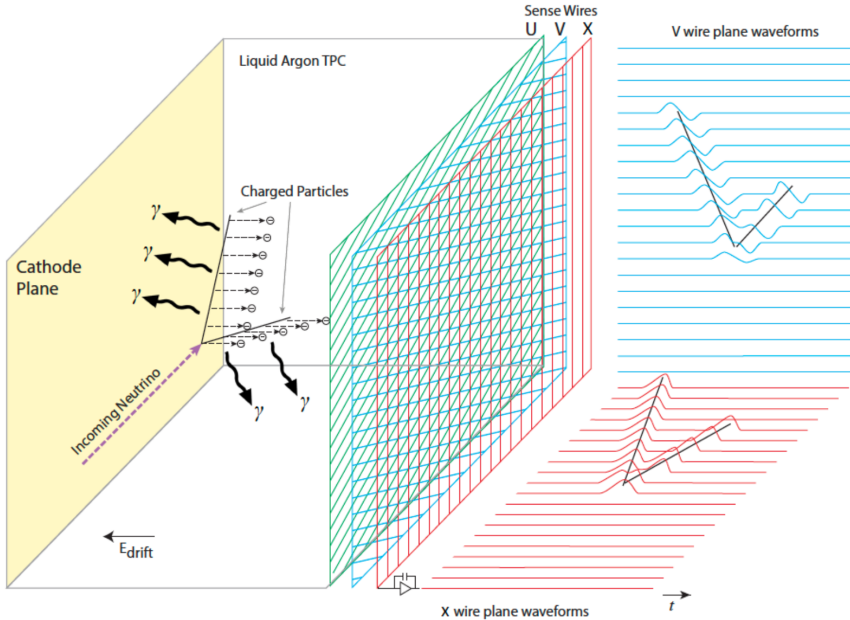


Figure 3.13: Schematic diagram showing the operating principle of a LArTPC with wire readout. Figure taken from Ref. [70].

1265 3.6 Far Detector

1266 The DUNE FD complex will sit 1300 km away from the beam target and 1.5 km
 1267 underground at SURF, South Dakota. Two caverns will host the four FD modules, two
 1268 of them per cavern, each embedded in cryostats of dimensions 18.9 m (w) \times 17.8 m (h) \times
 1269 65.8 m (l). A central, smaller cavern will host the cryogenic system.

1270 Three out of the four modules will be liquid argon (LAr) time projection chamber
 1271 detectors, often refer to as LArTPCs, with a LAr fiducial mass of at least 10 kt each.
 1272 The first and second FD modules, FD-1 and FD-2, will use a Horizontal Drift (HD)
 1273 technology, whereas the third module, FD-3, will have a Vertical Drift (VD) direction.
 1274 The technology for the fourth module is still to be decided,

1275 For each event, with energies ranging from a few MeV to several GeV, these detectors
 1276 collect both the scintillation light and the ionisation electrons created when the charged
 1277 particles produced in neutrino-nucleus interactions ionise the argon nuclei. In both HD
 1278 and VD designs the characteristic 128 nm scintillation light of argon is collected by a
 1279 photon detection system (PDS). This light will indicate the time at which electrons

CHAPTER 3. THE DEEP UNDERGROUND NEUTRINO EXPERIMENT

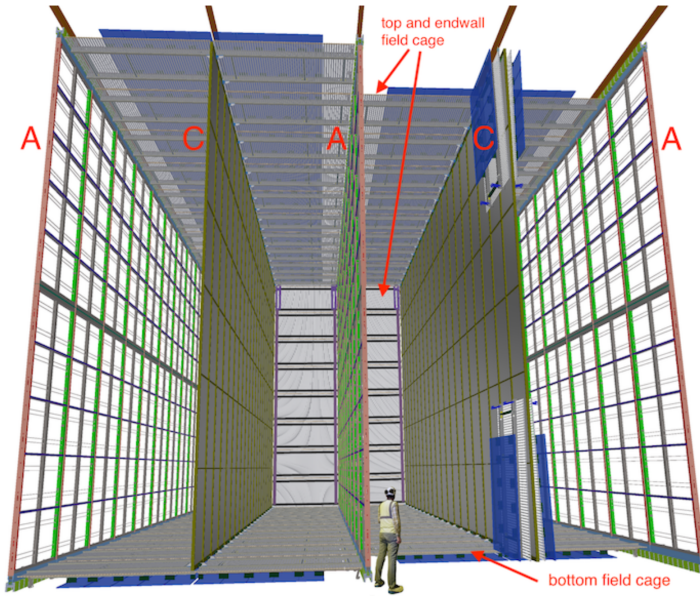


Figure 3.14: Proposed design for the FD-1 and FD-2 modules following the HD principle. Figure taken from Ref. [70].

start to drift, thus enabling reconstruction over the drift coordinate when compared to the time when the first ionisation electron arrives to the anode. Reconstruction of the topology in the transverse direction is achieved using the charge readout. Fig. 3.13 illustrates the detection principle described, for the case of a HD detector with a wire readout.

3.6.1 Horizontal Drift

The HD design the ionisation electrons produced as charged particles traverse the LAr drift horizontally towards the anode planes, due to the effect of an electric field. These anode planes are made out of three layers of wire readout. This design, previously known as single-phase (SP), was tested by the ProtoDUNE-SP detector at CERN. The prototype collected data from a hadron beam and cosmic rays, providing high-quality data sets for calibration and performance studies.

Each FD HD detector module is divided in four drift regions, with a maximum drift length of 3.5 m, by alternating anode and cathode walls. The surrounding field cage ensures the uniformity of the 500 V/cm horizontal electric field across the drift volumes.

3.6. FAR DETECTOR

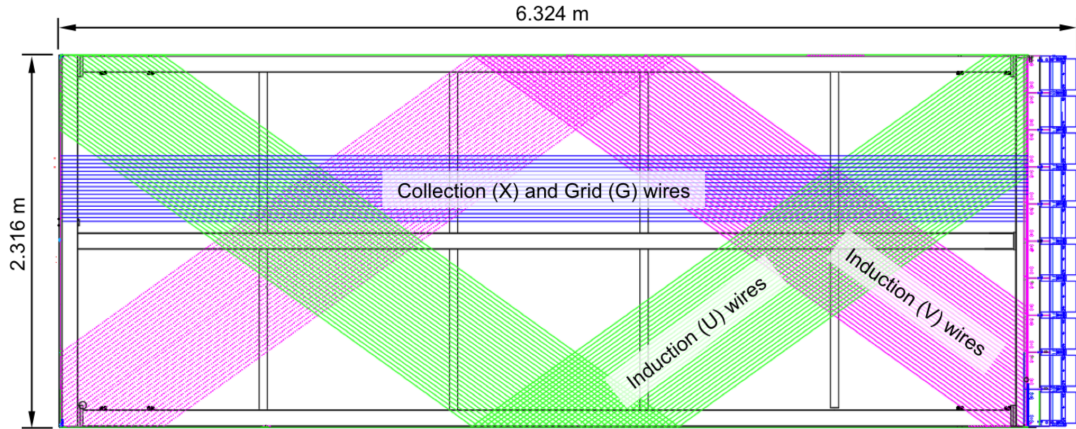


Figure 3.15: Schematic representation of an APA. The black lines represent the APA steel frame. The green and magenta lines correspond to the direction of the U and V induction wires respectively. The blue lines indicate the direction of the X collection wires and the wire shielding G. Figure taken from Ref. [70].

1295 The three anode walls, which constitute the charge readout of the detector, are built by
 1296 stacking anode plane assemblies (APAs), 2 high times 25 wide. The design of the HD
 1297 modules is shown in Fig. 3.14.

1298 Each APA is made of 2560 active wires arranged in three layers, plus an extra grid
 1299 layer, wrapped around a metal frame. The two induction wire planes, U and V, sit at
 1300 $\pm 35.7^\circ$ to the vertical on each side of the APA. The collection and shielding plane wires,
 1301 X and G, run parallel to the vertical direction. The ionisation electrons drift past the
 1302 induction planes, generating bipolar signals on those wires, and are collected by the
 1303 collection plane, producing a monopolar positive signal. The spacing between the wires
 1304 is ~ 5 mm, and it defines the spatial resolution of the APA.

1305 The front-end readout electronics, or cold electronics as they are immerse in the LAr,
 1306 are attached to the top of the up APAs and the bottom of the down APAs. Mounted on
 1307 the front-end mother boards we have a series of ASICs that digitize the signals from the
 1308 collection and induction planes. Each wire signal goes to a charge-sensitive amplifier,
 1309 then there is a pulse-shaping circuit and this is followed by the analogue-to-digital
 1310 converter. This part of the process happens inside the LAr to minimise the number of
 1311 cables penetrating the cryostat. The digitised signals come out finally via a series of

CHAPTER 3. THE DEEP UNDERGROUND NEUTRINO EXPERIMENT

1312 high-speed serial links to the warm interface boards (WIBs), from where the data is sent
1313 to the back-end DAQ through optical fibers.

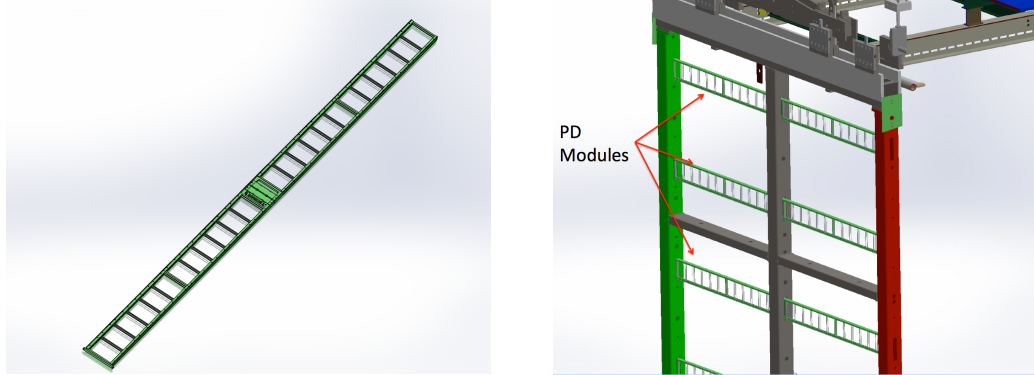


Figure 3.16: A PDS module containing 24 X-ARAPUCAs (left) and the location of the modules on the APAs (right). Figure taken from Ref. [70].

1314 The PDS uses modules of X-ARAPUCA devices, mounted on the APA frames
1315 between the wire planes. Each X-ARAPUCA consists of layers of dichroic filter and
1316 wavelength-shifter. They shift the VUV scintillation light into the visible spectrum,
1317 sending then the visible photons to silicon photomultiplier (SiPM) devices. The PDS
1318 modules are 209 cm × 12 cm × 2 cm bars, containing 24 X-ARAPUCAs. There are 10
1319 of these PDS modules per APA. Fig. 3.16 shows a PDS module (left) and the placement
1320 of the modules on the APAs (right).

1321 3.6.2 Vertical Drift

1322 In the VD case the ionisation electrons will drift vertically until they meet a printed
1323 circuit board-based (PCB) readout plane. It is based on the original dual-phase (DP)
1324 design deployed at CERN, known as ProtoDUNE-DP, used a vertical drift design with
1325 an additional amplification of the ionization electrons using a gaseous argon (GAr) layer
1326 above the liquid phase. The VD module incorporates the positive features of the DP
1327 design without the complications of having the LAr-GAr interface.

1328 The current design of the FD VD module counts with two drift chambers with a
1329 maximum drift distance of 6.5 cm. A cathode plane splits the detector volume along the
1330 drift direction while the two anode planes are connected to the bottom and top walls

3.6. FAR DETECTOR

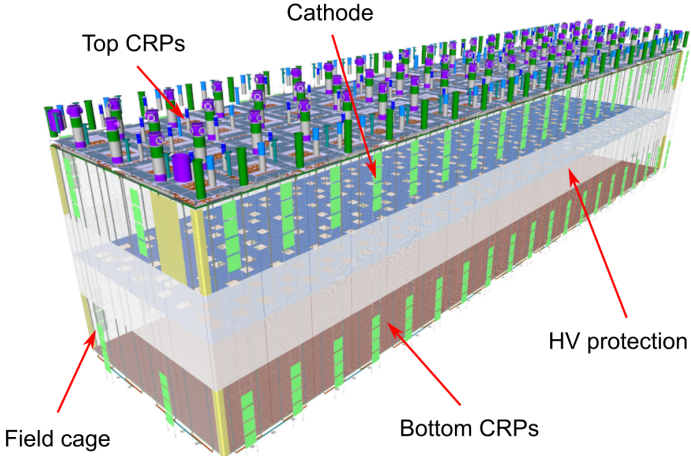


Figure 3.17: Proposed design for the FD-3 module following the VD principle. Figure adapted from Ref. [87].

of the detector. The layout of the VD module is shown in Fig. 3.17. Compared with the HD design, the VD option offers a slightly larger instrumented volume and a more cost-effective solution for the charge readout.

As in the HD design, each drift volume features a 500 V/cm electric field and a field cage that ensures its uniformity. The anode planes are arrays of $3.4\text{ m} \times 3\text{ m}$ charge-readout planes (CRPs). These are formed by a pair of charge-readout units (CRUs), which are built from two double-sided perforated PCBs, with their perforations aligned. The perforations allow the drift electrons to pass between the layers.

The PCB face opposite to the cathode has a copper guard plane which acts as shielding, while its reverse face is etched with electrode strips forming the first induction plane. The outer PCB has electrode strips on both faces, the ones facing the inner PCB form the second induction plane while the outermost ones form the collection plane. Fig. 3.18 shows the layout of the electrode strips for the top (left) and bottom (right) CRUs. The magenta and blue lines represent the first and second induction planes respectively, and the green lines correspond to the collection plane.

The PDS in the VD module will use the same X-ARAPUCA technology developed for the HD design. The plan is to place the PDS modules on the cryostat walls and on

CHAPTER 3. THE DEEP UNDERGROUND NEUTRINO EXPERIMENT

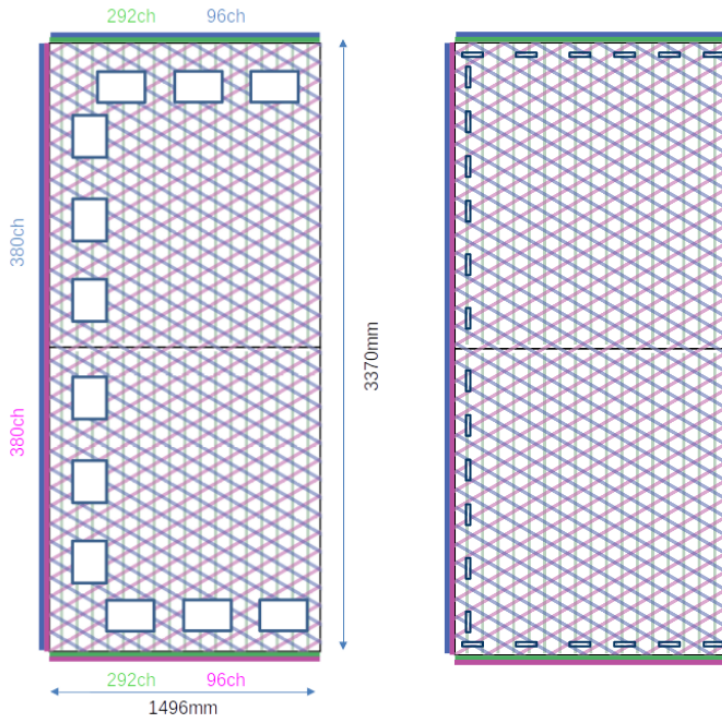


Figure 3.18: Schematic representation of the electrode strip configuration for a top (left) and bottom (right) CRU. Figure taken from Ref. [87].

1348 the cathode, in order to maximise the photon yield.

1349 3.6.3 FD Data Acquisition System

1350 The data acquisition (DAQ) system receives, processes and stores data from the detector
 1351 modules. In the case of DUNE the DAQ architecture is designed to work for all FD
 1352 modules interchangeably, except some aspects of the upstream part which may depend
 1353 on the specific module technology.

1354 The enormous sample rate and the number of channels in TPC and PD readouts
 1355 will produce a very large volume of data. These pose really strong requirements and
 1356 challenges to the DUNE FD DAQ architecture. It will be required to read out data of
 1357 the order of ten thousand or more channels at rates of a few MHz. To cope with the
 1358 huge data volume, segmented readouts and compression algorithms are used to reduce
 1359 the data rate to manageable levels.

1360 The DAQ system of the DUNE FD is composed of five different subsystems. The

3.6. FAR DETECTOR

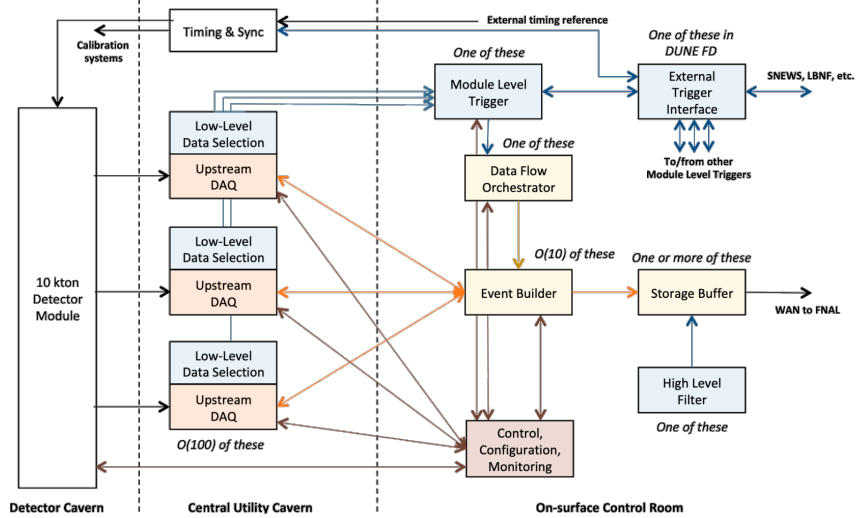


Figure 3.19: Detailed diagram of the DUNE FD DAQ system. Figure taken from Ref. [88].

1361 first one is the upstream DAQ, which receives the raw data from the detector, buffers it
 1362 and perform some low-level pre-processing. The minimally processed data is then fed
 1363 into a hierarchical data selection system, which then performs a module level trigger
 1364 decision. In case of a positive decision a trigger command is produced and executed by
 1365 the data flow orchestrator, located in the back-end (BE) DAQ subsystem. Subsequently
 1366 the DAQ BE retrieves the relevant data from the buffers located in the upstream DAQ,
 1367 adds all the data into a cohesive record and saves it to permanent storage. Watching
 1368 over all the other subsystems we also have the control, configuration and monitoring
 1369 subsystem and the time and synchronization subsystem. Figure 3.19 shows a schematic
 1370 diagram of the DAQ system, showing the different subsystems and their relations.

1371 A notorious challenge for the DUNE DAQ system comes from its broad physics
 1372 goals. We must be prepared to process events spanning a wide range of time windows
 1373 (from 5 ms in the case of beam and cosmic neutrinos and nucleon decay to 100 s in the
 1374 case of SNBs) and therefore this requires a continuous readout of the detector modules.
 1375 Moreover, because of the off-beam measurements we need to ensure the capabilities
 1376 of online data processing and self-triggering. Having this into account, together with
 1377 the technical constraints, the DUNE FD DAQ faces a series of challenges: it needs to

CHAPTER 3. THE DEEP UNDERGROUND NEUTRINO EXPERIMENT

- 1378 be fault tolerant and redundant to reduce downtime, accommodate new components
- 1379 while it keeps serving the operational modules, have large upstream buffers to handle
- 1380 SNB physics, be able to support a wide range of readout windows and last reduce the
- 1381 throughput of data to permanent storage to be at most 30 PB/year.

1382

1383

Matched Filter approach to Trigger

1384

Primitives

4.1 Motivation

1385 The filter implemented in the firmware of the upstream DUNE FD DAQ is a 32nd-order
1386 low-pass finite impulse-response (FIR) filter. The output of such filter for a discrete
1387 system can be written as:

$$y[i] = \sum_{j=0}^N h[j]x[i-j], \quad (4.1)$$

1388 where N is the order of the filter, y is the output sequence, x is the input sequence and h
1389 is the set of coefficients of the filter. The current implementation within `dtp-firmware`
1390 [89] uses a set of 16 non-zero integer coefficients.

1391 Filtering is a vital step in the hit finder chain. It helps to suppress the noise and
1392 enhance the signal peaks with respect to the noiseless baseline. A good filtering strategy
1393 allows us to use lower thresholds when forming the trigger primitives (TPs) and thus
1394 increasing the sensitivity of our detector to low energy physics events. In such events,
1395 the hits produced by the ionisation electrons tend to have lower amplitudes than those
1396 of interest to the baseline physics programme of the DUNE experiment.

1397 This is particularly important for the induction planes. In general, signal peaks in
1398 the induction wires have smaller amplitude than the ones in the induction plane. This,
1399 together with the fact that the pulse shapes are bipolar, reduces our capacity to detect

CHAPTER 4. MATCHED FILTER APPROACH TO TRIGGER PRIMITIVES

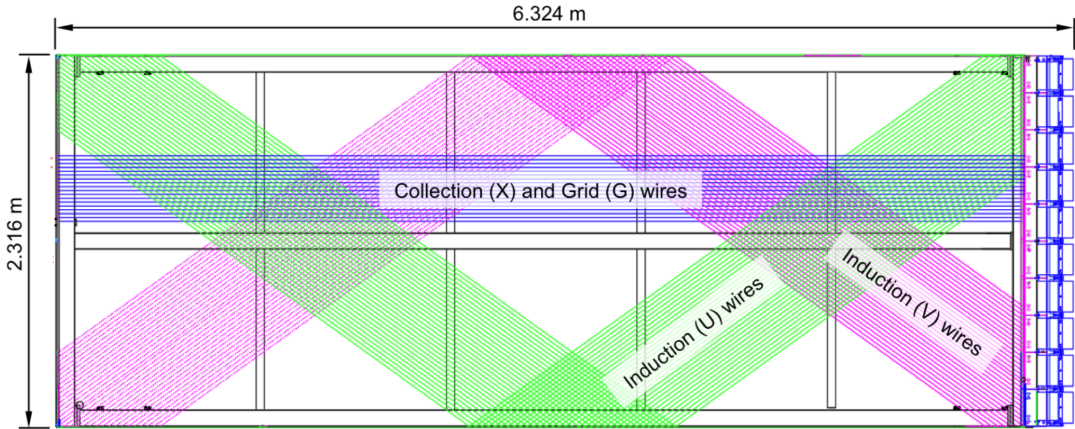


Figure 4.1: Schematic representation of an APA. The black lines represent the APA steel frame. The green and magenta lines correspond to the direction of the U and V induction wires respectively. The blue lines indicate the direction of the X collection wires and the wire shielding G.

1401 the hits on these channels. The inefficiency of detecting TPs in the induction planes
 1402 (denoted as U and V planes) lead trigger algorithms to focus mainly on the TPs from
 1403 the collection plane (so-called X plane). As a result, the possibility of making trigger
 1404 decisions based on the coincidence of TPs across the three wire planes remains nowadays
 1405 unexploited in DUNE. Fig. 4.1 shows a schematic view of an anode plane assembly
 1406 (APA), with the different wire plane orientations highlighted.

1407 A possible improvement of the current hit finder chain could require optimising
 1408 the existing or choosing a new filter implementation. A filter strategy which improves
 1409 the induction signals may be able to enhance the detection efficiency of TPs from the
 1410 induction planes and ideally make it comparable to that of the collection plane.

1411 The goal is to implement a better finite-impulse response filter design and to evaluate
 1412 its performance relative to the current filter. To do so, we need to take into account the
 1413 limitations of the firmware: the FIR filter shall have maximum 32 coefficients (so-called
 1414 taps) whose values are 12-bit unsigned integers. Although it is technically possible to
 1415 include non-integer coefficients, it would be a technical challenge as we have 40 FIR
 1416 instances per APA, as there are 4 FIR per optical link and 10 optical links per APA.
 1417 With these restrictions, the task is to provide a set of 32 coefficients which yield an

4.2. SIGNAL-TO-NOISE RATIO DEFINITION

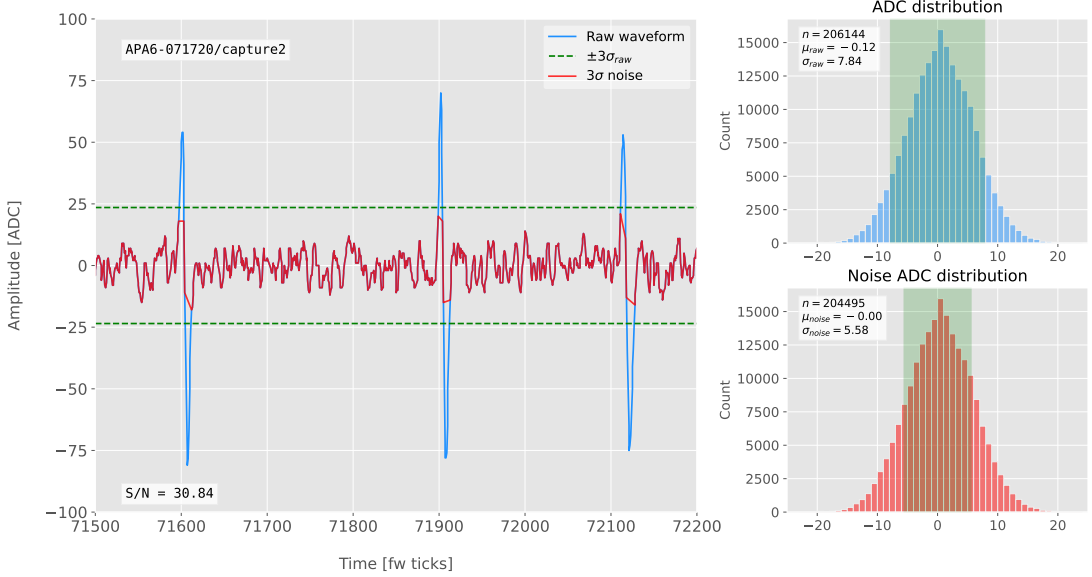


Figure 4.2: Left panel: Zoomed unfiltered waveform corresponding to channel 7840 from the ProtoDUNE-SP raw data capture `felix-2020-07-17-21:31:44` (blue line). The green dashed lines mark the region $\pm 3\sigma_{\text{raw}}$. The resulting noise waveform is also shown (red line). Top right panel: ADC distribution for channel 7840, where the green shaded region represents $\pm \sigma_{\text{raw}}$. Bottom right panel: noise ADC distribution for channel 7840, where the green shaded region represents $\pm \sigma_{\text{noise}}$.

1418 optimal filter performance for the induction wires.

1419 4.2 Signal-to-noise ratio definition

1420 I introduce the signal to noise ratio (S/N) as a measure of the FIR filter performance
1421 and demonstrate how to extract its value for a set of ProtoDUNE-SP data. The S/N
1422 metrics allow us to compare different filter implementations and serve as a basis for more
1423 detailed studies presented later in this document. Specifically, I use the ADC capture
1424 `felix-2020-07-17-21:31:44` (data capture taken for firmware validation purposes). I
1425 defined S/N as the height of the signal peaks relative to the size of the noise peaks.
1426 To quantify this quantity channel by channel one first need to estimate the standard
1427 deviation of the ADC data for each channel, σ_{ADC} . Then, I define the corresponding
1428 noise waveform to be the ADC values in the range $\pm 3\sigma_{\text{ADC}}$. From this new noise data
1429 one can estimate again the mean and standard deviation, μ_{noise} and σ_{noise} , so I can

CHAPTER 4. MATCHED FILTER APPROACH TO TRIGGER PRIMITIVES

1430 write the S/N for any given channel as:

$$\text{S/N} = \frac{\max [ADC] - \mu_{noise}}{\sigma_{noise}}, \quad (4.2)$$

1431 where $\max [ADC]$ is simply the maximum ADC value found in the corresponding channel.

1432 One can apply this definition of the S/N with a waveform from one of the channels
 1433 of the data capture¹. Fig. 4.2 shows a zoomed region of the waveform corresponding to
 1434 channel 7840 (blue line), where one can clearly see three signal peaks and continuous
 1435 additive noise (we actually see 6 peaks, 3 positive and 3 negative, but, because by design
 1436 for induction channels the expected signal pulse shapes are bipolar, I treat them as a
 1437 collection of 3 individual signal peaks). I estimated the standard deviation of this raw
 1438 waveform to be $\sigma_{raw} = 7.84$ ADC, so I am able to define the noise waveform (red line)
 1439 as the ADC values in the range ± 23.52 ADC. This way one obtains $\mu_{noise} = 0$ and
 1440 $\sigma_{noise} = 5.58$ ADC, which gives $\text{S/N} = 30.84$.

1441 We can repeat this calculation now for the corresponding filtered waveform (using the
 1442 current firmware FIR filter). In Fig. 4.3 I plotted the same time window for the filtered
 1443 waveform from channel 7840 (blue line). In this case, the standard deviation of the
 1444 waveform is larger than before, giving $\sigma_{raw} = 10.99$ ADC. The resulting noise waveform
 1445 (red line) results from selection the ADC values in the range ± 32.91 ADC, giving now
 1446 $\mu_{noise} = -0.47$ ADC and $\sigma_{noise} = 7.03$ ADC. Finally, one obtains $\text{S/N} = 24.68$. Notice
 1447 that the value of S/N decreases after the filtering. Clearly, one can see that the noise
 1448 baseline has increased by a factor of 1.35 when we applied the FIR filter and at the same
 1449 time the amplitude of the signal peaks has remained almost unchanged, leading to this
 1450 poorer S/N value.

¹All the original work was done within the `dtp-simulation` package [90], which offers a variety of tools to read raw data and emulate the TPG block (pedestal subtraction, filtering and hit finder). However, the results shown in this report were re-worked later using the C++ based `dtpemulator` package [91]. Its main purpose is the emulation of the TPG block and, in the same way as its predecessor, it has been cross-checked against the current firmware implementation.

4.3. LOW-PASS FIR FILTER DESIGN

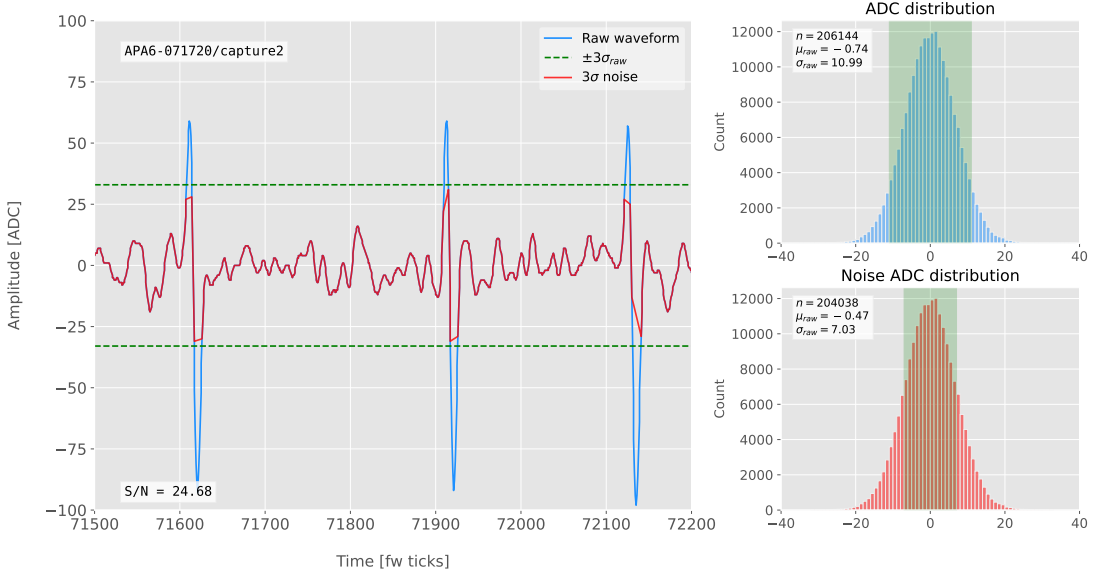


Figure 4.3: Left panel: Zoomed filtered waveform corresponding to channel 7840 from the ProtoDUNE-SP raw data capture `felix-2020-07-17-21:31:44` (blue line). The filter used was the current implementation of the low-pass FIR filter in `dtp-firmware`. The green dashed lines mark the region $\pm 3\sigma_{\text{raw}}$. The resulting noise waveform is also shown (red line). Top right panel: ADC distribution for channel 7840 after filtering, where the green shaded region represents $\pm \sigma_{\text{raw}}$. Bottom right panel: noise ADC distribution for channel 7840 after filtering, where the green shaded region represents $\pm \sigma_{\text{noise}}$

1451 4.3 Low-pass FIR filter design

1452 In general, when one uses a method to optimize the frequency response of a digital filter,
 1453 such as the Parks-McClellan algorithm, one finds a set of N real coefficients that give
 1454 the best response for the specified pass-band and order of the filter [92].

1455 In our case, as the sampling frequency is defined as 1 ticks^{-1} , the Nyquist frequency
 1456 will simply be $1/2 \text{ ticks}^{-1}$. The current implementation of the filter seems to have as
 1457 pass-band the range $[0, 0.1] \text{ ticks}^{-1}$. This can be seen in Fig. 4.4, where I show the
 1458 power spectrum, in decibels, of such filter implementation (blue solid line). For instance,
 1459 the Park-McClellan algorithm finds the optimal Chebyshev FIR filter taking as input
 1460 the boundaries of the target pass-band and stop-band, which can be written in the form:

$$\left\{ \begin{array}{l} [0, f_c] \\ [f_c + \delta f, f_N] \end{array} \right. , \quad (4.3)$$

CHAPTER 4. MATCHED FILTER APPROACH TO TRIGGER PRIMITIVES

where f_c is the cut-off frequency, δf is the transition width and f_N is the aforementioned Nyquist frequency. A similar behaviour to the one in the current filter can be obtained by setting $f_c = 0$ and $\delta f = 0.1 \text{ ticks}^{-1}$. The response of the resulting filter is also shown in Fig. 4.4 (blue solid line). Notice that the suppression of the stop-band is enhanced for this optimal filter. For comparison I included the power response of the filter obtained by taking the integer part of the coefficients resulting from the Parks-McClellan method (red dashed line). One can see that it does not suppress that much the stop-band, in a similar way to the current implementation of the filter.

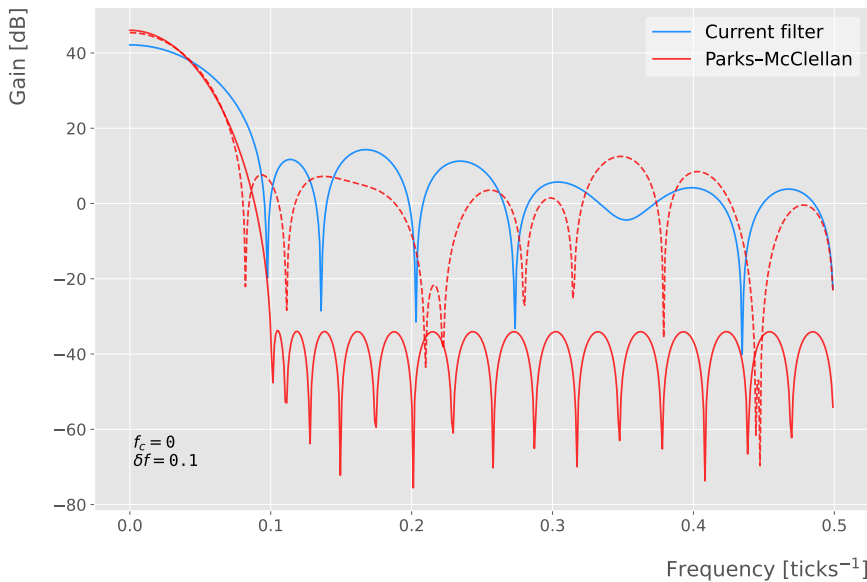


Figure 4.4: Power spectrum in decibels for the current implementation of the low-pass FIR filter in `dtp-firmware` (blue line), compared to the response of an optimal filter obtained using the Parks-McClellan algorithm for the same pass-band (red line). Also for comparison I include the spectrum of the optimal filter when taking only the integer part of the coefficients (red dashed line).

At this point, I tried to improve the performance of the FIR filter using the Parks-McClellan method, i.e. maximize the overall S/N, using the available data captures. I did so by varying the values of the two quantities that parametrize the pass-band and stop-band, the cut-off frequency f_c and the transition width δf .

Fig. 4.5 shows the average relative change in the S/N (i.e. the ratio between the value of the S/N after and before the filtering) for capture `felix-2020-07-17-21:31:44`,

4.3. LOW-PASS FIR FILTER DESIGN

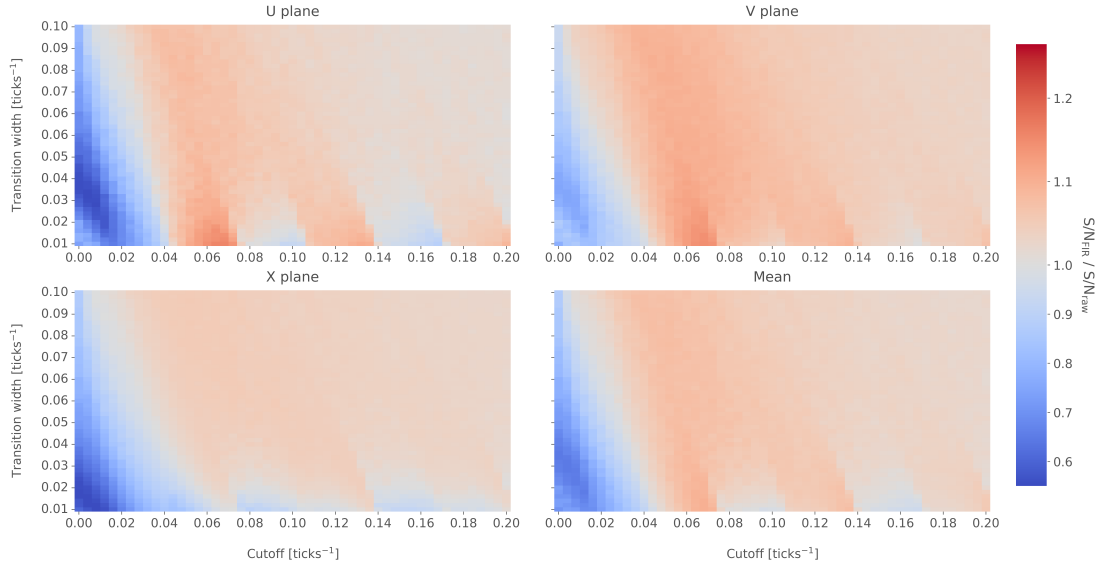


Figure 4.5: Relative change in the S/N for the ProtoDUNE-SP raw data capture `felix-2020-07-17-21:31:44`, using different values of the cutoff frequency f_c and the transition width δf . The optimal Chebyshev filters were applied using just the integer part of the coefficients given by the Parks-McClellan algorithm.

when using filters designed with the Parks-McClellan algorithm for the specified values of the cut-off frequency f_c and the transition width δf , restricted to integer values for the filter coefficients. One can clearly distinguish different regions where we get an improvement of up to a factor of 1.35 for the U plane. For large values of $f_c + \delta f$ the ratio tends to 1, as expected (in that limit the width of the stop-band goes to 0, meaning that no frequencies are filtered out and thus the waveform remains the same).

Using the configuration which gives the best mean performance for the three planes (see bottom right panel of Fig. 4.5), i.e. $f_c = 0.068 \text{ ticks}^{-1}$ and $\delta f = 0.010 \text{ ticks}^{-1}$, we can see how such filter affects the different channels. Fig. 4.6 shows the distribution of the S/N improvement values for all the channels in the raw ADC capture `felix-2020-07-17-21:31:44`, separated by wire plane, after the optimal Chebyshev filter was applied. One can see that there is a clear improvement for both U and V induction wire planes, obtaining a mean change of 1.25 and 1.30 for them respectively. However, in the case of the collection plane X the mean of this distribution is roughly 1, meaning that a good fraction of channels in that plane get a slightly worse S/N after the

CHAPTER 4. MATCHED FILTER APPROACH TO TRIGGER PRIMITIVES

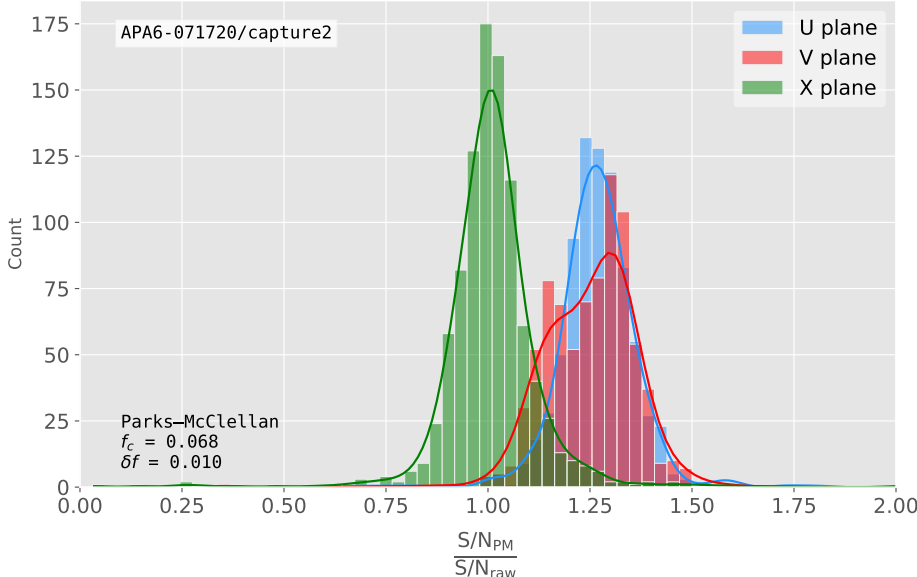


Figure 4.6: Distribution of the relative change of the S/N on the different wire planes from the ProtoDUNE-SP raw data capture *felix-2020-07-17-21:31:44* after the optimal Chebyshev filter was applied. The filter was computed with the Parks-McClellan algorithm using a cutoff of $f_c = 0.068 \text{ ticks}^{-1}$ and a transition width $\delta f = 0.010 \text{ ticks}^{-1}$.

filter is applied. In any case, this is not a big issue as the S/N for collection channels is usually much higher than the one for induction channels.

The results I obtained optimising the low pass filter with the Parks-McClellan method are promising. Nonetheless, the improvement found is rather marginal so I wondered if there could be an alternative approach to the filtering problem which yields better outputs. At this point, I found a possible alternative in matched filters. By construction, this kind of filters offer the best improvement on the S/N.

4.4 Matched filters

In the context of signal processing, a matched filter is the optimal linear filter for maximising the signal-to-noise ratio (S/N) in the presence of additive noise, obtained by convolving a conjugated time-reversed known template with an unknown signal to detect the presence of the template in the signal [93].

Given a known signal sequence $s(t)$ and another (a priori unknown) noise sequence

4.4. MATCHED FILTERS

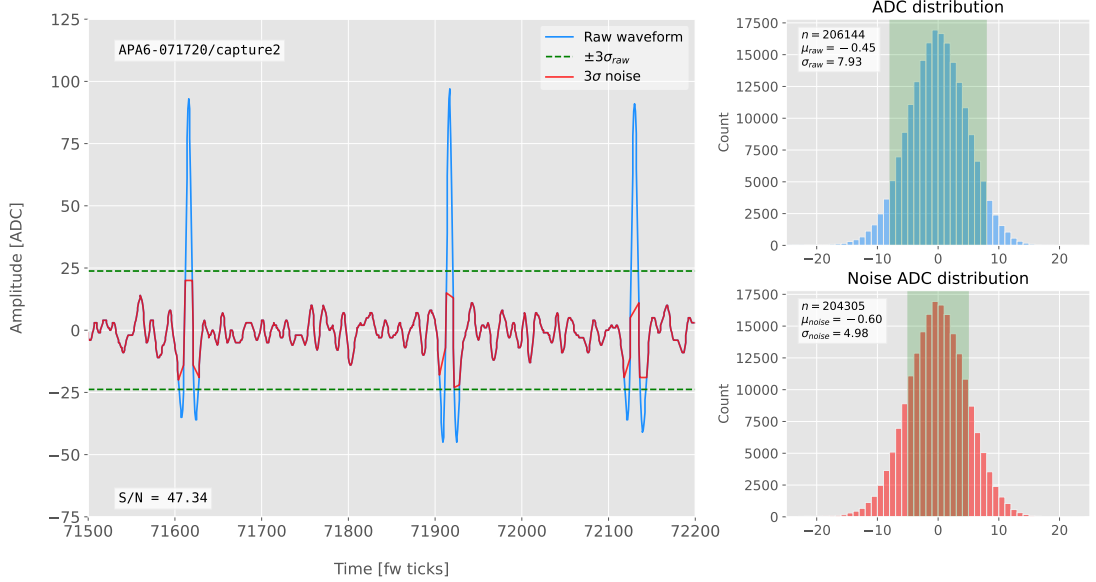


Figure 4.7: Left panel: Zoomed match filtered waveform corresponding to channel 7840 from the ProtoDUNE-SP raw data capture felix-2020-07-17-21:31:44 (blue line). The filter used was directly extracted from the data, being the 32 values around the first peak in the original waveform. The green dashed lines mark the region $\pm 3\sigma_{\text{raw}}$. The resulting noise waveform is also shown (red line). Top right panel: ADC distribution for channel 7840 after match filtering, where the green shaded region represents $\pm \sigma_{\text{raw}}$. Bottom right panel: noise ADC distribution for channel 7840 after match filtering, where the green shaded region represents $\pm \sigma_{\text{noise}}$

1503 $n(t)$, the input signal can be written as:

$$x(t) = s(t) + n(t). \quad (4.4)$$

1504 Now, considering a linear time-invariant filter, whose impulse-response function I
1505 will refer to as $h(t)$, one can write the output signal as:

$$\begin{aligned} y(t) &= x(t) * h(t) \\ &= (s(t) + n(t)) * h(t) \\ &= y_s(t) + y_n(t), \end{aligned} \quad (4.5)$$

1506 where $y_s(t)$ and $y_n(t)$ are simply the outputs of the filter due to the signal and the noise
1507 components respectively.

CHAPTER 4. MATCHED FILTER APPROACH TO TRIGGER PRIMITIVES

1508 The goal of the matched filter is to detect the presence of the signal $s(t)$ in the input
 1509 sample $x(t)$ at a certain time t_0 , which effectively means we need to maximise the S/N.
 1510 This way, what one wants is to have a filter which gives a much bigger output when the
 1511 known signal is present than when it is not. Putting it in other words, the instantaneous
 1512 power of the signal output $y_s(t)$ should be much larger than the average power of the
 1513 noise output $y_n(t)$ at some time t_0 .

1514 For the case of the filtered signal, one can easily re-write it as an inverse Fourier
 1515 transform:

$$y_s(t) = \frac{1}{2\pi} \int_{-\infty}^{\infty} d\omega H(\omega)S(\omega)e^{i\omega t}, \quad (4.6)$$

1516 where $H(\omega)$ and $S(\omega)$ are the Fourier transforms of the impulse-response function (i.e.
 1517 the transfer function of the filter) and of the input signal, respectively.

1518 Now focusing on the noise, we can use the Wiener-Khinchin theorem [94] to write
 1519 the mean power of the noise after filtering as:

$$E|y_n(t)|^2 = \frac{1}{2\pi} \int_{-\infty}^{\infty} d\omega |H(\omega)|^2 S_n(\omega), \quad (4.7)$$

1520 where $S_n(\omega)$ is the power spectral density of the noise.

1521 Having these, one can write the instantaneous S/N at time t_0 as:

$$\begin{aligned} \left(\frac{S}{N} \right)_{t_0} &= \frac{|y_s|^2}{E|y_n(t)|^2} \\ &= \frac{1}{2\pi} \frac{\left| \int_{-\infty}^{\infty} d\omega H(\omega)S(\omega)e^{i\omega t_0} \right|^2}{\int_{-\infty}^{\infty} d\omega |H(\omega)|^2 S_n(\omega)}. \end{aligned} \quad (4.8)$$

1522 Once we have this expression, we need to find the upper limit of it to determine what
 1523 would be the optimal choice for the transfer function. One can use the Cauchy-Schwarz
 1524 inequality, which in the present case takes the form:

$$\left| \int_{-\infty}^{\infty} dx f(x)g(x) \right|^2 \leq \int_{-\infty}^{\infty} dx |f(x)|^2 + \int_{-\infty}^{\infty} dx |g(x)|^2, \quad (4.9)$$

4.4. MATCHED FILTERS

1525 for any two analytical functions $f(x)$ and $g(x)$. One can prove that making the choice:

$$\begin{aligned} f(x) &= H(\omega) \sqrt{S_n(\omega)} e^{i\omega t_0}, \\ g(x) &= \frac{S(\omega)}{\sqrt{S_n(\omega)}}, \end{aligned} \quad (4.10)$$

1526 leads to the following upper bound for the S/N:

$$\left(\frac{S}{N} \right)_{t_0} \leq \frac{1}{2\pi} \int_{-\infty}^{\infty} d\omega \frac{|S(\omega)|^2}{S_n(\omega)}. \quad (4.11)$$

1527 From Eqs. (4.8), (4.9) and (4.10) one can also derive the form of the transfer function
1528 such that the upper bound is exactly reached [95]:

$$H(\omega) \propto \frac{S^*(\omega) e^{-i\omega t_0}}{S_n(\omega)}. \quad (4.12)$$

1529 From this last expression we can clearly see the way the matched filter acts. As the
1530 transfer function is proportional to the Fourier transform of the signal it will try to only
1531 pick the frequencies present in the signal [96].

1532 The matched filter transfer function can be greatly simplified if the input noise is
1533 Gaussian. In that case, the power spectral density of the noise is a constant, so it can be
1534 re-absorbed in the overall normalisation of the transfer function. Moreover, considering
1535 that the input signal is a real function, one can simply set $S^*(\omega) = S(-\omega)$, which gives:

$$H(\omega) \propto S(-\omega) e^{-i\omega t_0}. \quad (4.13)$$

1536 For a discrete signal, one can think of the input and impulse-response sequences as
1537 vectors of \mathbb{R}^N . Then, the matched filter tries to maximise the inner product of the signal
1538 and the filter while minimising the output due to the noise by choosing a filter vector
1539 orthogonal to the later. In the case of additive noise, that leads to the impulse-response
1540 vector:

$$h = \frac{1}{\sqrt{s^\dagger R_n^{-1} s}} R_n^{-1} s, \quad (4.14)$$

CHAPTER 4. MATCHED FILTER APPROACH TO TRIGGER PRIMITIVES

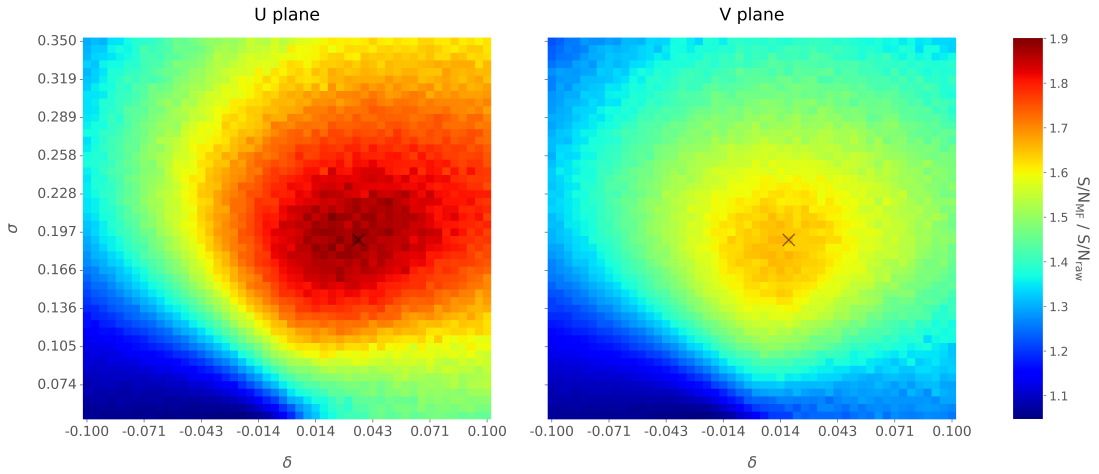


Figure 4.8: Relative improvement in the S/N for the raw data capture `felix-2020-07-17-21:31:44`, using the matched filter following the parametrisation in Eq. (4.17). The black crosses in both panels denote the location of the maximum ratio value.

1541 where s is a reversed signal template sequence of length N equal to the order of the filter
 1542 and R_n is the covariance matrix associated with the noise sequence n . For the Gaussian
 1543 noise case, the covariance matrix is simply the unit matrix, so the above expression
 1544 simplifies again to:

$$h = \frac{s}{|s|}. \quad (4.15)$$

1545 For this first stage of the study, I use a definition of the S/N per channel given by:

$$\text{S/N} = \frac{\max [ADC] - \mu_{noise}}{\sigma_{noise}}, \quad (4.16)$$

1546 where the subscript *noise* refers to a subset of the data obtained by only taking into
 1547 account waveform values within a $\pm 3\sigma$ range around the mean of the data and $\max [ADC]$
 1548 is the maximum of the original waveform. This definition is further discussed in App.
 1549 4.2, where I also show examples of its application to raw data and to a waveform filtered
 1550 with the current low-pass FIR filter.

1551 To test whether this choice of filter is appropriate one needs to choose a signal
 1552 template. As an example of how a matched filter would affect our signal, I simply took
 1553 the filter coefficients to be the 32 ADC values around a signal peak present in the data.

4.4. MATCHED FILTERS

1554 In Fig. 4.7 (left panel) I plotted a zoomed region for channel 7840 in the raw data capture
1555 `felix-2020-07-17-21:31:44`, after applying the matched filter described before (blue
1556 line). When compared to the raw and FIR filtered case (see App. 4.2), after applying
1557 the match filter the standard deviation of the noise waveform (red line) decreases and at
1558 the same time the signal peaks are enhanced. This leads to an improvement of the S/N
1559 by a factor of 1.92 when compared to the raw waveform.

1560 In order to obtain the matched filter that is more suitable for our data, I explored
1561 different configurations of signal templates. In order to perform this exploration, I
1562 parametrised the signal using the bipolar function:

$$f(x) = -A(x + \delta) e^{-x^2/\sigma^2}, \quad (4.17)$$

1563 where the parameter δ controls the asymmetry between the positive and negative peaks
1564 and σ controls their width. The amplitude parameter A is set such that it keeps the
1565 height of the biggest peak to be less than 200 ADC in absolute value.

1566 As this parametrisation is only adequate for bipolar signals I will focus exclusively
1567 on the induction channels. Also, the optimal configurations I found for the U and V
1568 plane will be kept separate, i.e. I will have two sets of coefficients that will be applied to
1569 either the U and V planes of wires. I do so as I found this was the choice giving the
1570 best performance. Even so, as I will discuss, the differences are not very pronounced. In
1571 case it is not technically possible to separate channels in the firmware according to the
1572 wire plane they come from and use different sets of filter coefficients for them, we can
1573 just find a common unique set of coefficients. In such case, I do not expect our results
1574 to change dramatically.

1575 In Fig. 4.8 I present the results of our parameter scan, for channels in the induction
1576 planes U (left panel) and V (right panel). For each configuration of σ and δ the resulting
1577 matched filter was applied to all channels in the corresponding plane within the data
1578 capture `felix-2020-07-17-21:31:44`, the S/N improvement was computed with respect
1579 to the raw waveforms and then the S/N mean value was kept as a score for such filter.

CHAPTER 4. MATCHED FILTER APPROACH TO TRIGGER PRIMITIVES

1580 One can see that the improvement obtained for the U plane is in general higher than the
1581 one for the V plane. In any case, I got substantially higher ratios than the ones obtained
1582 for the low-pass FIR filters. For the optimal configurations I attained improvements up
1583 to a factor of 1.85 for the U plane and 1.65 for the V plane.

1584 The sets of optimal matched filter coefficients were obtained for the parameters
1585 $\delta = 0.035$, $\sigma = 0.191$ for the U plane and $\delta = 0.018$, $\sigma = 0.191$ for the V plane. I
1586 show these two sets of coefficients in Fig. 4.9 (left panel). Also in Fig. 4.9 (right
1587 panel) I plot the distribution of the S/N improvement after the optimal match filters
1588 for the U and V were applied to the corresponding channels in the raw data capture
1589 `felix-2020-07-17-21:31:44`. As mentioned before, the mean improvement achieved
1590 for the U plane channels is slightly bigger than the one for the V channels. Note, however,
1591 that the spread of the distribution for the V plane is also smaller than the one for the U
1592 plane.

1593 I also performed a similar scan for the case of a low-pass FIR filter using the Parks-
1594 McClellan algorithm. In that case, the parameters to check were the cutoff frequency
1595 and the transition width of the filter. A summary of the results is given in App. 4.3.

1596 Overall, one can see that the improvements on the S/N are much more significant in
1597 the case of the matched filter than it is for the low-pass FIR filters. The analysis of this
1598 and other raw data captures from ProtoDUNE-SP suggest that matched filters increase
1599 the S/N of induction channels by a factor of 1.5 more than the optimal low-pass FIR
1600 filters.

1601 Although these results are by themselves great points in favour of the matched
1602 filter, more studies are needed to completely assess the robustness of this approach. I
1603 proceeded then to test the matched filter with simulated data samples.

1604 4.5 Using simulated samples

1605 In order to further test the matched filter, the next step was to generate and process
1606 data samples using *LArSoft* [97]. In this way, one can control the particle content of

4.5. USING SIMULATED SAMPLES

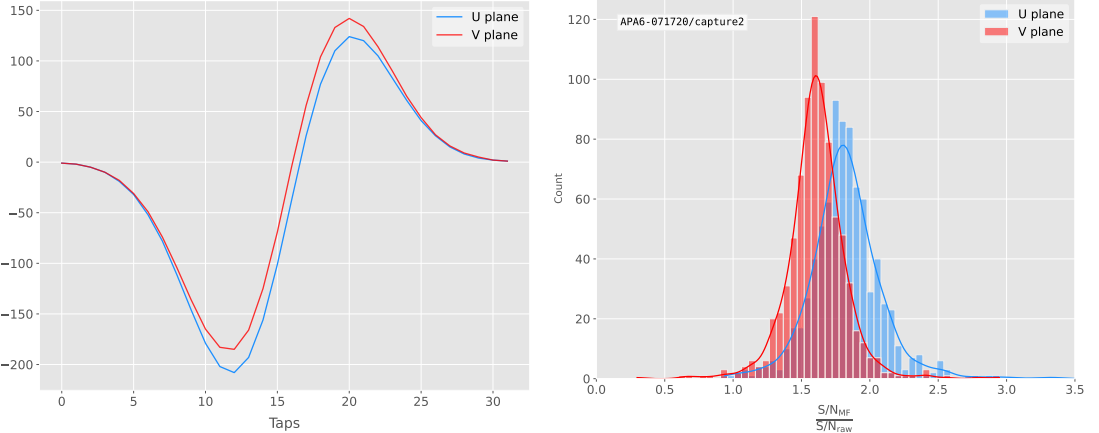


Figure 4.9: Left panel: Optimal matched filter coefficients for the U (blue line) and V (red line) planes. The filters were computed with our parametrisation in Eq. (4.17) for the parameter values $\delta = 0.035$, $\sigma = 0.191$ and $\delta = 0.018$, $\sigma = 0.191$ respectively. Right panel: Distribution of the relative change of the S/N on the two induction wire planes from the ProtoDUNE-SP raw data capture *felix-2020-07-17-21:31:44* after their respective optimal matched filters were applied.

1607 the samples, the orientation of the tracks and their energy, and therefore see how the
1608 matched filter behaves in various situations.

1609 To begin with, I prepared different monoenergetic and isotropic samples containing
1610 a single particle per event. Each sample contains a different particle species, namely
1611 electrons, muons, protons and neutral pions all with a kinetic energy of $E_k = 100$ MeV.
1612 I chose these because of the fairly different topologies they generate in the liquid argon,
1613 ranging from shower-like to track-like. The procedure I followed to generate the samples
1614 and process them is discussed in detail in App. ??.

1615 These were generated with the single particle gun and the Geant4 stage of the
1616 *LArSoft* simulation [97] was performed with the standard configuration for the DUNE
1617 FD 10kt module.

1618 For simplicity, I restricted the particles to start drifting in a single TPC volume
1619 (in this case TPC 0), so I can focus exclusively on the signals coming from one APA.
1620 The chosen kinetic energy for all the particles in my first trial is $E_k = 100$ MeV, so a
1621 necessary check is to see if all our tracks will be typically contained in one TPC volume.
1622 Fig. 4.10 (left panel) shows the distributions of the track lengths in the liquid argon

CHAPTER 4. MATCHED FILTER APPROACH TO TRIGGER PRIMITIVES

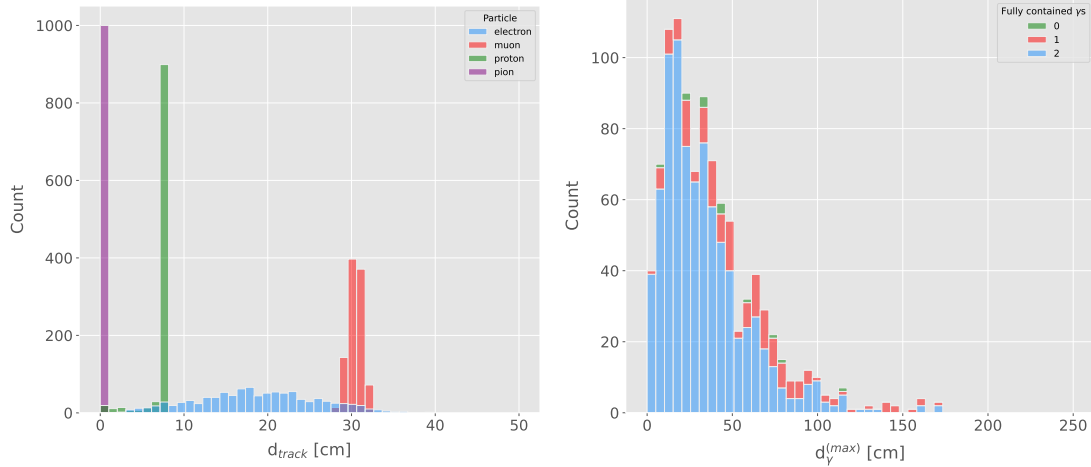


Figure 4.10: Left panel: distributions of the particles track length in the liquid argon for the generated $E_k = 100$ MeV monoenergetic samples, electrons (blue), muons (red), protons (green) and neutral pions (purple). Right panel: distribution of the length of the longest photon in the neutral pion sample after the decay process $\pi^0 \rightarrow \gamma\gamma$.

of all generated particles with $E_k = 100$ MeV. One can see that, in the case of the track-like particles (i.e. muons and protons), their length distributions are quite sharp and centered at relatively low distances (30 and 8 cm, respectively). For electrons, the distribution is quite broad but it does not extend past ~ 30 cm. The case of neutral pions can be misleading, as they decay promptly the track length associated with the true Monte Carlo particle is always < 1 cm. In Fig. 4.10 (right panel) I show the effective length distribution of the longest photon after the pion decays as $\pi^0 \rightarrow \gamma\gamma$, highlighting the number of fully contained photons in the TPC volume per event (either zero, one or both). One can see that the vast majority of events has both photons contained and that just a negligible number of them has none of them contained in the TPC volume. In any case, for the sake of caution, I will only keep the pion events with both photons contained.

Once I have prepared a sample at the Geant4 level, I need to process it through the detector simulation. In order to make adequate estimations of the noise levels and run the filtering and hit finder as I did with the ProtoDUNE data, one needs to turn off the default zero-suppression of the waveforms produced by the simulation. At this first stage I am only concerned with the waveforms with the noise added, so I keep the noise

4.5. USING SIMULATED SAMPLES

addition option as true in the configuration. However, for studies related to the hit finder performance one will also need to store the noiseless waveforms in order to retrieve the truth information of the hits. I will discuss this approach next.

After the detector simulation stage, one needs to extract the no zero-suppressed noisy waveforms, along with their offline channel numbers, and store them in a certain format to be analysed later. To reduce the amount of data that will go for processing, I used the information from the Geant4 step of the simulation to select only the active channels, i.e. the channels where some ionisation electrons arrive. Moreover, as said previously, I only extract the waveforms from APA 0 and exclusively the ones coming from induction channels. The resulting ROOT file contains a tree with two branches, one containing the waveforms for each event and channel and the other with the corresponding offline channel numbers.

Finally, to extract the truth values for the orientation of the tracks and the energies of the particles I used a modified analysis module. This gives a ROOT file with a single tree, containing several branches with different information such as the components of the initial momentum of the particles, initial and final xyz location, track length, etc.

For the analysis of the resulting waveforms and truth values I used a custom set of Python libraries (available at [??]). Among other functionalities, these enable the user to read the ROOT files, export the raw data as pandas objects, apply the filters and compute the S/N of both the raw and filtered signals. So far, the default configuration for the filtering uses the set of optimal matched filter coefficients that I found using the ProtoDUNE data samples.

Additionally, for the analysis of the samples it was necessary to use two different reference frames, to study separately the signals coming from the U and V induction wire planes. As I am focussing on a single APA, the U and V wires have a different orientation in the yz plane. In the case of U wires, these are tilted 35.7° clockwise from the vertical (y direction), whereas the V wires are at the same angle but in the counter clockwise direction. Because of this, the best option is to deal with two new coordinate systems rotated by $\pm 35.7^\circ$ along the x axis, so the new y' and y'' directions are aligned with the

CHAPTER 4. MATCHED FILTER APPROACH TO TRIGGER PRIMITIVES

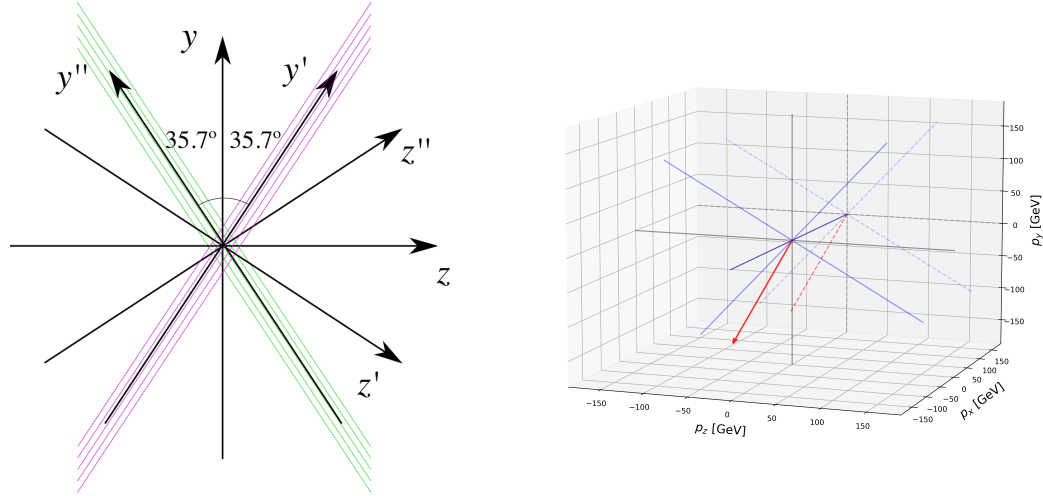


Figure 4.11: Left panel: schematic representation of the two new rotated reference frames used in this analysis (denoted as prime and double prime), viewed from the yz plane. The magenta stack of lines represent the wires in the U plane, whereas the green lines correspond to the wires in the V plane. Right panel: 3D representation of the momentum of one of the generated monoenergetic muons (red arrow) in the original reference frame (black lines), along with the new reference frame used for the U plane waveforms (blue lines). In the yz plane I added the projection of these three.

1669 U and V induction wires. Fig. 4.11 (left panel) shows a schematic representation of
 1670 the original reference frame together with the two rotated ones (denoted by primed and
 1671 double primed). This way, one can easily understand how parallel was a track to the
 1672 wires in the two induction planes. Fig. 4.11 (right panel) shows a 3D representation of
 1673 the momentum of a track (red arrow) in the original reference frame (black lines), along
 1674 with the new reference frame for U wires (blue lines). I added the projection in the yz
 1675 plane of this three, to show the usefulness of the new reference frame to tell whether a
 1676 track is parallel or normal to the wires in the induction plane.

1677 Fig. 4.12 shows the distribution of the average S/N improvement per event when one
 1678 applies the optimal matched filters. I produced separate distributions for the channels
 1679 in the U (red) and V (blue) induction wire planes. Notice that the S/N distributions
 1680 for the track-like particles, i.e. muons (top left panel) and protons (bottom left panel),
 1681 have significantly larger mean values than the distributions of the shower like particles,
 1682 i.e. electrons (top right panel) and neutral pions (bottom right panel). An important

4.5. USING SIMULATED SAMPLES

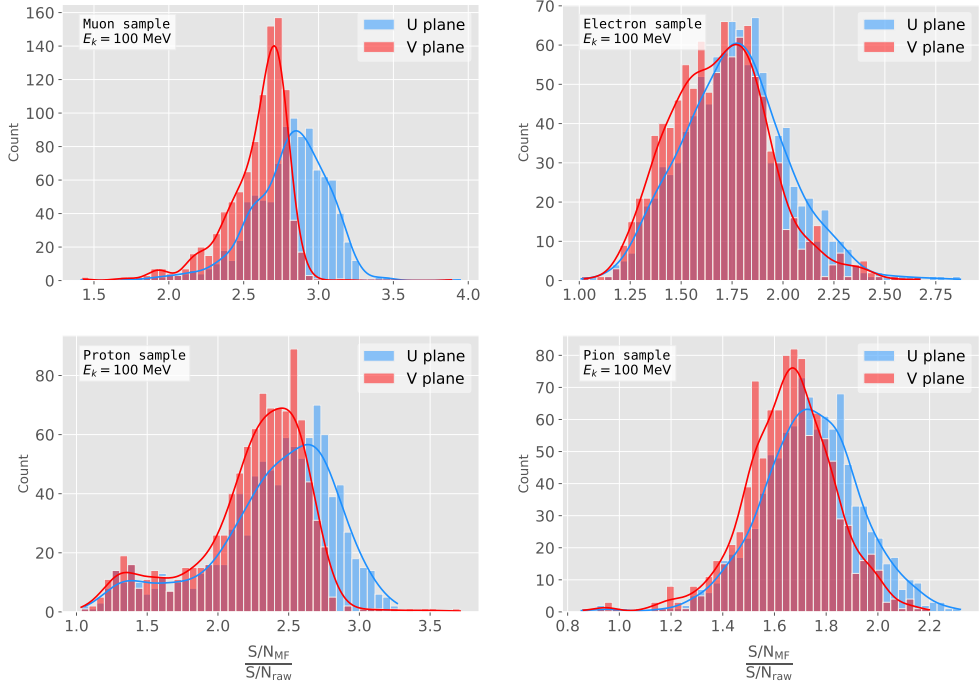


Figure 4.12: Distributions of the mean S/N improvement per event for the corresponding sample after applying the matched filters. Here I separated the change in the U plane (blue) and the V plane (red) channels. From top left to the right: muon, electron, proton and neutral pion. All the events have a fixed kinetic energy of $E_k = 100 \text{ MeV}$.

difference between these results and the ones seen before for ProtoDUNE data is that, overall, the improvements that I get for simulated data are bigger. This could be due either to the default noise model used in the *LArSoft* simulation or to the simulated hits having higher energy than the ones in the recorded data. Nonetheless, the concluding message is that the previously optimised matched filters give an overall significant improvement of the S/N for the different samples.

About the convention I followed for the plots and results, in the case of the raw and filtered S/N of each event in the sample I simply took the average of the quantities over all the active channels in the event. That is, if a certain event has N_{chan} active channels these two quantities are computed as:

$$(S/N_{fir})_{event} = \frac{\sum_{i=0}^{N_{chan}} (S/N_{fir})_i}{N_{chan}}, \quad (4.18)$$

$$(S/N_{raw})_{event} = \frac{\sum_{i=0}^{N_{chan}} (S/N_{raw})_i}{N_{chan}}.$$

CHAPTER 4. MATCHED FILTER APPROACH TO TRIGGER PRIMITIVES

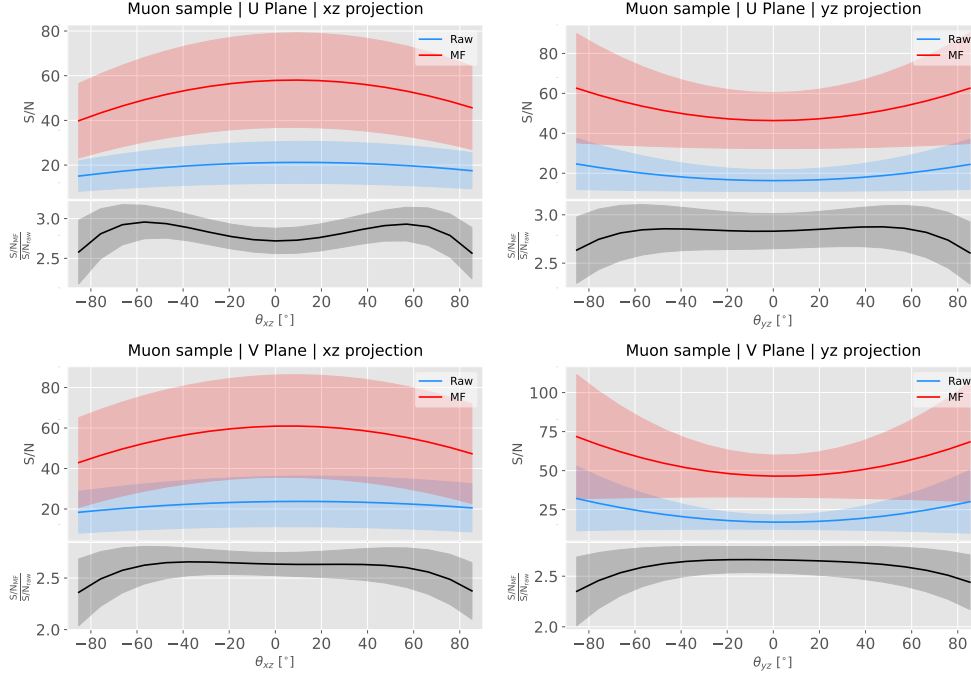


Figure 4.13: Angular dependence of the mean S/N and the S/N improvement, for the different monoenergetic samples considered (from top to bottom: electrons, muons, protons and neutral pions). The two columns on the left represent the values for the U plane waveforms. The top subplots show the mean S/N for raw (green) and filtered (red) waveforms whereas the bottom subplots depict the averaged S/N improvement (black).

1693 However, for the ratio of the raw and filtered S/N (what I called the S/N improvement)
 1694 per event I am not just taking the ratio of the previous two quantities but computing
 1695 the average of the individual ratios per channel in the event:

$$\left(\frac{S/N_{fir}}{S/N_{raw}} \right)_{event} = \frac{\sum_{i=0}^{N_{chan}} \left(\frac{S/N_{fir}}{S/N_{raw}} \right)_i}{N_{chan}}, \quad (4.19)$$

1696 and so:

$$\left(\frac{S/N_{fir}}{S/N_{raw}} \right)_{event} \neq \frac{(S/N_{fir})_{event}}{(S/N_{raw})_{event}}. \quad (4.20)$$

1697 4.5.1 Angular dependence

1698 Having these monoenergetic samples, one can also study the angular dependence of the
 1699 performance of the matched filter. This is an important point, as it is a well established

4.5. USING SIMULATED SAMPLES

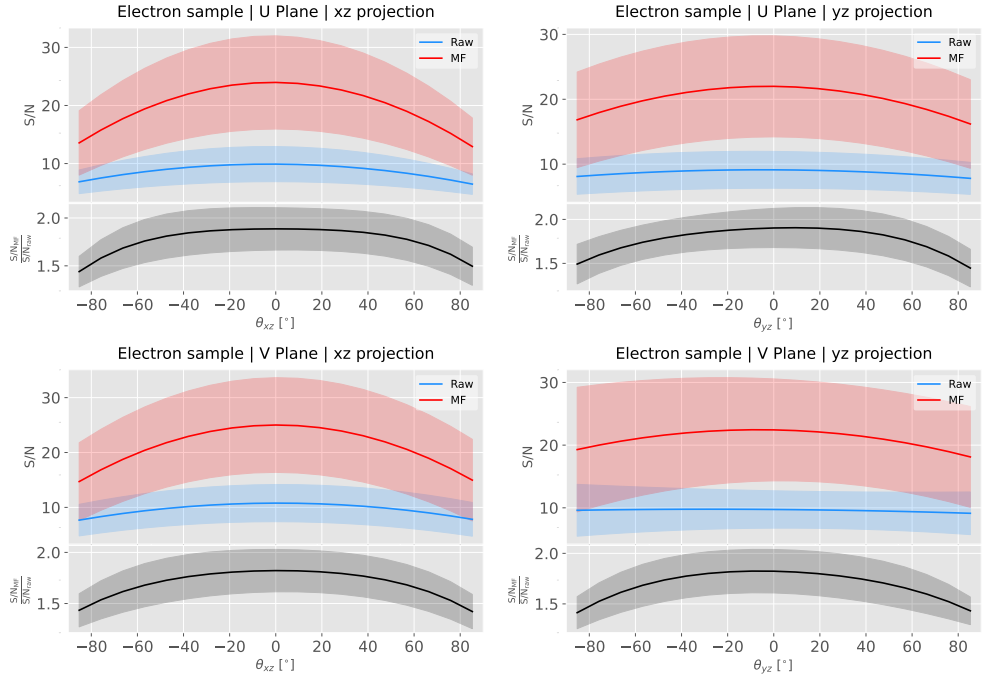


Figure 4.14: Angular dependence of the mean S/N and the S/N improvement, for the different monoenergetic samples considered (from top to bottom: electrons, muons, protons and neutral pions). The two columns on the left represent the values for the U plane waveforms. The top subplots show the mean S/N for raw (green) and filtered (red) waveforms whereas the bottom subplots depict the averaged S/N improvement (black).

fact that for certain configurations (an extreme case configuration being signals normal to the wire plane and perpendicular to the induction wires at the same time) the S/N is much lower than average as the corresponding waveforms are severely distorted. In this sense, I am interested to see how the matched filter behaves for these cases and how the S/N improvement on those compare to the average.

Fig. 4.13 shows the angular dependence of the S/N for the monoenergetic $E_k = 100$ MeV isotropic muons, for the different induction wire planes and projections. The angles for each event are given by the components of the initial value of the momentum of the particles, taking the angles of the projections on the xz and yz planes with respect to the z axis (more accurately, one needs to compute these angles twice for each event, a pair for the $xy'z'$ coordinate system and the other for the $xy''z''$). The top row shows the dependence on the angles corresponding to the U plane, i.e. $\theta_{xz'}$ and $\theta_{y'z'}$, whereas the bottom row shows the angular dependence viewed from the V plane, $\theta_{xz''}$ and $\theta_{y''z''}$. In

CHAPTER 4. MATCHED FILTER APPROACH TO TRIGGER PRIMITIVES

each plot, the top subplot represents the mean values of the S/N for the raw (blue) and matched filtered (red) signals, and the bottom subplot the averaged S/N improvement (black). The solid lines represent the mean value obtained for the corresponding angular value, whereas the semitransparent bands represent one standard deviation around the mean at each point.

As expected, the S/N is in general higher when tracks are parallel to the APA (i.e. $\theta_{xz} \sim 0$) and lower when it is normal to the plane ($\theta_{xz} \sim \pm 90^\circ$). In the same way, tracks parallel to the wires ($\theta_{yz} \sim \pm 90^\circ$) tend to have higher S/N than those perpendicular to these ($\theta_{yz} \sim \pm 0$).

Fig. 4.14 shows the corresponding angular dependence information for the $E_k = 100$ MeV electrons sample. Notice that, in this case, the S/N behaviour discussed above does not hold. A possible explanation can be that, because most hits in these events are produced by the secondary particles generated in the EM shower, the signal peaks whose S/N ratios were computed do not correspond to the directional information of the primary electron.

4.5.2 Distortion and peak asymmetry

As a little case of study, I selected two of the simulated $E_k = 100$ MeV monoenergetic muon events. With respect to the U induction plane, one is parallel to the APA (low $\theta_{xz'}$) and to the wires (high $\theta_{y'z'}$) and the other is normal to the APA plane (high $\theta_{xz'}$) and perpendicular to the wires (low $\theta_{y'z'}$). As expected from the results on the angular dependence discussed above, the former has a higher S/N (before and after the filtering) when compared to the latter. An interesting thing to notice about these two samples is that, even though one has a much bigger S/N than the other, it is the one with the smallest S/N the one that got the biggest averaged S/N improvement. In Table 4.1 I included all the relevant parameters of these two $E_k = 100$ MeV muon events I am considering, namely, the angles with respect to the $xy'z'$ reference frame, the values of the S/N, the S/N improvement and also the so-called peak asymmetry Δ_{peak} that I will discuss next.

4.5. USING SIMULATED SAMPLES

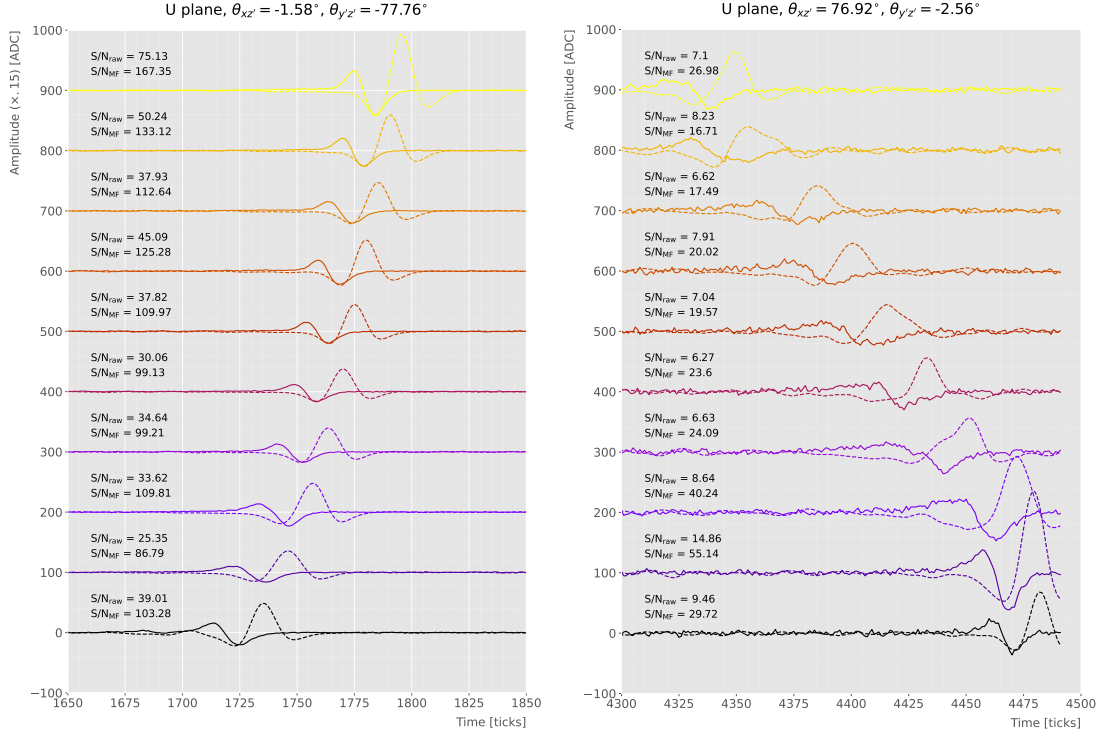


Figure 4.15: Selected consecutive waveforms corresponding to two monoenergetic $E_k = 100$ MeV muon events, one is parallel to the APA and to the wires in the U plane (left panel) and the other is normal to the APA plane and perpendicular to the U plane wires (right panel). The solid lines represent the raw waveforms whereas the dashed lines correspond to the waveforms after the matched filter was applied. The waveforms on the left panel have been scaled by a factor of 0.15 to have similar amplitude to the ones on the right panel.

Table 4.1: Characteristic parameters of the two monoenergetic muon events selected, relative to the U plane: projected angles in the xz' and yz' planes, S/N values for the raw and filtered waveforms, mean improvement of the S/N and peak asymmetry.

	$\theta_{xz'} (\circ)$	$\theta_{yz'} (\circ)$	S/N_{raw}	S/N_{MF}	$\frac{S/N_{\text{MF}}}{S/N_{\text{raw}}}$	$\Delta_{\text{peak}} (\text{ADC})$
High ("parallel")	-1.58	-77.76	41.65	112.44	2.83	-35.73
Low ("normal")	76.92	-2.56	8.07	25.46	3.12	-10.38

1741 One can try to understand better what is going on with these two events by looking
 1742 at the raw and filtered data from some of their active channels. Fig. 4.15 shows a
 1743 selection of consecutive raw and filtered U plane waveforms from the event with high S/N
 1744 (left panel) and the one with low S/N (right panel). Notice that to show both collections
 1745 of waveforms at a similar scale I had to apply a factor of 0.15 to the waveforms with
 1746 high S/N. Additionally, next to each waveform I included the values of the raw and

CHAPTER 4. MATCHED FILTER APPROACH TO TRIGGER PRIMITIVES

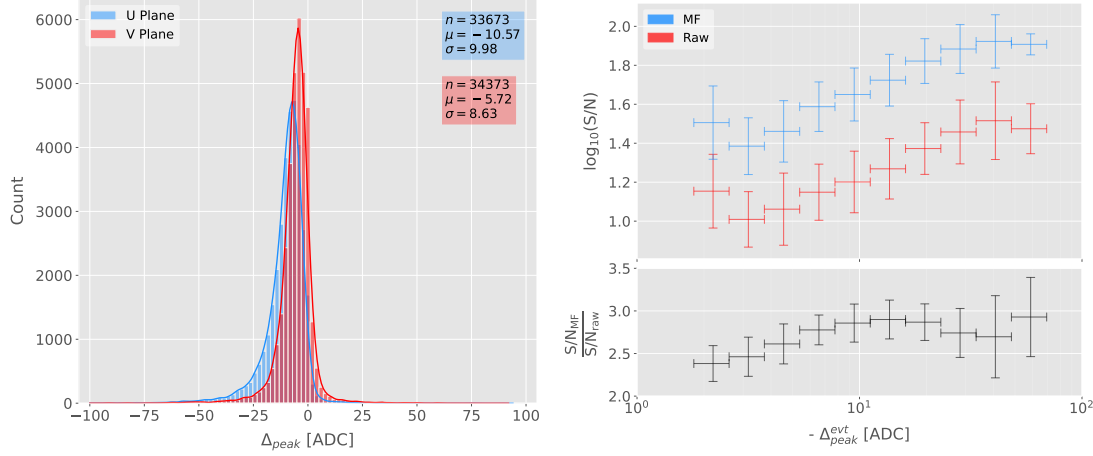


Figure 4.16: Left panel: peak asymmetry distribution for the case of the monoenergetic $E_k = 100$ MeV muon sample. Each value corresponds to a single bipolar signal peak from a channel in any event. The blue distribution represents the peaks on U plane channels, whereas the red corresponds to signal peaks in V wires. Right panel: relation between the mean peak asymmetry per event with the S/N for U channel waveforms from the $E_k = 100$ MeV muon sample. The top subplot shows the decimal logarithm of the mean S/N for the raw (red) and the matched filtered (blue) waveforms. The bottom subplot contains the mean S/N improvement ratio after the matched filter was applied.

1747 matched filtered S/N for the corresponding channel. The first thing to notice in this plot
 1748 is that the amplitude of the signal peaks from the normal track have a much smaller
 1749 amplitude, and also appear quite distorted when compared to the others. On the other
 1750 hand, although the matched filtered S/N is still smaller, the relative improvement is
 1751 bigger than in the parallel case.

1752 A way I found to quantify the difference between the shapes within these two events
 1753 is their different peak asymmetry. One can define the peak asymmetry as the (signed)
 1754 difference between the positive and the negative peaks of the bipolar shape, i.e.:

$$\Delta_{peak} \equiv h_+ - h_-, \quad (4.21)$$

1755 where both heights h_+ and h_- are positive defined. Fig. 4.16 (left panel) shows the
 1756 distribution of this peak asymmetry for all the waveforms corresponding to channels
 1757 in the U (blue) and V (red) planes for the monoenergetic muon sample. One can
 1758 see that these distributions are clearly shifted to negative values (with mean values

4.5. USING SIMULATED SAMPLES

1759 $\mu_{\Delta}^U = -10.57$ ADC and $\mu_{\Delta}^V = -5.72$ ADC respectively). It is interesting to notice
1760 that the peak asymmetry value of the sample with high S/N sits at the left tail of the
1761 distribution whereas the corresponding value of the sample with low S/N lies around
1762 the mean.

1763 Now, one can try to correlate the peak asymmetry with the S/N and the S/N change
1764 per event. Fig. 4.16 (right panel) shows the result of comparing (minus) the mean
1765 peak asymmetry per event to the averaged raw (red) and matched filtered (blue) S/N
1766 per event (top subplot). The horizontal lines sit at the mean value obtained in the fit
1767 and represent the width of the $-\Delta_{peak}$ bins used, while the vertical lines indicate one
1768 standard deviation around that mean value. Notice that, when taking decimal logarithm
1769 on both, there is an approximate linear relation between these quantities, except for
1770 peak asymmetry values bigger than -5 ADC where the S/N remains constant.

1771 Also, in the bottom subplot of Fig. 4.16 (right panel) I show the relation between
1772 the peak asymmetry and the mean S/N improvement. In this case, one see that there is
1773 a maximum at $\Delta_{peak} \sim -10$ ADC. As mentioned previously, this is also the value of the
1774 mean of the peak asymmetry distribution. In fact, it is expected that our filter favours
1775 the signal peaks with the most common values of the peak asymmetry, as this was one
1776 of the features I target in our filter coefficient optimisation through the parameter δ .

1777 These results suggest that events with poorer values of the mean S/N, usually
1778 associated to non-favourable track orientations, tend to have smaller values of the mean
1779 peak asymmetry (in absolute value). Nonetheless, because our matched filters have
1780 been optimised to account for these asymmetries, the improvement on the S/N for these
1781 events is sizeable if not better than the one for events which already had a high S/N.

1782 4.5.3 Hit sensitivity

1783 One of the advantages of the matched filter, directly related to increasing the S/N, is
1784 the capability of picking hits that before fell below the threshold. For instance, Fig. 4.17
1785 shows the raw ADC data from an example event (electron, $E_k = 100$ MeV) with the
1786 produced true hits superimposed (black boxes), together with the hits produced by the

CHAPTER 4. MATCHED FILTER APPROACH TO TRIGGER PRIMITIVES

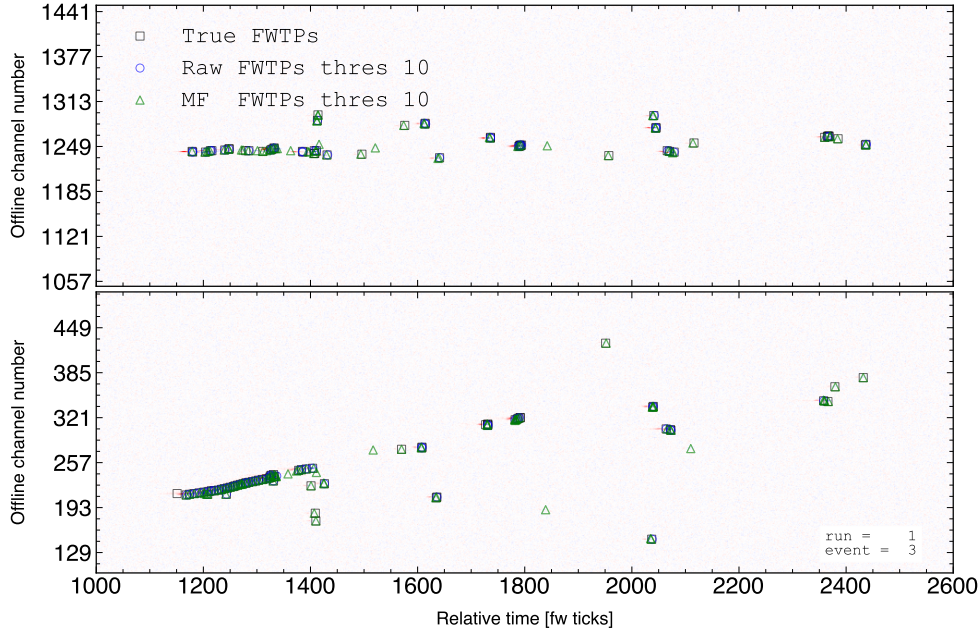


Figure 4.17: Raw data display in the plane time (in firmware ticks) vs. offline channel number for an $E_k = 100$ MeV electron event. The produced true hits are superimposed (black boxes) as well as the hits coming from the standard hit finder chain (blue circles) and the hit finder using the matched filter (green triangles).

standard hit finder chain (blue circles), i.e. using the current FIR filter, and the hits obtained using the matched filters (green triangles). Both the standard and the matched filter hit finders were run with a threshold of 10 ADC. Notice that the standard hits match well the true ones at the initial part of the event (where we have a track-like object), but they miss most of the hits produced by the EM shower at later times. On the other hand, the hits produced with the matched filter have a better agreement with the true hits even for the more diffuse shower activity.

Notwithstanding that now I get more hits with this combination of matched filter and low threshold as a results of the enhancement of the signal peaks relative to the noise level, it is also true that I pick some spurious hits not related to any real activity if one lowers the thresholds too much. Therefore, some optimisation of the threshold is needed. Basically one will need to make a trade-off between precision and sensitivity.

Having this in mind, I tried to compare the produced hits one gets from the standard hit finder and the ones resulting from applying the matched filter with the true hits.

4.5. USING SIMULATED SAMPLES

1801 By running the hit finders on our samples with different values of the threshold one
1802 can understand, for instance, how low one can set the threshold without getting mostly
1803 spurious hits and then evaluate the gains obtained from this.

1804 Because now I am also interested in seeing how the hit sensitivity changes with the
1805 energy, I prepared new isotropic samples with the same types of particles as before
1806 (muons, electrons, protons and neutral pions) but with a flat kinetic energy distribution
1807 ranging from 5 to 100 MeV.

1808 In order to estimate the hit sensitivity, given a certain sample, one needs to recover
1809 the set of true hits to be able to compare these with the ones produced. To do so,
1810 a modification in the procedure I was using to extract the raw waveforms is needed.
1811 For this kind of study I run the detector simulation in two steps, first I produce the
1812 waveforms without noise and extract them in the same format I used for the raw data,
1813 then the noise is added and the noisy waveforms are then written to a file as well.

1814 To have a better comparison between the true hits and the ones produced from
1815 the raw waveforms after applying the two filters, I applied also the FIR filter and the
1816 matched filters to the noiseless waveforms and then I run the hit finder with a minimal
1817 threshold (in this case I used 1 ADC) on these noiseless filtered waveforms. In this way
1818 I generated two sets of true hits, I will refer to them as standard true hits (with the
1819 current/default FIR filter) and matched filter true hits respectively. This allows a more
1820 precise matching between the different groups of hits produced, as it will account for
1821 any delays and distortions introduced by the FIR and the matched filters.

1822 In the case of the raw waveforms (with noise), I run the hit finder on them, with
1823 different values of the threshold, after applying either the FIR or the matched filters. I
1824 will name them simply standard hits and matched filter hits respectively. Then, I match
1825 the generated hits to the true hits (the standard hits with the standard true hits and
1826 the matched filter hits with the matched filter true hits). The matching is performed by
1827 comparing the channel number and the timestamp of the hits. To count as a match,
1828 I require that all hits with the same channel number and timestamp have overlapping
1829 hit windows, i.e. the time windows between their hit end and hit start times need to

CHAPTER 4. MATCHED FILTER APPROACH TO TRIGGER PRIMITIVES

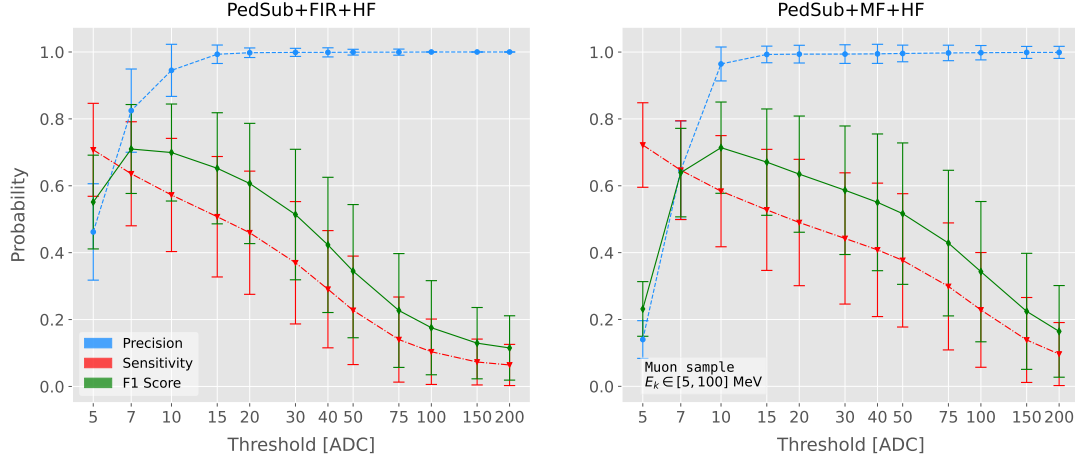


Figure 4.18: Dependence of the precision (blue), sensitivity (red) and F_1 (green) scores on the threshold values used in the hit finder, for the FIR (left panel) and matched filter (right panel) cases. The results were obtained after matching the hits to the true hits in the case of the isotropic muon sample with kinetic energy in the range 5 to 100 MeV, taking only into account the induction plane channels. The points represent the mean value while the error bars indicate one standard deviation around that mean value.

overlap. If more than one hit in one of the groups have hit overlap with the same hit in the other group I only count the hit with closer hit peak time value.

The generation of the samples, the procedure to produce the standard hits (with the default FIR filter) and matched filter hits and the matching of these with the true hits is described in detail in App. ??.

To quantify the performance of the two hit finder approaches, I use a classical method from statistical classification known as confusion matrix [98]. This is basically a way of sorting the outputs of a binary classifier, considering the true values of the classification and the predicted values. It divides the outputs in four categories: true positive (TP, both true and predicted values are 1), false negative (FN, true value is 1 but predicted is 0), false positive (FP, true value is 0 but predicted is 1) and true negative (TN, both true and predicted values are 0)).

The contents of the confusion matrix allow us to compute other derived scores to judge the performance of our classifiers. In this study, I will make use of three of these

4.5. USING SIMULATED SAMPLES

1844 metrics, namely the precision or positive predictive value:

$$\text{PPV} = \frac{\text{TP}}{\text{TP} + \text{FP}}, \quad (4.22)$$

1845 the sensitivity or true positive rate:

$$\text{TPR} = \frac{\text{TP}}{\text{TP} + \text{FN}}, \quad (4.23)$$

1846 and the F_1 score [99]:

$$F_1 = \frac{2\text{TP}}{2\text{TP} + \text{FP} + \text{FN}}, \quad (4.24)$$

1847 which is the harmonic mean of the precision and the sensitivity.

1848 In our specific case I am not going to make use of the true negative value, as its
1849 definition in this context can be ambiguous because one does not have clear instances in
1850 the classification process. This way, I will only count the number of true positives as the
1851 total amount of hits I can match between true and raw populations, the number of false
1852 negatives will be the number of missing true hits and the false positive the number of
1853 hits which do not match any true hit.

1854 In Fig. 4.18 I show the precision (blue), sensitivity (red) and F_1 (green) scores I
1855 obtained for different values of the threshold used in the hit finder for the case of the
1856 muon sample. Because the matched filters are only applied to induction channels, I only
1857 consider here hits coming from the U and V planes. The panel on the left corresponds
1858 to the scores I got when I ran the hit finder on the FIR filtered waveforms, whereas the
1859 right panel contains the scores for the matched filter case. The points are centered at
1860 the threshold value used and represent the mean value obtained for each score using all
1861 the generated events, while the error bars indicate one standard deviation around the
1862 mean value.

1863 One can see that the precision for the matched filter case is lower when the thresholds
1864 are very low, as the noise baseline is slightly amplified, but then rises to high values
1865 quicker than for the FIR case. The other difference one can spot is that the sensitivity

CHAPTER 4. MATCHED FILTER APPROACH TO TRIGGER PRIMITIVES

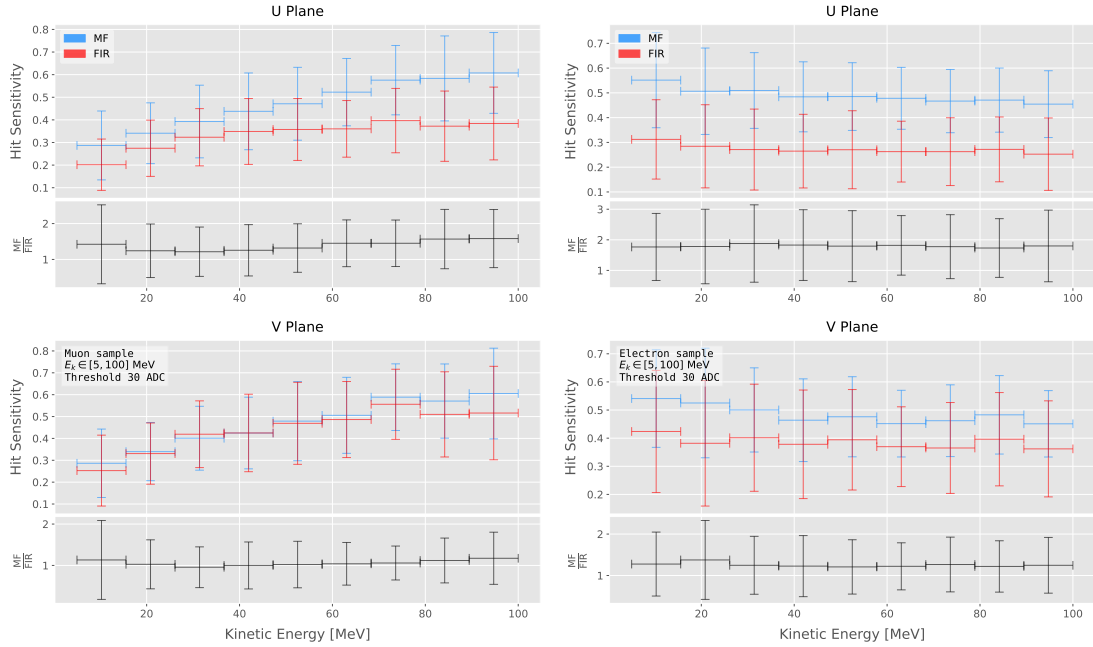


Figure 4.19: Dependence of the averaged hit sensitivity on the kinetic energy of the events for the matched filter (blue) and standard (red) hits, for the case of the muon (left panel) and electron (right panel) samples, separated between U (top plots) and V (bottom plots) induction wire planes. The top subplots contain the hit sensitivities for the two hit finder alternatives, while the bottom subplots show the ratio between the two. The horizontal lines sit at the mean value and represent the size of the energy bins, while the vertical error bars indicate one standard deviation around that mean value.

in the FIR case starts dropping faster at around the same threshold values where the precision stabilizes around 1, while in contrast for the matched filter this rapid decrease starts at higher threshold values. A similar scan for the same thresholds was performed for the electron sample in the same energy range, yielding similar results.

In Fig. 4.19 I show the averaged hit sensitivity versus the kinetic energy of the events, both for the matched filter hits (blue) and the standard hits (red). The left panel corresponds to the muon sample, whereas the one on the right corresponds to the electron sample, both with kinetic energies between 5 and 100 MeV. In each panel the top plot corresponds to hits in the U plane, while the bottom plot contains the same information for the V plane. Each plot contains two subplots, the one on the top shows the hit sensitivity values for the matched filter and standard hits separate, while the bottom subplot depicts the ratio between the matched filter and standard sensitivities.

4.5. USING SIMULATED SAMPLES

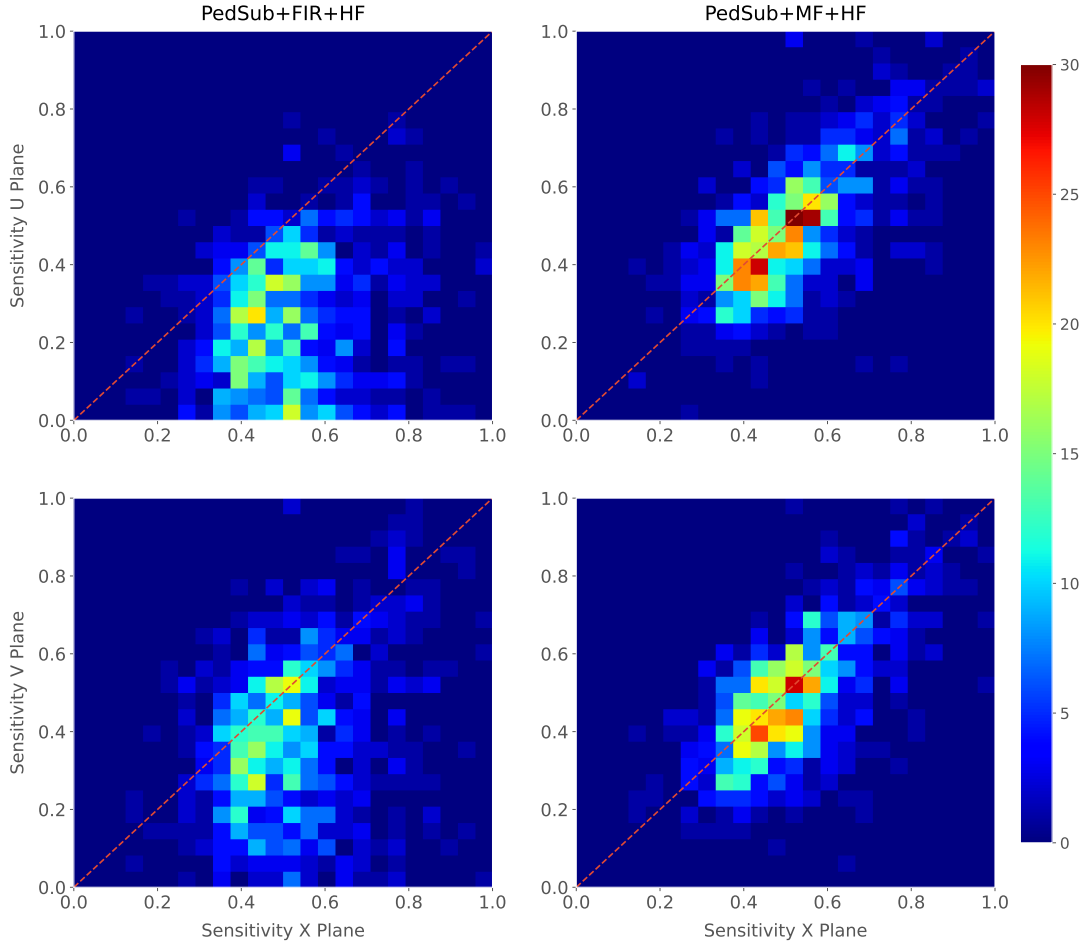


Figure 4.20: Distributions of the hit sensitivity in the U (top panels) and V (bottom panels) planes versus the hit sensitivity in the X plane, both for the standard hits (left panels) and the matched filter hits (right panels), in the case of the electron sample and a threshold of 30 ADC.

1878 The horizontal lines are placed at the mean value obtained in the fit and represent the
 1879 width of the E_k bins used, while the vertical error bars indicate one standard deviation
 1880 around that mean value. In both cases the threshold used was 30 ADC, as I required
 1881 the precision to be higher than 0.99 for both matched filter and standard cases.

1882 One can see that, in general, the improvements are better for the U than for the V
 1883 plane. While for the U channels I achieved a mean improvement of 50% and 80% for
 1884 muons and electrons respectively, the improvement in the V plane is stalled at 10% and
 1885 25%. Nevertheless, if I look at the sensitivities for the matched filter hits in both planes
 1886 one can see these have similar mean values for each energy bin, while on the contrary

CHAPTER 4. MATCHED FILTER APPROACH TO TRIGGER PRIMITIVES

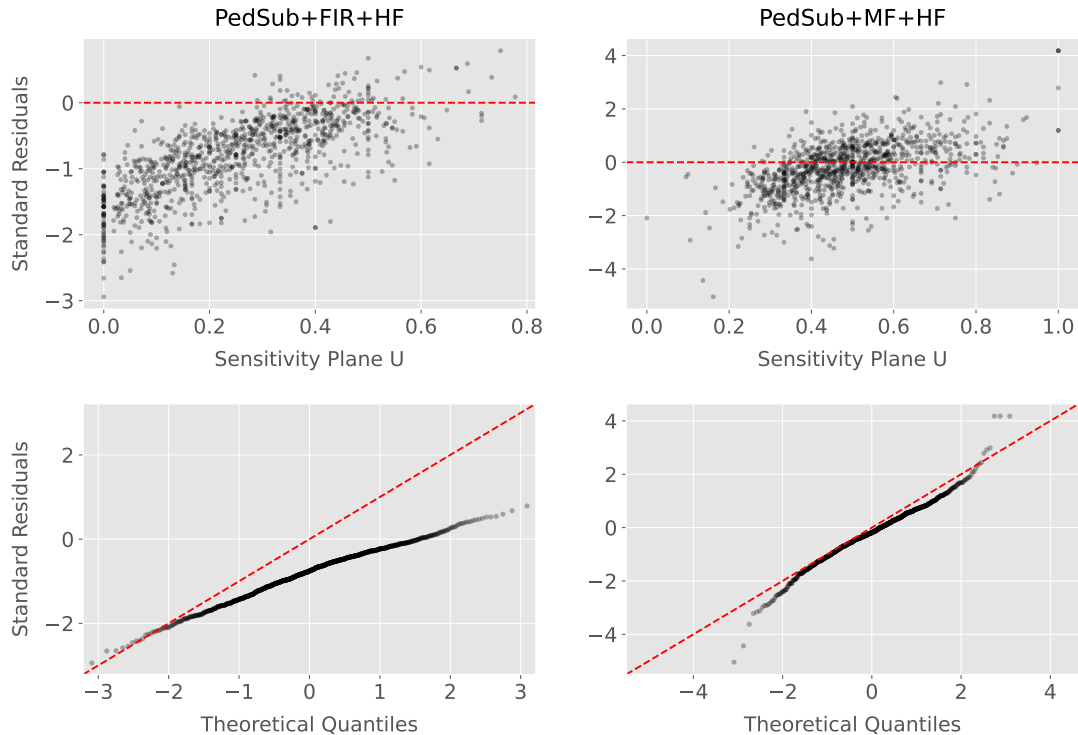


Figure 4.21: Top panels: standard residual plots of the hit sensitivities between the X and U planes. Bottom panels: quantile-quantile plots of the hit sensitivity standard residuals between the X and U planes. In all cases, the left panel corresponds to the standard hits while the right panel represents the matched filter case, all from the electron sample with a 30 ADC threshold.

for the standard hits the sensitivity remains relatively high for the V plane. This way, it looks there was a less significant gain because the hit sensitivity was already high.

Another interesting observation is the different behaviors for muons and electrons. While hit sensitivity for muons grows significantly with energy, in the case of electrons this slightly decreases the higher the kinetic energy of the event is. In any case, when it comes to the improvement on the sensitivities, this remains almost constant in all cases.

Furthermore, we can look at how the concurrence of hits between the different wire planes has changed. For any given event, I expect to have a similar number of hits in the three planes. As the ionisation electrons need to cross the U and V planes prior to reach the collection plane X they will induce current in those wire planes. A way to check the concurrence of hits across planes is looking at the relation between the hit sensitivities for each individual event. One cannot expect the sensitivities to be exactly equal across

4.5. USING SIMULATED SAMPLES

1899 planes, but ideally they should be normally distributed around the diagonal.

1900 Fig. 4.20 shows the hit sensitivity in the U (top panels) and V (bottom panels)
1901 planes versus the hit sensitivity in the X plane, for the case of the standard hits (left
1902 panels) and the matched filter hits (right panels). All plots were generated for the
1903 electron sample and a threshold of 30 ADC. From these one can see a clear trend,
1904 when I use the standard hit finder chain the sensitivities in the induction planes are
1905 systematically lower than the hit sensitivity in the X plane, i.e. most of the points sit
1906 below the diagonal (red dashed line). In contrast, when the matched filters are applied,
1907 the majority of the events are distributed around the diagonal. This points out that the
1908 concurrence of hits across planes has improved.

1909 To exemplify the improvement I obtained, one can consider the residuals of the hit
1910 sensitivities for the X and U planes. Assuming the diagonal hypothesis, i.e. given a
1911 dataset of the form (x, y) for any x I take the predicted y value to be equal to the value
1912 of x , I can compute the standard residuals for the hit sensitivities in U given the ones for
1913 X. In Fig. 4.21 (top panels) I show these standard residuals against the corresponding
1914 values of the hit sensitivity in the U plane, for our electron sample with kinetic energy
1915 between 5 and 100 MeV. If I compare the scatter points in the case of the standard
1916 hits (left panel) and the matched filter hits (right panel), I see that the residuals of the
1917 standard hit finder case follow a certain pattern and their mean deviates from 0.

1918 To see clearly if the residuals are normally distributed, in Fig. 4.21 (bottom panels)
1919 I plot the corresponding quantile-quantile plot for both the standard (left panel) and
1920 matched filter (right panel) standard residuals. One can clearly see that the points for
1921 the standard case follow a strongly non-linear pattern, suggesting that the residuals
1922 do not follow a normal distribution. In contrast, for the matched filter hits the points
1923 conform to a roughly linear path, implying that in this case the normality condition is
1924 fulfilled.

1925 All these results hint at the fact that the concurrence of hits across the wire planes
1926 can be strengthened by applying the matched filters.

1928 DM searches with neutrinos from the Sun

1929 5.1 Motivation

1930 The idea of detecting neutrino signals coming from the Sun’s core to probe DM is not
1931 new. The main focus of these searches has usually been high-energy neutrinos originated
1932 from DM annihilations into heavy particles [100–103], although recent studies have
1933 proposed to look at the low-energy neutrino flux arising from the decay of light mesons
1934 at rest in the Sun [104–107] previously thought undetectable.

1935 In this chapter I try to demonstrate the capability of DUNE to constrain different
1936 DM scenarios. I used the neutrino fluxes arising from DM annihilations in the core
1937 of the Sun to compute the projected limits that DUNE would be able to set on the
1938 annihilation rates in the Sun and the DM scattering cross sections.

1939 5.2 Gravitational capture of DM by the Sun

1940 The Sun and the centre of the Earth are possible sources of DM annihilations, specially
1941 interesting because of their proximity. Their gravitational attraction ensured the capture
1942 of DM from the local halo through repeated scatterings of DM particles crossing them.
1943 Only neutrinos produced from DM annihilations can escape the dense interior of these
1944 objects. Therefore, neutrino telescopes are the most useful experimental layouts to
1945 pursue DM searches from their cores.

1946 The neutrino flux from DM annihilations inside the Sun depends on the DM capture

CHAPTER 5. DM SEARCHES WITH NEUTRINOS FROM THE SUN

1947 rate, which is proportional to the DM scattering cross section, and the annihilation rate,
 1948 which is proportional to the velocity-averaged DM annihilation cross-section. The total
 1949 number of DM particles inside the Sun follows the Boltzmann equation [104]:

$$\frac{dN_{DM}}{dt} = C_\odot - A_\odot N_{DM}^2, \quad (5.1)$$

1950 where C_\odot and A_\odot are the total Sun DM capture and annihilation rates respectively.
 1951 In this expression I neglected the evaporation term, proportional to N_{DM} , which only
 1952 contribute for $m_{DM} \lesssim 4$ GeV [108]. As the current threshold of neutrino telescopes
 1953 is a few GeV, this region falls below the probed range but can be important in future
 1954 low-energy projects.

1955 This equation has an equilibrium solution:

$$N_{DM}^{eq} = \sqrt{\frac{C_\odot}{A_\odot}}, \quad (5.2)$$

1956 which represents the amount of DM inside the Sun if the capture and annihilation have
 1957 reached equilibrium. As the Sun is approximately 4.6 Gyr old, it is usually assumed that
 1958 equilibrium has been achieved. Therefore, the anomalous neutrino flux from the Sun
 1959 would only depend on the DM scattering cross section, enabling us to set limits on this
 1960 quantity. If one does not assume equilibrium, some assumptions on the DM annihilation
 1961 cross section are necessary to extract predictions from neutrino signals.

1962 Here, I am going to consider three possible scenarios for the DM interactions: DM
 1963 scattering off electrons, spin-dependent (SD) and spin-independent interactions off nuclei.
 1964 For the case of these last two, the cross sections will be given in terms of the SD and
 1965 SI elastic scattering DM cross section off protons (assuming that DM interactions off
 1966 protons and neutrons are identical), σ_p^{SD} and σ_p^{SI} , as [2, 104]:

$$\sigma_i^{\text{SD}} = \left(\frac{\tilde{\mu}_{A_i}}{\tilde{\mu}_p} \right)^2 \frac{4(J_i + 1)}{3J_i} |\langle S_{p,i} \rangle + \langle S_{n,i} \rangle|^2 \sigma_p^{\text{SD}}, \quad (5.3)$$

$$\sigma_i^{\text{SI}} = \left(\frac{\tilde{\mu}_{A_i}}{\tilde{\mu}_p} \right)^2 A_i^2 \sigma_p^{\text{SI}}, \quad (5.4)$$

5.2. GRAVITATIONAL CAPTURE OF DM BY THE SUN

where $\tilde{\mu}_{A_i}$ is the reduced mass of the DM-nucleus i system, $\tilde{\mu}_p$ is the reduced mass of the DM-proton system, A_i and J_i the mass number and total angular momentum of nucleus i and $\langle S_{p,i} \rangle$ and $\langle S_{n,i} \rangle$ the expectation value of the spins of protons and neutrons averaged over all nucleons, respectively (see Ref. [109] for a review on spin expectation values).

Since the Sun is mainly composed of Hydrogen, the capture of DM from the halo is expected to occur mainly through spin-dependent scattering. However, since the spin-independent cross section is proportional to the square of the atomic mass, heavy elements can contribute to the capture rate (even though they constitute less than 2% of the mass of the Sun). Heavy elements can also contribute to the spin-dependent cross section if the DM has also momentum-dependent interactions.

DM particles can get captured by the Sun if after repeated scatterings off solar targets their final velocity is lower than the escape velocity of the Sun. In the limit of weak cross sections, this capture rate can be approximately written as [2]:

$$C_{\odot}^{\text{weak}} = \sum_i \int_0^{R_{\odot}} dr 4\pi r^2 \int_0^{\infty} du_{\chi} \frac{\rho_{\chi}}{m_{\chi}} \frac{f_{v_{\odot}}(u_{\chi})}{u_{\chi}} \omega(r) \int_0^{v_e(r)} dv R_i^-(\omega \rightarrow v) |F_i(q)|^2, \quad (5.5)$$

where the summation extends over all possible nuclear targets. In this expression, R_{\odot} is the radius of the Sun, ρ_{χ} is the local DM density, m_{χ} the mass of the DM particle, $f_{v_{\odot}}(u_{\chi})$ the DM velocity distribution seen from the Sun's reference frame, $R_i^-(\omega \rightarrow v)$ is the differential rate at which a DM particle with velocity v scatters a solar target of mass m_i to end up with a velocity ω and $|F_i(q)|$ is the nuclear form factor of target i .

The differential scattering rate takes a rather simple form when considering velocity-independent and isotropic cross sections. In that case, this quantity is given by [2, 110]:

$$R_i^-(\omega \rightarrow v) = \frac{2}{\sqrt{\pi}} \frac{\mu_{i,+}^2}{\mu_i} \frac{v}{\omega} n_i(r) \sigma_i \left[\chi(-\alpha_-, \alpha_+) + \chi(-\beta_-, \beta_+) e^{\mu_i(\omega^2 - v^2)/u_i^2(r)} \right], \quad (5.6)$$

CHAPTER 5. DM SEARCHES WITH NEUTRINOS FROM THE SUN

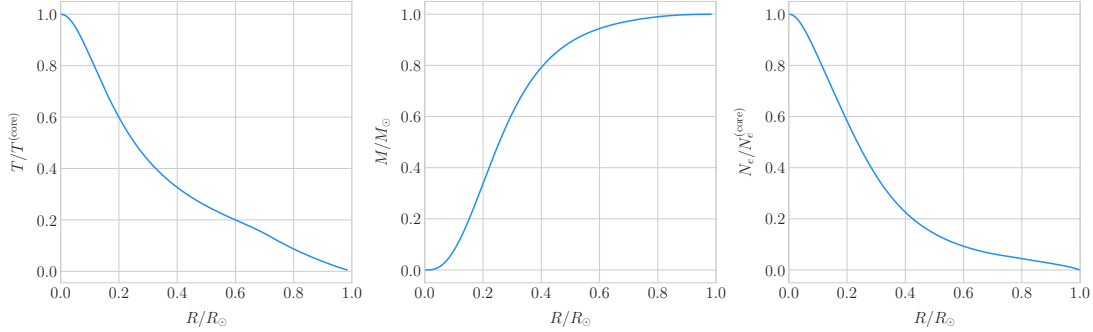


Figure 5.1: Input solar parameters used in our capture rate computation as functions of the Sun's radius, from left to right: temperature (with respect to the temperature at the core), mass (in solar masses) and electron number density (with respect to the electron density at the core). All quantities shown correspond to the standard solar model BS2005-OP [1].

1988 where μ_i is the ratio between the DM mass and the mass of target i , $\mu_{i,\pm}$ is defined as:

$$\mu_{i,\pm} \equiv \frac{\mu_i \pm 1}{2}, \quad (5.7)$$

1989 $n_i(r)$ is the density profile of target i in the solar medium, $u_i(r)$ is the most probable
1990 velocity of target i given by:

$$u_i(r) = \sqrt{\frac{2T_\odot(r)}{m_i}}, \quad (5.8)$$

1991 where $T_\odot(r)$ is the temperature of the Sun, the quantities α_\pm and β_\pm are defined as:

$$\alpha_\pm \equiv \frac{\mu_{i,+}v \pm \mu_{i,-}\omega}{u_i(r)}, \quad (5.9)$$

$$\beta_\pm \equiv \frac{\mu_{i,-}v \pm \mu_{i,+}\omega}{u_i(r)}, \quad (5.10)$$

1992 and the function $\chi(a, b)$ is a Gaussian integral of the form:

$$\chi(a, b) \equiv \int_a^b dx e^{-x^2}. \quad (5.11)$$

1993 Finally, if one assumes the DM halo velocity distribution in the galactic rest frame
1994 to be a Maxwell-Boltzmann distribution, one can write the halo velocity distribution for

5.2. GRAVITATIONAL CAPTURE OF DM BY THE SUN

1995 an observer moving at the speed of the Sun with respect to the DM rest frame as:

$$f_{v_\odot}(u_\chi) = \sqrt{\frac{3}{2\pi}} \frac{u_\chi}{v_\odot v_d} \left(e^{-\frac{3(u_\chi - v_\odot)^2}{2v_d^2}} - e^{-\frac{3(u_\chi + v_\odot)^2}{2v_d^2}} \right), \quad (5.12)$$

1996 where:

$$\omega^2 = u_\chi^2 + v_e(r)^2, \quad (5.13)$$

1997 is the DM velocity squared, v_\odot the relative velocity of the Sun from the DM rest frame
1998 and $v_d \simeq \sqrt{3/2}v_\odot$ the velocity dispersion.

1999 For the case of strong scattering cross section, Eq. (5.5) ceases to be valid, as it
2000 escalates indefinitely with the cross section. In that limit, the capture rate saturates to
2001 the case where the probability of interaction is equal to one, which can be written as:

$$C_\odot^{\text{geom}} = \pi R_\odot^2 \left(\frac{\rho_\chi}{m_\chi} \right) \langle v \rangle \left(1 + \frac{3}{2} \frac{v_e^2(R_\odot)}{v_d^2} \right) \xi(v_\odot, v_d), \quad (5.14)$$

2002 where $v_d = \sqrt{8/3\pi}v_\odot$ is the mean velocity in the DM rest frame and the factor $\xi(v_\odot, v_d)$
2003 accounts for the suppression due to the motion of the Sun:

$$\xi(v_\odot, v_d) = \frac{v_d^2 e^{-\frac{3v_\odot^2}{2v_d^2}} + \sqrt{\frac{\pi}{6}} \frac{v_d}{v_\odot} (v_d^2 + 3v_e^2(R_\odot) + 3v_\odot^2) \operatorname{Erf} \left(\sqrt{\frac{3}{2}} \frac{v_\odot}{v_d} \right)}{2v_d^2 + 3v_e^2(R_\odot)}. \quad (5.15)$$

2004 Having these into account, one can write the total capture rate as a combination of
2005 both contributions, allowing a smooth transition between the two, as:

$$C_\odot = C_\odot^{\text{weak}} \left(1 - e^{C_\odot^{\text{geom}} / C_\odot^{\text{weak}}} \right). \quad (5.16)$$

2006 I computed the capture rate from Eq. (5.16) in the case of interactions with
2007 electrons. To do so, I used the standard solar model BS2005-OP [1]. Fig. 5.1 shows the
2008 three parameters from the solar model that are needed for the computation, the solar
2009 temperature (left panel), mass (central panel) and electron density (right panel) profiles.

2010 For the case of the interactions off nuclei, the computations are more convoluted

CHAPTER 5. DM SEARCHES WITH NEUTRINOS FROM THE SUN

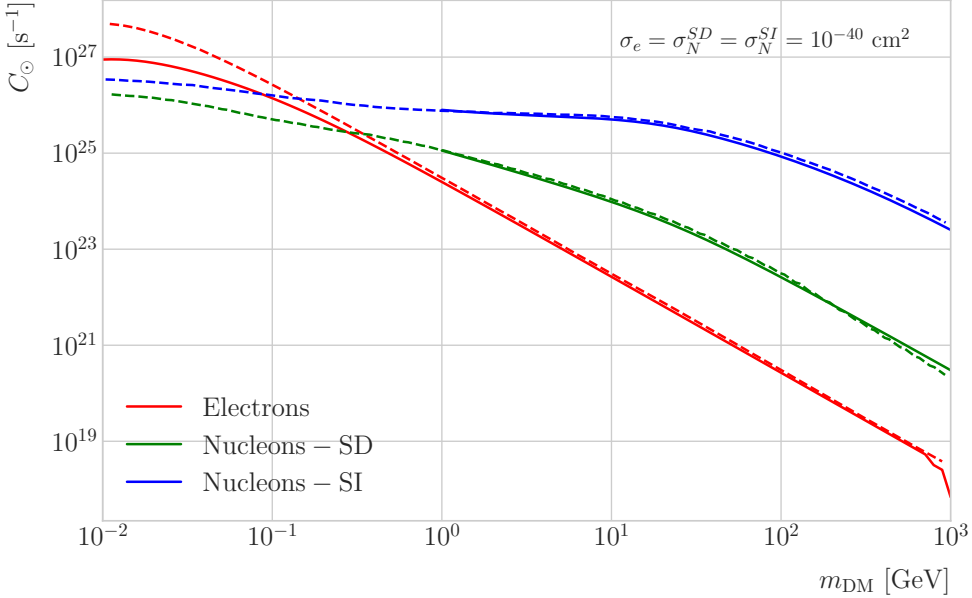


Figure 5.2: Capture rates as a function of the DM mass for the DM-electron interactions (red lines), SD DM-nucleons interactions (green lines) and SI DM-nucleons interactions (blue lines). Solid lines represent the values computed in this work while the dashed lines are the one given in Ref. [2]. All the rates are shown for a choice of scattering cross section of $\sigma_i = 10^{-40} \text{ cm}^2$.

as one needs to add up the contributions of the different most abundant nuclei in the Sun. Also, in contrast to the electron scenario where the form factor is trivially $|F_e(q)|^2 = 1$, for any nucleus i one would need to consider some appropriate nuclear density distribution (either a Gaussian approximation, a Woods-Saxon distribution, etc) which would complicate the calculations even further.

That is the reason why, at this stage of our study, I decided to take an alternative approach to the computation of the DM-nucleus capture rates. I used the **DarkSUSY** software, that allows us to compute these quantities performing a full numerical integration over the momentum transfer of the form factors. The default standard solar model used by **DarkSUSY** is BP2000¹ [111].

In Fig. 5.2 I show the results I obtained for the capture rates, for the case of interactions off electrons (red solid line), SD (green solid line) and SI (blue solid line)

¹This is what they say in their manual, but I fear it is somewhat outdated. It appears to me this model is relatively old and do not see why they are not using others like [1]. Maybe one can double-check in the code to make sure.

5.2. GRAVITATIONAL CAPTURE OF DM BY THE SUN

interactions of nucleons. In all cases I used a value of the scattering cross sections of $\sigma_i = 10^{-40} \text{ cm}^2$. Note here one of the limitations of the **DarkSUSY** approach, one can not extend the computation below $m_{\text{DM}} = 1 \text{ GeV}$. Nevertheless, this is not something to worry about in this case, as I will discuss next. As a comparison, I added also the values computed in Ref. [2] (same color scheme, dashed lines). One can see there is good agreement between these and the **DarkSUSY** computation of the SD and SI interactions for $m_{\text{DM}} \geq 1 \text{ GeV}$. In this regime their computations also matches quite well our result for the electron capture rate. However, these start to differ significantly below $m_{\text{DM}} = 1 \text{ GeV}$, being their estimate up to a factor of 5 bigger than ours for low masses.

Let us comment briefly about the assumption I made before about not including an evaporation term in the Boltzmann equation. If I include this term in the equation (which will be proportional to the number of DM particles) the equilibrium solution takes the form:

$$N_{\text{DM}}^{eq} = \sqrt{\frac{C_{\odot}}{A_{\odot}}} \frac{1}{\kappa + \frac{1}{2} E_{\odot} \tau_{eq}}, \quad (5.17)$$

where E_{\odot} is the total evaporation rate, τ_{eq} is the equilibrium time in the absence of evaporation:

$$\tau_{eq} = \frac{1}{\sqrt{C_{\odot} A_{\odot}}}, \quad (5.18)$$

and κ is defined as:

$$\kappa \equiv \sqrt{1 + \left(\frac{E_{\odot} \tau_{eq}}{2} \right)^2}. \quad (5.19)$$

Now, it is easy to proof that in case evaporation dominates $\kappa \gg 1$ and therefore:

$$N_{\text{DM}}^{eq} \simeq \frac{C_{\odot}}{E_{\odot}}. \quad (5.20)$$

In contrast, if evaporation is irrelevant $\kappa \simeq 1$ and one recovers Eq. (5.2).

In this way, one can define the evaporation mass as the mass for which the number of DM particles in equilibrium approaches Eq. (5.20) at 10% level:

$$\left| N_{\text{DM}}^{eq}(m_{\text{evap}}) - \frac{C_{\odot}(m_{\text{evap}})}{E_{\odot}(m_{\text{evap}})} \right| = 0.1 N_{\text{DM}}^{eq}(m_{\text{evap}}). \quad (5.21)$$

CHAPTER 5. DM SEARCHES WITH NEUTRINOS FROM THE SUN

2043 This can be regarded as the minimum testable mass one can reach using the annihilation
2044 products of the DM in the Sun.

2045 It was reported in Ref. [2] that, in the case of both SD and SI DM interactions
2046 off nuclei, this value ranges from 2 to 4 GeV depending on the specific scattering
2047 cross section value, compatible with the usual assumptions in the literature. What is
2048 interesting is the case of the electron capture. It was found that, when one applies a
2049 cutoff in the velocity distribution of the DM trapped in the Sun slightly below the escape
2050 velocity, the evaporation mass for the DM-electron interaction decreases remarkably. For
2051 a moderate choice of $v_c(r) = 0.9v_e(r)$ one gets an evaporation mass of around 200 to
2052 600 MeV. This possibility opens a region of the parameter space that could be tested
2053 with neutrino detectors.

2054 5.3 Neutrino flux from DM annihilations

2055 When WIMPs annihilate inside the Sun a flux of high-energy neutrinos is expected from
2056 heavy quarks, gauge bosons and $\tau^+\tau^-$ final states, which decay before losing energy in
2057 the dense solar medium, as they will produce a continuum spectra up to $E_\nu \sim m_\chi$ (in
2058 the case of direct annihilation to neutrinos one would have a line at $E_\nu = m_\chi$) [105].
2059 This kind of signal has been extensively studied in the literature, allowing to put strong
2060 limits on the SD WIMP-proton cross section for large m_χ . However, the number of
2061 high-energy neutrinos per WIMP annihilation is small and the spectrum depends on the
2062 unknown final state. Moreover, background rejection is easier for large m_χ but neutrinos
2063 with $E_\nu \gtrsim 100$ GeV are significantly attenuated by interactions in the Sun.

2064 Nevertheless, most WIMP annihilation final states eventually produce a low-energy
2065 neutrino spectrum. In this case one does not just consider the more massive final states
2066 but also annihilations into e^+e^- , $\mu^+\mu^-$ and light quarks [104]. In particular, light
2067 mesons would be produced and stopped in the dense medium, thus decaying at rest and
2068 producing a monoenergetic neutrino signal. The decay-at-rest of kaons will produce
2069 a $E_\nu = 236$ MeV ν_μ while in the case of pions one would have a $E_\nu = 29.8$ MeV ν_μ .

5.4. COMPUTING LIMITS FROM SOLAR NEUTRINO FLUXES

2070 In practice only K^+ and π^+ contribute to these signals, as K^- and π^- are usually
 2071 Coulomb-captured in an atomic orbit and get absorbed by the nucleus. There is also a
 2072 low-energy neutrino signal coming from muon decays, which are produced in kaon or
 2073 pion decays, leptonic decays of other hadrons and heavy leptons or even directly from
 2074 WIMP annihilations, which can decay at rest and contribute to the previous low-energy
 2075 neutrino flux with a well known spectrum below 52.8 MeV.

2076 These monoenergetic MeV neutrinos were previously considered undetectable but,
 2077 due to the large yield, the known spectra and the modern advances in the detector
 2078 technology, these low-energy neutrino flux can be a good probe of the SD WIMP-proton
 2079 cross-section in standard solar WIMP capture scenario, as it is sensitive to low WIMP
 2080 masses and insensitive to the particular final state. A good place to look for these signals
 2081 are next-generation neutrino experiments such as DUNE.

2082 5.4 Computing limits from solar neutrino fluxes

2083 In order to use the neutrino fluxes from DM annihilations in the Sun, the first thing I
 2084 need to do is to determine the expected number of atmospheric background events, for
 2085 a given exposure, after directionality selection has been applied. I can write this number
 2086 as:

$$N_B = \eta_B \int d\Omega \int_{E_{min}}^{E_{max}} dE_\nu \frac{d^2\Phi_{atm}^\mu}{dE_\nu d\Omega} \times \left(A_{eff}^{(\mu)}(E_\nu) T \right), \quad (5.22)$$

2087 where η_B is the background efficiency, E_{min} and E_{max} the minimum and maximum
 2088 energies to integrate over, $d^2\Phi_{atm}^\mu/dE_\nu d\Omega$ the differential flux of atmospheric muon
 2089 neutrinos, $A_{eff}^{(\mu)}$ is the effective area of DUNE to muon neutrinos and T is the exposure
 2090 time. The effective area can be expressed as the product of the neutrino-nucleus scattering
 2091 cross section and the number of nuclei in the fiducial volume of the detector. This way
 2092 for DUNE I can write:

$$A_{eff}^{(\mu)}(E_\nu) = (6.0 \times 10^{-10} \text{ m}^2) \left(\frac{\sigma_{\nu-\text{Ar}}^{(\mu)}(E_\nu)}{10^{-38} \text{ cm}^2} \right) \left(\frac{M_{target}}{40 \text{ kT}} \right), \quad (5.23)$$

CHAPTER 5. DM SEARCHES WITH NEUTRINOS FROM THE SUN

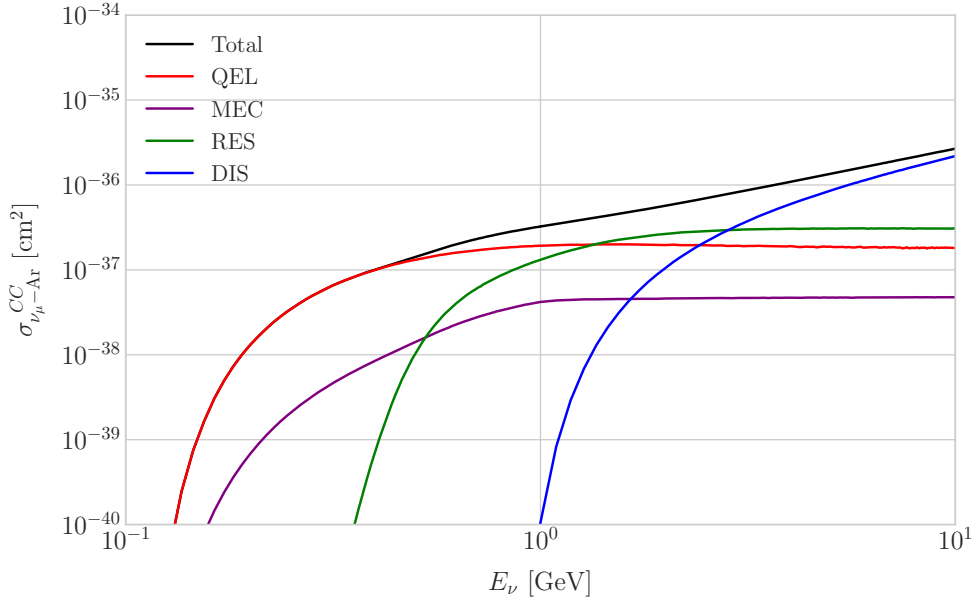


Figure 5.3: *NuWro* computed $\nu_\mu - {}^{40}\text{Ar}$ charged-current scattering cross section as a function of the neutrino energy E_μ . The black line shows to the total cross section, whereas the others correspond to the different contributions (in red quasi-elastic scattering, in green resonant pion exchange, in blue deep inelastic scattering and in purple meson exchange current).

where $\sigma_{\nu-\text{Ar}}^{(\mu)}$ is the $\nu_\mu - {}^{40}\text{Ar}$ charged-current scattering cross section. In Fig. 5.3 I show the computed value of this cross section as a function of the neutrino energy E_ν , in the range of interest both for the atmospheric background and signal events. It was computed using the *NuWro* Monte Carlo neutrino event generator [112], including the charged-current contributions of the quasi-elastic scattering (red line), resonant pion exchange (green line), deep inelastic scattering (blue line) and meson exchange current (purple line).

The background rejection will depend on the resolution of the detector and the selection one applies on the events. A geometry argument can be used to estimate the maximum background rejection one can achieve in this case, considering one can efficiently discriminate all events coming from a direction different from that of the Sun. In that case, the optimal background efficiency will simply be the relative angular coverage of the Sun. Taking the angular diameter of the Sun as seen from the Earth to

5.4. COMPUTING LIMITS FROM SOLAR NEUTRINO FLUXES

2106 be 0.5° , I have:

$$\eta_B^{(opt)} \approx \frac{\pi \left(\frac{0.5}{2}\right)^2}{360 \times 180} \simeq 3.03 \times 10^{-6}. \quad (5.24)$$

2107 This value will give a very optimistic estimate of the number of background events.

2108 However, it can be regarded as an lower limit, as it represents the best case scenario.

2109 In Fig. 5.4 I show the fluxes of atmospheric neutrinos at the Homestake mine during
2110 solar minimum, taken from Ref. [3]. The values are averaged over the two angular
2111 directions. In blue I have the flux of muon neutrinos while in red I indicate the flux
2112 of electron neutrinos. Additionally, the dashed lines correspond to both antineutrino
2113 species.

2114 Using these values for the muon neutrino and the corresponding total CC cross
2115 section, one can compute the number of expected background events by integrating over
2116 the given energy range (as in this case the angular integral is trivial). As for the energy
2117 range to integrate over, I choose the range for DUNE specified in [72], $E_{min} = 10^{-1}$ GeV
2118 and $E_{max} = 10$ GeV. Taking all these into account, I found the number of background
2119 events to be:

$$N_B \simeq \eta_B \times (3.827 \times 10^4) \times \left(\frac{\text{exposure}}{400 \text{ kT yr}} \right). \quad (5.25)$$

2120 In order to estimate the sensitivity of DUNE to this kind signal, one can consider a
2121 hypothetical data set where the number of observed neutrinos is taken to be the expected
2122 number of background events rounded to the nearest integer, $N_{obs} = \text{round}(N_B)$ [113].
2123 Now, if I assume that the number of signal and background events seen by DUNE are
2124 given by Poisson distributions with means equal to the expected number of signal and
2125 background events, N_S and N_B , one can denote by N_S^{90} to the number of expected
2126 signal events such that the probability of having an experimental run with a number of
2127 events greater than N_{obs} is 90%. This number can be obtained as the numerical solution
2128 to the equation:

$$1 - \frac{\Gamma(N_{obs} + 1, N_S^{90} + N_B)}{N_{obs}!} = 0.9, \quad (5.26)$$

2129 where $\Gamma(x, y)$ is the upper incomplete gamma function.

CHAPTER 5. DM SEARCHES WITH NEUTRINOS FROM THE SUN

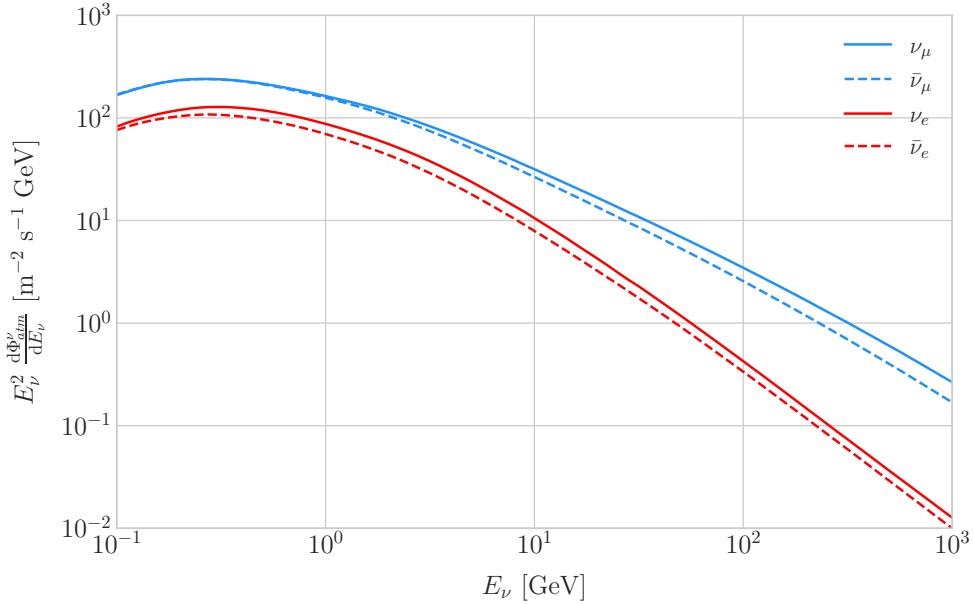


Figure 5.4: Expected atmospheric neutrino flux as a function of the neutrino energy E_ν at Homestake at solar minimum, taken from Ref. [3]. The blue solid (dashed) line correspond to muon neutrinos (antineutrinos) and the red solid (dashed) line correspond to electron neutrinos (antineutrinos).

2130 The number of signal events is related to the neutrino flux from DM annihilations in
 2131 a similar way as the background events to the atmospheric neutrino flux. In this case I
 2132 have:

$$N_S = \eta_S \Gamma_A^{eq} \int_{z_{min}}^{z_{max}} dz \frac{dN_\nu}{dAdN_A dz} \times (A_{eff}^\mu(z)T), \quad (5.27)$$

2133 where η_S is the signal efficiency, Γ_A^{eq} is the total annihilation rate of DM particles at
 2134 equilibrium, $\Gamma_A^{eq} = A_\odot (N_{DM}^{eq})^2$, z_{min} and z_{max} the minimum and maximum relative
 2135 energies to integrate over (in such a way that $z_{min,max} \leq E_{min,max}/m_{DM}$ for each m_{DM})
 2136 and $dN_\nu/dAdN_A dz$ the muon neutrino flux per DM annihilation in the Sun.

2137 Knowing N_S^{90} one can use the relation in Eq. (5.27) to obtain $\Gamma_A^{eq,90}$ for different
 2138 values of the DM mass. From there I can directly translate those values into the
 2139 upper limits for DUNE on the DM scattering cross sections, for a given exposure. The
 2140 relation between the annihilation rate and the DM-nucleon cross section comes from the
 2141 equilibrium condition through the solar DM capture rate. The details of the evolution
 2142 of the number of DM particles inside the Sun and the computation of the capture rates

5.5. EXAMPLE: KALUZA-KLEIN DARK MATTER

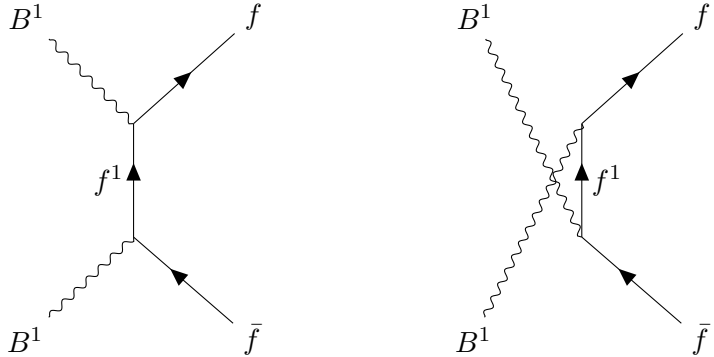


Figure 5.5: Feynman diagrams for $B^1 B^1$ annihilation into SM fermions.

2143 are discussed in App. 5.2.

2144 5.5 Example: Kaluza-Klein Dark Matter

2145 Even though there are plenty of BSM theories which provide viable dark matter
2146 candidates, Kaluza-Klein type of models [114, 115] within the universal extra dimensions
2147 (UED) paradigm naturally predict the existence of a massive, stable particle that can
2148 play the role of the dark matter. In the UED scenario all the SM fields can propagate
2149 in one or more compact extra dimensions [116], as opposed to the idea of brane worlds
2150 [117, 118], where just gravity can propagate in the bulk while SM particles live at fixed
2151 points.

2152 Furthermore, in UED there is no violation of the translational invariance along the
2153 extra dimensions, thus leading to degenerate KK modes masses and also the conservation
2154 of the KK number in the effective four dimensional theory. At loop level, radiative
2155 corrections and boundary terms shift the masses of the KK modes and break KK
2156 number conservation into a KK parity. As a result, this theory only contains interactions
2157 between an even number of odd KK modes and therefore the lightest among the first KK
2158 excitations will be stable. This particle is usually denoted as the lightest Kaluza-Klein
2159 particle (LKP) and its mass is proportional to $1/R$, being R the size of the extra
2160 dimension.

2161 A viable DM candidate needs to be electrically neutral and non-baryonic, therefore

CHAPTER 5. DM SEARCHES WITH NEUTRINOS FROM THE SUN

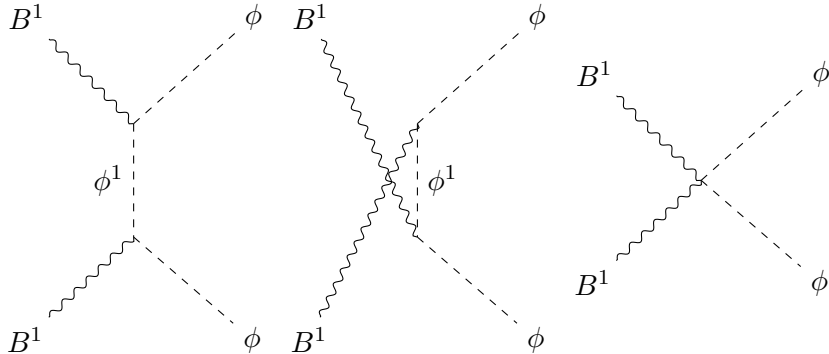


Figure 5.6: Feynman diagrams for B^1B^1 annihilation into a Higgs boson pair.

good candidates among the first Kaluza-Klein excitations would be the KK neutral gauge bosons and the KK neutrinos [119]. Another possible candidate is the first KK excitation of the graviton, which receives negligible radiative corrections and therefore has a mass almost equal to $1/R$, but it has been shown that the lightest eigenstate from the mixing of the gauge mass states (B^1, W_3^1) would be lighter, as B^1 and W_3^1 receive negative radiative corrections [120]. It is also understood that, when these corrections become sizeable, the eigenstates become approximately pure B^1 and W_3^1 states as the Weinberg mixing angle grows small with the KK number [120]. In that case, the LKP can be well-approximated as being entirely B^1 .

I need to compute the neutrino flux produced by the annihilations of the LKP in the core of the Sun, taking into account their propagation in the solar medium, as well as neutrino oscillations. To this end I used `WimpSim` [121, 122] to generate one million annihilation events in the Sun over a time span of four years and propagate them to the DUNE FD location ($44^\circ 20' \text{ N}, 103^\circ 45' \text{ W}$), for different values of M_{LKP} . In Fig. 5.7 I show the obtained muon neutrino spectra arriving to the detector from LKP annihilations in the Sun, per unit area and per annihilation, plotted in relative energy units for different values of the mass. As one could expect the spectra get steeper the higher is the mass, due to the absorption of high-energy neutrinos in the solar medium. Also, one can see the peak at $z = 1$ due to the direct annihilation into neutrinos $\chi\bar{\chi} \rightarrow \nu\bar{\nu}$.

5.5. EXAMPLE: KALUZA-KLEIN DARK MATTER

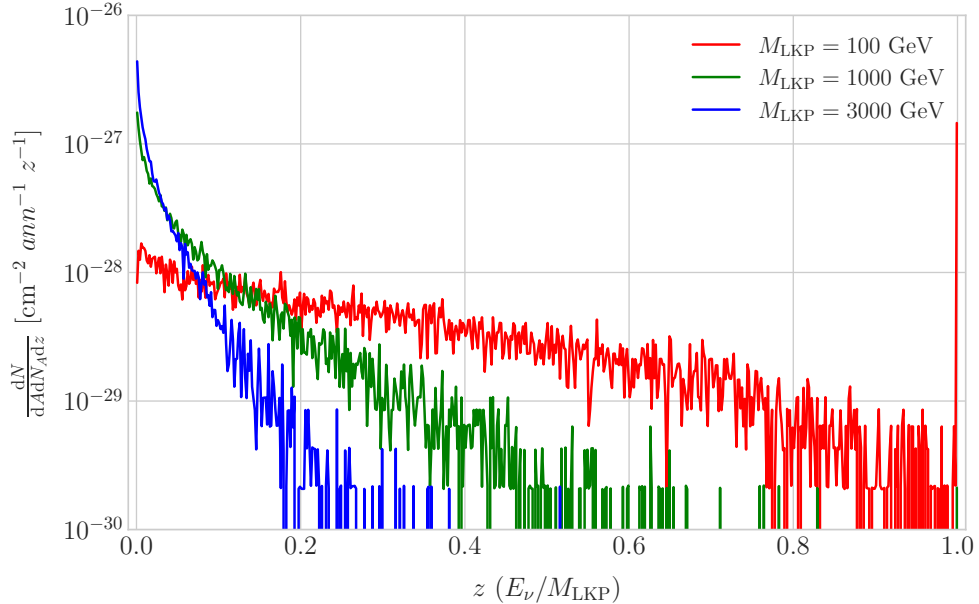


Figure 5.7: Computed spectra of muon neutrinos at the DUNE FD site from B^1 annihilations in the Sun for three different values of M_{LKP} , plotted in relative energy units for legibility.

Now, one can estimate the sensitivity of DUNE to this particular model by using the methods I previously discussed. To begin with, I will use the optimistic estimation of the background efficiency in Eq. (5.24) to get our upper bound. Using it, one can directly compute the number of expected background events to be $N_B = 0.1101$ for an exposure of 400 kT yr. Then, Eq. (5.26) give us a value of $N_S^{90} = 2.20$ for the 90% exclusion number of expected signal events. By using the NuWro generated cross sections and the computed neutrino fluxes from B^1 annihilations in the Sun I can estimate the limits on the SD and SI DM-nucleus cross section using the relation in Eq. (5.2) and the capture rates I computed with DarkSUSY.

In Fig. 5.8 I show the projected sensitive for DUNE on the spin-dependent B^1 -proton scattering cross section versus the mass of the DM particle, for a exposure of 400 kT yr (green dots). I also include the previous results from IceCube [4] (blue line) and Antares [5] (red line). The shaded area represents the disfavoured region from combined searches for UED by ATLAS and CMS [6].

From the experimental point of view, this estimation lacked a detailed simulation of

CHAPTER 5. DM SEARCHES WITH NEUTRINOS FROM THE SUN

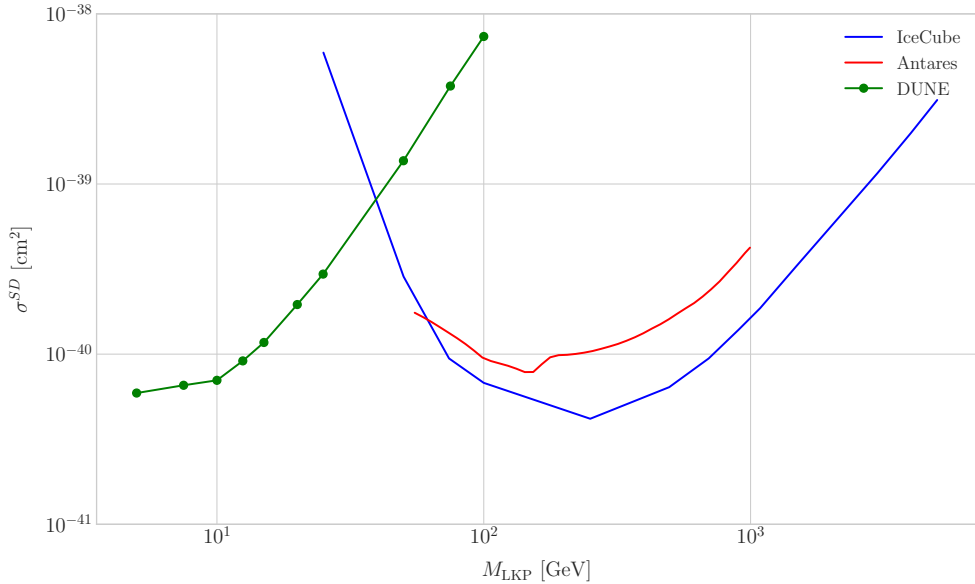


Figure 5.8: Projected 90% confidence level upper limit for DUNE (400 kT yr) on the spin-dependent B^1 -proton scattering cross section as a function of M_{LKP} (green dots). I also show the previous limits from IceCube [4] (blue line) and Antares [5] (red line) on the LKP cross section. The shaded area represents the disfavoured region (at 95% confidence level) on the mass of the LKP from LHC data [6].

the detector response and thus this must be consider as a mere optimistic sensitivity computation. However, it shows the potential of DUNE to constrain this kind of exotic scenarios, showing the region where it will be in a position to compete with other neutrino telescopes. A more detailed analysis is needed if I am to make a realistic estimation. Even though the region of the parameter space where DUNE would be sensitive to this particular model is quite constrained by collider searches [6] and other rare decay measurements [123, 124], it still constitutes an alternative indirect probe.

5.6 High energy DM neutrino signals

To have better estimates on the capability of the DUNE FD to constrain the parameter space of DM using solar neutrino fluxes, I need to start accounting for the detector resolution effects and the topologies of the different signatures. As a starting point, I will focus on specific annihilation channels. For the case of DUNE, the relevant ones are mainly the hard channels $\tau^+\tau^-$ and $\nu\bar{\nu}$ and the soft channel $b\bar{b}$. These are the open

5.6. HIGH ENERGY DM NEUTRINO SIGNALS

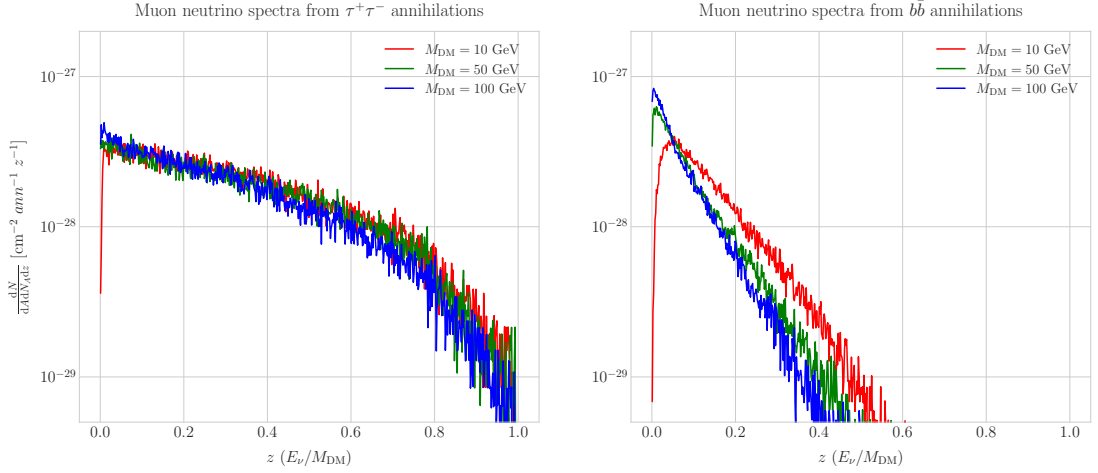


Figure 5.9: Computed spectra of muon neutrinos at the DUNE FD site from $\tau^+\tau^-$ (left panel) and $b\bar{b}$ (right panel) annihilations in the Sun for the DM masses $m_{\text{DM}} = 10 \text{ GeV}$ (red line), 50 GeV (green line) and 100 GeV (blue line), plotted in relative energy units.

annihilation channels for relatively low mass WIMPs that will actually give neutrino fluxes. Other channels, like W^+W^- and ZZ , are open for more massive WIMPs, but those will produce usually a higher energy neutrino flux that will be out of reach for DUNE (usually the maximum neutrino energy is taken to be $E_{\max} = 10 \text{ GeV}$).

In Fig. 5.9 I show the `WimpSim` [121, 122] generated muon neutrino spectra at the DUNE FD location ($44^\circ 20' \text{ N}, 103^\circ 45' \text{ W}$) from $\tau^+\tau^-$ (left panel) and $b\bar{b}$ (right panel) annihilations in the core of the Sun, for different DM masses. Here, one can clearly see the meaning of the previous distinction between hard and soft channels. For the same DM mass value, the muon neutrino spectrum from the $\tau^+\tau^-$ channel is more flat and reaches higher energies than the one from the $b\bar{b}$ channel, which drops faster.

In this case, I prepared two sets of files, one for $\tau^+\tau^-$ and the other for $b\bar{b}$, for DM masses in the range from 5 to 100 GeV (actually for $b\bar{b}$ the first mass point I took is 7.5 GeV, as a WIMP with $m_{\text{DM}} = 5 \text{ GeV}$ can not kinematically self annihilate into $b\bar{b}$). Then, I prepared the `WimpSim` output fluxes in a specific way to use them as inputs to `NuWro`, which simulates the neutrino interaction with the argon.

Because `WimpSim` outputs an event list together with the fluxes, I can use the former to generate the events. The direction of these is given in terms of the azimuth and

CHAPTER 5. DM SEARCHES WITH NEUTRINOS FROM THE SUN

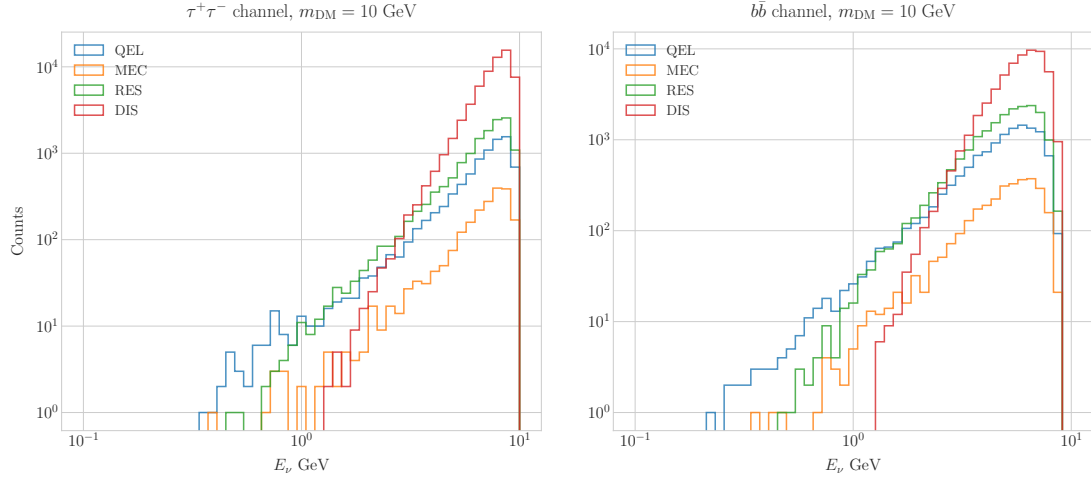


Figure 5.10: Distribution of the muon neutrino energies from the $\tau^+\tau^-$ (left panel) and $b\bar{b}$ (right panel) annihilation channels, for $m_{\text{DM}} = 10$ GeV, separated by CC interaction type: QEL (blue), MEC (orange), RES (green) and DIS (red).

altitude angles viewed from the specified location, so first I need to convert these into the DUNE FD coordinates. Once I have done it, each event can be processed with `NuWro`. To increase the number of samples and optimise the computation time, I generate 100 interactions (i.e. `NuWro` events) for each `WimpSim` event². I restrict the event generation to charged current interactions, but I allow all the different contributions to the CC cross section, i.e. quasielastic scattering (QEL), meson exchange current process (MEC), resonant pion production (RES) and deep inelastic scattering (DIS). I just take into account the CC contribution because I am only interested in final states with charged leptons, as we have better chances of reconstructing the kinematics of CC events.

For the atmospheric fluxes I follow a similar procedure, only that this time I do not have a set of events but the fluxes binned in azimuth and altitude angles. This way, I transform these to DUNE coordinates and process the fluxes for each bin separated with `NuWro`.

At this point, I have two sets of events with different energies and final states. In Fig. 5.10 one can see the distribution of the muon neutrino energies for the case

²This also solves a problem related with the generation of the neutrino interactions in `NuWro`, as if you only produce one event each time you launch `NuWro` it will always produce an interaction of the dominant interaction type for that particular energy.

5.6. HIGH ENERGY DM NEUTRINO SIGNALS

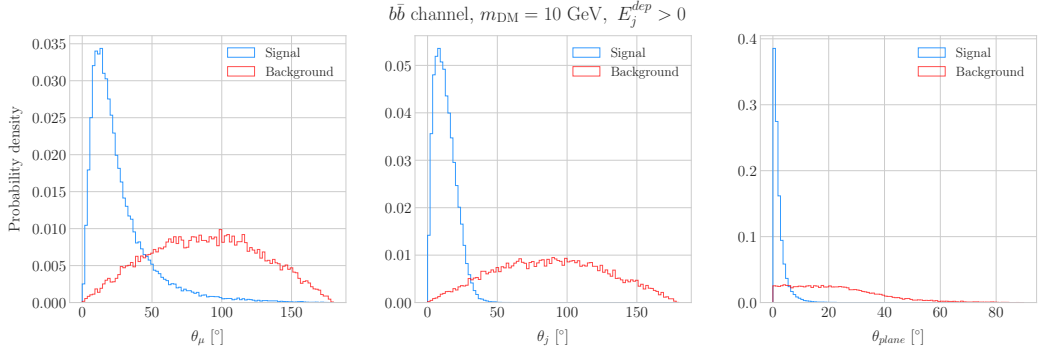


Figure 5.11: Distributions of θ_μ (left panel), θ_j (central panel) and θ_{plane} (right panel) for the $b\bar{b}$ sample with $m_{\text{DM}} = 10$ GeV (blue) and the atmospheric background (red).

2242 $m_{\text{DM}} = 10$ GeV, both for the $\tau^+\tau^-$ (left panel) and $b\bar{b}$ (right panel) channels, separated
2243 by interaction. One can clearly see that there are different energy regimes where the
2244 primary interaction type is different. This leads to a plurality of event topologies,
2245 therefore making it difficult to implement a general approach to the selection of events
2246 in detriment of the background. As a way to proceed, I decided to split our samples,
2247 based on the different interaction modes and contents of the final state, into a CC DIS
2248 sample and a single proton CC QEL sample.

2249 **5.6.1 DIS events**

2250 To begin with, I consider the high energy part of the spectrum. In this region DIS events
2251 dominate, i.e. interactions of the form $\nu_\mu + q_d(\bar{q}_u) \rightarrow \mu^- + q_u(\bar{q}_d)$. Therefore, our final
2252 estates will contain a muon and a hadronic jet from the fragmentation of the outgoing
2253 quark. As all these events have $E_\nu \gtrsim 1$ GeV the momentum transfer to the remnant
2254 nucleus is negligible, for this reason the neutrino energy can be effectively reconstructed
2255 just taking into account the momenta of the muon and the jet. This technique was
2256 successfully used in Ref. [125] to select monoenergetic DM solar neutrino events from
2257 $\nu\bar{\nu}$ annihilation channels.

2258 Using momentum conservation one sees that the plane generated by the momenta
2259 of the muon and the jet needs to also contain the momentum of the neutrino. As we
2260 are interested in neutrinos coming from the Sun, the momentum of the neutrino can be

CHAPTER 5. DM SEARCHES WITH NEUTRINOS FROM THE SUN

regarded as known beforehand. This will allow us to define the angle of the outgoing muon and jet with respect to the incoming neutrino. Moreover, one can also use that information to reject poorly reconstructed jets, checking for deviations of these from the momentum conservation plane.

To account for the limited angular resolution of the detector, I smeared the momenta of the muons and hadrons. In a liquid argon TPC muons are expected to be tracked with high precision, therefore I take the associated angular resolution to be 1° . In the case of jets, it is expected that for the hadrons dominating the cascade a detector like DUNE has an angular resolution between 1° to 5° [72], so I take the latter, more conservative, estimate.

As a first selection step, I will just take into account particles with kinetic energies above the detection threshold of DUNE. For muons and photons the specified threshold energy is 30 MeV, for charged pions 100 MeV and for other hadrons 50 MeV [72]. This way, if the outgoing muon in a certain event has an energy lower than the required threshold I will drop such event. For the case of hadrons and photons, I will only require to have at least one particle above the energy threshold, so then one can compute the jet momentum using the (smeared) momenta of the N particles above threshold as:

$$\vec{p}_j = \sum_{i=1}^N \vec{p}_i. \quad (5.28)$$

Additionally, I will also define an estimation of the deposited hadronic energy as:

$$E_j^{dep} = m_{^{39}\text{Ar}} - m_{^{40}\text{Ar}} + \sum_{i=1}^N \sqrt{|\vec{p}_i|^2 + m_i^2}. \quad (5.29)$$

This quantity is useful to select events with enough hadronic visible energy in the detector. For events where most of the hadronic energy is scattered across plenty of hadrons with individual energies below the detection threshold, this estimation will give $E_j^{dep} \leq 0$. In these cases it could be expected that the jet momentum is poorly reconstructed, and therefore I require events to pass the cut $E_j^{dep} > 0$.

5.6. HIGH ENERGY DM NEUTRINO SIGNALS

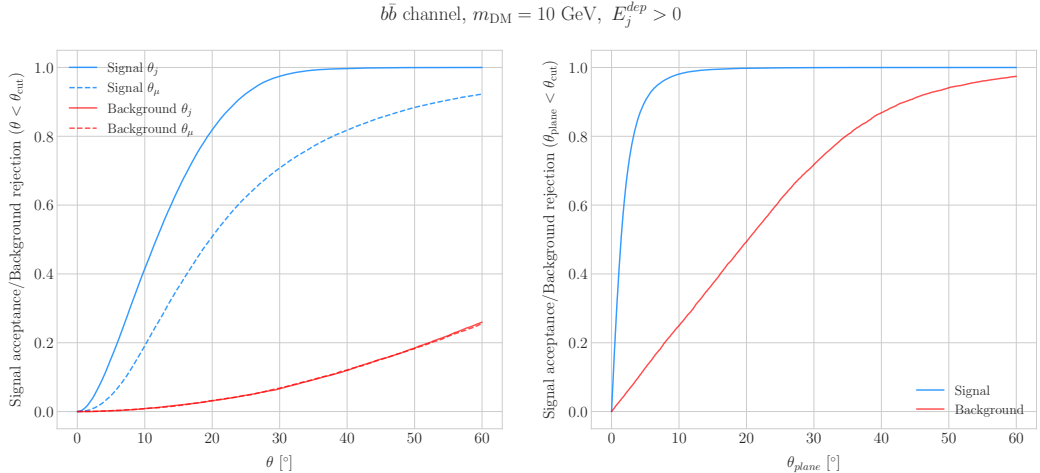


Figure 5.12: Left panel: signal efficiencies (blue lines) and background rejections (red lines) for events passing the cuts $\theta < \theta_{cut}$ for the jet (solid lines) and muon (dashed lines) angles. Right panel: signal efficiency (blue line) and background rejection (red line) for events passing the cut $\theta_{plane} < \theta_{cut}$ for the momentum conservation plane deviation.

2284 For the events I can compute the angles for the muon and jet with respect to the
 2285 incoming neutrino as:

$$\cos \theta_\mu = \hat{p}_\nu \cdot \hat{p}_\mu, \quad (5.30)$$

$$\cos \theta_j = \hat{p}_\nu \cdot \hat{p}_j, \quad (5.31)$$

2286 and the deviation from the momentum conservation plane as:

$$\sin \theta_{plane} = \left| \frac{\hat{p}_\mu \times \hat{p}_\nu}{|\hat{p}_\mu \times \hat{p}_\nu|} \cdot \hat{p}_j \right|. \quad (5.32)$$

2287 In Fig. 5.11 I show some distributions of these quantities for the case of the $b\bar{b}$ sample
 2288 with $m_{DM} = 10$ GeV (blue histograms) and for the atmospheric backgrounds (red).
 2289 In order to select the atmospheric events I followed the same criteria as for the signal
 2290 events. However, because in the signal case I used the true direction of the neutrino
 2291 as input, as it should be that of the Sun at that time and therefore known, in the
 2292 atmospheric case I used a set of solar positions as our ansatz for the neutrino direction.
 2293 From the distributions, one can see that the muon and the jet for the signal events are

CHAPTER 5. DM SEARCHES WITH NEUTRINOS FROM THE SUN

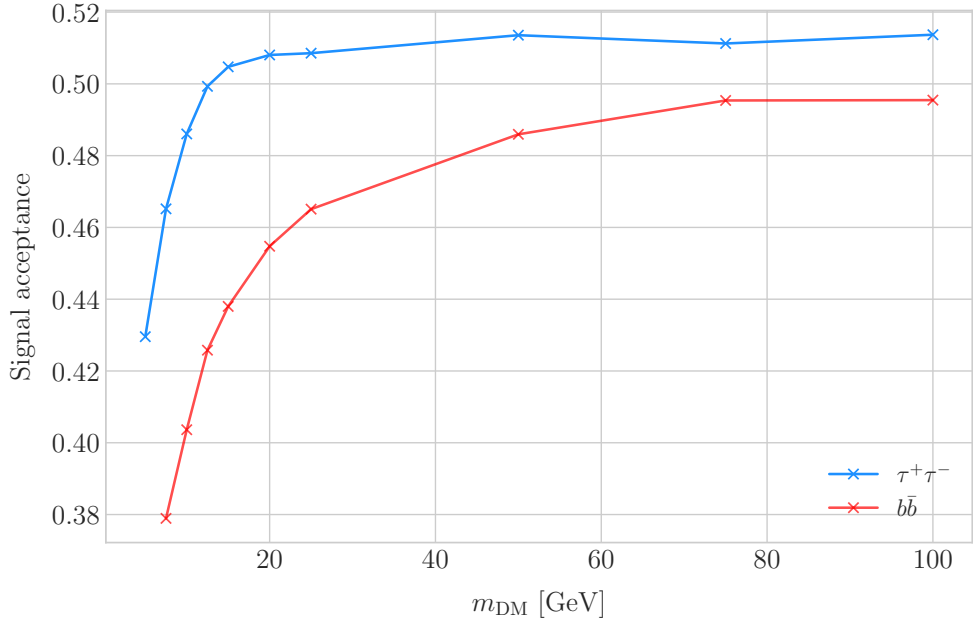


Figure 5.13: Signal efficiencies for the $\tau^+\tau^-$ (blue line) and $b\bar{b}$ (red line) DIS samples as functions of the DM mass, m_{DM} , obtained by applying the optimal angular cuts $\theta_\mu < 27^\circ$, $4^\circ < \theta_j < 26^\circ$ and $\theta_{\text{plane}} < 3.5^\circ$.

2294 predominantly forward and also that the deviations from the momentum conservation
 2295 plane are peaked at zero, as one should expect.

2296 Now, I can start applying cuts to maximise our signal selection efficiency while at
 2297 the same time I try to minimise the amount of atmospheric background events passing
 2298 the selection. To this end, I will need to find some lower and upper cuts for θ_j and
 2299 θ_μ and an upper bound for θ_{plane} . In Fig. 5.12 I show how upper bound cuts in the
 2300 different angular variables affect the signal efficiency (blue lines) and the background
 2301 rejection (red lines). Notice that the signal efficiency behaves in a quite different way
 2302 when I apply cuts in the jet and the muon angles. On the contrary, the cuts on both
 2303 variables have a similar effect on the background rejection.

2304 In order to obtain the optimal set of cuts, I perform a multidimensional scan. I
 2305 do this separately for the $\tau^+\tau^-$ and the $b\bar{b}$ samples. For each case, I scan the possible
 2306 cuts for each mass point and then I take the mean value of the signal efficiency for
 2307 each configuration, to get the mean efficiency for each set of cuts. I do a similar scan
 2308 for the atmospheric sample independently. Then, I take the sets of cuts such that

5.6. HIGH ENERGY DM NEUTRINO SIGNALS

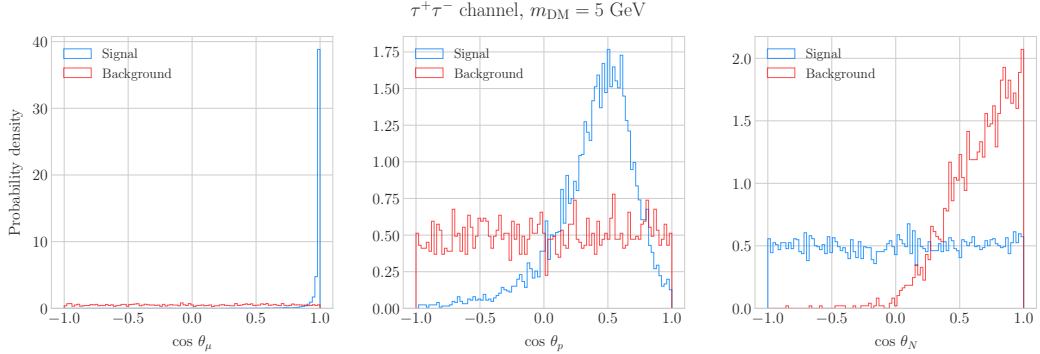


Figure 5.14: Distributions of $\cos \theta_\mu$ (left panel), $\cos \theta_p$ (central panel) and $\cos \theta_N$ (right panel) for the $\tau^+\tau^-$ QEL sample with $m_{\text{DM}} = 5 \text{ GeV}$ (blue) and the atmospheric background (red).

the background rejection achieved is greater than 99.8% and search for the one which maximises the $\tau^+\tau^-$ and $b\bar{b}$ sample mean efficiencies. I found that with the cuts $\theta_\mu < 27^\circ$, $4^\circ < \theta_j < 26^\circ$ and $\theta_{\text{plane}} < 3.5^\circ$ I get a background rejection of 99.80% while achieving a 49.40% and 44.92% mean signal efficiencies for the $\tau^+\tau^-$ and $b\bar{b}$ signals respectively.

In Fig. 5.13 I show the signal efficiencies as a function of the DM mass for the $\tau^+\tau^-$ (blue line) and the $b\bar{b}$ (red line) DIS events, after applying the cuts discussed above, as well as the energy threshold and hadronic visible energy selections. One can see that the efficiency grows with the mass, as annihilations of more massive DM particles will produce a neutrino spectrum centered at higher energies, where DIS events dominate. Notice also that the efficiency is higher for the $\tau^+\tau^-$ case at every mass point, as in general this channel produces neutrinos at higher energies than the corresponding $b\bar{b}$ channel.

5.6.2 Single proton QEL events

Now, one can try to explore the low energy tail of the neutrino energy distributions. This regime is dominated by the QEL interactions, i.e. events of the type $\nu_\mu + n \rightarrow \mu^- + p$. In this case, as the typical energies are $E_\nu \lesssim 1 \text{ GeV}$, the momentum transfer to the remnant nucleus is sizeable. Therefore, I can not make the approximation I did before and assume that the momentum of the muon and the proton will give an adequate

CHAPTER 5. DM SEARCHES WITH NEUTRINOS FROM THE SUN

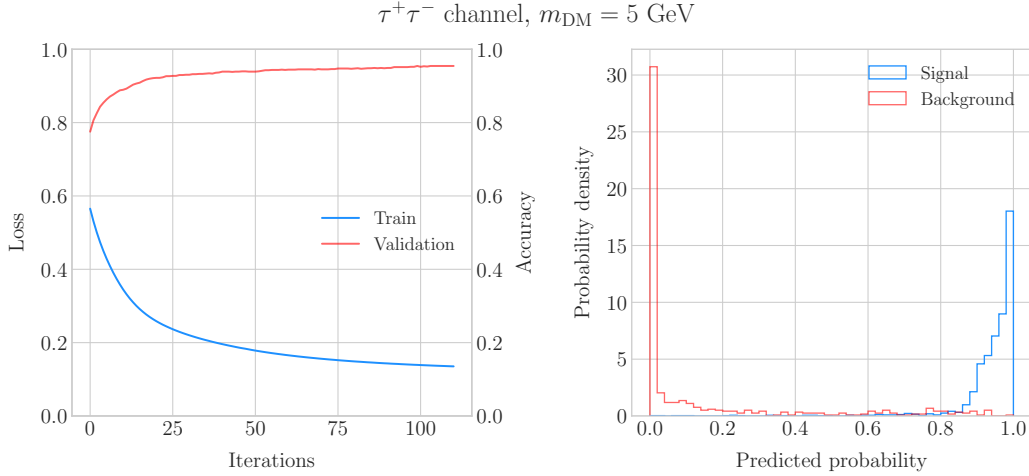


Figure 5.15: Left panel: value of the loss function for the training sample (blue line) and accuracy for the validation sample (red line) versus the number of iterations for the MLP classifier training. Right panel: distributions of the predicted probabilities assigned by the MLP classifier to the test sample for the $\tau^+\tau^-$ QEL signal with $m_{\text{DM}} = 5 \text{ GeV}$ (blue) and the atmospheric background (red).

2327 estimation of the reconstructed neutrino energy.

2328 In any case, as before, I can take the direction of the incoming neutrino as known.

2329 That way, one can estimate the energy of the neutrino as:

$$E_\nu^{reco} = E_\mu + E_p + m_{^{39}\text{Ar}} - m_{^{40}\text{Ar}}, \quad (5.33)$$

2330 and using momentum conservation I can write the momentum of the remnant nucleus

2331 as:

$$\vec{p}_N = \hat{p}_\nu (E_\mu + E_p + m_{^{39}\text{Ar}} - m_{^{40}\text{Ar}}) - \vec{p}_\mu - \vec{p}_p. \quad (5.34)$$

2332 As in the previous case, I need to drop the events where the muon or the proton fall
 2333 below the kinetic energy detection threshold [72]. Also, I again apply a smearing to the
 2334 momenta of the particles, a 1% for muons and 5% for protons.

2335 Having done that, one can compute the following angular variables for our selected
 2336 events:

$$\cos \theta_\mu = \hat{p}_\nu \cdot \hat{p}_\mu, \quad (5.35)$$

5.6. HIGH ENERGY DM NEUTRINO SIGNALS

$$\cos \theta_p = \hat{p}_\nu \cdot \hat{p}_p, \quad (5.36)$$

$$\cos \theta_N = \hat{p}_\nu \cdot \hat{p}_N. \quad (5.37)$$

2337 Fig. 5.14 shows the distributions of these angular variables for the $\tau^+\tau^-$ QEL
 2338 sample with $m_{\text{DM}} = 5$ GeV (blue) and the atmospheric background (red). Again, for
 2339 the atmospheric events I used a random solar position as the ansatz for the incoming
 2340 neutrino direction. Notice that now, opposed to the DIS case where the signal had very
 2341 sharp distributions for the variables considered, the shapes of the angular distributions
 2342 for signal and background are not that much different.

2343 This effectively means that the usual approach of applying simple angular cuts would
 2344 not work as well as in the previous situation. Therefore, as a possible solution, I tried to
 2345 use a multilayer perceptron (MLP) classifier to separate between signal and background
 2346 events. Thus, the power of the hypothesis test will serve as an estimate of the signal
 2347 efficiency, and in the same way one can take the size of the test to be our background
 2348 rejection.

2349 For each DM mass value and channel, as well as for the background sample, I divide
 2350 our events into training, validation and test samples. The input variables for the classifier
 2351 were the reconstructed neutrino energy from Eq. (5.33) and the angular variables defined
 2352 in Eqs. (5.35 - 5.37). I used the MLP classifier implemented in **scikit-learn** [126], with
 2353 a total of five hidden layers, the rectified linear unit activation function and adaptive
 2354 learning rate. In order to account for fluctuations due to artifacts in the training process I
 2355 repeated the training a thousand times for each sample, redefining each time the training,
 2356 validation and test subsets, so one can take as our signal efficiency and background
 2357 rejection the mean values of the powers and sizes of the tests.

2358 The results of one of these training processes for the $\tau^+\tau^-$ QEL signal with $m_{\text{DM}} =$
 2359 5 GeV is shown in Fig. 5.15. On the left panel I show the loss function values (blue) and
 2360 accuracy (red) at each iteration for the training and the validation samples respectively.
 2361 The training stops either when the maximum number of iterations is reached (1000 in
 2362 this case) or when the accuracy for the validation sample reaches a certain tolerance

CHAPTER 5. DM SEARCHES WITH NEUTRINOS FROM THE SUN

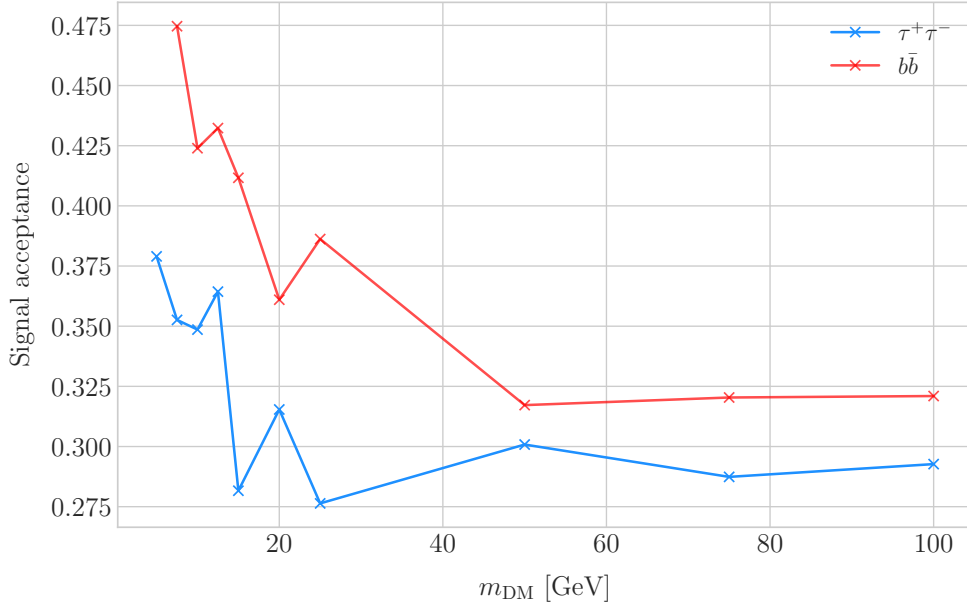


Figure 5.16: Signal efficiencies for the $\tau^+\tau^-$ (blue line) and $b\bar{b}$ (red line) single proton QEL samples as functions of the DM mass, m_{DM} , obtained by requiring a minimum predicted probability from the MLP classifier of 0.97 in order to achieve a background rejection greater than 99.8%.

(I chose 10^{-4} as our tolerance). On the right panel I have the distributions for the predicted probability by the model, separated in true signal (blue) and background (red) events, for the test sample. One can see that both populations are well separated, obtaining a power of 44.97% and a size of 0.17% when I require a predicted probability greater than 0.97.

Applying this criteria for each sample, I obtain the mean signal efficiencies shown in Fig. 5.16. Notice that the efficiencies for the channel $\tau^+\tau^-$ (blue line) are consistently lower than the ones for the $b\bar{b}$ channel (red line). This can be due to the fact that, for each DM mass point, the neutrino spectrum coming from the $b\bar{b}$ annihilation channel is centered at lower energies when compared to the $\tau^+\tau^-$ spectrum. This directly translates into more low energy neutrinos undergoing QEL interactions, which give signals that can be easily separated from the atmospheric background. This explanation also help us understand why in both cases the signal acceptance drops when the DM mass increases. In all cases, the background rejection took values between 99.8% to 99.9%. I will assume

5.6. HIGH ENERGY DM NEUTRINO SIGNALS

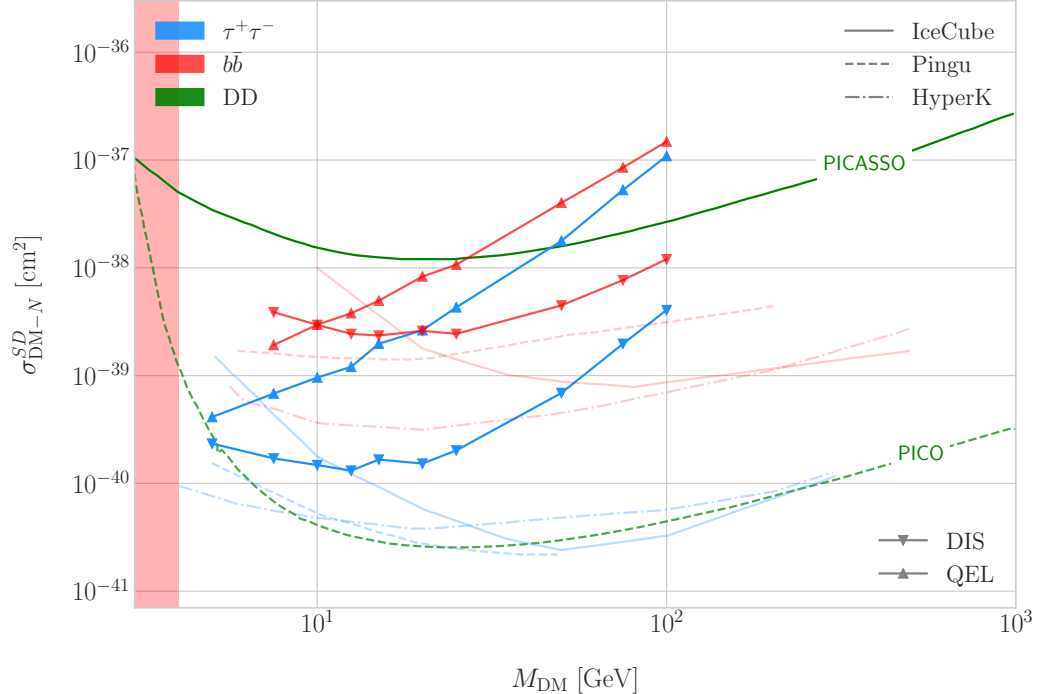


Figure 5.17: Projected 90% confidence level upper limit for DUNE (400 kT yr) on the spin-dependent DM-nucleon scattering cross section as a function of m_{DM} , for the annihilation channels $\tau^+\tau^-$ (blue) and $b\bar{b}$ (red) separated by interaction type (up triangles denote DIS interactions whereas down triangles represent QEL interactions). I also show the previous limits from IceCube [7] (solid lines) and the projected sensitivities for Pingu [8] (dashed lines) and Hyper-Kamiokande [9] (dash-dotted lines), as well as the direct detection limits from PICASSO [10] (solid green line) and PICO-60 C₃F₈ [11] (dashed green line).

2377 a 99.8% background rejection value in all cases to keep our estimation conservative.

2378 **5.6.3 Results**

2379 In order to estimate the DM-nucleon cross section sensitivities in the present case I need
 2380 again to compute the expected number of background events. As I am now separating
 2381 events by interaction type Eq. (5.25) does not hold anymore, as in that case I integrated
 2382 over the total neutrino-argon cross section. In this instance, the expected background
 2383 events for DIS events is approximately given by:

$$N_B^{DIS} \simeq \eta_B^{DIS} \times (4.655 \times 10^3) \times \left(\frac{\text{exposure}}{400 \text{ kT yr}} \right), \quad (5.38)$$

CHAPTER 5. DM SEARCHES WITH NEUTRINOS FROM THE SUN

2384 whereas for QEL events we have:

$$N_B^{QEL} \simeq \eta_B^{QEL} \times (2.248 \times 10^4) \times \left(\frac{\text{exposure}}{400 \text{ kT yr}} \right). \quad (5.39)$$

2385 Now, using these together with Eqs. (5.26) and (5.27) one can obtain the 90% C.L.
2386 upper limit on the total annihilation rate at equilibrium for both kind of events. Then,
2387 applying the computed DM-nucleons capture rates I can translate these into limits on
2388 the DM-nucleon cross section by means of Eqs. (5.2), (5.5) and (5.6).

2389 Fig. 5.17 shows the obtained limits on the SD DM-nucleon cross section for DUNE,
2390 using the DIS (up triangles) and QEL (down triangles) events both for the $\tau^+\tau^-$ (blue)
2391 and the $b\bar{b}$ (red) samples, for an exposure of 400 kT yr. I also include the corresponding
2392 current limits from IceCube [7] (solid lines), as well as the projected sensitivities of
2393 Pingu [8] (dashed lines) and Hyper-Kamiokande [9] (dash-dotted lines). For comparison,
2394 I also show the reported direct detection limits from PICASSO [10] (solid green line)
2395 and PICO-60 C_3F_8 [11] (dashed green line).

2396 Notice that, for most of the mass range, the limits one can set by using the DIS
2397 events are stronger than those of the QEL interactions, except for the low mass part
2398 of both the $\tau^+\tau^-$ and the $b\bar{b}$ curves where the QEL events dominate. In general, the
2399 expected sensitivity of DUNE for DM masses $\lesssim 25$ GeV surpasses the stronger current
2400 indirect limits. However, experiments like Hyper-Kamiokande are foreseen to have an
2401 overall better sensitivity in this kind of searches, as they have a bigger active volume
2402 and accept a broader energy range.

2403 A pending question is what happens when we add the RES and MEC charged-current
2404 interaction contributions. In that case it would probably be more convenient to split
2405 the samples by final state interaction topologies. Also, another necessary improvement
2406 would be adding a full detector simulation and reconstructions. This will also require
2407 considering the effect of poorly reconstructed events or final states containing neutral
2408 particles such that they mimic the desired topology at the reconstruction level.

5.7. EXAMPLE: LEPTOPHILIC DARK MATTER

2409 5.7 Example: Leptophilic Dark Matter

2410 In general, the capture rate of DM particles by the Sun via interactions with electrons is
2411 several orders of magnitude smaller than the capture via DM-nucleus scattering. Thus,
2412 it would be sub-leading even when nucleon capture is loop suppressed. As I showed in
2413 Fig. 5.2, the capture rate via scattering off electrons only surpasses the capture rates
2414 via DM-nucleons interactions for DM masses $\lesssim 100 - 500$ MeV.

2415 However, if one considers a model where DM-nucleon interactions are forbidden even
2416 at loop level, then electron interactions will be the sole contributor to DM capture in
2417 the Sun. One can describe such scenario where the DM particles couple to leptons but
2418 not to the quark sector using effective operators.

2419 In general, assuming that the DM particle is a Dirac fermion, the dimension six
2420 operators describing the interaction between two DM particles and two leptons can be
2421 written as:

$$\mathcal{L}_{eff} = G \sum_i (\bar{\chi} \Gamma^i \chi) (\bar{\ell} \Gamma^i \ell), \quad (5.40)$$

2422 where $G = 1/\Lambda^2$ is the effective coupling strength, Λ the cut-off of the effective field
2423 theory and ℓ denotes any lepton. In principle, one should consider all the possible
2424 Lorentz structures Γ_f^i in order to have a complete set of effective operators.

2425 However, some combinations will induce interactions with nucleons at loop level.
2426 As we are specifically interested in interactions which forbid any communication with
2427 the quark sector, I will not consider those [127]. In addition, some of the effective
2428 operators give rise to velocity-suppressed scattering cross sections between DM particles
2429 and leptons. I will also neglect those, as the suppression goes with the square of the DM
2430 halo velocity which in units of the speed of light is $\sim 10^{-6}$.

2431 This way, the only Lorentz tensor structure that do not induce interactions with
2432 quarks at loop level and gives a contribution to the scattering cross section that is not
2433 velocity suppress is the axial-axial interaction. The effective Lagrangian is then given

CHAPTER 5. DM SEARCHES WITH NEUTRINOS FROM THE SUN

2434 by:

$$\mathcal{L}_{eff} = \frac{c_A^\chi c_A^\ell}{\Lambda^2} (\bar{\chi} \gamma^\mu \gamma^5 \chi) (\bar{\ell} \gamma_\mu \gamma^5 \ell), \quad (5.41)$$

2435 where c_A^χ and c_A^ℓ are the couplings for the different species. As the DM coupling appears
2436 as a common factor for any lepton choice, I will redefine the corresponding coupling c_A^ℓ
2437 to absorb c_A^χ . Also, for simplicity, I will assume that the couplings between the DM
2438 particles and the leptons are flavour independent, i.e. I have just two couplings, c_A^e for
2439 charged leptons and c_A^v for neutrinos.

2440 In the case of a scalar DM particle, the lowest order effective interaction with
2441 leptons happens through a dimension five operator, generating scalar and pseudoscalar
2442 interactions. However, the former induces interactions with quarks at two loop level
2443 whereas the latter gives a velocity suppressed scattering cross section.

2444 From the effective Lagrangian in Eq. (5.41) it can be shown that the axial-axial
2445 contribution to the scattering cross section for the fermionic DM and a charged lepton
2446 is given by:

$$\sigma_{DM-e}^{AA} = 3 (c_A^e)^2 \frac{m_e^2}{\pi \Lambda^4}. \quad (5.42)$$

2447 If the DM interacts exclusively with fermions, then the only annihilation channels
2448 that will give us a measurable neutrino flux coming out of the Sun are $\tau^+ \tau^-$ and $\nu \bar{\nu}$. The
2449 former channel, already explored previously in the more mainstream scenario of the DM
2450 capture via scattering off nucleons, is open only for $m_{DM} > m_\tau \simeq 1776.86 \pm 0.12$ MeV
2451 [128], a mass region where the solar DM capture by electrons is at least one order of
2452 magnitude smaller than the capture via interactions with nucleons. On the contrary, the
2453 latter allows us to explore a region where the capture rate via scattering off electrons
2454 dominates over the rest.

2455 One downside of focusing in such low mass range is that it falls below the usual
2456 limit of $m_{evap} \sim 4$ GeV usually explored in the literature. The pretext to explore this
2457 region is the result discussed previously reported in Ref. [2], where DM evaporation in
2458 the Sun for the case of capture via electron scattering could be negligible for masses
2459 as low as $m_{evap} \sim 200$ MeV. This result is quite sensitive to the high velocity tail of

5.7. EXAMPLE: LEPTOPHILIC DARK MATTER

the DM velocity distribution in equilibrium inside the Sun, and therefore full numerical simulations would be needed to asses the impact of this effect. However, this falls out of the scope of our work.

In this case, as I have an specific realisation of the interaction between the DM and leptons, one can estimate the relic density of our DM for different values of the couplings and the effective field theory scale Λ . The first step to do so is compute the self-annihilation cross section. Because I consider cold relics, at the freeze-out time our DM particles were non-relativistic and so one can expand the annihilation cross section in terms of the relative velocity v between two annihilating DM particles as [129]:

$$\sigma_{ann}^{AA}|v| \approx \frac{1}{2\pi\Lambda^4} \sum_{\ell} \left(c_A^{\ell}\right)^2 m_{\chi}^2 \sqrt{1 - \frac{m_{\ell}^2}{m_{\chi}^2} \left[\frac{m_{\ell}^2}{m_{\chi}^2} + \frac{1}{12} \left(2 - \frac{m_{\ell}^2}{m_{\chi}^2}\right) v^2 \right]}, \quad (5.43)$$

where the sum includes all the possible lepton final states with mass m_{ℓ} .

Solving the Boltzmann equation for the evolution of the DM density gives as a solution a relic density of:

$$\Omega_{\chi} h^2 \approx \frac{(1.04 \times 10^9) x_F}{M_{Pl} \sqrt{g_*} (a + 3b/x_F)}, \quad (5.44)$$

where $x_F = m_{\chi}/T_F$ being T_F the freeze-out temperature, g_* the number of relativistic degrees of freedom at freeze-out and a and b the terms in the annihilation cross section expansion $\sigma_{ann}|v| \approx a + bv^2 + \mathcal{O}(v^4)$. Using the current best fit for the relic DM density $\Omega_{\chi} h^2 = 0.1198 \pm 0.0012$ [130] one can use these relations to compute the required effective theory scale Λ at which the correct density is achieved for any combinations of m_{χ} and c_A^{ℓ} .

As discussed before, in the low DM mass region QEL interactions dominate. Moreover, if I focus on direct annihilation to neutrinos, the energy of the muon neutrino flux is known as it must be equal to the mass of the DM particle, $E_{\nu} = m_{\chi}$. That way, now I do not need to use Eq. (5.33) in order to estimate the momentum transfer to the

CHAPTER 5. DM SEARCHES WITH NEUTRINOS FROM THE SUN

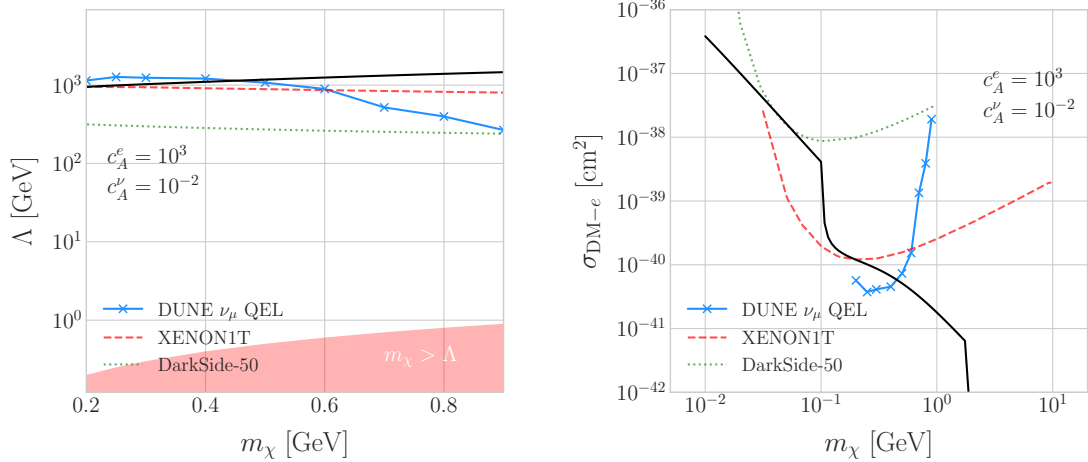


Figure 5.18: Left panel: Projected 90% confidence level sensitivity of DUNE (400 kT yr) to the scale Λ of an EFT containing only leptophilic DM axial-axial interactions (blue line). Right panel: In both cases the corresponding limits from DarkSide-50 [12] (dotted green line) and XENON1T [13] (dashed red line) are also shown, together with the configurations for which the correct relic density is achieved (black line), all for the coupling values $c_A^e = 10^3$ and $c_A^\nu = 10^{-2}$.

2482 remnant nucleus, I can simply take:

$$\vec{p}_N = \hat{p}_\nu m_\chi - \vec{p}_\mu - \vec{p}_p. \quad (5.45)$$

2483 To estimate the signal efficiency and background rejection for this case I used again
 2484 the MLP classifier from `scikit-learn`, using the same specifications as before. The
 2485 only difference now is that I add also the reconstructed neutrino energy as one of the
 2486 features to train the classifier with, because the characteristic monoenergetic flux for
 2487 each m_χ value will help to distinguish between signal and background events.

2488 In this case, for masses below ~ 500 MeV I obtain a signal efficiency close to unity
 2489 while keeping a background rejection of 99.9%. For bigger values of the mass, the signal
 2490 efficiency drops significantly if I require to keep the background acceptance under 0.01%.
 2491 However, because this kind of search is dominated by the background, sacrificing the
 2492 signal acceptance to keep the background rejection to a minimum enhances the reach
 2493 of the analysis. This way, for DM masses of the order of $m_\chi \sim 1$ GeV I end up with
 2494 efficiencies as low as 1%.

5.7. EXAMPLE: LEPTOPHILIC DARK MATTER

Now, estimating the number of background events using Eq. (5.39) one can go on and apply Eqs. (5.26) and (5.27) together with Eq. (5.42) to derive the sensitivity of DUNE to this kind of model. Fig. 5.18 (left panel) shows the potential reach of DUNE to constrain the EFT scale Λ this model containing only leptophilic DM axial-axial interactions (blue line), for a choice of couplings $c_A^e = 10^3$ and $c_A^\nu = 10^{-2}$. I also included the current limits on the DM-electron scattering cross section from DarkSide-50 [12] (dotted green line) and XENON1T [13] (dashed red line), reworked with Eq. (5.42) to show their implications for the EFT scale. The values of Λ for which the correct DM relic density value is achieved for each mass are also shown (black line). This tells us that, for that specific choice of couplings, DUNE would be sensitive to DM configurations allowed by the relic density constraint up to a mass of $m_\chi \sim 400$ MeV.

In Fig. 5.18 (right panel) I show the same upper limits but for the DM-electron scattering cross section. From this view one can see that DUNE would be able to offer complementary information to the low energy DM-electron interaction searches performed by direct detection experiments, in a slightly higher mass range.

With the present example, although it focuses on a very specific realisation of the DM interactions, I show the potential of DUNE to constrain exotic DM scenarios. Thanks to its low backgrounds and superb angular resolution DUNE will be able to help with the systematic searches for dark sectors physics.

2514

2515

Particle ID in GArSoft

2516 ND-GAr is a magnetised, high-pressure gaseous argon TPC (HPgTPC), surrounded by
2517 an electromagnetic calorimeter (ECal) and a muon detector (commonly refer to as μ ID).
2518 A detailed discussion on the requirements, design, performance and physics of ND-GAr
2519 can be found in the DUNE ND CDR [78] and the ND-GAr whitepaper (cite).

2520 In DUNE Phase II ND-GAr will fulfill the role of TMS, measuring the momentum
2521 and sign of the charged particles exiting ND-LAr. Additionally, it will be able to measure
2522 neutrino interactions inside the HPgTPC, achieving lower energy thresholds than those
2523 of the ND and FD LArTPCs. By doing so ND-GAr will allow to constrain the relevant
2524 systematic uncertainties for the LBL analysis even further.

2525 The goal of the present chapter is to review the requirements that the physics program
2526 of DUNE impose on ND-GAr, present the current status of its design and describe the
2527 GArSoft package, its simulation and reconstruction software.

2528 As decided during the DUNE Phase II workshop in June 2023 [reference], we want
2529 to build ND-GAr physics case by showing:

- 2530 • That ND-GAr can constrain systematic uncertainties that ND-LAr might miss.
- 2531 • The impact on the neutrino oscillation results if such systematic uncertainties are
2532 missed.
- 2533 • That ND-GAr is necessary to reach DUNE's main physics goals.

2534 This way, the design of ND-GAr will be physics driven.

CHAPTER 6. PARTICLE ID IN GArSOFT

2535 In order to study the effects of final state interactions (FSI) in CC interactions,
2536 ND-GAr should be able to measure the spectrum of protons and charged pions at low
2537 energies. ND-GAr also needs to be able to measure the pion multiplicity, specially for
2538 energies above 100 MeV as at these energies the pions shower in the LAr, to inform the
2539 pion mass correction in the ND and FD LArTPCs.

2540 In order to correctly identify electrons, muons, pions, kaons and protons ND-GAr
2541 can use a combination of: dE/dx measurements in the HPgTPC, E_{ECAL}/p using the
2542 ECAL total energy and the momentum obtained from magnetic spectroscopy in the
2543 HPgTPC and penetration information through the ECAL and muon tagger.

2544 6.1 GArSoft

2545 GArSoft is a software package developed for the simulation and reconstruction of events
2546 in ND-GAr. It is inspired by the LArSoft toolkit used for the simulation of LArTPC
2547 experiments, like the DUNE FD modules. It is based on `art`, the framework for event
2548 processing in particle physics experiments [131]. Other of its main dependencies are
2549 `ROOT`, `NuTools`, `GENIE` and `Geant4`. It allows the user to run all the steps of a generation-
2550 simulation-reconstruction workflow using FHiCL configuration files.

2551 6.1.1 Event generation

2552 The standard generator FHiCLs in GArSoft run the event generation and particle
2553 propagation simulation (i.e. Geant4) in the same job by default. However, it is possible
2554 to split them up if needed. The current version of GArSoft provides five different event
2555 generators, each of them producing `simb::MCTruth` products defined in `NuTools`. The
2556 available modules are:

- 2557 • **SingleGen**: particle gun generator. It produces the specified particles with a given
2558 distribution of momenta, initial positions and angles.
- 2559 • **TextGen**: text file generator. The input file must follow the `hepevt` format¹, the

¹In brief, each event contains at least two lines. The first line contains two entries, the event number

6.1. GARSOFT

2560 module simply copies this to `simb::MCTruth` data products.

2561 • **GENIEGen**: GENIE neutrino event generator. The module runs the neutrino-nucleus
2562 interaction generator using the options specified in the driver FHiCL file (flux file,
2563 flavour composition, number of interactions per event, t_0 distribution, ...). Current
2564 default version is v3_04_00.

2565 • **RadioGen**: radiological generator. It produces a set list of particles to model
2566 radiological decays. Not tested.

2567 • **CRYGen**: cosmic ray generator. The module runs the CRY event generator with a
2568 configuration specified in the FHiCL file (latitude and altitude of detector, energy
2569 threshold, ...). Not tested.

2570 The module **GArG4** searches for all the generated `simb::MCTruth` data products, using
2571 them as inputs to the Geant4 simulation with the specified detector geometry. A constant
2572 0.5 T magnetic field along the drift coordinate is assumed. The main outputs of this step
2573 are `simb::MCParticle` objects for the generated Geant4 particles, `gar::EnergyDeposit`
2574 data products for the energy deposits in the HPgTPC and `gar::CaloDeposit` data
2575 products for the energy deposits in the ECal and muon system.

2576 6.1.2 Detector simulation

2577 The standard detector simulation step in GArSoft is all run with a single FHiCL, but
2578 the different modules can be run independently as well. First the `IonizationReadout`
2579 module simulates the charge readout of the HPgTPC, and later the `SiPMReadout` module
2580 runs twice, once for the ECal and then for the muon system, with different configurations.

2581 The `IonizationAndScintillation` module collects all the `gar::EnergyDeposit`
2582 data products, to compute the equivalent number of ionization electrons for each energy

and the number of particles in the event. Each following line contains 15 entries to describe each particle. The entries are: status code, pdg code for the particle, entry of the first mother for this particle, entry of the second mother for this particle, entry of the first daughter for this particle, entry of the second daughter for this particle, x component of the particle momentum, y component of the particle momentum, z component of the particle momentum, energy of the particle, mass of the particle, x component of the particle initial position, y component of the particle initial position, z component of the particle initial position and time of the particle production.

CHAPTER 6. PARTICLE ID IN GArSOFT

deposit. The `ElectronDriftAlg` module simulates the electron diffusion numerically both in the longitudinal and transverse directions and applies an electron lifetime correction factor. The induced charge on the nearest and neighbouring readout pads is modeled using the provided pad response functions. The digitisation of the data is then simulated with the `TPCReadoutSimAlg` module. By default, the ADC sampling rate used is 50.505 MHz. The resulting raw waveforms for each channel are stored with zero-suppression, in order to save memory and CPU time. The algorithms keep blocks of ADC values above a certain threshold, plus some adjustable additional early and late tick counts. The results of these three steps are `gar::raw::RawDigit` data products.

For the ECal and the muon system the `SiPMReadout` module calls either the `ECALReadoutSimStandardAlg` or `MuIDReadoutSimStandardAlg` modules. These take all the `gar::CaloDeposit` data products in the corresponding detector and do the digitisation depending on whether the hit was in a tile or strip layer. They include single photon statistics, electronic noise, SiPM saturation and time smearing. The resulting objects are `gar::raw::CaloRawDigit` data products.

6.1.3 Reconstruction

The reconstruction in GArSoft is also run as a single job by default. It first runs the hit finding, clustering, track fitting and vertex identification in the HPgTPC, followed by the hit finding and clustering in the ECal and muon system. After those it produces the associations between the associations between the tracks and the ECal clusters.

Focusing first on the HPgTPC reconstruction, the `CompressedHitFinder` module takes the zero-suppressed ADCs from the `gar::raw::RawDigit` data products. The reconstructed hits largely correspond to the above threshold blocks, however the hit finder identifies waveforms with more than one maximum, diving them in multiple hits if they dip below a certain threshold. The data products produced are of the form `gar::rec::Hit`. These are the inputs to the clustering of hits in the `TPCHitCluster` module. Hits close in space and time are merged, and the resulting centroids are found. This module outputs `gar::rec::TPCClusters` objects and associations to the input

6.1. GARSOFT

2611 hits.

2612 The following step prior to the track fitting is pattern recognition. The module
2613 called `tpcvechitfinder2` uses the `gar::rec::TPCClusters` data products to find track
2614 segments, typically called vector hits. They are identified by performing linear 2D fits
2615 to the positions of the clusters in a 10 cm radius, one fit for each coordinate pair. A
2616 3D fit defines the line segment of the vector hit, using as independent variable the one
2617 whose sum of (absolute value) slopes in the 2D fits is the smallest. The clusters are
2618 merged to a given vector hit if they are less than 2 cm away from the line segment. The
2619 outputs are `gar::rec::VecHit` data products, as well as associations to the clusters. The
2620 `tpcpatrec2` module takes the `gar::rec::VecHit` objects to form the track candidates.
2621 The vector hits are merged together if their direction matches, their centers are within
2622 60 cm and their direction vectors point roughly to their respective centers. Once
2623 the clusters of vector hits are formed they are used to make a first estimation of the
2624 track parameters, simply taking three clusters along the track. The module produces
2625 `gar::rec::Track` data products and associations between these tracks and the clusters
2626 and vector hits.

2627 The track is fitted by means of a Kalman filter in the `tpctrackfit2` module, using
2628 the position along the drift direction as the independent variable. Two different fits are
2629 performed per track, a forward and a backwards fit, each starting from one of the track
2630 ends. The Kalman filter state vector ($y, z, R, \phi, \tan\lambda$) is estimated at each point along
2631 the track using a Bayesian update. The track parameters reported in the forward and
2632 backwards fits are the ones computed at the opposite end where the fit started. The
2633 main outputs of the track fit are the `gar::rec::Track` objects. Additionally, the module
2634 stores the fitted 3D positions along the track in the `gar::rec::TrackTrajectory` data
2635 products and the total charge and step sizes for each point also get stored in the form of
2636 `gar::rec::TrackIonization` objects.

2637 After the tracking step, the `vertexfinder1` module looks at the reconstructed
2638 `gar::rec::Track` products, creating vertex candidates with the track ends that are
2639 within 12 cm of each other. The vertices are then fitted using linear extrapolations from

CHAPTER 6. PARTICLE ID IN GARSOFT

2640 the different track ends associated. The results are `gar::rec::Vertex` data products,
2641 and associations to the tracks and corresponding track ends.

2642 For the ECal and muon tagger, the `SiPMHitFinder` module runs twice with different
2643 configurations, adapted to the particular capabilities of both. The module simply takes
2644 the `gar::raw::CaloRawDigit` products, applies a calibration factor to convert the ADC
2645 counts to MeV and for the strip layer hits it calculates the position along the strip using
2646 the times recorded of both SiPMs. This module produces `gar::rec::CaloHit` data
2647 products. Next, these objects are used as inputs to the `CaloClustering` module. It
2648 merges the hits based on a simple nearest neighbours (NN) algorithm. For the resulting
2649 clusters it also computes the total energy and position of the centroid. The results are
2650 stored as `gar::rec::Cluster` data products, with associations to the hits.

2651 The last step in the reconstruction is associating the reconstructed tracks in the
2652 HPgTPC to the clusters formed in the ECal and muon system. The `TPCECALAssociation`
2653 module checks first the position of the track end points, considering only the points
2654 that are at least 215 cm away from the cathode or have a radial distance to the center
2655 greater than 230 cm. The candidates are propagated up to the radial position, in the
2656 case of clusters in the barrel, or the drift coordinate position, for the end cap cluster, of
2657 the different clusters in the collection using the track parameters computed at the end
2658 point. The end point is associated to the cluster if certain proximity criteria are met.
2659 This module creates associations between the tracks, the end points and the clusters.
2660 The criteria for the associations are slightly different for the ECal and the muon tagger.

2661 6.2 **dE/dx** measurement in the TPC

2662 Among the parameters extracted from the track fitting, ionisation is particularly useful
2663 for particle identification, as it is a function of the particle velocity. Although for the
2664 case of relativistic particles this dependence is not very strong, measuring the track on
2665 a large number of points may allow us to estimate the amount of ionisation accuratel.
2666 This, paired with a measurement of the momentum, may allow us to identify the particle

6.2. dE/dx MEASUREMENT IN THE TPC

2667 type.

2668 The first calculation of the energy loss per unit length of relativistic particles using a
 2669 quantum-mechanical treatment is due to Bethe [132]. Using this approach, the mean
 2670 ionisation rate of a charged particle traveling through a material medium is (using
 2671 natural units $G = \hbar = c = 1$):

$$\left\langle \frac{dE}{dx} \right\rangle = \frac{4\pi Ne^4}{m_e \beta^2} z^2 \left(\log \frac{2m_e \beta^2 \gamma^2}{I} - \beta^2 \right), \quad (6.1)$$

2672 where N is the number density of electrons in the medium, e the elementary charge, m_e
 2673 is the electron mass, z the charge of the particle in units of e , β is the velocity of the
 2674 particle, $\gamma = (1 - \beta^2)^{-1}$ and I denotes the effective ionisation potential averaged over
 2675 all electrons. This relation is known as the Bethe-Bloch formula.

2676 From Eq. (6.1) one can see that the ionisation loss does not depend explicitly on
 2677 the mass of the charged particle, that for non-relativistic velocities it falls as β^{-2} , then
 2678 goes through a minimum and increases as the logarithm of γ . This behaviour at high
 2679 velocities is commonly known as the relativistic rise. The physical origin of this effect
 2680 is partly due to the fact that the transverse electromagnetic field of the particle is
 2681 proportional to γ , therefore as it increases so does the cross section.

2682 It was later understood that the relativistic rise could not grow indefinitely with γ .
 2683 A way to add this feature in the Bethe-Bloch formula is by introducing the so-called
 2684 density effect term. It accounts for the polarisation effect of the atoms in the medium,
 2685 which effectively shield the electromagnetic field of the charged particle halting any
 2686 further increase of the energy loss [133]. Denoting the correction as $\delta(\beta)$, one can rewrite
 2687 Eq. (6.1) as:

$$\left\langle \frac{dE}{dx} \right\rangle = \frac{4\pi Ne^4}{m_e \beta^2} z^2 \left(\log \frac{2m_e \beta^2 \gamma^2}{I} - \beta^2 - \frac{\delta(\beta)}{2} \right). \quad (6.2)$$

2688 In general, the form of $\delta(\beta)$ depends on the medium and its state of aggregation,
 2689 involving the usage of tabulated parameters and implicit relations [134].

2690 Another standard method to compute the amount of ionisation a charged particle
 2691 produces is the so-called photo-absorption ionisation (PAI) model proposed by Allison

CHAPTER 6. PARTICLE ID IN GARSOFT

and Cobb [135]. Within their approach, the mean ionisation is evaluated using a semiclassical calculation in which one characterises the continuum material medium by means of a complex dielectric constant $\varepsilon(k, \omega)$. However, in order to model the dielectric constant they rely on the quantum-mechanical picture of photon absorption and collision. Therefore, in the PAI model the computation of the ionisation loss involves a numerical integration of the measured photo-absorption cross-section for the relevant material.

In a particle physics experiment, the typical way of determining the energy loss per unit length as a function of the particle velocity is studying identified particles over a range of momenta. Once we have established this relation we can use it for other, unknown particles. In this sense, it makes sense to have a regular mathematical expression for this relation that one can use.

It happens that neither the Bethe-Bloch theory nor the PAI model from Allison and Cobb offer a close mathematical form for the ionisation curve. This is the reason why a full parametrisation of the ionisation curves can be useful. A parametrisation originally proposed for the ALEPH TPC [136] and later used by the ALICE TPC [137] group that manages to capture the features of the ionisation energy loss is:

$$f(\beta\gamma) = \frac{P_1}{\beta^{P_4}} \left(P_2 - \beta^{P_4} - \log \left[P_3 + \frac{1}{(\beta\gamma)^{P_5}} \right] \right), \quad (6.3)$$

where P_i are five free parameters. Hereafter, we will refer to Eq. (6.3) as the ALEPH dE/dx parametrisation.

6.2.1 Energy calibration

In order to obtain the amount of energy loss by a charged particle due to ionisation in our TPC we need to determine the conversion between the charge deposited in our readout planes and the actual energy depositions. This procedure is known as energy calibration.

In a general, the first step of the calibration involves a non-uniformity correction, to make sure that the detector response is uniform throughout the TPC. These are

6.2. dE/dx MEASUREMENT IN THE TPC

2717 typically divided into three categories, non-uniformities in the transverse YZ plane,
2718 non-uniformities along the drift direction X and variations of the detector response
2719 over time (would not apply to us as the detector is not built yet). These would correct
2720 for effects such as electron diffusion and attenuation, space charge effects or channel
2721 misconfiguration. However, because at the moment I am only interested in making sure
2722 we recover a sensible result from our simulation, I will not apply uniformity corrections
2723 to our charge deposits.

2724 Other effects, like electron-ion recombination or ADC saturation, lead to a non-linear
2725 relation between the observed charge and the deposited energy in the detector, with the
2726 observed readout charge saturating at high ionisation energies. In this case, because we
2727 are dealing with gaseous argon and therefore recombination is not as important as in
2728 liquid, we do not simulate recombination effects in the TPC. Even so, the simulation of
2729 the electronic response will still introduce charge saturation, and one needs to correct
2730 for it in order to obtain the exact amount of energy loss due to ionisation.

2731 By default, the track fitting algorithm in GArSoft provides a `TrackIonization`
2732 object associated to each reconstructed track. It contains two collections of charge
2733 deposits, one for each fitting direction, consisting on pairs of charge values (dQ , in ADC)
2734 and step sizes (dx , in cm).

2735 In order to estimate the ionisation loss in the ND-GAr TPC, I have used an MC
2736 sample consisting of single, isotropic protons propagating in the TPC. The starting points
2737 of the protons were sampled inside a $50 \times 50 \times 25$ cm box centered at $(100, -150, 1250)$,
2738 and their momenta are uniformly distributed in the range $0.25 - 1.75$ GeV. I ran the
2739 simulated sample through GArSoft's default detector simulation and reconstruction, and
2740 then a custom analyser module that extracts the ionisation data together with other
2741 reconstructed track information from the Kalman fit.

2742 For studying the energy loss of the protons I select the reconstructed tracks that
2743 range out (i.e. slow down to rest) inside the TPC. A characteristic feature of the energy
2744 loss profile of any stopping ionising particle is the so-called Bragg peak, a pronounced
2745 peak that occurs immediately before the particle comes to rest. From Eq. (6.1) we can

CHAPTER 6. PARTICLE ID IN GARSOFT

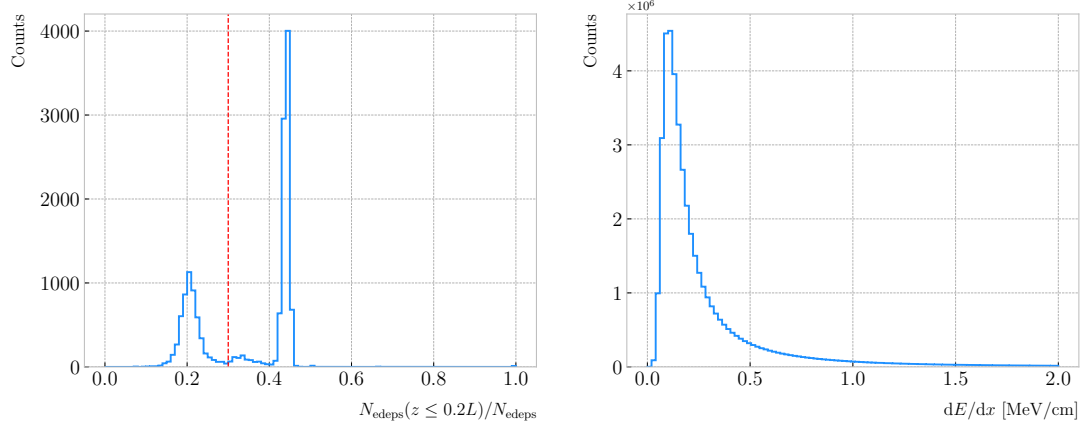


Figure 6.1: Left panel: distribution of the fraction of Geant4-level energy deposits per track with residual range less than 20% of the total track length, for the isotropic proton sample. Right panel: distribution of the ionisation per unit length of the energy deposits in the proton sample after removing the tracks with less than 30% of their energy deposits in the last 20% of the track.

2746 see that this behaviour is expected, as the energy loss for non-relativistic particles is
 2747 inversely proportional to β^2 . In data, a way of identifying the Bragg peak, and thus
 2748 select the stopping particles, is checking the number of energy deposits towards the
 2749 end of the track. In this case, I count the fraction of the Geant4 simulated energy
 2750 deposits with a residual range value (the distance from a given energy deposit to the
 2751 last deposit in the track trajectory) less than a 20% of the corresponding track length².
 2752 The distribution of this fraction of energy deposits for our proton sample is shown in
 2753 Fig. 6.1 (left panel). We can clearly see two well separated peaks in this distribution,
 2754 one centered at 0.2 and another, narrower, one centered at a higher value. The first
 2755 one corresponds to non-stopping protons, as in that case the number of energy deposits
 2756 towards the end of the track is uniformly distributed due to the absence of the Bragg
 2757 peak. In that way, I apply a cut in this distribution, requiring that at least 30% of the
 2758 simulated energy deposits sit in the last 20% of the tracks, to ensure that the Bragg
 2759 peak is present.

2760 Figure 6.1 (right panel) shows the distribution of the energy loss per unit length for

²As we are applying this selection at the Geant4 level we could have simply selected the stopping protons using the `EndProcess` labels from the simulation. However, the Bragg peak identification method displayed here could serve as a starting point for a selection of stopping protons in real data.

6.2. dE/dx MEASUREMENT IN THE TPC

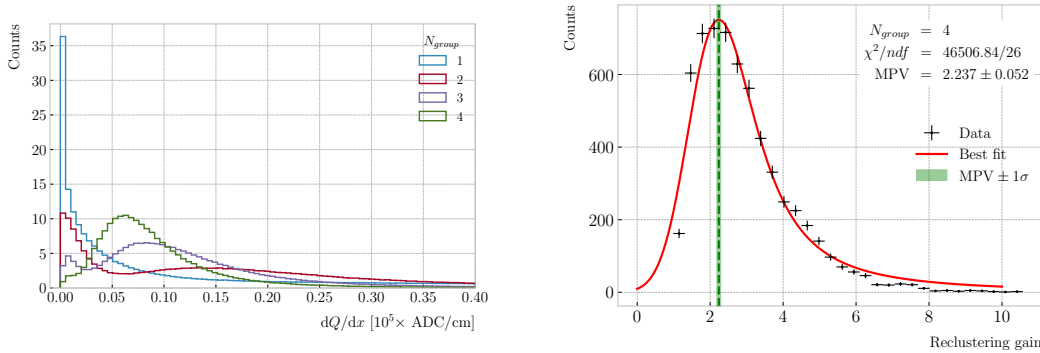


Figure 6.2: Left panel: distribution of the reconstructed ionisation charge per unit length for our MC stopping proton sample. The different colors indicate how many consecutive dQ/dx pairs were grouped together. Right panel: distribution of the median change in dQ/dx per track after $N_{group} = 4$ clusters were reclustered together.

2761 the Geant4 simulated energy deposits of the selected stopping protons. We can see that
 2762 it follows the expected shape of a Landau distribution, which describes the fluctuations of
 2763 the ionisation energy losses [138]. This distribution has a characteristic asymmetric PDF,
 2764 with a long right tail that translates into a high probability for high-energy ionisation
 2765 losses. The origin of these fluctuations is mainly the possibility of transferring a high
 2766 enough energy to an electron, so it becomes a ionising particle itself.

2767 Now, from the point of view of the reconstruction, the objects that we have available
 2768 to extract the ionisation information for the different reconstructed tracks are the
 2769 collections of dQ and dx pairs, as stated before. The dQ values come from adding up
 2770 the amplitude of all the reconstructed hits in a cluster, which is the input object to the
 2771 Kalman fit.

2772 Figure 6.2 (left panel) shows the distribution of the ionisation charge deposits
 2773 per unit length for the track in the stopping proton sample (blue line). As one can
 2774 notice, this distribution does not resemble the expected shape of the Landau PDF. This
 2775 distribution peaks sharply at 0 and has a heavy tailed behaviour. Notice, however, how
 2776 the distribution changes its shape as we group together N_{group} consecutive charge deposit
 2777 pairs (red, purple and green lines). The distribution in the $N_{group} = 4$ case already has
 2778 a shape which resembles that of the Geant4-level ionisation per unit length, so I will
 2779 proceed using this amount of reclustering for the reconstruction-level depositions.

CHAPTER 6. PARTICLE ID IN GARSOFT

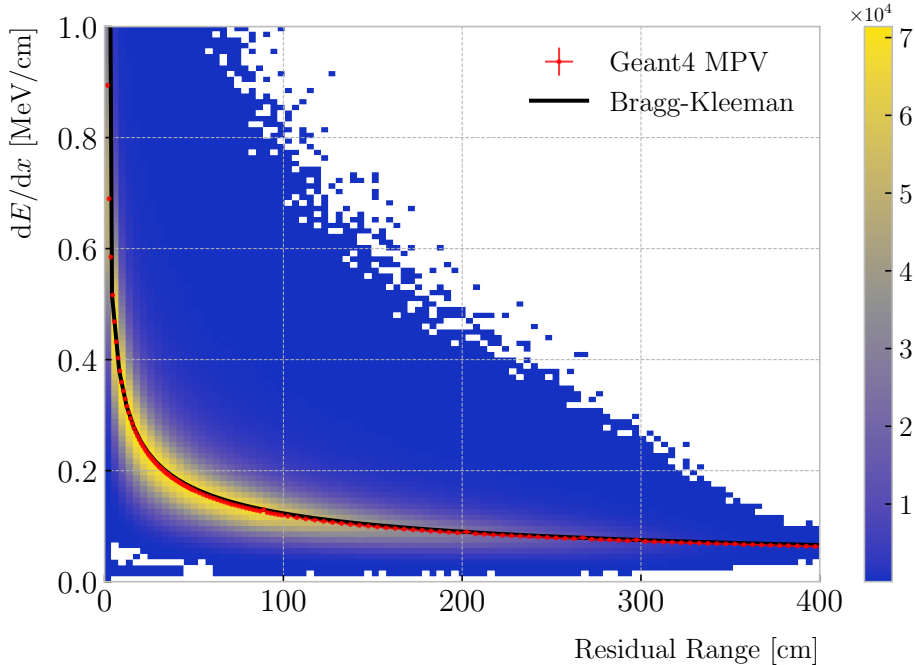


Figure 6.3: Distribution of the Geant4-simulated energy losses per unit length versus residual range for the stopping proton sample. The overlaid points represent the fitted most probable value of the dE/dx distribution in each residual range bin, whereas the curve is their best fit to the Bragg-Kleeman formula from Eq. (6.4).

2780 An extra factor I need to account for, when reclustering is applied, is how the overall
 2781 dQ/dx per track changes. To do so, we can look at the ratio between the median dQ/dx
 2782 after and before the reclustering. Figure 6.2 (right panel) shows the median enhancement
 2783 in dQ/dx per track for the stopping proton sample in the case $N_{group} = 4$. Fitting a
 2784 Landau distribution convolved with a Gaussian³, I estimate the most probable value of
 2785 this ratio to be $G_{group} = 2.24 \pm 0.05$.

2786 At this point, I am left with determining the conversion between the charge deposits
 2787 per unit length dQ/dx and the energy deposits per unit length dE/dx . To this end, we
 2788 need a way of comparing the two. I can use the residual range z to get a prediction of

³In the literature, this distribution is often referred to as Landau+Gaussian or langau. In the following, I will use LanGauss to refer to such PDF.

6.2. dE/dx MEASUREMENT IN THE TPC

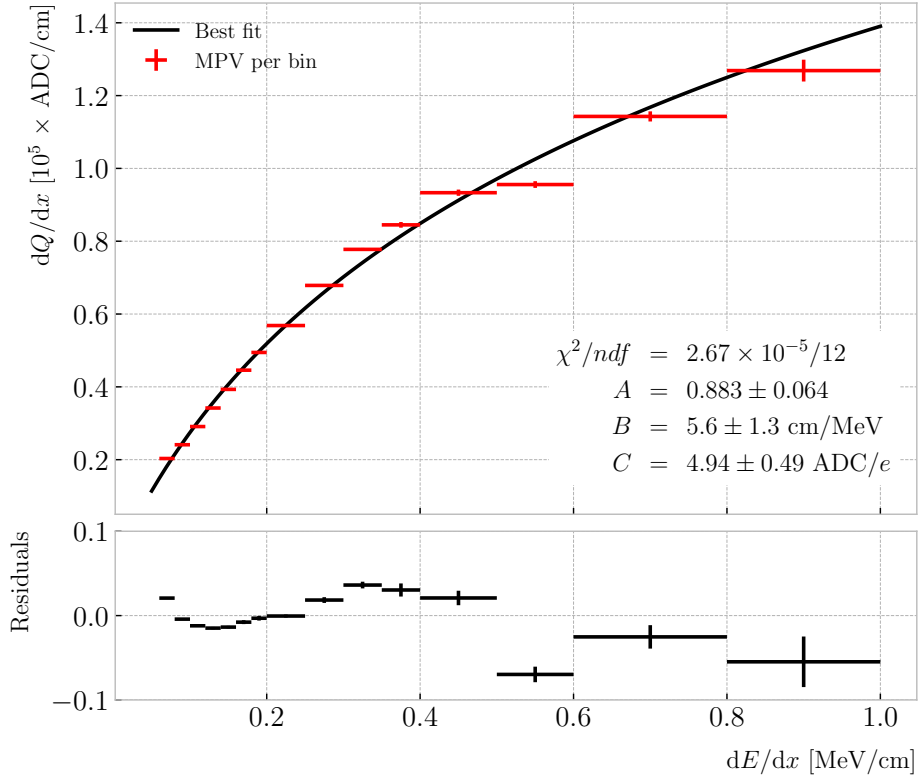


Figure 6.4: Fitted most probable dQ/dx values for each dE/dx bin (red points), obtained from the stopping proton sample. The overlaid curve (black line) represents the best fit to the logarithmic calibration function from Eq. (6.5).

2789 the most probable dE/dx by using the following empirical parametrisation [139]:

$$\frac{dE}{dx}(z) = \frac{z^{\frac{1}{p}-1}}{p\Lambda^{\frac{1}{p}}}, \quad (6.4)$$

2790 which is quoted in the literature as the Bragg-Kleeman formula. In order to obtain the
 2791 p and Λ parameters I perform a fit using the energy losses and the residual ranges given
 2792 by the Geant4 stage of our proton sample.

2793 Within our simulation, the residual range is sampled with a maximum size of
 2794 5 mm. Therefore, to perform the fit to the Bragg-Kleeman formula, we can use a
 2795 fine-grained residual range binning. For each of the residual range bins I extract the
 2796 dE/dx distribution and fit it to a LanGauss distribution, to obtain the value of the
 2797 most probable dE/dx in the bin together with a statistical uncertainty. I then fit Eq.

CHAPTER 6. PARTICLE ID IN GARSOFT

(6.4) to these most probable values and the centres of the residual range bins. This procedure is depicted in Fig. 6.3, where I show the distribution of the energy loss per unit length versus the residual range, together with the most probable dE/dx values and their uncertainty in each bin (red points) and the curve with the best fit of the Bragg-Kleeman relation to those values (black line). The best fit is obtained for the parameter values $p = 1.8192 \pm 0.0005$ and $\Lambda = 0.3497 \pm 0.0008 \text{ cm}/\text{MeV}^p$ ⁴.

Having an analytical expression that relates the residual range to dE/dx , I can take our reconstruction-level residual ranges from the stopping proton sample and compute the most probable energy loss associated.

In order to parametrise the charge saturation, we can use the following logarithmic function inspired by the modified box model for recombination:

$$\frac{dE}{dx} = \frac{e^{\frac{dQ}{dx}B\frac{W_{ion}}{G_{group}C}} - A}{B}, \quad (6.5)$$

where A and B are the calibration parameters we need to determine, W_{ion} is the average energy to produce an electron-ion pair, G_{group} is the gain from the reclustering discussed above and C is the calibration constant to convert number of electrons to ADC counts, commonly refer to as gain (also to be obtained in the fit). In this case, I use a value for the electron-ion production energy of $W_{ion} = 26.4 \text{ eV}$ [140]. This value, used in our simulation as well, was measured for gaseous argon in normal conditions, and therefore should be checked in the future to describe correctly the high-pressure argon-CH₄ mixture of ND-GAr.

For the calibration fit I follow a procedure similar to the previous one for Eq. (6.4). Binning the dE/dx range, I fit a LanGauss distribution to the corresponding dQ/dx distribution to obtain the most probable value. The resulting data points (red bars) are shown in Fig. 6.4 (top panel), the horizontal error bars depict the width of the dE/dx bin whereas the vertical bars represent the error associated to the most probable value estimation. A fit to the logarithmic function in Eq. (6.5) is also shown (black line).

⁴These strange units for Λ come from dimensional analysis, just to keep the Bragg-Kleeman formula (6.4) consistent.

6.2. dE/dx MEASUREMENT IN THE TPC

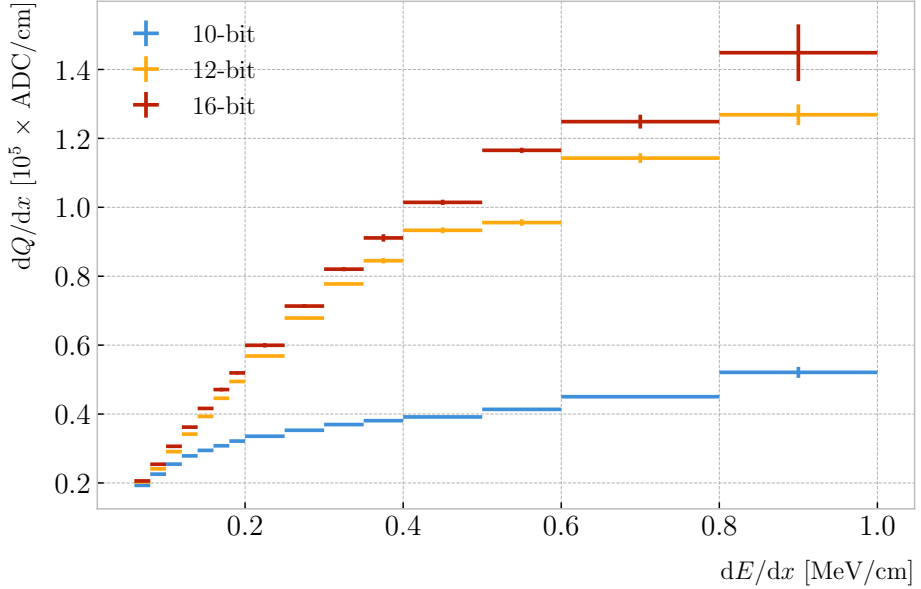


Figure 6.5: Fitted most probable dQ/dx values for each dE/dx bin for three different ADC bit limits, 10 (blue points), 12 (default, yellow points) and 16-bit (red points).

Table 6.1: Calibration parameters obtained from the fit of the ND-GAr simulated stopping proton sample to the calibration function from Eq. (6.5). The fits were performed for the 10, 12, and 16-bit ADC limits.

	χ^2/ndf	Best fit $\pm 1\sigma$		
		A	B (cm/MeV)	C (ADC/e)
10-bit	$1.83 \times 10^{-6}/12$	-9.3 ± 3.9	270 ± 69	27.1 ± 5.4
12-bit	$2.67 \times 10^{-5}/12$	0.883 ± 0.064	5.6 ± 1.3	4.94 ± 0.49
16-bit	$1.44 \times 10^{-5}/12$	0.949 ± 0.024	3.53 ± 0.58	4.52 ± 0.29

For this I weighted the data points using the inverse of their relative error, obtaining a reduced chi-square value of $\chi^2/ndf = 2.22 \times 10^{-6}$. The best fit parameters I found from this fit are $A = 0.883 \pm 0.064$, $B = 5.6 \pm 1.3$ cm/MeV and $C = 4.94 \pm 0.49$ ADC/e. Figure 6.4 (bottom panel) shows the residuals between the data points and the fit.

The value for the gain I obtained from the fit is in reasonable agreement with our expectation. This value is set in GArSoft to 5 ADC/e by default.

One interesting thing to check is what induces this non-linear relation between charge and energy. The only effects that modify the amount of electrons reaching the readout planes in the simulation are the transverse diffusion and the finite electron lifetime.

CHAPTER 6. PARTICLE ID IN GArSOFT

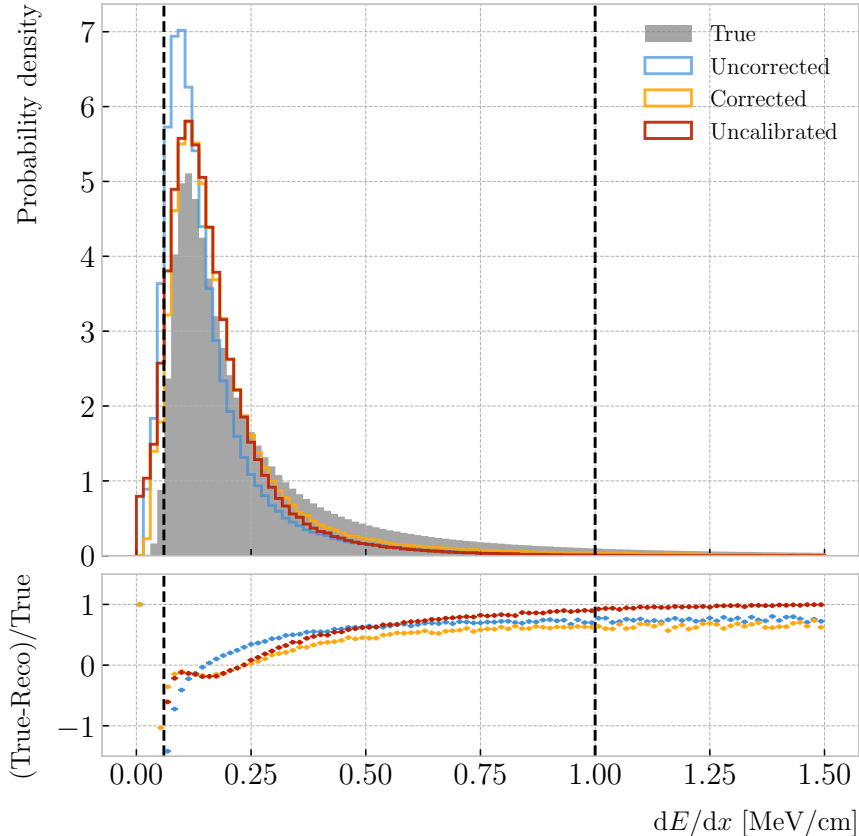


Figure 6.6: Top panel: area normalised dE/dx distributions for the true (solid grey) and the reconstructed energy deposits in the stopping proton sample, both after applying the calibration (blue) and the calibration and the normalisation correction (yellow). Also shown is the distribution obtained by applying a correction factor to the dQ/dx values but not the calibration (red). Bottom panel: fractional residuals for the uncorrected (blue), corrected (yellow) and uncalibrated (red) samples.

2832 Once the electrons reach the readout chambers, the pad response functions are applied,
 2833 together with an electrons-to-ADC conversion and the ADC saturation limit.

2834 By default, GArSot applies a 12-bit ADC limit, which can be changed in the
 2835 simulation configuration. However, it can only be increased up to 16-bit, as we represent
 2836 the ADC collection as a `std::vector<short>`. This way, I tried to change the saturation
 2837 parameter to see how it affects the relation between reconstructed charge and energy.
 2838 Figure 6.5 shows a comparison between the most probable dQ/dx for 10, 12 and 16-
 2839 bit ADC limits. As expected, the lower the limit is the sooner the charge saturates.
 2840 For higher ADC limits the relation between energy and charge remains linear up to

6.2. dE/dx MEASUREMENT IN THE TPC

2841 higher dE/dx values, but even for the 16-bit limit the saturation is noticeable for values
2842 $\gtrsim 0.5$ MeV/cm.

2843 Table 6.1 shows the results of fitting the samples with 10 and 16-bits ADC limits to
2844 the calibration function from Eq. (6.5), using the weights based on their relative error
2845 as described previously. One interesting feature to notice is how different the best fit
2846 points look for the 10-bit ADC saturation when compared to the other two, which are
2847 consistent with each other.

2848 At this point we can compare the dE/dx distribution one gets from Geant4, i.e. the
2849 true energy loss distribution, and the distribution I found by applying the calibration
2850 function to our collection of reconstructed dQ/dx values. Figure 6.6 (top panel) shows
2851 the true (solid grey) and reconstructed (blue, labeled as uncorrected) distributions
2852 together. The dashed vertical lines indicate the region of validity of the calibration fit, i.e.
2853 the left and right edges of the first and last dE/dx bin respectively. Notice that these
2854 histograms are area-normalised, as the total number of true energy deposits is much
2855 higher than the number of reconstructed charge deposits. This is due to a combination
2856 of effects, like the finite spatial resolution of the detector, the hit clustering used in the
2857 track fitting and the reclustering we have applied here.

2858 The two distributions are significantly different. That can be seen clearly when
2859 looking at the fractional residuals, shown in Fig. 6.6 (bottom panel). In particular,
2860 the position of the peak is off, which could bias the mean energy loss predictions. It
2861 seems like the difference between these may be due to an overall scaling factor. One
2862 possibility is to scale the most probable value of the reconstructed distribution to
2863 the most probable value predicted by Geant4. I do this by fitting both distributions
2864 using a LanGauss function, obtaining $dE/dx_{MPV, true} = 0.1145 \pm 0.0005$ MeV/cm and
2865 $dE/dx_{MPV, reco} = 0.0928 \pm 0.0005$ MeV/cm for the true and reconstructed most probable
2866 values respectively. These can be translated into an scaling factor $S = 0.579 \pm 0.006$.

2867 The result of applying the scaling correction can be seen in Fig. 6.6 (top panel).
2868 The corrected dE/dx distribution (yellow, labeled as corrected) peaks around the same
2869 value the true distribution does, as expected. Moreover, the high energy region is also

CHAPTER 6. PARTICLE ID IN GArSOFT

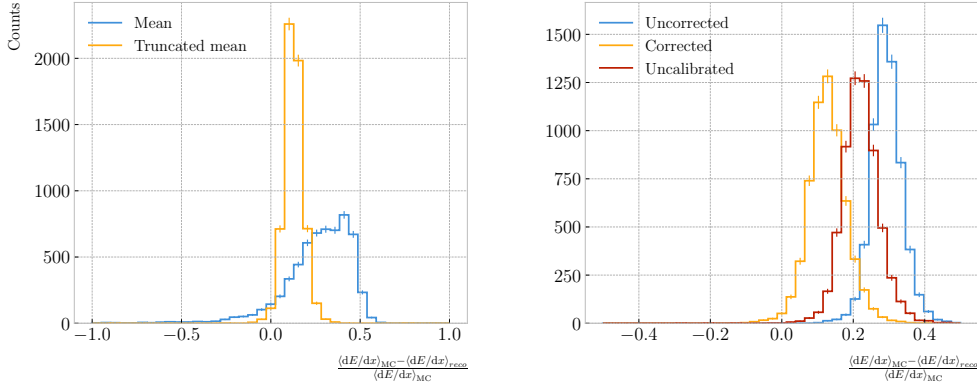


Figure 6.7: Left panel: fractional residuals between the true and the corrected dE/dx means (blue) and the 60% truncated means (yellow), for each event in the stopping proton sample. Right panel: fractional residuals between the true and the uncorrected (blue), corrected (yellow) and uncalibrated (red) dE/dx 60% truncated means, for each event in the stopping proton sample.

slightly better described. For low ionisations, below the lower limit of the calibration fit, the differences between true and reconstructed are still significant. This low energy excess may be migration of some events from the peak region. The overall effect of the correction can be seen in the fractional residual plot in Fig. 6.6 (bottom panel).

One can also check what happens if instead of applying the logarithmic calibration we simply scale the dQ/dx distribution (post reclustering) to have the same most probable value as the true dE/dx distribution. In this case, following an analogous procedure to the one described earlier, I found the scaling factor $S_{uncalibrated} = 0.414 \pm 0.002$ MeV/ADC⁵. The resulting distribution (red, labeled as uncalibrated) is also shown in Fig. 6.6 (top panel). The behaviour of the new distribution is similar to the corrected case at low energy losses, around the peak of the true distribution, but it is worse at describing the high energy tail. This is expected, it is in the high ionisation regime where saturation effects apply and therefore calibration is needed.

6.2.2 Truncated dE/dx mean

Once we have a collection of dE/dx values for each reconstructed track, we can compute the corresponding most probable ionisation loss per unit length of the particle. This

⁵Notice that now the scaling factor is not dimensionless, as it acts more like a conversion factor here.

6.2. dE/dx MEASUREMENT IN THE TPC

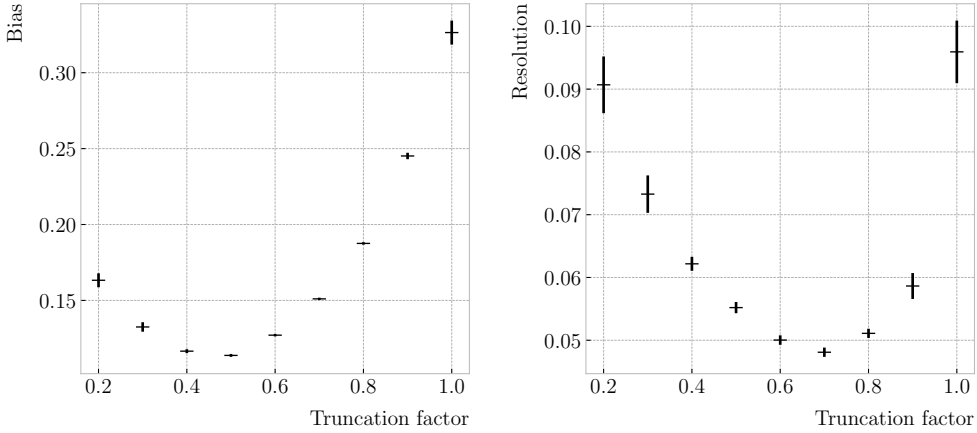


Figure 6.8: Estimated values of the mean dE/dx bias (left panel) and resolution (right panel) obtained using the corrected data from the stopping proton sample, for different values of the truncation factor.

2886 is the value predicted by the Bethe-Bloch or the PAI models, and together with a
2887 measurement of the momentum it allows for particle identification.

2888 However, estimating the most probable dE/dx value for each reconstructed track
2889 is not a trivial task. As mentioned before, the dE/dx distributions follow Landau-like
2890 distributions. Therefore, one should perform e.g. a LanGauss fit to correctly estimate
2891 the most probable values. Automating this kind of fits is often problematic, as they
2892 usually incur in convergence problems. Moreover, the reconstructed dE/dx distributions
2893 we obtain tend to have relatively small statistics, which may also produce poor fits. In
2894 practice, doing these unsupervised fits may degrade our performance, and a more robust
2895 method is preferred.

2896 A possibility could be taking the mean of the reconstructed dE/dx distribution for
2897 each particle. The problem with this approach is that the high energy Landau tail,
2898 combined with our limited statistics, can induce large fluctuations in the computation
2899 of the mean. Imagine you have two protons with the same kinetic energy, but due to
2900 reconstruction problems in one case you did not get as many charge deposits reconstructed
2901 in its high ionisation loss region. If you do not remove the tails the computed dE/dx
2902 means will be significantly different.

2903 In order to avoid those fluctuations, one can compute the mean of a truncated dE/dx

CHAPTER 6. PARTICLE ID IN GARSOFT

2904 distribution instead. By keeping only a given fraction of the lowest energy deposits
 2905 we obtain an estimate of the mean energy loss that is more resilient to reconstruction
 2906 inefficiencies and statistical effects. Figure 6.7 (left panel) shows a comparison between
 2907 the $\langle dE/dx \rangle$ computed by taking the mean of the full distribution (blue line) and the
 2908 60% lowest energy clusters (yellow line), for the stopping proton sample. The fractional
 2909 residuals are computed for each proton, taking the corresponding means using their
 2910 collections of true and reconstructed energy deposits. One can see that using the simple
 2911 mean translates into a high bias and uncertainty in the $\langle dE/dx \rangle$ estimation, whereas
 2912 applying the truncation reduces both significantly.

2913 Additionally, I performed a comparison between the 60% truncated mean dE/dx
 2914 obtained using the different calibration methods discussed earlier, namely the uncorrected
 2915 (blue), corrected (yellow) and uncalibrated (red) distributions. The results are shown
 2916 in Fig. 6.7 (right panel). While the widths of these distributions are similar, the bias
 2917 obtained for the corrected sample, i.e. calibration function and correction factor applied,
 2918 is a factor of ~ 2 lower than in the uncalibrated case and almost three times smaller
 2919 than for the uncorrected sample.

2920 The next step is to optimise the level of truncation we are going to apply to our
 2921 data. To do so, I used different truncation factors, i.e. the percentage of energy-ordered
 2922 reconstructed energy deposits we keep to compute the mean, on the corrected dE/dx
 2923 sample of the stopping protons. Then, following the same procedure of computing the
 2924 fractional residuals as before, I fitted the resulting histograms using a double Gaussian
 2925 function. This is simply the sum of two Gaussian functions of the type:

$$g(x; \mu, \sigma, A) = A e^{-\frac{(x-\mu)^2}{2\sigma^2}}. \quad (6.6)$$

2926 I do not add the classical normalisation factor of the Gaussian, $1/\sqrt{2\pi}\sigma$, therefore
 2927 the amplitude A simply represents the maximum of the function. One of the two
 2928 Gaussian functions describes the core part of the distribution, while the other captures
 2929 the behaviour of the tails.

6.2. dE/dx MEASUREMENT IN THE TPC

2930 For each truncation factor, I look at the bias and the resolution I obtain. I define
 2931 these as the weighted means of the corresponding parameters in the fits:

$$\bar{x} = \frac{A_{core} x_{core} + A_{tail} x_{tail}}{A_{core} + A_{tail}}, \quad (6.7)$$

2932 where A_{core} and A_{tail} are the amplitudes of the core and tail distributions respectively
 2933 and x is either the mean μ or the width σ of said distributions.

2934 Figure 6.8 shows the bias (left panel) and the resolution (right panel) I obtained
 2935 for the stopping proton sample, using different values of the truncation. From these, it
 2936 can be seen that a truncation factor of 50% minimises the bias in the estimation, while
 2937 70% gives the best resolution. That way, I settled on the intermediate value of 60%
 2938 truncation, which yields a $\langle dE/dx \rangle$ resolution of 5.00 ± 0.08 % for stopping protons.

2939 6.2.3 Mean dE/dx parametrisation

2940 Now that we have a way to estimate the mean energy loss of a particle in the HPgTPC,
 2941 we can determine the value of the free parameters in the ALEPH formula, Eq. (6.3).
 2942 For this, I used a sample of 10^5 reconstructed FHC neutrino events inside ND-GAr. In
 2943 this case I cannot use the stopping proton sample, as we need to cover the full kinematic
 2944 range of interest for the neutrino interactions in our detector.

2945 The original data does not contain an estimation of the velocity of the tracks, instead
 2946 the tracks have a value for the reconstructed momentum and the associated PDG code
 2947 of the Geant4-level particle that created the track. Therefore, one can select some of the
 2948 particles in the data, in this case I selected electrons, muons, pions and protons, and
 2949 compute β and γ using the reconstructed momentum and their mass. In terms of $\beta\gamma$
 2950 the mean dE/dx does not depend on the particle species, so one can consider all the
 2951 dataset as a whole. For this fit, I will express β in terms of the $\beta\gamma$ product as:

$$\beta = \frac{\beta\gamma}{\sqrt{1 + (\beta\gamma)^2}}, \quad (6.8)$$

CHAPTER 6. PARTICLE ID IN GARSOFT

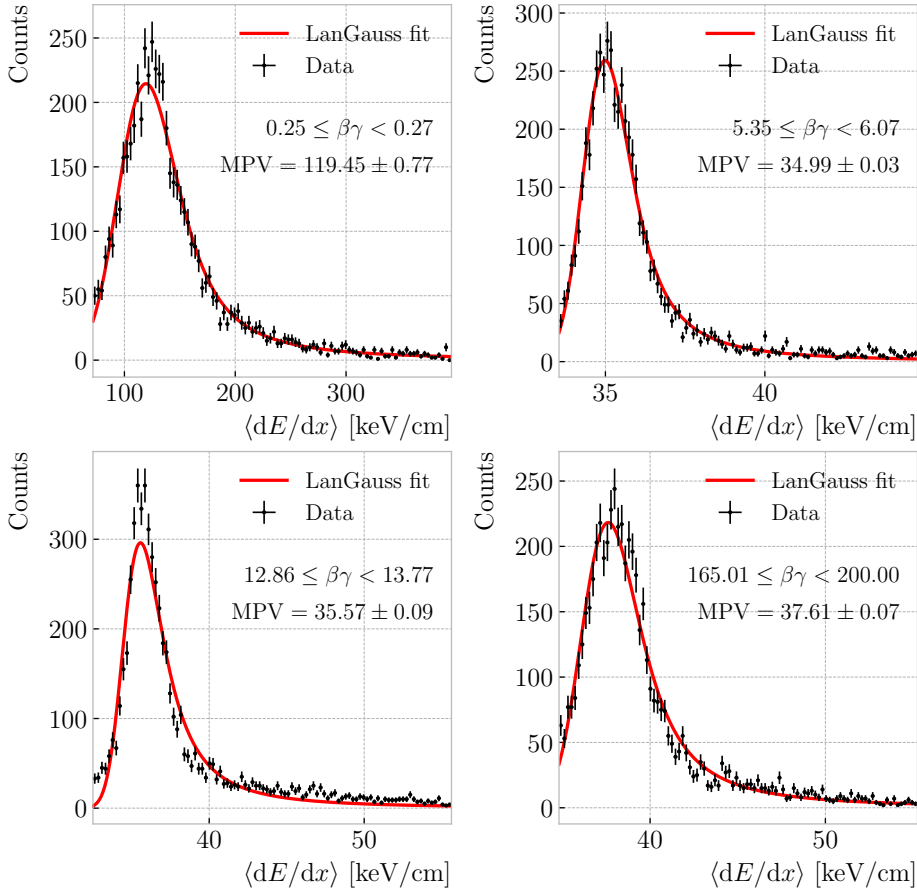


Figure 6.9: Examples of the truncated mean $\langle dE/dx \rangle$ LanGauss fits for various $\beta\gamma$ bins, from a simulated FHC neutrino sample.

2952 which can be easily proven from the definition of γ .

2953 Next, I bin the data in $\beta\gamma$. I chose a fine binning so as to capture the different
 2954 features of the ionisation curve. Instead of fixing the bin width, I select them so each one
 2955 has approximately the same statistics. Then, for each $\beta\gamma$ slice, I compute the median
 2956 and the interquartile range (IQR) of the $\langle dE/dx \rangle$ distribution. Using these, I make a
 2957 histogram in the range [median - IQR, median + 5 IQR], which I fit to a LanGauss
 2958 function in order to extract the MPV. Using this range accounts for the asymmetric
 2959 nature of the distributions, while also helps avoiding a second, lower maximum present
 2960 at low $\beta\gamma$, probably a result of reconstruction failures.

2961 A few examples of these fits are shown in Fig. 6.9. The chosen values of $\beta\gamma$ sit in
 2962 very distinct points along the $\langle dE/dx \rangle$ curve, going from the high ionisation region at

6.2. dE/dx MEASUREMENT IN THE TPC

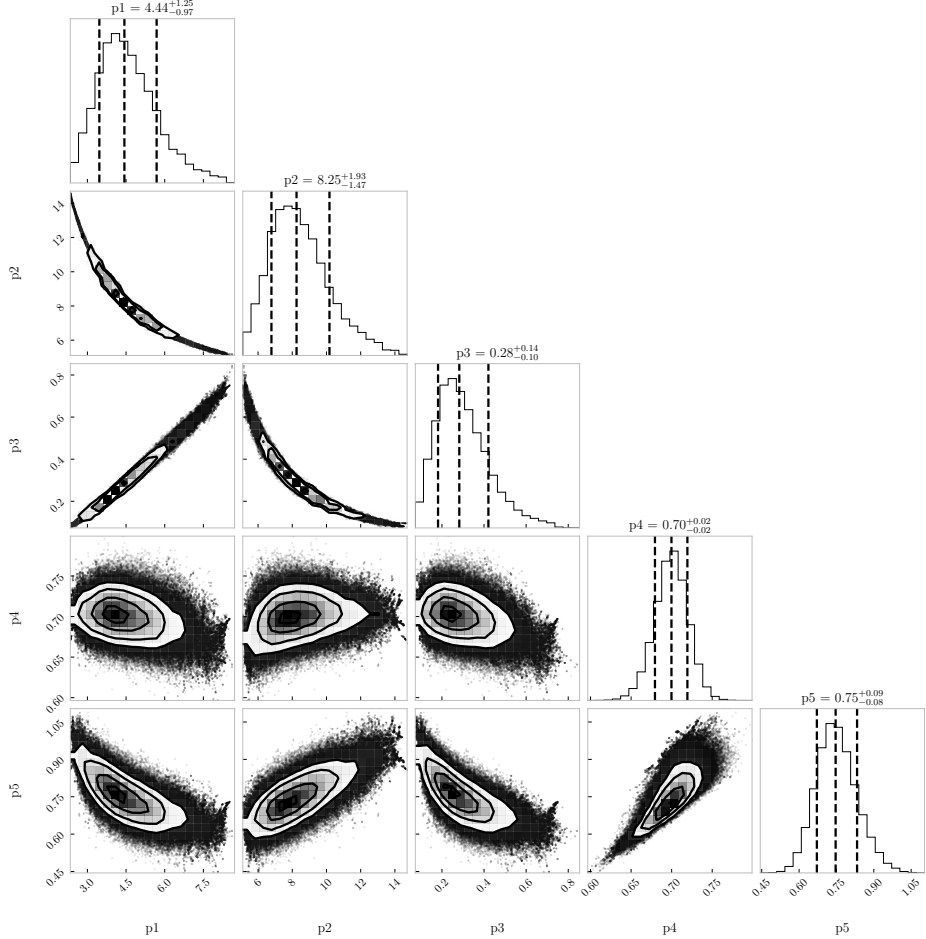


Figure 6.10: Resulting one and two dimensional projections of the posterior probability distributions of the ALEPH $\langle dE/dx \rangle$ parameters obtained by fitting the 60% truncated mean dE/dx values from a FHC neutrino sample in ND-GAr. The vertical dashed lines in the 1D distributions represent the 16th, 50th and 84th percentiles.

2963 low velocities (top left panel), to the minimum point (top right panel), the beginning of
 2964 the relativistic rise (bottom left panel), and the plateau produced by the density effect
 2965 (bottom right panel).

2966 I used the resulting most probable $\langle dE/dx \rangle$ values and the centres of the $\beta\gamma$ bins as
 2967 the points to fit to the ALEPH formula. For this particular fit I used the least-squares
 2968 method to get a first estimation of the ALEPH parameters. Applying some uniform
 2969 priors, I then used these values as the starting point of a 100000 steps MCMC. Figure 6.10
 2970 shows the posterior probability distributions I obtain for each parameter. The reported
 2971 best fit points are based on the 16th, 50th, and 84th percentiles in the marginalised

CHAPTER 6. PARTICLE ID IN GARSOFT

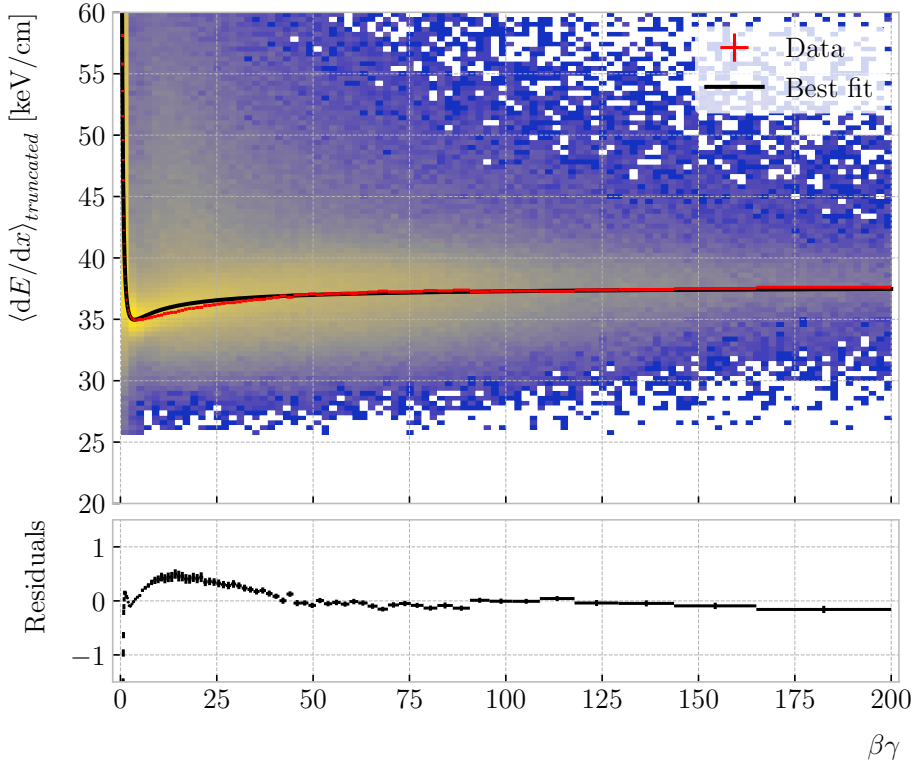


Figure 6.11: Truncated mean dE/dx obtained for the FHC neutrino sample as a function of the $\beta\gamma$ product (upper panel). Also shown are the fitted most probable values for each $\beta\gamma$ bin (red points) and the best fit obtained using the ALEPH parametrisation (black line). The residuals resulting from the fit are shown in the lower panel.

2972 distributions.

2973 The resulting fit (black line), compared to the data points (red points) and the
 2974 underlying distribution is shown in Fig. 6.11 (top panel). The overall fit is good, with a
 2975 reduced chi-squared of $\chi^2/ndf = 1.02$. However, there are some regions where the fit
 2976 does not describe the data correctly, like the very low $\beta\gamma$ regime, where the fit severely
 2977 underestimates for energy losses $\gtrsim 50$ keV/cm, and the start of the relativistic raise,
 2978 where we have a slight overestimation. This is a result of those points having a larger
 2979 uncertainty when compared to the ones around the dip or the plateau areas. These
 2980 differences can be better seen in the residual plot, Fig. 6.11 (bottom panel).

6.3. MUON AND PION SEPARATION IN THE ECAL AND MUID

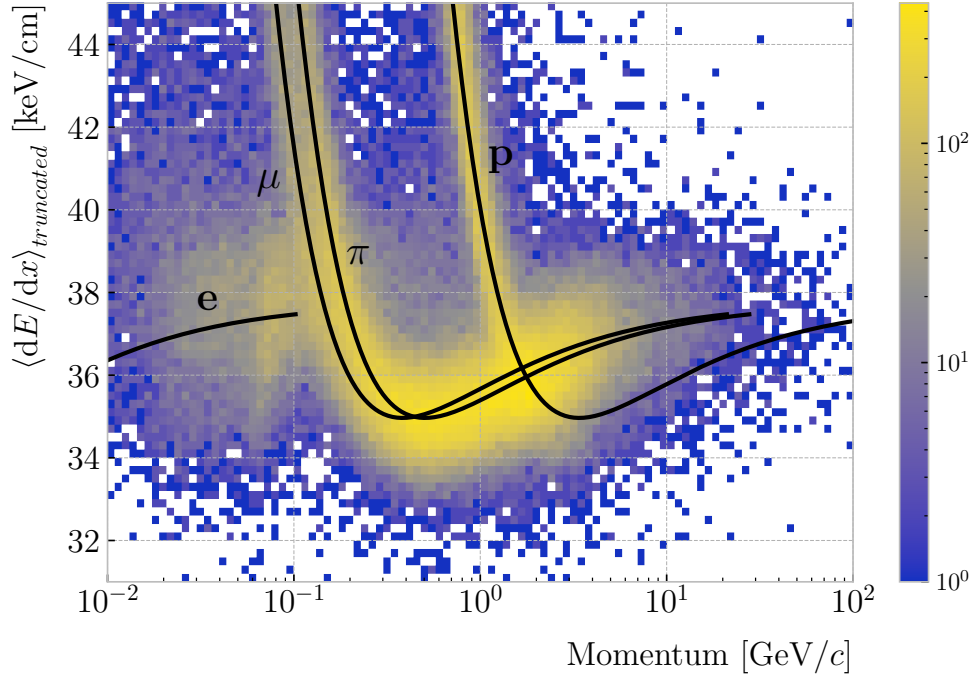


Figure 6.12: Distribution of the 60% truncated mean dE/dx versus reconstructed momentum for the FHC neutrino sample. The black lines indicate the predictions of the ALEPH parametrisation for electrons, muons, charged pions and protons.

2981 6.2.4 Particle identification

2982 6.3 Muon and pion separation in the ECal and MuID

2983 As it could be seen from Fig. 6.12, it is not possible to separate muons and charged pions
 2984 in the HPgTPC using dE/dx for momenta $\gtrsim 300$ MeV/ c . In ND-GAr, approximately
 2985 70% of the interactions in FHC mode will be ν_μ CC (compared to the 47% of $\bar{\nu}_\mu$ CC
 2986 interactions when operating in RHC mode), while 24% are neutral currents. Out of
 2987 these, around 53% and 47% of them will produce at least one charged pion in the final
 2988 state, respectively. Figure 6.14 shows a comparison between the spectra of the primary
 2989 muons and the charged pions for ν_μ CC interactions in ND-GAr producing one or more
 2990 charged pions. From this, one can see that (i) the majority of muons and charged pions
 2991 are not going to be distinguishable with a $\langle dE/dx \rangle$ measurement, and that (ii) particle
 2992 identification is necessary both to classify correctly the ν_μ CC events and identify the

CHAPTER 6. PARTICLE ID IN GARSOFT

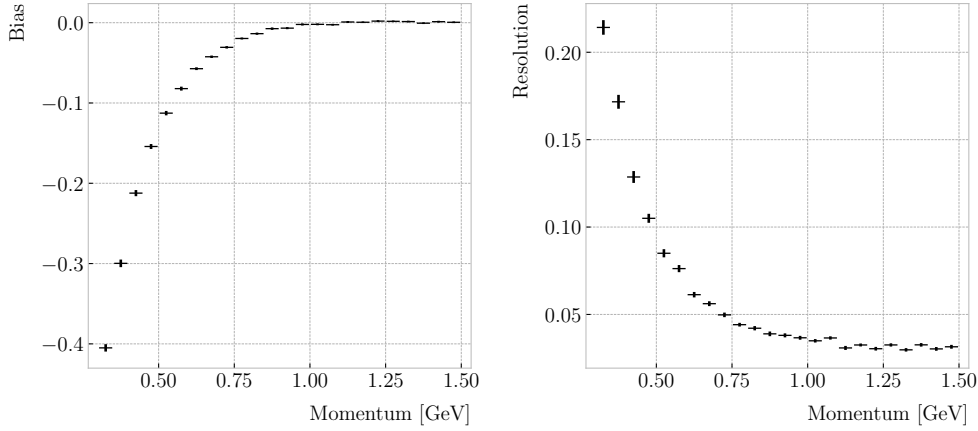


Figure 6.13: Estimated values of the mean dE/dx bias (left panel) and resolution (right panel) obtained for the true protons in a FHC neutrino sample.

2993 primary muon within them.

2994 ND-GAr features two other subdetectors which can provide additional information
 2995 for this task, namely the ECal and MuID. The current ECal design, described in (ref
 2996 section), consists of 42 layers, made of 5 mm of Pb, 7 mm of plastic scintillator and a
 2997 1 mm PCB board. The total thickness of this calorimeter is 1.66 nuclear interaction
 2998 lengths or 1.39 pion interaction lengths. The MuID design is in a more conceptual
 2999 stage, however it is envisioned to feature layers with 10 cm of Fe and 2 cm of plastic
 3000 scintillator⁶. With its three layers, it will have a thickness of 1.87 or 1.53 nuclear or pion
 3001 interaction lengths, respectively.

3002 Because pion showers are dominated by inelastic nuclear interactions, the signatures
 3003 of these particles in the calorimeter will look significantly different from those of muons.
 3004 Although our ECal is not thick enough to fully contain the hadronic showers of the
 3005 charged pions at their typical energies in FHC neutrino interactions, they can still be
 3006 used to understand whether the original particle was more hadron-like or MIP-like. In
 3007 Fig. 6.15 I show two examples of energy distributions created by a muon (left panel)
 3008 and a charged pion (right panel) of similar momenta interacting in the ECal. These
 3009 figures represent the transverse development of the interactions. For each of them, I

⁶It is not mentioned anywhere, but I assume that there should also be another layer of PCB board of 1 mm. However, in this case its contribution to the total thickness of the sampling calorimeter would be negligible.

6.3. MUON AND PION SEPARATION IN THE ECAL AND MUID

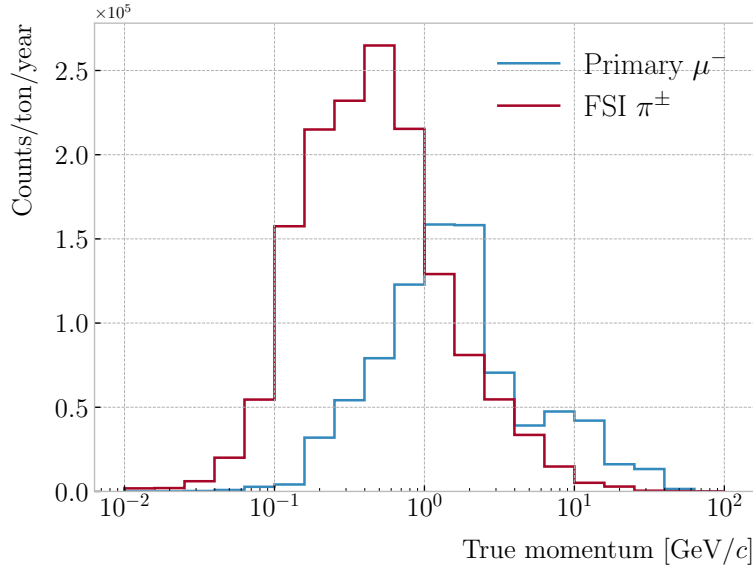


Figure 6.14: True momentum distribution for the primary muon in ν_μ CC $N\pi^\pm$ interactions inside the fiducial volume of ND-GAr (blue line), compared to the post FSI charged pion spectrum (red line).

3010 computed the principal component and centre of mass of the interaction, projecting
 3011 the position of the hits onto the plane perpendicular to that direction, and taking the
 3012 distances relative to the centre. It can be seen that the muon follows an almost MIP-like
 3013 behaviour, being the central bin in the histogram the one with the highest deposited
 3014 energy. On the other hand, the pion not only deposits more energy overall, but also this
 3015 energy is more spread-out among the different hits. It is this kind of information that
 3016 would allow us to tell apart muons from pions.

3017 This way, I identify three main action points that need to be addressed if one wants
 3018 to use these detectors to distinguish between muons and charged pions. These are:

- 3019 1. the way we make the associations between tracks in the HPgTPC to the activities
 3020 (what in GArSoft we call clusters) in the ECal and the MuID,
- 3021 2. what variables or features one can extract from the calorimeters that encapsulate
 3022 the information we are interested about,
- 3023 3. and how to carry out the classification problem.

CHAPTER 6. PARTICLE ID IN GArSOFT

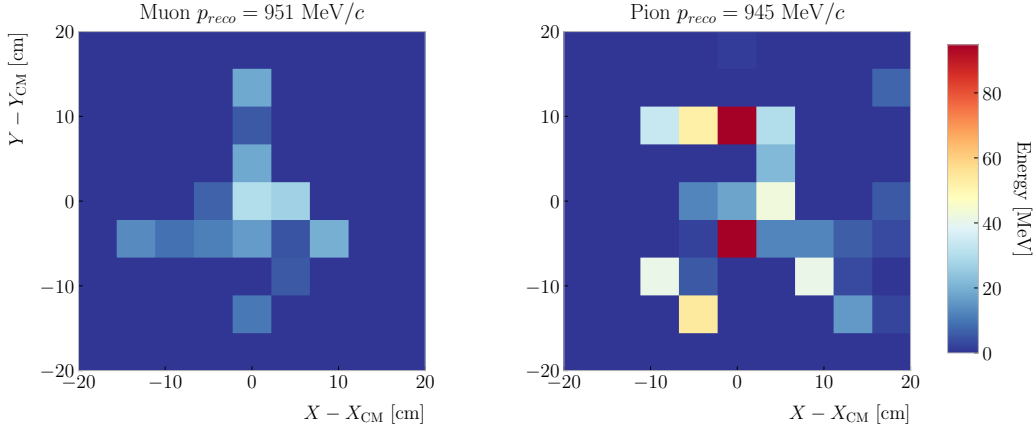


Figure 6.15: Distributions of energy deposits in the ECal for a muon (left panel) and a charged pion (right panel) with similar momenta. The energy is projected onto the plane perpendicular to the principal component of the hits, and the positions are relative to the center of the interaction.

6.3.1 Track-ECal matching

One of the main players in the muon and pion separation is the way we associate clusters in the ECal to reconstructed tracks in the TPC. Missing some associations or making wrong ones can bias the ECal quantities that we can use for classifying particles. The current algorithm in GArSoft provides precise associations, i.e. most of the associations that it produces are correct, but it appears to miss an important number of associations (at least when using the default configuration).

The current TPC track-ECal cluster association algorithm is divided in four parts. It first checks whether the track end point fulfils certain conditions to be extrapolated. There are two cut values in this step, one for the drift direction and other radial.

If the point can be extrapolated, the code computes the coordinates of the centre of curvature using the Kalman fit estimates at the track end ($y, z, 1/R, \phi, \tan\lambda$). It then compares the distance between this and the cluster in the (z, y) plane with R . This introduces another cut in the perpendicular direction.

The next step is different for clusters in the barrel or in one of the end caps. If it is a barrel cluster the algorithm extrapolates the track up to the radial distance of the cluster. There are three possible outcomes, the extrapolated helix can cut the cylinder

6.3. MUON AND PION SEPARATION IN THE ECAL AND MUID

3041 of radius r_{clus} two, one or zero times. I get the cut point that is closer to the cluster and
3042 check that it is either in the barrel or the end caps. Computing the difference between
3043 the x coordinates of the cluster and the extrapolated point, the module checks that this
3044 is not greater than a certain cut. If the cluster is in an end cap, I propagate the track
3045 up to the x position of the cluster. Then, the algorithm computes the angle in the (z, y)
3046 plane between the centre of curvature and the cluster, α , and the centre of curvature
3047 and the propagated point, α' . A cut is applied to the quantity $(\alpha - \alpha')R$.

3048 If the cluster contains more than a certain number N of hits, I apply an extra cut to
3049 the dot product of the direction of the track at the propagated x value and the cluster
3050 direction.

3051 The code makes sure to only associate one end of the track (if any) to a cluster.
3052 However, it can associate more than one track to the same cluster. This makes sense,
3053 as different particles can contribute to the same cluster in the ECal, but it makes it
3054 difficult to quantify the relative contributions of the tracks to a certain cluster.

3055 As a way of comparing the performance of this algorithm, a new, simpler association
3056 module was written. The goal was to have a simple and robust algorithm, which depends
3057 on as few parameters as possible and that can produce a one-to-one matching between
3058 tracks and ECal clusters.

3059 For each reconstructed track, the new algorithms applies the same procedure to the
3060 forward and the backward fits irrespective of their end point positions. It first gets the
3061 Kalman fit parameters at the corresponding end point together with the X position, x_0 ,
3062 ($y_0, z_0, 1/R, \phi_0, \tan\lambda$).

3063 For each ECal cluster, I compute the radial distance to the centre of the TPC and
3064 find the ϕ value in the range $[\phi_0, \phi_0 + \text{sign}(R)\phi_{max}]$ that makes the propagated helix
3065 intersect with the circle defined with such radius. The (x, y, z) position of the helix for
3066 the ϕ value found (if any) is then computed. In case there are two intersections, I keep
3067 the one that minimises the distance between (y, z) and (y_c, z_c) .

3068 I then calculate χ^2 value based on the Euclidean distance between the propagated

CHAPTER 6. PARTICLE ID IN GARSOFT

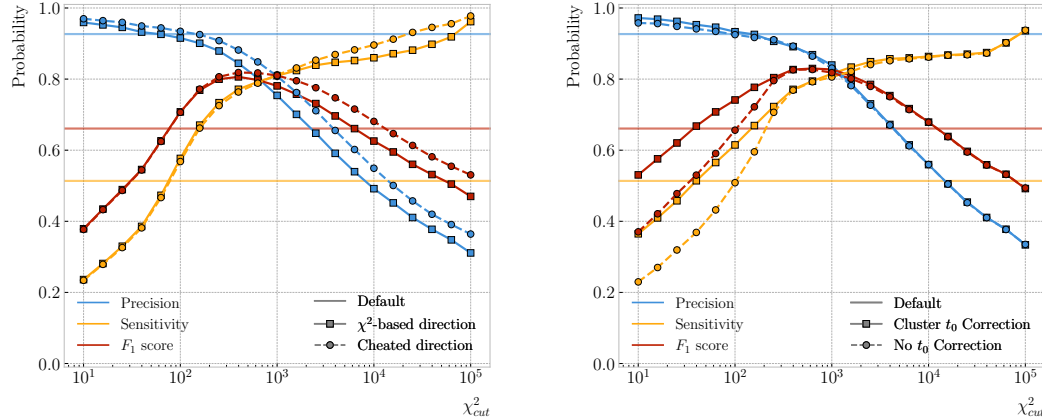


Figure 6.16: Left panel: comparison between the precision (blue), sensitivity (yellow) and F_1 score (red) obtained for the default (horizontal lines) and new algorithms, both with the χ^2 -based direction estimator (squares) and cheating the directions (circles), for different values of the χ^2 cut. Right panel: comparison of the performance of the new algorithm when applying the cluster t_0 correction (squares) and when (circles).

3069 point and the cluster:

$$\chi^2/ndf = \frac{\sum_{n=0}^2 (x^{(n)} - x_c^{(n)})^2}{3}. \quad (6.9)$$

3070 If there was no intersection I store a -1 instead. In the end, for each reconstructed track
3071 in the event one ends up with two collections of χ^2 values, one for each ECal cluster
3072 and fit directions.

3073 The current code only supports having ECal clusters associated to one end of each
3074 track. We have two options to decide what track end to keep. The first one tries to
3075 cheat the selection, looking at the distance between the two track ends and the true
3076 start position of the associated MC particle. The second one keeps the track end with
3077 more χ^2 entries below the cut.

3078 This feature of only considering one track end limits the algorithm, making it not
3079 suitable for reconstructing events with particles originating outside the TPC. However,
3080 as for the moment the main concern of the group is the study of neutrino interactions
3081 off the gaseous argon, this is an acceptable assumption.

3082 In order to associate a cluster to a track, I take all clusters with a χ^2 value in the
3083 range $[0, \chi^2_{cut}]$. If a cluster has been assigned to more than one track we leave it with

6.3. MUON AND PION SEPARATION IN THE ECAL AND MUID

3084 the one with the lowest χ^2 .

3085 This default behaviour of the algorithm can be modified to associate more than one
3086 track to each cluster. Not only that, but the χ^2 values can be used to assign relative
3087 weights to the different contributions.

3088 To evaluate the performance of the association method, I use a binary classification
3089 approach. In this case, I check the leading MC Track IDs associated to the reconstructed
3090 tracks and ECal clusters. I count an association as true positive (TP) if both Track
3091 IDs coincide. An association is considered false positive (FP) when the Track IDs are
3092 different. If a cluster has not been associated to any track but it shares the Track ID
3093 with a reconstructed track it is counted as a false negative (FN).

3094 For the testing, I used a sample of 10000 FHC neutrino events inside the HPgTPC.
3095 Figure 6.16 (left panel) shows the precision (blue line), sensitivity (yellow line), and F_1
3096 score (red line) I obtained for different values of χ_{cut}^2 . For comparison, the same metrics
3097 computed for the default algorithm with the current configuration are also shown (dashed
3098 lines). In the case of the new algorithm, I used both the χ^2 -based method to estimate
3099 the track direction described earlier (square markers) and the cheated direction from the
3100 Geant-level information (circle markers). For either of these we achieve similar values of
3101 the precision compared to the old code, while having a considerably higher sensitivity.
3102 It can be seen that cheating the direction of the tracks only makes a difference at high
3103 χ_{cut}^2 , past the optimal value of the cut around the F_1 score maximum. Therefore, I set
3104 the χ^2 method as the default.

3105 One of the possible weak points of this approach is that it relies on the position along
3106 the drift direction to make the decisions. Within the current ND-GAr design implemented
3107 in GArSoft, the timing information is provided by the ECal. That effectively means
3108 that prior to make the track-ECal associations the reconstructed x positions of the track
3109 trajectories differ from the simulated ones by an amount:

$$x_{reco}^{(n)} - x_{sim}^{(n)} = v_{drift} t_0, \quad (6.10)$$

CHAPTER 6. PARTICLE ID IN GArSOFT

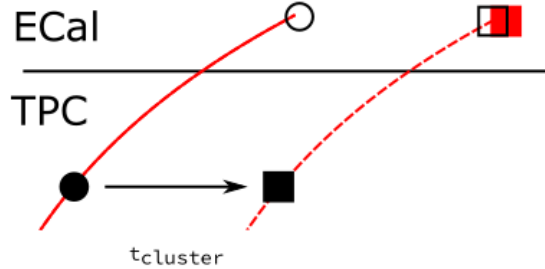


Figure 6.17: Schematics of a possible option to deal with track-ECal associations in non-zero t_0 neutrino interaction events, trying to correct for the drift direction uncertainty in a cluster-by-cluster basis using the cluster time, $t_{cluster}$.

3110 where v_{drift} is the mean drift velocity in our medium and the initial time is in the range
 3111 $t_0 \in [0, t_{spill}]$ where t_{spill} is the spill length. For a $10 \mu\text{s}$ spill this translates into a
 3112 maximum 30 cm uncertainty on the drift direction position.

3113 The current default in GArSoft sets $t_0 = 0$, but the functionality to randomly sample
 3114 this within the spill time is in place. Therefore, we need to understand what is the impact
 3115 of a non-zero t_0 on the associations algorithm and foresee possible ways of minimising a
 3116 loss in performance.

3117 Figure 6.17 represents a possible option to tackle the association problem when
 3118 having events with a non-zero initial time t_0 . The black and white circles represent the
 3119 original points, whereas the squares indicate the corrected positions. The end points of
 3120 the track and the propagated points up to the cluster radius are indicated using filled
 3121 and unfilled markers respectively. The red square represents the position of the cluster.

3122 Here I try to correct for the drift coordinate position using the time associated to the
 3123 cluster. Assuming that the drift time is much larger than the propagation time, $t_{cluster}$
 3124 could be used as a good estimation of the t_0 . An alternative can be using the earliest
 3125 time associated to a hit in said cluster. Doing this for each cluster before computing
 3126 the χ^2 value could be used as an alternative to knowing the specific value of the t_0 , as
 3127 when the association is correct this will provide the right correction but its impact is
 3128 small enough to not change the position significantly in the case the cluster does not
 3129 correspond to a given track.

6.3. MUON AND PION SEPARATION IN THE ECAL AND MUID

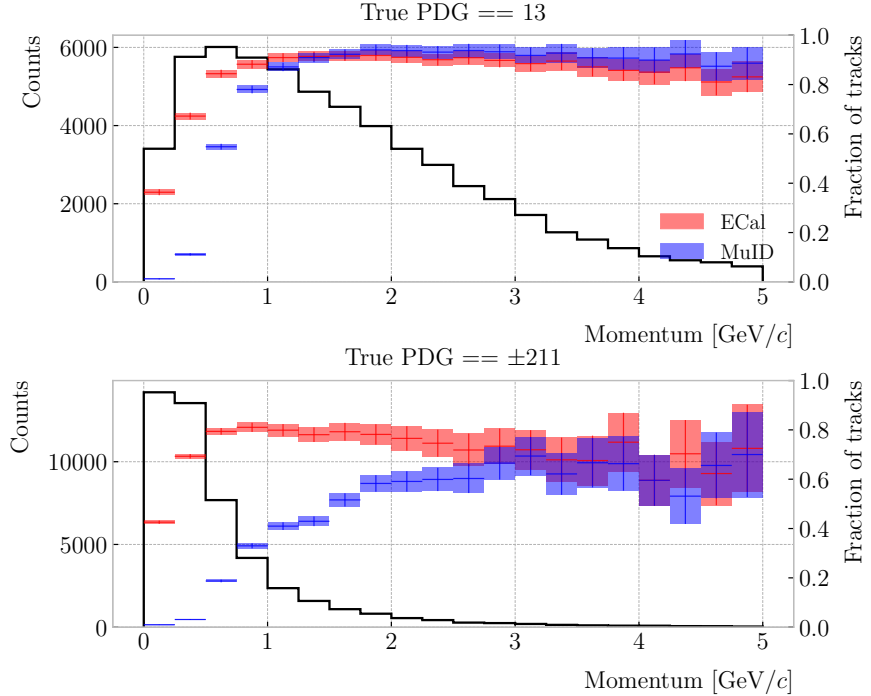


Figure 6.18: Momentum distribution for the reconstructed muons (top panel) and charged pions (bottom panel) in a FHC neutrino sample, together with the fraction of them reaching the ECal (red) and MuID (blue). Each entry corresponds to a reconstructed track, backtracked to a true muon or pion which has not produced any other reconstructed track.

3130 I tested the effect of this correction again using a sample of 10000 FHC neutrino
 3131 events. Figure 6.16 (right panel) shows the precision (blue line), sensitivity (yellow line),
 3132 and F_1 score (red line) for the case the cluster t_0 correction is applied (square markers)
 3133 and for the no correction case (circle markers), as a function of χ^2_{cut} . In this case, the
 3134 differences are particularly notorious at low values of the cut. It makes sense, as the t_0
 3135 effect becomes subdominant when the distance we consider grows large. Overall, the
 3136 correction increases the sensitivity while keeping the precision almost unchanged. As a
 3137 result, I apply the t_0 correction to the generated samples as the default.

3138 **6.3.2 Classification strategy**

3139 The problem of the muon and charged pion separation has to be viewed in the broader
 3140 context of the particle identification in our detector. Focusing on the beam neutrino

CHAPTER 6. PARTICLE ID IN GARSOFT

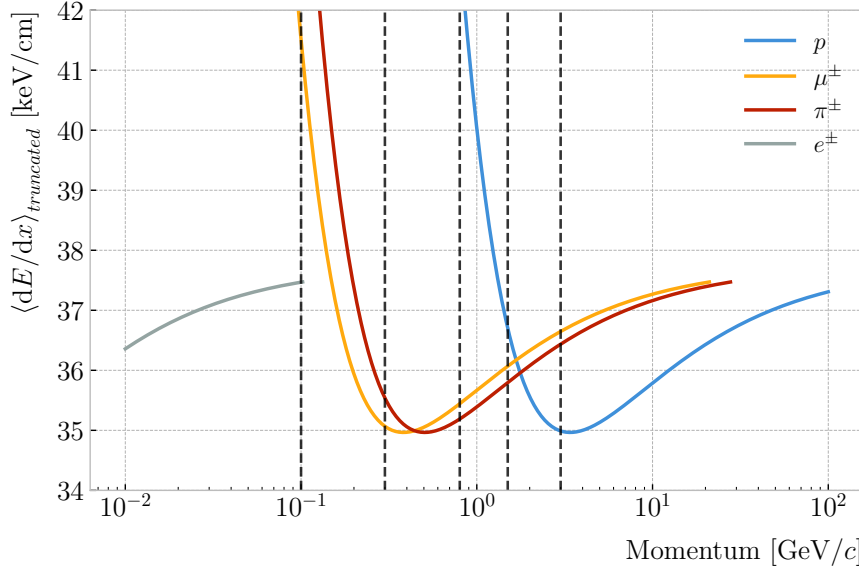


Figure 6.19: Predicted truncated mean dE/dx versus momentum, for electrons, muons, charged pions and protons, obtained using the ALEPH parametrisation. The vertical dashed lines represent the boundaries of the six regions used for the muon and pion classification training.

3141 interactions, it is clear that we are going to have muons and pions spanning a broad
 3142 momentum range. Not only that, but we will also have other particles with similar
 3143 characteristics that will make the classification even more challenging. Therefore, we are
 3144 presented with a task that will depend heavily on the kinematic range we are looking at
 3145 each time, as both the available information and the possible impurities of other particle
 3146 species vary.

3147 For instance, distinguishing muons from pions could be difficult at low momenta, as
 3148 a great number of them do not reach the ECal. Therefore, we could think of tailoring a
 3149 version of the classification for that particular case, which could be complemented with
 3150 a dE/dx measurement. Likewise, for momenta $\gtrsim 1$ GeV muons and pions reach the
 3151 calorimeters efficiently, but so do protons. Because of this, one can try to train another
 3152 classifier for this energy range, and rely on other methods to remove as many of the
 3153 protons as possible.

3154 Figure 6.18 shows the momentum distribution of the reconstructed muons (top) and
 3155 pions (bottom) in a FHC sample. It also contains the fraction of particles reaching the

6.3. MUON AND PION SEPARATION IN THE ECAL AND MUID

Table 6.2: Momentum ranges and description of the PID approach assumed for the muon and pion classification task.

Momentum range	Description
$< 0.1 \text{ GeV}/c$	All tracks can be separated with dE/dx
$[0.1, 0.3) \text{ GeV}/c$	Use ECal for reaching muons and pions, dE/dx for the rest
$[0.3, 0.8) \text{ GeV}/c$	Use ECal for muons and pions, dE/dx for protons
$[0.8, 1.5) \text{ GeV}/c$	Use ECal and MuID for muons and pions, dE/dx for protons
$[1.5, 3.0) \text{ GeV}/c$	Use ECal and MuID for muons and pions, ToF for protons
$\geq 3.0 \text{ GeV}/c$	Use ECal and MuID for muons and pions, dE/dx and ToF for protons

3156 ECal (red) and MuID (blue), for the different momentum bins. In Fig. 6.19 I show the
 3157 mean dE/dx of different particles as a function of the momentum, computed using the
 3158 ALEPH parametrisation with the best fit parameters found in Subsec. 6.2.2.

3159 Using these two figures as references, I decided to approach the classification by
 3160 dividing the problem into six different momentum regions. A summary of these can be
 3161 found in Tab. 6.2. The basic idea is to exploit all the information that is available in
 3162 each region and . For the problem at hand, I prepared separated samples of isotropic
 3163 single muons and pions, with momenta uniformly distributed along the corresponding
 3164 momentum range. Each sample contains 50000 events of the corresponding particle
 3165 species. I did not generate samples for the first region, as it is assumed that the separation
 3166 can be achieved using dE/dx only. For the last region, I generated particles up to a
 3167 momentum of 10 GeV/c , as that is well above the typical energies of muons and pions
 3168 from FHC neutrino interactions in ND-GAr.

3169 Additionally, I prepared another sample of 100000 FHC neutrino events. For each
 3170 interaction, I select the reconstructed particles which were backtracked to true muons or
 3171 charged pions. I use this dataset to perform validation checks, to see how the models
 3172 trained with the single particle data generalise to a more realistic scenario.

3173 To tackle this classification problem, I make use of Boosted Decision Trees (BDT). A
 3174 decision tree uses a flowchart-like structure to make decisions based on some input data.
 3175 It starts from a root node, which represents the complete dataset, and then it splits

CHAPTER 6. PARTICLE ID IN GARSOFT

3176 this based on the variable or feature which gives the best separation between classes,
3177 creating two new nodes. The process repeats for each node until it reaches a certain
3178 limit, like a maximum number of splits or some tolerance criteria. The last set of nodes
3179 are often called leave nodes, and represent the final prediction of the classifier.

3180 Boosting refers to a family of methods to combine the predictions from multiple
3181 classifiers, following a sequential approach where each new model learns from the errors
3182 of the previous one. The process starts with a simple decision tree, which is used to
3183 make predictions on the training data. Then, the data points misclassified by the first
3184 model are assigned higher weights, and another decision tree is trained on the data with
3185 adjusted weights. The predictions of the two trees are then combined, and the cycle
3186 repeats for a predefined number of iterations. Gradient boosting uses the direction of
3187 the steepest error descent to guide the learning process and improve the accuracy with
3188 each iteration.

3189 6.3.3 Feature selection and importance

3190 Using the reconstructed tracks as a starting point, I compute a number of ECal and
3191 MuID variables for each of them. As there can be more than one cluster associated to a
3192 track, what I do is collect all associated clusters and compute these variables from the
3193 complete collection of associated hits. For the MuID, because it only features three layers
3194 and typically there will be less hits, I also allow single hits to be associated with tracks⁷.
3195 I can roughly divide the variables in three types: energy-related, geometry-related and
3196 statistical. In the following, I briefly describe the variables related exclusively to the
3197 ECal:

3198 • Energy-related ECal

3199 – ECal total energy (ClusterTotalEnergy): sum of the energy of all the ECal
3200 hits.

⁷At the reconstruction level what happens is that non-clustered hits are put into single hit clusters, instead of being thrown away. This is necessary to keep the consistency of the track-cluster association code.

6.3. MUON AND PION SEPARATION IN THE ECAL AND MUID

- 3201 – Mean ECal hit energy (HitMeanEnergy): mean of the hit energy distribution.
- 3202 – Standard deviation ECal hit energy (HitStdEnergy): standard deviation of
- 3203 the hit energy distribution.
- 3204 – Maximum ECal hit energy (HitMaxEnergy): maximum of the hit energy
- 3205 distribution.

3206 • Geometry-related ECal

- 3207 – Mean distance hit-to-cluster (DistHitClusterMean): mean of the distance
- 3208 distribution between the hits and the corresponding cluster's main axis.
- 3209 – RMS distance hit-to-cluster (DistHitClusterRMS): root mean square of the
- 3210 distance distribution between the hits and the corresponding cluster's main
- 3211 axis.
- 3212 – Maximum distance hit-to-centre (DistHitCenterMax): maximum of the
- 3213 distance distribution between the hits and the centre of the TPC.
- 3214 – Time-of-Flight velocity (TOFVelocity): slope obtained when fitting a straight
- 3215 line to the hit time versus hit distance to the centre (i.e. $d = v \times t$).

3216 • Energy and geometry ECal

- 3217 – Radius 90% energy (Radius90E): distance in the hit-to-cluster distribution
- 3218 for which 90% of the total energy is contained in the hits that are closer to
- 3219 the axis (i.e. radius that contains 90% of the energy).

3220 • Statistical ECal

- 3221 – Number of hits (NHits): total number of hits associated to the track.
- 3222 – Number of layers with hits (NLayers): not really a count of all layers with
- 3223 hits but the difference between the last and the first layer with hits.

3224 Figure 6.20 shows the distributions of three different ECal variables, separating true
3225 muons (blue) and charged pions (red), for the five momentum ranges considered. I chose

CHAPTER 6. PARTICLE ID IN GArSOFT

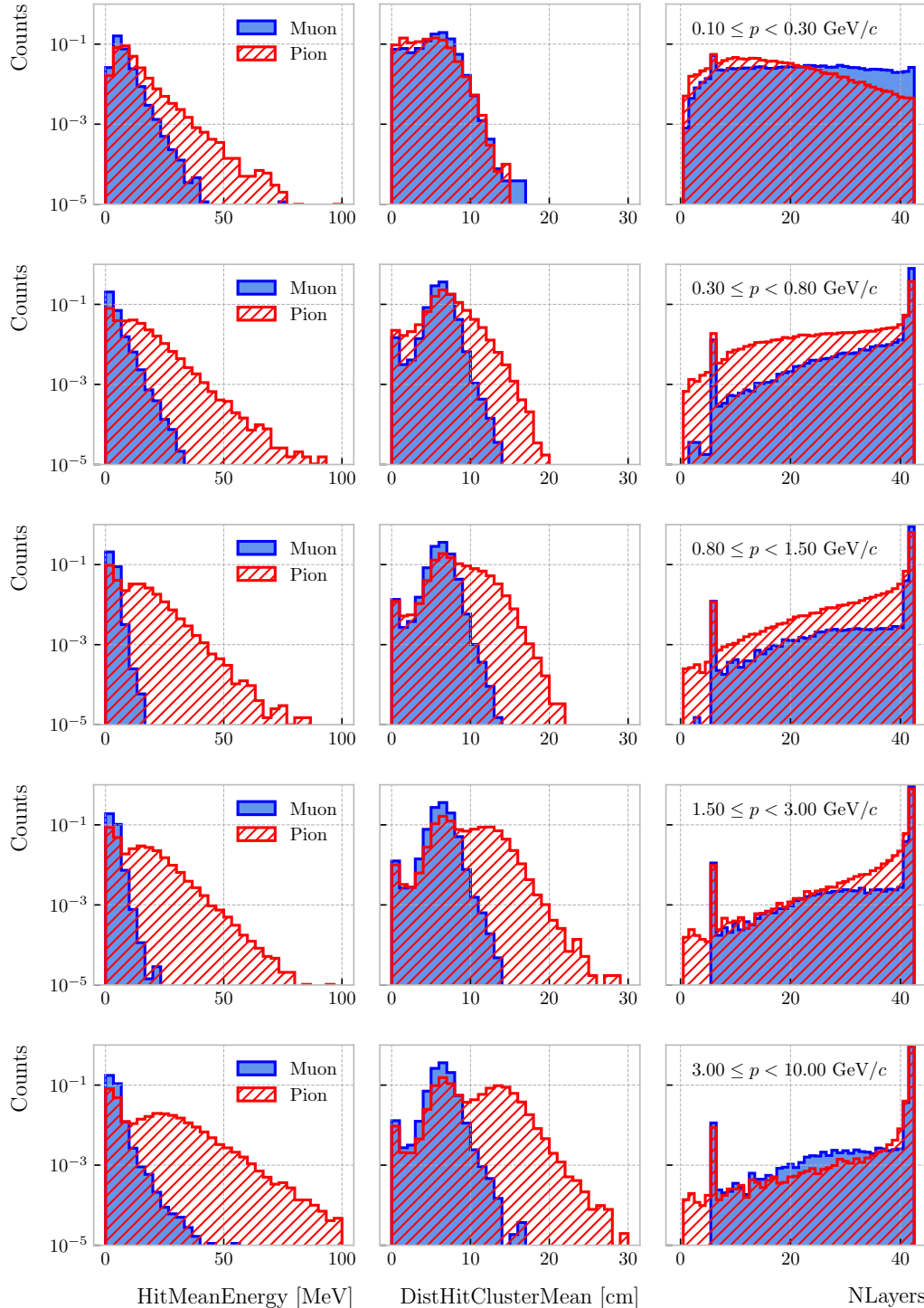


Figure 6.20: Example ECal feature distributions for muons (blue) and charged pions (red) in the five different momentum ranges considered (from top to bottom, in ascending momentum order). From left to right: mean hit energy, mean distance hit-to-cluster, and number of layers with hits.

6.3. MUON AND PION SEPARATION IN THE ECAL AND MUID

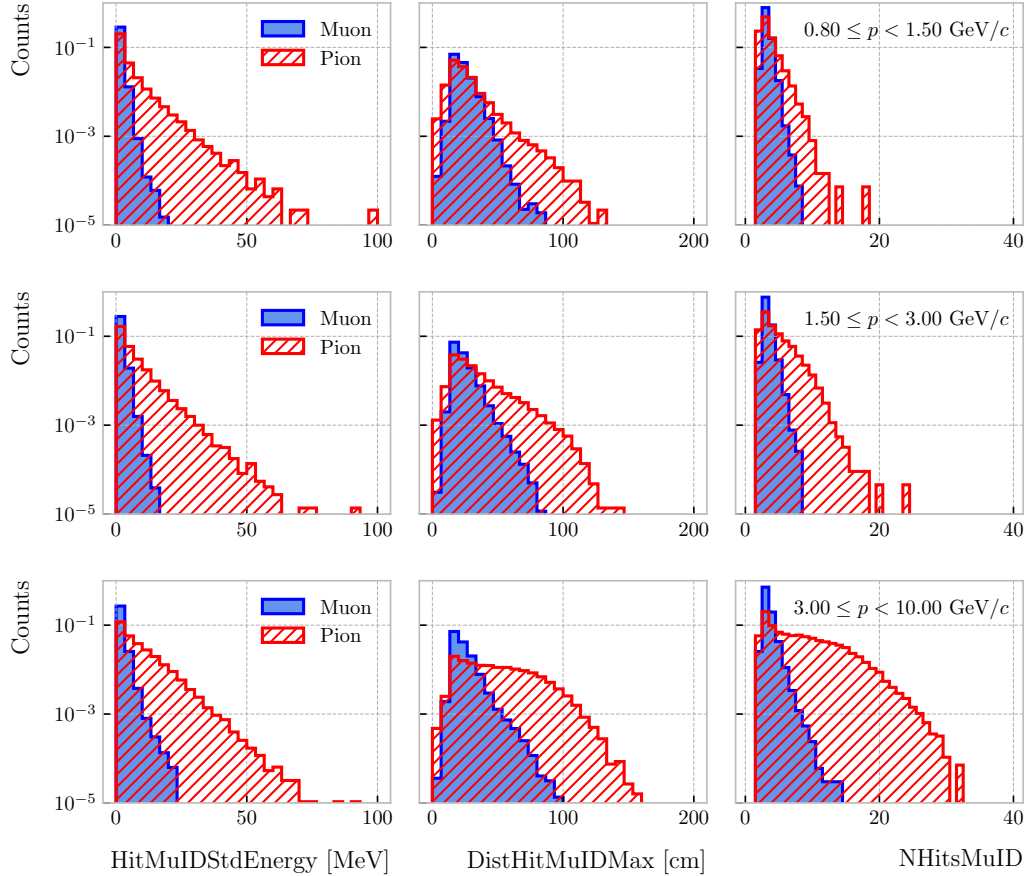


Figure 6.21: Example MuID feature distributions for muons (blue) and charged pions (red) in the three different momentum ranges considered (from top to bottom, in ascending momentum order). From left to right: standard deviation hit energy, maximum distance hit-to-hit, and number of hits.

3226 to show one feature from each category, namely the mean energy per hit (left column),
 3227 the mean distance between the hits and the centre of the cluster (middle column), and
 3228 the number of ECal layers with hits (right column). These give an idea of the separating
 3229 power of the different features, and how it changes considerably with the energy. In
 3230 the number of layers with hits distributions, the peak at 6 is due to the fact that the
 3231 first six ECal layers sit inside the pressure vessel⁸. Therefore, some of the particles get
 3232 stopped crossing it, never making it to the seventh layer.

3233 In the case of the MuID, because at low momenta a significant fraction of the particles

⁸Note to self: check this. I thought the ECal barrel had 8 layers of tiles, and that all of them were inside the pressure vessel.

CHAPTER 6. PARTICLE ID IN GARSOFT

3234 do not make it past the ECal, I only consider the information coming from this detector
3235 for momenta $\geq 0.8 \text{ GeV}/c$, i.e. for the last three momentum regions. The variables I
3236 extract from it are the following:

3237 • **Energy-related MuID**

- 3238 – MuID total energy (ClusterMuIDTotalEnergy): sum of the energy of all the
3239 MuID hits.
- 3240 – Mean MuID hit energy (HitMuIDMeanEnergy): mean of the MuID hit energy
3241 distribution.
- 3242 – Standard deviation MuID hit energy (HitMuIDStdEnergy): standard deviation
3243 of the MuID hit energy distribution.
- 3244 – Maximum MuID hit energy (HitMuIDMaxEnergy): maximum of the MuID
3245 hit energy distribution.

3246 • **Geometry-related MuID**

- 3247 – Maximum distance MuID hit-to-hit (DistHitMuIDMax): maximum distance
3248 between pairs of MuID hits (not sure this is a good variable, distribution
3249 looks nuts).
- 3250 – Maximum distance MuID hit-to-centre (DistHitCenterMuIDMax): maximum
3251 of the distance distribution between the MuID hits and the centre of the
3252 TPC.

3253 • **Statistical MuID**

- 3254 – Number of hits (NHitsMuID): total number of MuID hits associated to the
3255 track.
- 3256 – Number of layers with hits (NLayersMuID): not really a count of all layers
3257 with MuID hits but the difference between the last and the first layer with
3258 MuIDhits.

6.3. MUON AND PION SEPARATION IN THE ECAL AND MUID

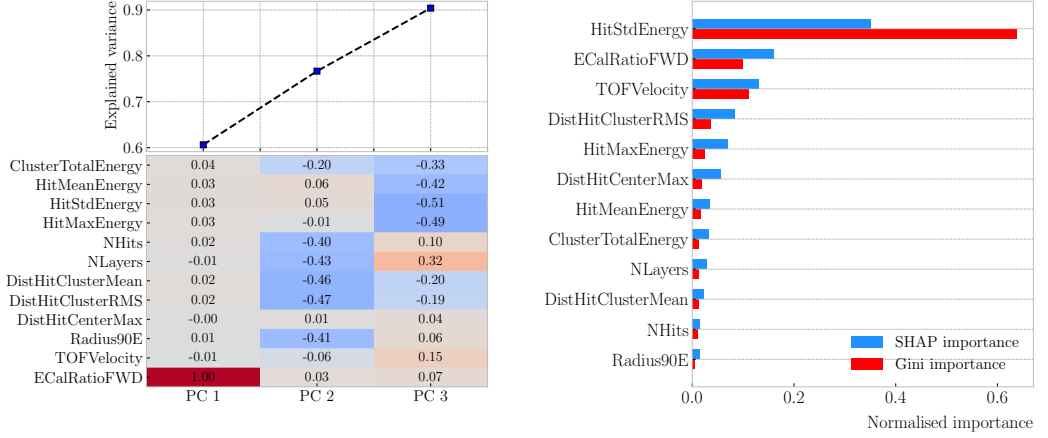


Figure 6.22: Left panel: cumulative explained variance for the first three principal components (top panel) and contribution of the different features to the principal axes in feature space (bottom panel). Right panel: Shapley (blue) and Gini (red) feature importances for the different input features. Both figures correspond to the samples in the momentum range $0.3 \leq p < 0.8$ GeV/c.

3259 Figure 6.21 shows the distributions of three different MuID variables, separating true
 3260 muons (blue) and charged pions (red), for the three momentum ranges which use the
 3261 muon tagger information. In this case I decided to standard deviation of the MuID hit
 3262 energy distribution (left column), the maximum distance between the MuID hit pairs
 3263 (middle column), and the number of MuID hits (right column). These variables are used
 3264 together with the ECal features at high momenta, providing additional disambiguation
 3265 power.

3266 Once our features have been defined, one can do some exploratory analysis to
 3267 understand how well the variables describe the target class, and avoid the black-box
 3268 approach by what features are most relevant for the learning process. This way, I
 3269 performed a feature analysis for each of the momentum ranges I divided this classification
 3270 problem into. It follows three steps: first a principal component analysis (PCA), followed
 3271 by a feature importance study using Gini and Shapley values, and finally a feature
 3272 permutation importance analysis.

3273 The PCA is useful to understand the variance of the feature space. It is an
 3274 unsupervised machine learning technique that allows the user to perform a dimensionality
 3275 reduction. It uses a singular value decomposition of the input features to project them

CHAPTER 6. PARTICLE ID IN GARSOFT

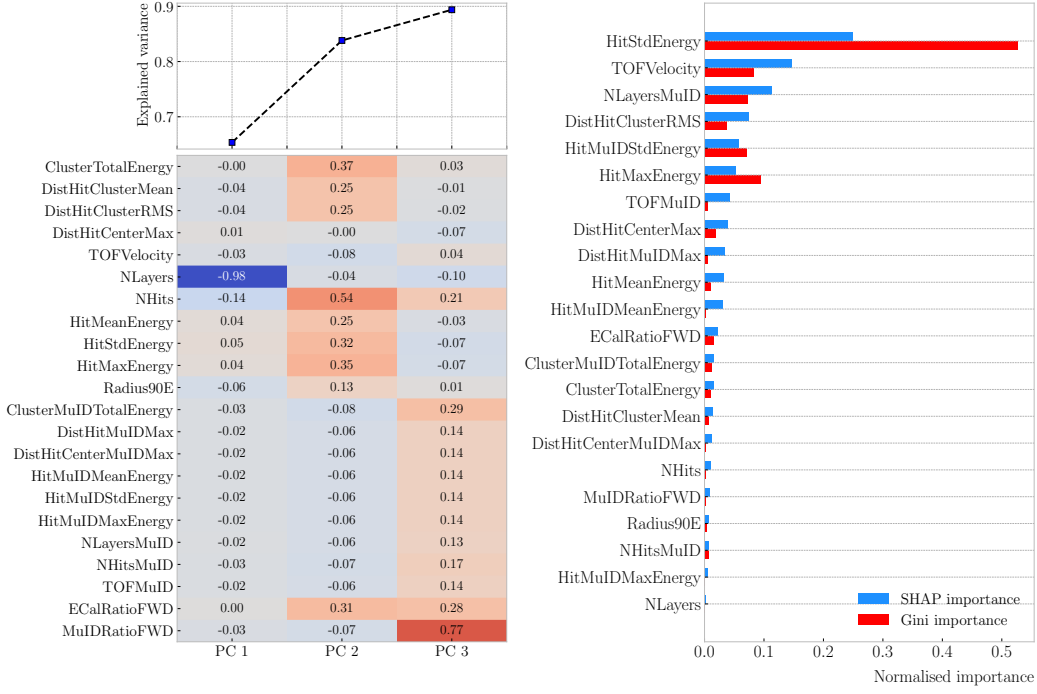


Figure 6.23: Left panel: cumulative explained variance for the first three principal components (top panel) and contribution of the different features to the principal axes in feature space (bottom panel). Right panel: Shapley (blue) and Gini (red) feature importances for the different input features. Both figures correspond to the samples in the momentum range $0.8 \leq p < 1.5$ GeV/c.

3276 into a lower dimensional space. The idea is to find the matrix \mathbf{C}_m , whose columns are
 3277 the first m orthonormal eigenvectors of the input covariance matrix. Consider the $n \times p$
 3278 real matrix of input data \mathbf{X} , where n is the number of samples and p the number of
 3279 features. If \mathbf{X} is centred, i.e. the means of its columns are equal to zero, we can write the
 3280 covariance matrix of \mathbf{X} as $\mathbf{C} = \mathbf{X}^\top \mathbf{X} / (n - 1)$. This matrix can be diagonalised, yielding:

$$\mathbf{C} = \mathbf{V} \mathbf{L} \mathbf{V}^\top, \quad (6.11)$$

3281 where \mathbf{V} is a matrix of eigenvectors and \mathbf{L} a diagonal matrix with eigenvalues λ_i . Then,
 3282 performing SVD on \mathbf{X} gives us:

$$\mathbf{X} = \mathbf{U} \mathbf{S} \mathbf{V}^\top, \quad (6.12)$$

3283 where \mathbf{U} is a unitary matrix, whose columns are called left singular vectors, \mathbf{S} is a

6.3. MUON AND PION SEPARATION IN THE ECAL AND MUID

3284 diagonal matrix of single values s_i , and \mathbf{W} is another unitary matrix, its columns known
 3285 as right singular vectors. This way, we can write:

$$\mathbf{C} = \mathbf{WSU}^\top \mathbf{USW}^\top / (n - 1) = \mathbf{W} \frac{\mathbf{S}^2}{n - 1} \mathbf{W}^\top. \quad (6.13)$$

3286 meaning that the right singular vectors are also the eigenvectors of the covariance matrix.
 3287 The SVD can be computed numerically following an iterative approach.
 3288 This way, taking an input data vector $X \in \mathbb{R}^n$, the resulting feature vector $Y \in \mathbb{R}^m$
 3289 is given by:

$$Y = \mathbf{C}_m^\top X. \quad (6.14)$$

3290 The new features capture most of the variance of the original sample, while being lower
 3291 dimensional, as $m < n$.

3292 Before applying the PCA reduction one needs to centre and scale the input data.
 3293 Centring is necessary when using SVD to obtain the eigenvectors of the covariance
 3294 matrix, as only in that case we can do the identification with the right singular vectors
 3295 from the input data. Scaling is needed when variables are on different scales, as some
 3296 can then dominate the PCA procedure.

3297 I used the PCA module of `scikit-learn`, together with the `RobustScaler`, which
 3298 centres the data and scales it based on the interquartile range. In Fig. 6.22 (left panel)
 3299 and Fig. 6.23 (left panel) I show the results I obtained from the PCA for the momentum
 3300 ranges $0.3 \leq p < 0.8 \text{ GeV}/c$ and $0.8 \leq p < 1.5 \text{ GeV}/c$, respectively. Notice that in
 3301 the second case the number of features increases considerably, as this is the first region
 3302 which uses the MuID variables. I found that, in all the cases, adding a fourth PC does
 3303 not add additional information. As it can be seen in the top panels of the figures, the
 3304 cumulative explained variance is already over 80% with three PCs.

3305 The bottom panels show the contribution of the variables to the principal axes. For
 3306 the two first momentum regions, I observe a tendency of the energy-related and the
 3307 geometry-related ECal variables to be clustered together. For the other ranges, when
 3308 I include the MuID variables, there seems to be a division between ECal and MuID

CHAPTER 6. PARTICLE ID IN GARSOFT

variables. For these, it seems like the number of ECal layers with hits also plays an important role.

The next step in the analysis is to quantify the importance of the features based on two additional metrics, namely the Gini and the Shapley values. The Gini importance, often called mean decrease impurity, is based on how much a feature contributes to the purity improvement at the splits in each decision tree. The purity is measured in terms of the Gini impurity index, defined as:

$$I_G = 1 - \sum_i f_i, \quad (6.15)$$

where f_i is the fractional abundance of the i -th class. Then, for each split one can compute the weighted decrease in impurity as:

$$\Delta_G = \frac{N_t}{N} \left(I_G - \frac{N_t^R}{N_t} I_G^R - \frac{N_t^L}{N_t} I_G^L \right), \quad (6.16)$$

where N represents the total number of samples, N_t the number of samples at the current node, N_t^R and N_t^L the number of samples in the right and left children respectively, I_G is the Gini impurity at the current node, and I_G^R and I_G^L the Gini impurities of the resulting right and left children.

For each decision tree, one will have a normalised vector with the accumulated decrease in Gini impurity for each feature. In the case of a BDT, the feature importances are simply the mean for all the estimators in the ensemble⁹.

The concept of Shapley values originated in the context of game theory, and it measures the marginal contribution of a feature in enhancing the accuracy of a classifier. Take F to be the set of all features in a problem, and $S \subseteq F$ the subset of features. To compute the Shapley value of the i -th feature, one has to train a model with that feature present, $f_{S \cup \{i\}}$, and another model trained without it, f_S . This has to be repeated for all possible combinations of subsets $S \subset F \setminus \{i\}$, and evaluating the models predictions

⁹Note to self: this appears not to be the case. If you get the `feature_importance` for each tree in the BDT and take the average, the result is not the same to be one reported in the `feature_importance` attribute of the BDT.

6.3. MUON AND PION SEPARATION IN THE ECAL AND MUID

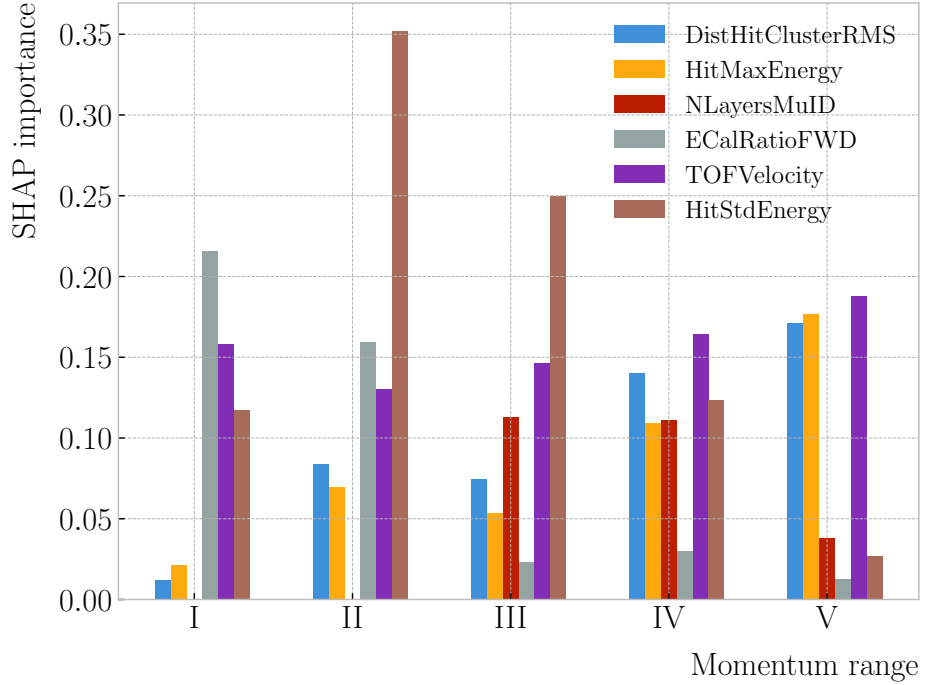


Figure 6.24: Evolution of the SHAP importance for the top six most important features across all five momentum ranges.

3331 on the appropriate sets of data x_S . This way, the Shapley value results:

$$\varphi_i = \sum_{S \subset F \setminus \{i\}} \frac{|S|! (|F| - |S| - 1)!}{|F|!} [f_{S \cup \{i\}}(x_{S \cup \{i\}}) - f_S(x_S)]. \quad (6.17)$$

3332 I trained the `GradientBoostingClassifier` from `scikit-learn` with the default
 3333 configuration in order to evaluate both the Gini and Shapley importances. The Gini
 3334 scores are automatically computed by `scikit-learn`, using the training data. For the
 3335 Shapley importance, I used the implementation from the `SHAP` package, computing
 3336 it using the test sample. The results can be seen in Fig. 6.22 (right panel) and
 3337 Fig. 6.23 (right panel), again for the momentum ranges $0.3 \leq p < 0.8 \text{ GeV}/c$ and
 3338 $0.8 \leq p < 1.5 \text{ GeV}/c$. The length of the bars denote either the SHAP (blue) or the Gini
 3339 (red) importance of the feature. One interesting thing to notice is that, when looking at
 3340 the Gini importance, there is always one feature that dominates over the rest. This is
 3341 not the case for the SHAP importance, where importances tend to be more balanced.

CHAPTER 6. PARTICLE ID IN GARSOFT

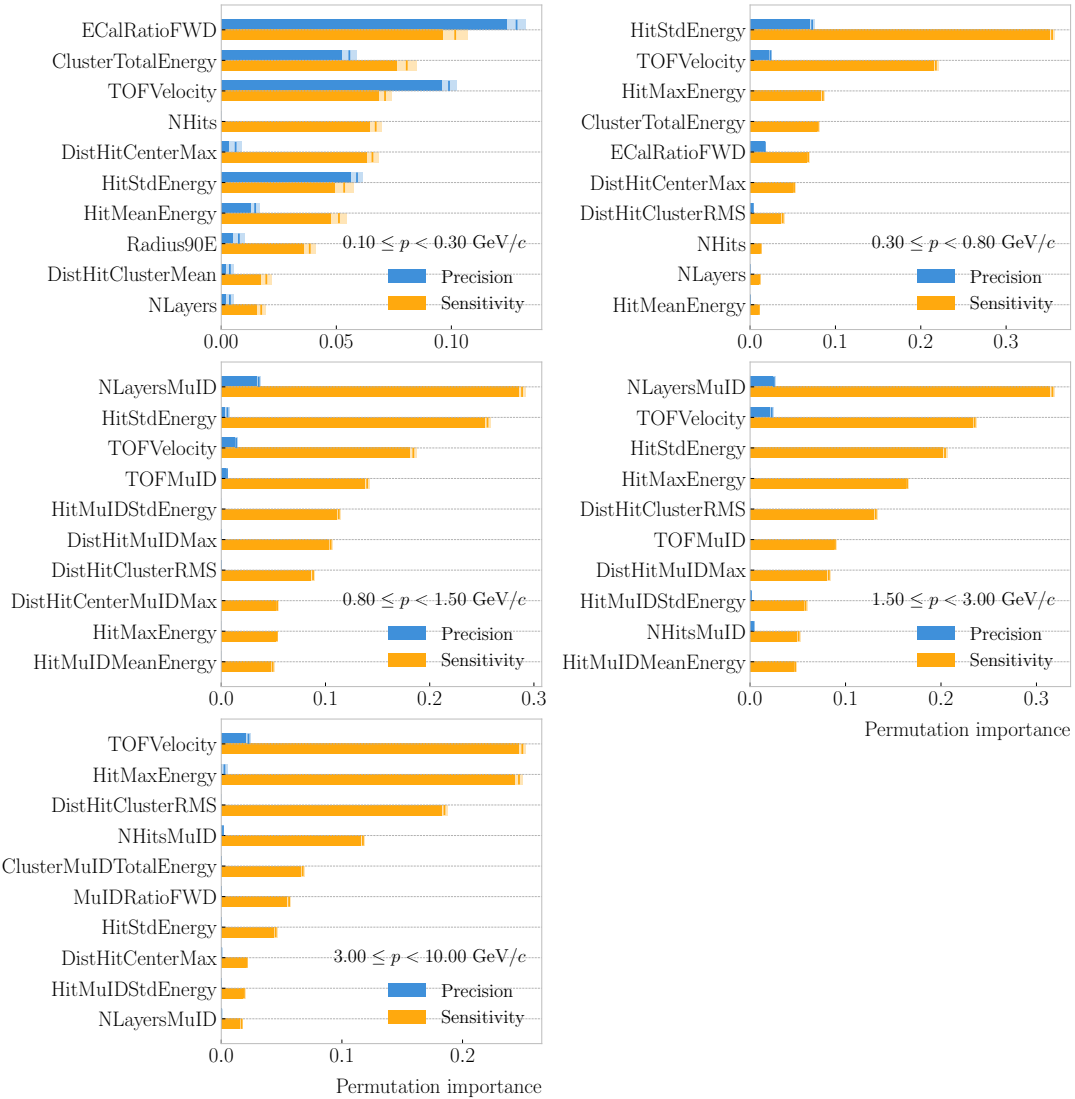


Figure 6.25: Permutation importances for the ten most important features in the different momentum ranges (from left to right, top to bottom, in increasing momentum order). The bars indicate the effect that permutations of each feature have on the purity (blue) and the sensitivity (yellow), the translucent regions representing one standard deviation around the central value.

6.3. MUON AND PION SEPARATION IN THE ECAL AND MUID

3342 Across all momentum ranges, I observe that the most important features are. For
3343 the five momentum ranges considered, only six variables sit in the top five at least once.
3344 Figure 6.24 shows the evolution of the SHAP importance of these six features. It is
3345 interesting to see that the time-of-flight variable keeps its importance almost unchanged
3346 for all momenta. Also, it looks like the ECal energy ratio gets less relevant the higher the
3347 momentum is, but the RMS of the hit-to-cluster distance distribution and the maximum
3348 ECal hit energy become more important in the last momentum ranges.

3349 The last step in the feature selection analysis is the feature permutation. This
3350 technique measures the contribution of each feature to the performance of a model by
3351 randomly shuffling its values and checking how some scores degrade. For the present
3352 case, I am interested in the precision or purity, and the sensitivity or efficiency, as these
3353 two are the most relevant metrics from a physics point of view. The `scikit-learn`
3354 module provides the user with a method to perform the permutation scans.

3355 The results of these are shown in Fig. 6.25. For the different momentum ranges
3356 I show the permutation importances for the ten most important features. For each
3357 of the variables I report the effect the permutations have on the precision (blue) and
3358 sensitivity (yellow) of the models. The bars indicate the importance value, with the
3359 lighter part representing one standard deviation around the mean (hinted as an additional
3360 vertical line). Something to notice is that, in the first momentum region, the feature
3361 permutations have an effect on both the precision and the sensitivity. However, for the
3362 rest the precision is almost unaffected, while the sensitivity changes are considerably
3363 larger.

3364 It is also interesting to see that most of the variables identified as important here
3365 are the same I found when looking at the Shapley values. The behaviour of these across
3366 the momentum ranges is also similar, with the same patterns of some features being
3367 important at low momenta and then dropping in importance for the high momentum
3368 ranges.

3369 Wit this, I conclude the study of the features. I have prepared the training and
3370 testing datasets and understood what features are likely to have the largest impact on

CHAPTER 6. PARTICLE ID IN GARSOFT

3371 the performance of the classifiers.

3372 6.3.4 Hyperparameter optimisation

3373 Any BDT requires the user to specify a number of parameters that will dictate its
3374 behaviour. They can be divided into two categories: (i) tree-specific parameters, which
3375 affect each individual tree in the model, and (ii) boosting parameters, which control the
3376 boosting operation in the model. The value of these so-called hyperparameters affect the
3377 performance and predictive power of the models. Therefore, one needs to carefully select
3378 their optimal values in order to extract as much information as possible from the data.

3379 From all the parameters used to define a tree in the `scikit-learn` implementation
3380 of the BDT classifier, I only consider a subset of them. This is due to the fact that some
3381 are mutually exclusive, but also because I noticed that others have little effect on the
3382 problem at hand. Therefore, the parameters I investigate are the following:

3383 • `min_samples_split`: defines the minimum number of samples required in a node
3384 to be considered for splitting. Higher values prevent a model from learning relations
3385 which might be highly specific to the particular sample, but may lead to under-fitting
3386 if the value is too low.

3387 • `min_samples_leaf`: defines the minimum samples required in a leaf node. For
3388 imbalanced problems it should take a low value, as there will not be many cases
3389 where the minority class dominates.

3390 • `max_depth`: maximum depth of a tree. Useful to prevent over-fitting, as higher
3391 depth will allow a model to learn relations specific to the training sample.

3392 In the case of the boosting parameters, the ones I look at are:

3393 • `learning_rate`: determines the impact of each tree on the final outcome. Low
3394 values make the model robust to the specific characteristics of a tree, and thus
3395 allow it to generalise well. However, that usually requires a large number of trees
3396 to model the data properly.

6.3. MUON AND PION SEPARATION IN THE ECAL AND MUID

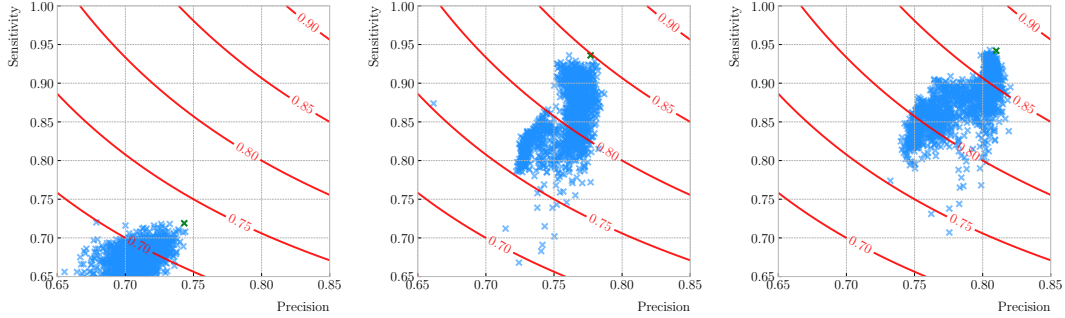


Figure 6.26: Values of the precision and sensitivity obtained for 10000 BDT hyperparameter configurations, for the momentum regions I, III and V. The red contours indicate the curves of equal F_1 -score, while the green crosses are the selected configurations.

3397 • `n_estimators`: number of sequential trees to be trained. In general, BDTs are
3398 fairly robust at higher number of trees but it can still overfit at a point.

3399 • `subsample`: fraction of observations to be selected for each tree. Values slightly
3400 less than 1 make the model robust by reducing the variance.

3401 In general, hyperparameters depend on each other. Thus, it is not possible to
3402 optimise them independently. In the literature, we find two main strategies to explore
3403 the hyperparameter space. We could use a grid search, in which one discretises a
3404 portion of the space of hyperparameters and evaluates the model at each point. Another
3405 approach is the randomised search, where a certain number of random configurations of
3406 hyperparameters are explored.

3407 In this case, I used the random search to scan the hyperparameter space. Also,
3408 because it is not guaranteed that a set of hyperparameters can be efficiently applied
3409 across different datasets, I perform the optimisation for each of the momentum ranges
3410 considered. Table 6.3 shows the list of hyperparameters considered, and the range within
3411 which I let them vary. I decided to fix the number of estimators to 400 in all cases, as
3412 its value is correlated with that of the learning rate.

3413 I evaluate 10000 different hyperparameter configurations for each momentum range.
3414 For the hyperparameter tuning, I used subsamples containing 10% of the full datasets,
3415 keeping the original proportions between classes, in order to reduce the computational

CHAPTER 6. PARTICLE ID IN GARSOFT

Table 6.3: Optimal values of the hyperparameters used by the BDT, for each momentum range.

Hyperparameter	Range	Best value				
		I	II	III	IV	V
<code>min_samples_split</code>	[0.001, 1]	0.10	0.06	0.05	0.27	0.06
<code>min_samples_leaf</code>	[0.001, 1]	0.02	0.03	0.01	0.02	0.07
<code>max_depth</code>	{2, 3, ..., 8}	8	2	4	2	7
<code>learning_rate</code>	[0.05, 1]	0.10	0.23	0.07	0.13	0.09
<code>subsample</code>	[0.01, 1]	0.75	0.65	0.79	0.86	0.95

3416 load. The performance of the models was assessed using a stratified 3-fold cross-validation
 3417 with replacement. Cross-validation involves dividing the data in a number of subsets,
 3418 training the model using some of them, and testing it with the rest. In our case, I
 3419 divide the data in 3 equal-sized subsets, maintaining the class proportions of the original
 3420 dataset. Then, for 3 consecutive iterations, I train the models using 2 of the subsets
 3421 while I compute the precision and sensitivity scores with the other. This approach
 3422 provides a more robust estimate of the performance on unseen data.

3423 Figure 6.26 shows the results in the precision versus sensitivity plane, for the
 3424 momentum regions I, III and V (from left to right). The contours represent the curves
 3425 of equal F_1 -score, i.e. the harmonic mean of the precision and the sensitivity. In order
 3426 to select the optimal configurations (indicated in the plots with a green cross), I chose
 3427 the point with the highest F_1 -score.

3428 The results for the different momentum ranges are summarised in Tab. 6.3. One
 3429 can see some consistency in hyperparameter choices, with models generally preferring
 3430 small values for the tree-specific parameters, small learning rate, and relatively large
 3431 subsample sizes.

3432 Now that I have obtained the optimal values of the hyperparameters, I can train
 3433 the different BDTs. In this case I use the complete datasets, keeping 20% of the data
 3434 for testing. Table 6.4 shows the values of the different performance metrics obtained
 3435 using the selected hyperparameters and 5-fold cross-validation. The last row indicates

6.3. MUON AND PION SEPARATION IN THE ECAL AND MUID

Table 6.4: Performance metrics of the BDTs with optimal hyperparameters, for the different momentum ranges.

Metric	Value $\pm 1\sigma$				
	I	II	III	IV	V
Accuracy	0.779 ± 0.003	0.812 ± 0.003	0.846 ± 0.002	0.861 ± 0.003	0.874 ± 0.002
Precision	0.769 ± 0.003	0.752 ± 0.005	0.788 ± 0.002	0.805 ± 0.003	0.815 ± 0.003
Sensitivity	0.745 ± 0.009	0.921 ± 0.006	0.965 ± 0.002	0.967 ± 0.002	0.976 ± 0.001
F_1 -score	0.757 ± 0.004	0.828 ± 0.003	0.867 ± 0.002	0.879 ± 0.002	0.889 ± 0.002
ROC AUC	0.868 ± 0.003	0.865 ± 0.003	0.899 ± 0.002	0.902 ± 0.002	0.911 ± 0.001

3436 the value of the area under the receiver operating characteristic (ROC) curve. This
 3437 represents the sensitivity of a model as a function of the false positive rate. I have
 3438 included it here as it is a classic model metric used in the machine learning community.
 3439 Overall, there is a clear trend of models performing better at higher momentum.

3440 6.3.5 Probability calibration

3441 So far, the trained BDTs are able to provide predictions of the class labels. Ideally,
 3442 one would like the output of a classifier to give a confidence level about the prediction.
 3443 However, it is not straightforward to interpret the outputs of our BDTs in terms of
 3444 probabilities.

3445 A way to visualise how well the predictions of a classifier are calibrated is using
 3446 reliability diagrams [141]. They represent the probability of the positive label versus the
 3447 probability predicted by the classifier. These can be obtained by binning the predicted
 3448 probabilities, and then compute the conditional probability $P(y_{true} = 1 | y_i \leq y_{pred} <$
 3449 $y_{i+1})$ by checking the fraction of true positive instances in each bin. The reliability
 3450 diagram of a perfectly calibrated classifier would be a diagonal line.

3451 In this case, I try to correct the raw response of the classifiers by applying a sigmoid
 3452 function:

$$\sigma(x; A, B) = \frac{1}{1 + e^{Ax+B}}, \quad (6.18)$$

3453 where the parameters A and B are real numbers determined using the method of least

CHAPTER 6. PARTICLE ID IN GARSOFT

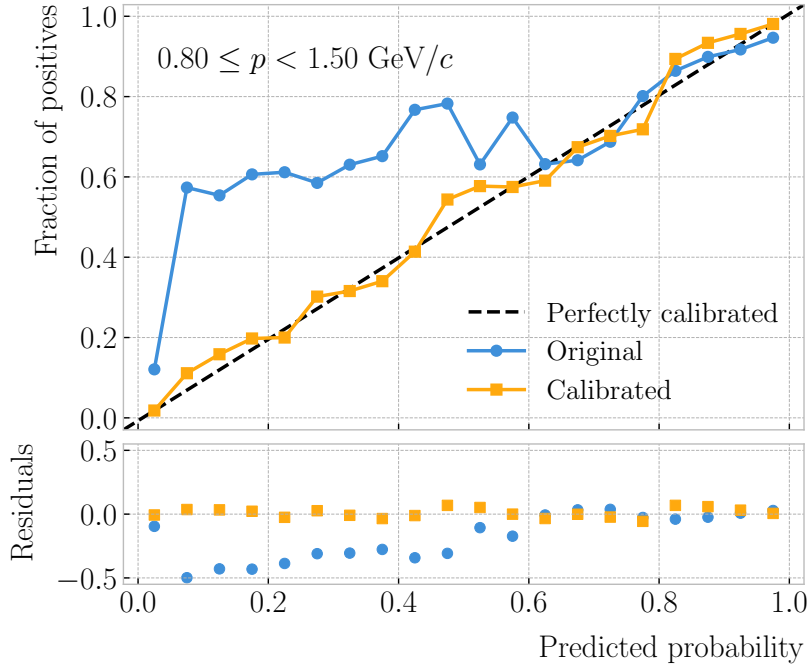


Figure 6.27: Reliability diagrams for the BDT classifier used in the momentum range $0.3 \leq p < 0.8 \text{ GeV}/c$, both for the original (blue circles) and calibrated (yellow squares) responses. For reference, the response of a perfectly calibrated classifier is also shown (black dashed line).

3454 squares.

3455 For each classifier, I perform a grid search to obtain the optimal values of A and B .
 3456 For any pair, I compute the predicted probabilities as $y_{pred} = \sigma(y_{raw}; A, B)$, where y_{raw}
 3457 are the raw predictions of the classifier¹⁰. Then, I calculate the corresponding reliability
 3458 curve, and take the sum of the squared residuals between it and the response of the
 3459 perfectly calibrated classifier.

3460 Figure 6.27 shows the reliability diagrams for the original (blue) and calibrated
 3461 (yellow) probability predictions of the classifier for the III momentum range, $0.3 \leq p <$
 3462 $0.8 \text{ GeV}/c$. The original response of the classifier is given by $y_{pred} = \sigma(y_{raw}; -2, 0)$,
 3463 which is the transformation applied by `scikit-learn` to produce the probability estimate.
 3464 Notice how the calibrated prediction matches the ideal response much better than the
 3465 original, across all the probability range.

¹⁰In `scikit-learn` these correspond to the outputs of the `decision_function` method.

6.4. ECAL TIME-OF-FLIGHT

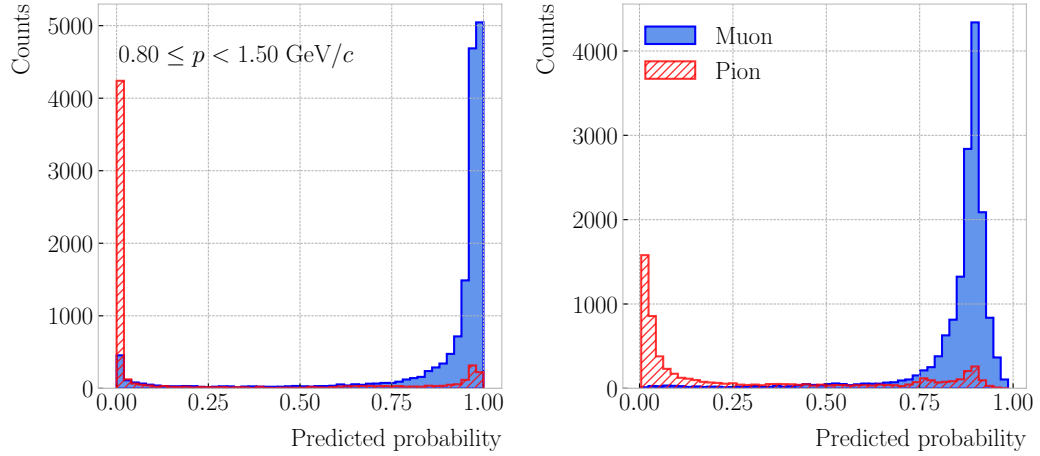


Figure 6.28: Uncalibrated (left panel) and calibrated (right panel) predicted probabilities assigned by the BDT classifiers for true muons (blue) and charged pions (red) in the momentum range $0.3 \leq p < 0.8 \text{ GeV}/c$.

3466 One can also compare the responses of the uncalibrated and calibrated classifiers
 3467 broken down by true particle type, as shown in Fig. 6.28. It can be seen that the
 3468 distributions for both muons (blue) and charged pions (red) smoothen after calibration,
 3469 but still the separating power of the classifier remains unchanged.

3470 At this point, having the trained classifiers and the probability calibration parameters,
 3471 I am able to assess the performance of the classification strategy in a physics-relevant
 3472 case.

3473 6.3.6 Performance

3474 6.4 ECal time-of-flight

3475 Looking at Fig. 6.19, it is clear that for momentum values in the range $1.0 - 3.0 \text{ GeV}/c$
 3476 it is not possible to separate pions and protons using a $\langle dE/dx \rangle$ measurement in the
 3477 HPgTPC. However, in the previous section I assumed that protons at those energies
 3478 could be identified by other means, and therefore were not an issue for the muon and
 3479 pion discrimination.

3480 Some detectors, like ALICE [142] or the ILD concept [143], complement the PID
 3481 capabilities of their gaseous trackers with time-of-flight measurements. The use of

CHAPTER 6. PARTICLE ID IN GArSOFT

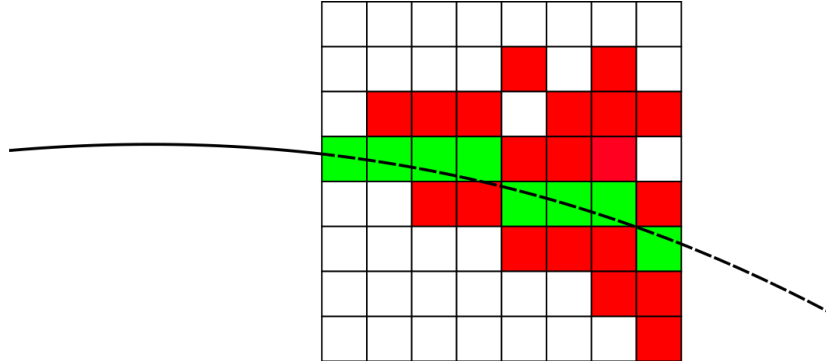


Figure 6.29: Schematic of the hit selection used for the ToF measurement. The grid represents the layers of the inner ECal, with coloured squares indicating the tiles with hits. Green squares indicate the selected hits.

3482 fast timing silicon sensors, with hit time resolutions under 100 ps, would allow for the
 3483 identification of charged hadrons via a ToF measurement up to 5.0 GeV/c. In the case
 3484 of ND-GAr, one could think of using the inner layers of the ECal, the ones consisting of
 3485 high-granularity tiles, to obtain a ToF-based PID, with some inputs from the TPC.

3486 Measuring the momentum and the velocity of a charged particle allows for a
 3487 determination of the mass through the relativistic momentum formula:

$$m = \frac{p}{\beta} \sqrt{1 - \beta^2}. \quad (6.19)$$

3488 In our case, the momentum is measured in the TPC, using the curvature and the dip
 3489 angle of the helix inside the magnetic field. The velocity of the particle can be written
 3490 as:

$$\beta = \frac{\ell_{track}}{c\tau}, \quad (6.20)$$

3491 where ℓ_{track} is the length of the track, and τ the arrival time to the ECal.

3492 In GArSoft, the track length is computed at the Kalman filter stage. It is simply the
 3493 sum of the line segments along the track, either in the forward or backward fit. In this
 3494 case, because we are only interested in the particles that make it to the ECal, I choose
 3495 the fit direction based on the results of the track-cluster associations.

6.4. ECAL TIME-OF-FLIGHT

3496 Additionally, because the last 30 cm of the TPC radius are uninstrumented¹¹, I need
 3497 to correct for the length of the tracks. Using the track fit parameters to propagate the
 3498 helix to its entry point in the ECal, one can write the total track length as:

$$\ell_{track} = \ell + \left| \frac{\phi_{EP} - \phi}{R^{-1}} \right| \sqrt{1 + \tan^2 \lambda}, \quad (6.21)$$

3499 where ϕ_{EP} is the angle of rotation at the entry point to the calorimeter, and ℓ , ϕ , R and
 3500 λ are the track length, angle of rotation, radius of curvature and dip angle at the last
 3501 point in the fit, respectively.

3502 To test the idea of performing a ToF measurement with the inner ECal, I generated
 3503 two data samples. Each consists of 10000 single particle events, either charged pions or
 3504 protons. Their momenta are uniformly distributed in the range $0.5 - 5.0$ GeV/ c , and
 3505 their directions are isotropic. I process each sample using different values of the time
 3506 resolution, from $\Delta\tau = 0$, the perfect time resolution case for comparison, to the current
 3507 nominal value of $\Delta\tau = 0.7$ ns, and the worse scenario of $\Delta\tau = 1.0$ ns.

3508 6.4.1 Arrival time estimations

3509 In the simulation, the limited time resolution of the ECal is taken into account by
 3510 applying a Gaussian smearing to the true hit times. Other effects, like the digitisation
 3511 of the signals, are not taken into account and fall beyond the scope of this study. After
 3512 the track-cluster, one ends up with a collection of ECal hits associated to each particle.
 3513 From these, the arrival time of the particle to the ECal can be extracted.

3514 The simplest possibilities are to either take the time of the earliest hit or the hit
 3515 closest to the entry point. Because these two coincide, in general, I focused only in
 3516 the earliest hit time. However, this needs to be corrected, to account for the distance
 3517 travelled from the entry point to the position of the hit:

$$\tau_{earliest} = \tau_{hit} - \frac{d_{EP-hit}}{c}, \quad (6.22)$$

¹¹Note to self: check this number.

CHAPTER 6. PARTICLE ID IN GArSOFT

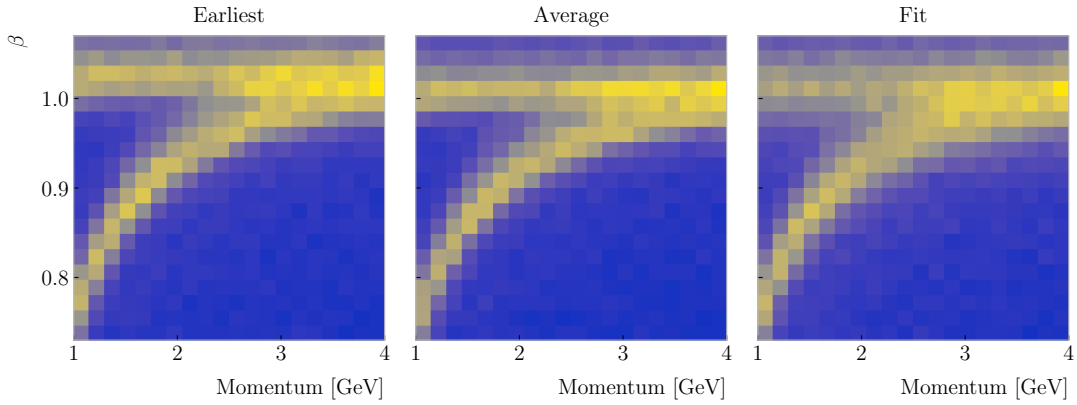


Figure 6.30: Particle velocity versus momentum measured with different ECal arrival time estimations. From left to right: earliest hit time, average hit time, and fitted hit time. In all cases the time resolution is $\Delta\tau = 0.1$ ns.

3518 where τ_{hit} is the time of the earliest hit, and d_{EP-hit} is the distance between that hit
 3519 and the entry point of the particle to the ECal. This is computed as the arc length
 3520 between the entry point and the point of the extrapolated helix up to the layer of the
 3521 hit. This way of correcting the time assumes c for the propagation of the particle, which
 3522 may lead to biased estimates.

3523 I also tried to estimate the arrival times using information from the rest of the hits.
 3524 In order to do this, as a simplifying assumption, I approximate the hadronic shower
 3525 considering only its MIP component. For each layer, I keep only the hit in the tile closest
 3526 to the point of the extrapolated track up to that layer. Figure 6.29 shows an example of
 3527 how this hit selection works. The dashed line represents the extrapolated track, while
 3528 the coloured squares are the tiles containing hits. Green indicates the tiles closer to the
 3529 track in each layer (in the sketch they correspond to the grid columns).

3530 Now, I can use these collections of hits to estimate the arrival times. A possibility
 3531 is to take the average of the times of the selected hits, denoted $\tau_{average}$. For that to
 3532 work, one needs to correct these times, in a similar way as in Eq. (6.22), before taking
 3533 the average. However, as before, this correction assumes that the particle travels at the
 3534 speed of light inside the ECal. Another option is to perform a linear fit to the hit times
 3535 and the distances to the entry point. In that case, the arrival time would be the fitted

6.4. ECAL TIME-OF-FLIGHT

3536 value of the intercept, τ_{fit} . This method would not assume a speed of light propagation.

3537 Figure 6.30 shows the velocity estimations as a function of the particle momentum,
3538 for the earliest hit time (left panel), average hit time (middle panel), and fitted hit time
3539 (right panel). The two bands correspond to the π^\pm and the p particles. $\Delta\tau = 0.1$ ns.
3540 Notice how, for the earliest hit time method, the velocities are significantly biased
3541 towards larger values. For the multi-hit methods, the τ_{fit} estimate appears to produce a
3542 larger variance than when using the $\tau_{average}$ method.

3543 6.4.2 Proton and pion separation

3544 Once we have the velocities of the particles, one can estimate their masses through
3545 Eq. (6.19). The resulting mass spectra are shown in Fig. 6.31. I computed the masses
3546 for the three arrival time estimates discussed above, and three different values of the
3547 time resolution: $\Delta\tau = 0.00$ (perfect time resolution), $\Delta\tau = 0.10$ ns, and $\Delta\tau = 0.70$ ns.
3548 Although in all cases we have the same number of events, it appears as if the entries
3549 in the histograms decrease as the time resolution increases. Sometimes, the particles
3550 get unphysical values of $\beta > 1$, and in turn they do not contribute to the mass spectra.
3551 This is more likely to happen for higher values of $\Delta\tau$.

3552 As noted before, the average hit time method produces the most robust estimates
3553 when increasing $\Delta\tau$. Intuitively this makes sense, as by taking the mean one averages
3554 out the effect of the Gaussian smearing. Going forward, I will use this arrival time
3555 estimator, as it appears to be the best performing one.

3556 It is possible to use the velocity estimations to select a sample of protons. In this
3557 case, I do so by dividing the relevant momentum range in bins of 0.1 GeV/ c . For each
3558 momentum bin, I compute the expected velocity for the protons via the inverse of Eq.
3559 (6.19), and then take the fractional residuals of the measured velocities. Using that
3560 distribution, I choose the cut that maximises the F_1 -score of the proton selection.

3561 The results can be seen in Fig. 6.32, for the case $\Delta\tau = 0.10$ ns. As expected from
3562 Fig. 6.30, the performance of the selection degrades rapidly with increasing momentum.
3563 However, the purity is still around 75% at 3.0 GeV/ c . This is likely to be sufficient, as

CHAPTER 6. PARTICLE ID IN GArSOFT

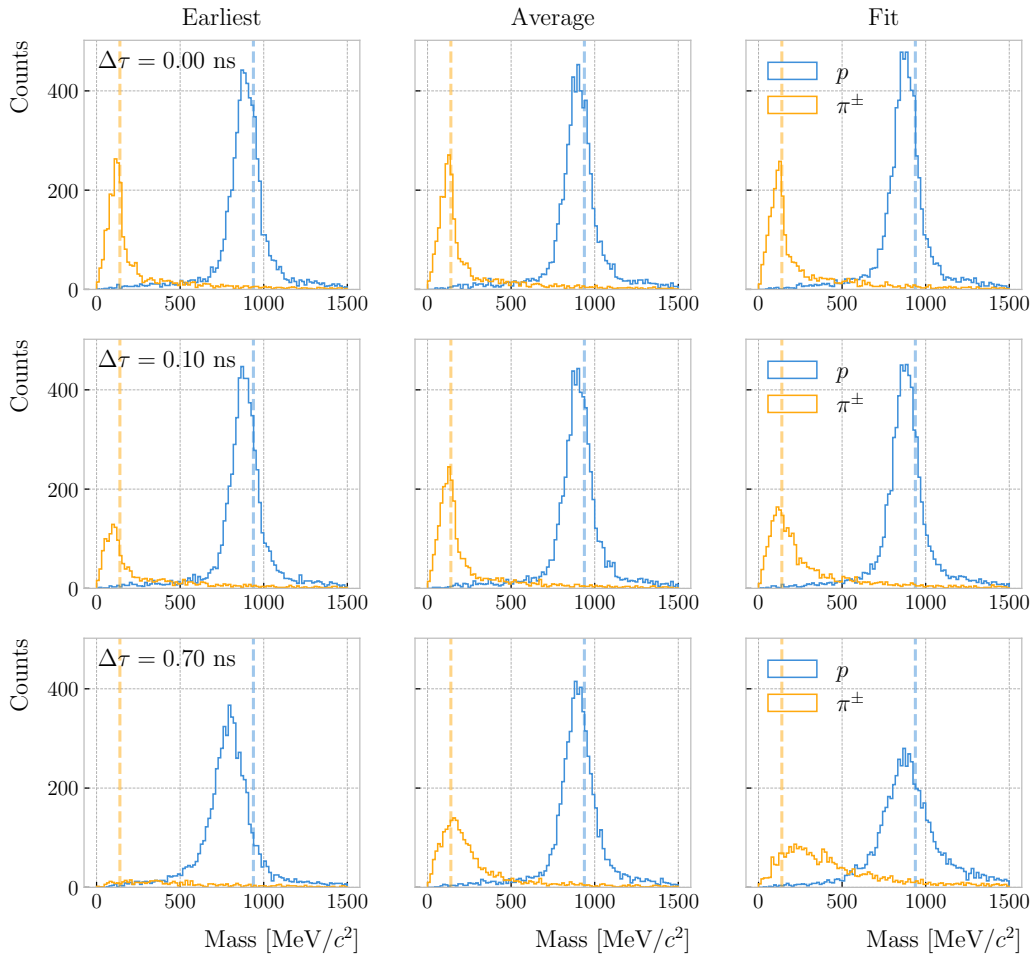


Figure 6.31: Mass spectra for p (blue) and π^\pm (yellow) particles, using different ECal time resolution values (from top to bottom, in ascending order), and arrival time estimates. From left to right: earliest hit time, average hit time, and fitted hit time. The dashed lines indicate the true masses of the particles.

3564 we do not expect protons or charged pions with higher energies from the beam neutrino

3565 interactions.

3566 Figure 6.33

3567 6.5 Charged pion decay in flight

3568 As discussed previously, in GArSoft the TPC tracks are formed after a pattern recognition

3569 algorithm and a Kalman filter are applied to the TPC clusters. These two steps can

3570 find discontinuities in the track candidates (e.g. due to a particle decay) when these

6.5. CHARGED PION DECAY IN FLIGHT

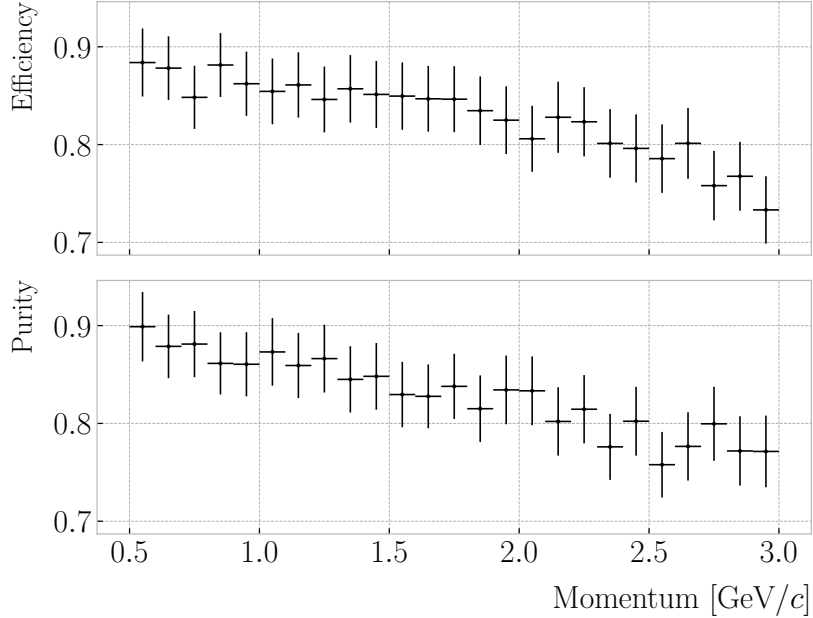


Figure 6.32: Efficiency (top panel) and purity (bottom panel) for the proton selection as a function of the momentum, for $\Delta\tau = 0.10$ ns.

so-called breakpoints are large enough. However, for some, more subtle, cases they may miss them and form a single reconstructed track. It has been noted in the literature that Kalman filters offer, as a by-product, additional information to form test statistics to identify these breakpoints [144, 145].

Considering the mean life of the charged pion, $\tau = (2.6033 \pm 0.0005) \times 10^{-8}$ s, one can estimate that about 12% of the pions with momentum $p \sim \mathcal{O}(500 \text{ MeV}/c)$ (roughly the peak of the pion momentum distribution in ν_μ CC interactions off argon) decay inside the TPC. Figure 6.34 (left panel) shows the amount of charged pions decaying in the full TPC and fiducial volumes from an isotropic, monoenergetic sample of 100000 negatively charged pions with $p = 500 \text{ MeV}/c$. We see that about 10% of those decayed, with more than half of them decaying inside the TPC fiducial volume.

Figure 6.34 (right panel) shows an example event display of a charged pion (magenta line) decays in flight inside the TPC, but because the angle of the muon (blue line) is small both were reconstructed as one single track (black line). In this case, the composite track reaches the ECal, where it undergoes a muon-like interaction, thus being classified

CHAPTER 6. PARTICLE ID IN GARSOFT

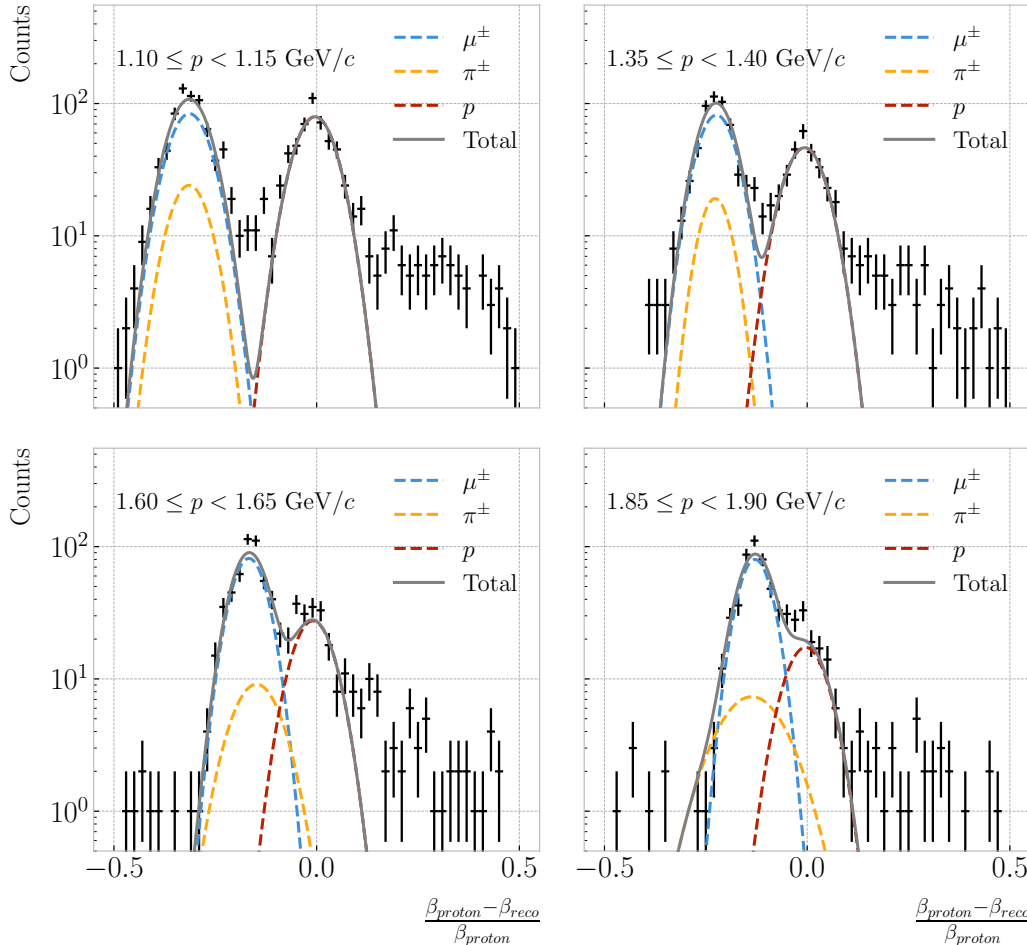


Figure 6.33: Distributions of the velocities measured by ToF with the inner ECal, for different momentum bins, in a FHC neutrino interaction sample. The Gaussian fits are performed around the maxima for each particle species.

3586 as a muon.

3587 A way to understand what decaying pion tracks were totally or partially reconstructed
 3588 together with the daughter muon is looking at the relative energy contributions to the
 3589 reconstructed track. In order to select a sample of such events, I require that a minimum
 3590 50% of the total energy comes from the pion and at least 20% from the muon.

3591 6.5.1 Track breakpoints

3592 To identify potential decays we can use the information we obtain from the Kalman
 3593 filter at each step of the fitted track. The simplest test we can think about is computing

6.5. CHARGED PION DECAY IN FLIGHT

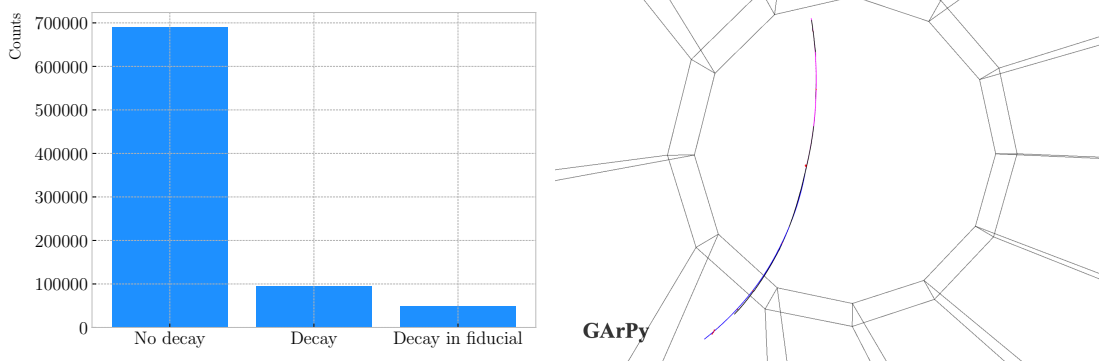


Figure 6.34: Left panel: number of non-decaying, decaying and decaying in the fiducial volume pions for a MC sample of 100000, $p = 500$ MeV/c isotropic positively charged pions inside the TPC. Right panel: event display for a positive pion decaying inside the fiducial volume, with a single reconstructed track for the pion and muon system.

3594 the χ^2 of the mismatch between all the parameters in the forward and the backward fits:

$$\chi_k^{2(FB)} = (\hat{x}_k^B - \hat{x}_k^F)^T [V^{(\hat{x}_k, B)} + V^{(\hat{x}_k, F)}]^{-1} (\hat{x}_k^B - \hat{x}_k^F), \quad (6.23)$$

3595 where \hat{x}_k^F , \hat{x}_k^B are the Kalman filter state vector estimates at step k in the forward and
3596 backward fits and $V^{(\hat{x}_k, F)}$, $V^{(\hat{x}_k, B)}$ the covariance matrices of \hat{x}_k^F and \hat{x}_k^B respectively.

3597 Using the values of the χ^2 at measurement k for the forward and backward fits we can
3598 compute another χ^2 value that characterises the overall track fit:

$$\chi_{track}^2 = \chi_k^{2(F)} + \chi_k^{2(B)} + \chi_k^{2(FB)}, \quad (6.24)$$

3599 which remains approximately constant for all k .

3600 An alternative approach proposed in the context of the NOMAD experiment was
3601 using a fit with a more elaborate breakpoint hypothesis, so we can perform a comparison
3602 of the χ^2 with and without breakpoints. This can be achieved by using some alternative
3603 parametrisation with extra parameters, which allows some of the track parameters to
3604 be discontinuous at certain points. A decay changes the momentum magnitude and
3605 direction, so we can use the new state vector:

$$\alpha = (y, z, 1/R_F, 1/R_B, \phi_F, \phi_B, \tan\lambda_F, \tan\lambda_B)^T. \quad (6.25)$$

CHAPTER 6. PARTICLE ID IN GArSOFT

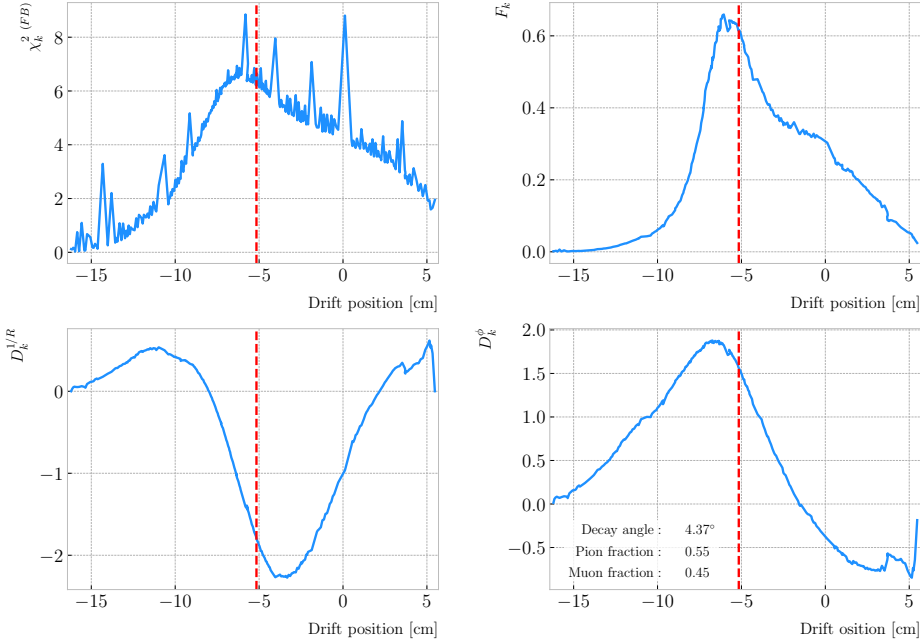


Figure 6.35: Values of $\chi_k^2 (FB)$ (top left panel), F_k (top right panel), $D_k^{1/R}$ (bottom left panel) and D_k^ϕ (bottom right panel) versus position along the drift direction for a reconstructed track in a positive pion decay event. The vertical red dashed line indicates the true location of the decay point.

3606 As we already have the estimates from the standard Kalman filter and their
 3607 covariance matrices at each point, we do not need to repeat the Kalman fit for the new
 3608 parametrisation. Instead, I can compute the values of α at each point k that minimise
 3609 the χ^2 resulting from comparing them to $\{\hat{x}_k^B, \hat{x}_k^F\}$. Introducing the two 5×8 matrices:

$$H^F = \begin{pmatrix} 1 & 0 & 0 & 0 & 0 & 0 & 0 & 0 \\ 0 & 1 & 0 & 0 & 0 & 0 & 0 & 0 \\ 0 & 0 & 1 & 0 & 0 & 0 & 0 & 0 \\ 0 & 0 & 0 & 0 & 1 & 0 & 0 & 0 \\ 0 & 0 & 0 & 0 & 0 & 0 & 1 & 0 \end{pmatrix}, \quad H^B = \begin{pmatrix} 1 & 0 & 0 & 0 & 0 & 0 & 0 & 0 \\ 0 & 1 & 0 & 0 & 0 & 0 & 0 & 0 \\ 0 & 0 & 0 & 1 & 0 & 0 & 0 & 0 \\ 0 & 0 & 0 & 0 & 0 & 1 & 0 & 0 \\ 0 & 0 & 0 & 0 & 0 & 0 & 0 & 1 \end{pmatrix}, \quad (6.26)$$

3610 we can write this as:

$$\begin{aligned} \chi_k^2 (FB)(\alpha) &= (\hat{x}_k^F - H^F \alpha)^T \left[V^{(\hat{x}_k, F)} \right]^{-1} (\hat{x}_k^F - H^F \alpha) \\ &\quad + (\hat{x}_k^B - H^B \alpha)^T \left[V^{(\hat{x}_k, B)} \right]^{-1} (\hat{x}_k^B - H^B \alpha). \end{aligned} \quad (6.27)$$

3611 The minimum of $\chi_k^2 (FB)(\alpha)$ is found when the measured new state vector takes the

6.5. CHARGED PION DECAY IN FLIGHT

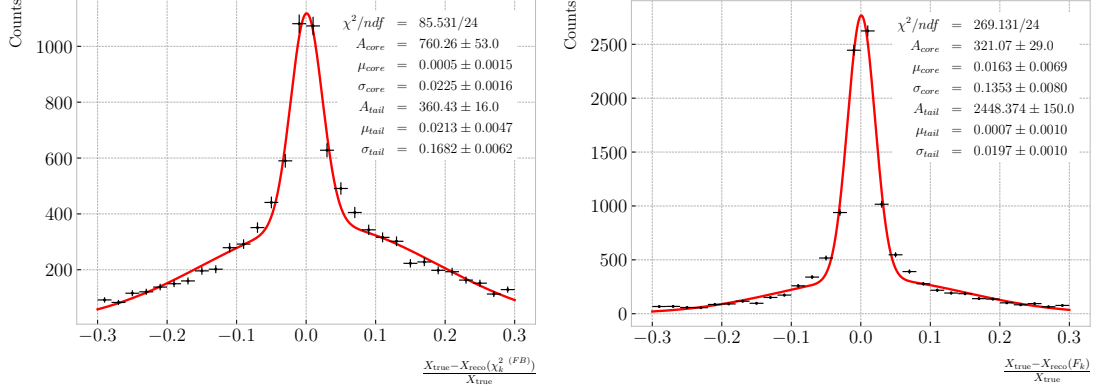


Figure 6.36: Fractional residual distributions of the true and reconstructed decay position along the drift coordinate, using the position of the maximum of $\chi_k^2(FB)$ (left panel) and F_k (right panel) as estimates of the decay position. Also shown are double Gaussian fits to these points (red lines).

3612 value:

$$\hat{\alpha}_k = V^{(\hat{\alpha}_k)} H^T (V^{(\hat{x}_k)})^{-1} \hat{X}, \quad (6.28)$$

3613 where $\hat{X} = \{\hat{x}_k^B, \hat{x}_k^F\}$, $V^{(\hat{x}_k)}$ is the block diagonal matrix formed by $V^{(\hat{x}_k, F)}$ and $V^{(\hat{x}_k, B)}$

3614 and $V^{(\hat{\alpha}_k)}$ is the covariance matrix of $\hat{\alpha}_k$, given by:

$$V^{(\hat{\alpha}_k)} = \left(H^T (V^{(\hat{x}_k)})^{-1} H \right)^{-1}. \quad (6.29)$$

3615 From these new fit estimates we can compute the F statistic, which tells us whether

3616 the model with breakpoint provides a statistically significant better fit:

$$F_k = \left(\frac{\chi_{track,k}^2 - \chi_{full,k}^2}{8 - 5} \right) / \left(\frac{\chi_{full,k}^2}{N - 8} \right). \quad (6.30)$$

3617 One can also compute the signed difference of the duplicated variables divided by

3618 their standard deviation at each point. These represent how significant the discontinuity

3619 in each variable is. For any variable η we can write it as:

$$D_k^\eta = \frac{\hat{\eta}_k^B - \hat{\eta}_k^F}{\sqrt{\text{Var}[\hat{\eta}_k^F] + \text{Var}[\hat{\eta}_k^B] - 2\text{Cov}[\hat{\eta}_k^F, \hat{\eta}_k^B]}}. \quad (6.31)$$

CHAPTER 6. PARTICLE ID IN GARSOFT

3620 In our case, the relevant ones to look at are $D_k^{1/R}$ and D_k^ϕ .

3621 Figure 6.35 shows the values of $\chi_k^2(FB)$, F_k , $D_k^{1/R}$ and D_k^ϕ as functions of the position
 3622 along the drift direction, for an example reconstructed track with 55.5% of the energy
 3623 coming from the charged pion and 45.5% from the daughter muon. The true position of
 3624 the decay is indicated (dashed red lines). Notice how $\chi_k^2(FB)$ and F_k , $D_k^{1/R}$ reach their
 3625 maxima near the decay point. In the former case this indicates a large forward-backward
 3626 difference in the track fit. In the later it represents that the extended state vector
 3627 improves the fit particularly around that point.

3628 I can estimate the decay position finding resolution by computing the difference
 3629 between the X position of the maxima of $\chi_k^2(FB)$ and F_k and the X position of the
 3630 true decay. Figure 6.36 represent the the fractional residual distributions for both
 3631 cases, from the sample of tracks containing pion decays. Fitting a double Gaussian to
 3632 the distributions (red lines) I find a resolution of $(3.31 \pm 0.15)\%$ and $(6.94 \pm 0.31)\%$
 3633 respectively.

3634 In principle, the F -statistic should follow a Fisher distribution with $(8 - 5)$ and
 3635 $(N - 8)$ degrees of freedom under the null hypothesis. In most of our cases $N \sim \mathcal{O}(100)$,
 3636 so the probability density functions will look very similar. In this case, it is safe to take
 3637 the limit $N \rightarrow \infty$ in the Fisher PDF:

$$\begin{aligned}\tilde{f}(x; a - b) &= \lim_{N \rightarrow \infty} f(x; a - b, N - a) \\ &= \frac{2^{-\frac{a-b}{2}}}{\Gamma(\frac{a-b}{2})} (a - b)^{\frac{a-b}{2}} x^{\frac{a-b}{2}-1} e^{-\frac{a-b}{2}x}.\end{aligned}\tag{6.32}$$

3638 In our case $a - b = 8 - 5 = 3$, so we would obtain a p-value of 0.05 at $x = 2.60$.

3639 Figure 6.37 contains the distributions of the maxima of $\chi_k^2(FB)$, F_k and D_k^ϕ and the
 3640 minima of $D_k^{1/R}$ for a sample of non-decaying pion tracks (blue) and another sample of
 3641 reconstructed tracks containing part of the pion and the daughter muon from a decay
 3642 inside the fiducial volume (red). Notice that, even though the values of $F_k^{(max)}$ for the
 3643 decay sample are typically larger than for the non-decaying one, just a small fraction of
 3644 the events go beyond the aforementioned value of $F = 2.60$. Therefore, from a practical

6.5. CHARGED PION DECAY IN FLIGHT

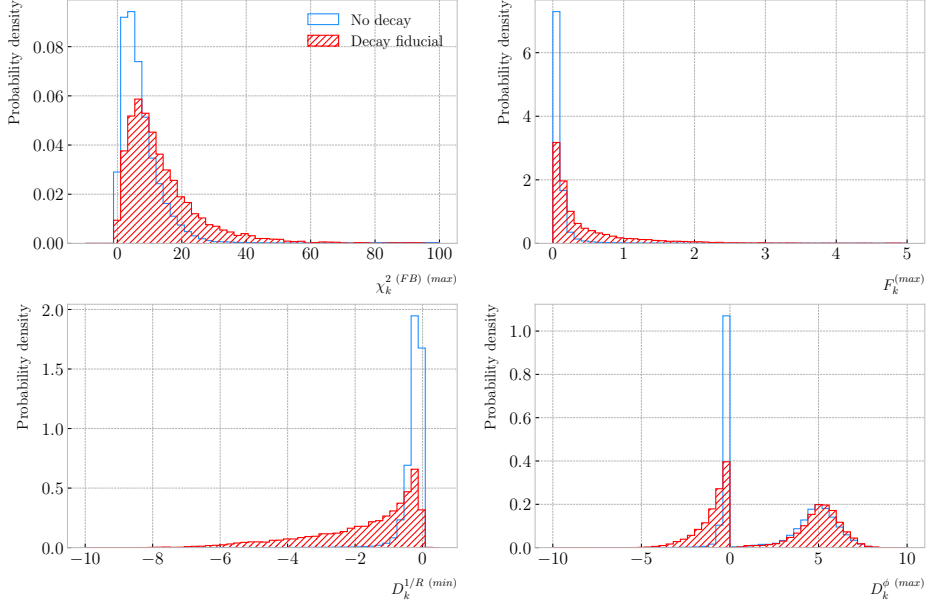


Figure 6.37: Distributions of the extreme values of $\chi_k^2 (FB)$ (top left panel), F_k (top right panel), $D_k^{1/R}$ (bottom left panel) and D_k^ϕ (bottom right panel) for non-decaying reconstructed pion tracks (blue) and tracks which include the decay inside the fiducial volume (red).

3645 point of view, it is not the most efficient variable to use for selecting the decay events.

3646 However, looking at the $D_k^{1/R} \text{ (min)}$ distribution we can see there is a big difference
 3647 between non-decaying and decaying events in this variable. One can use a combination
 3648 of these four variables to distinguish between the pion decay events (signal) and the
 3649 non-decaying pions (background).

3650 An approach to this classification could be using a boosted decision tree (BDT). One
 3651 of the advantages of BDTs is that they are easy to interpret and identify the relative
 3652 importance of the different input variables. Training a BDT with 400 estimators and a
 3653 maximum depth of 4 I can obtain an efficient classification without overtraining. Figure
 3654 6.38 (left panel) shows the distribution of probabilities predicted by the BDT for a test
 3655 sample. The signal efficiency as a function of background acceptance, the so-called ROC
 3656 curve, is shown in Fig. 6.38 (right panel). With a relative importance of 0.83, the most
 3657 important variable turned out to be $D_k^{1/R} \text{ (min)}$.

3658 One thing we can check is how the resolution to the decay and the signal efficiency in

CHAPTER 6. PARTICLE ID IN GARSOFT

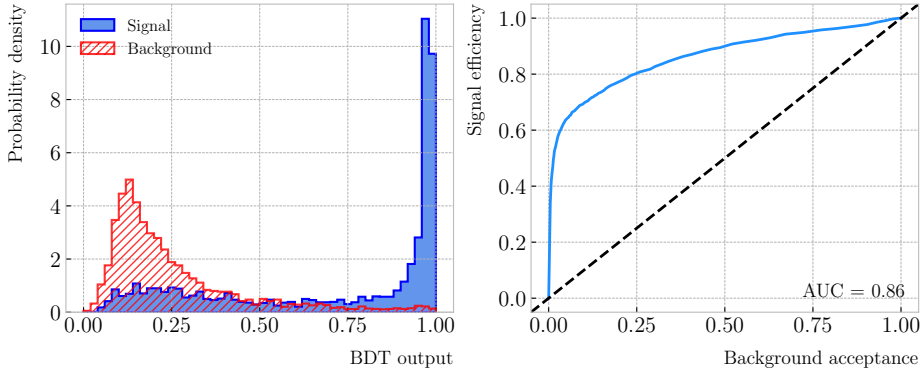


Figure 6.38: Left panel: distributions of the predicted probabilities assigned by the BDT classifier to a test sample of decaying pion+muon tracks (blue) and non-decaying pion tracks (red). Left: signal efficiency versus background acceptance (ROC curve) obtained from the BDT for the test sample.

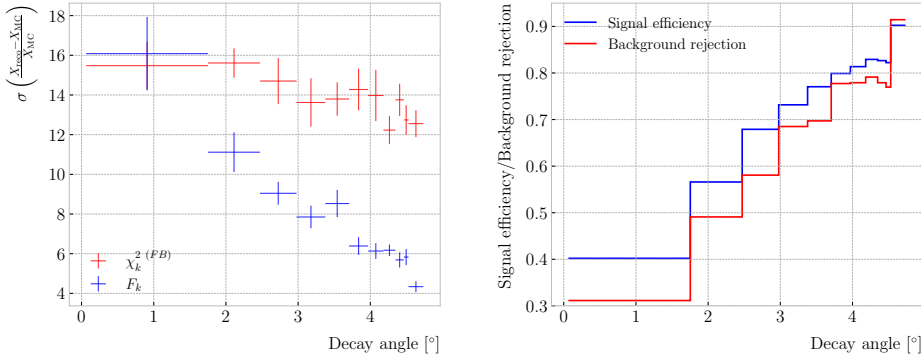


Figure 6.39: Left panel: dependence of the decay position finding resolution on the true value of the decay angle for the $\chi_k^2(FB)$ (red) and F_k (blue) methods. Right panel: signal efficiency (blue line) and background rejection (red line) from the BDT classifier versus true decay angle.

3659 the classification changes with the true decay angle. Using an equal-frequency binning
3660 for the decay angles, we can repeat the previous steps for each bin.

3661 Figure 6.39 (left panel) shows the dependence on the decay angle of the decay finding
3662 resolusion. We can see that for the $\chi_k^2(FB)$ maximum location method the resolution
3663 consistently lies between 12 to 16%. However, the $F_k^{(\max)}$ approach gives a significantly
3664 better resolution for high angle values, reaching the 4 – 6% range for decay angles $\geq 4^\circ$.

3665 For the classification dependence on the angle, I use the same classifier I trained
3666 before but evaluating the test sample for each individual angular bin. I compute the
3667 signal efficiency in each bin for a fixed value of the background rejection, in this case

6.6. NEUTRAL PARTICLE IDENTIFICATION

3668 90%. Similarly, for the background rejection estimation I use a fixed signal efficiency
3669 value of 90%. Figure 6.39 (right panel) represents the change in signal efficiency (blue)
3670 and background rejection (red) with the value of the true decay angles.

3671 6.6 Neutral particle identification

3672 6.6.1 ECal clustering

3673 Another important reconstruction item is the clustering algorithm of ECal hits in
3674 GArSoft. The default module features a NN algorithm that treats all hits in the same
3675 way, independently of the layer each hit comes from. However, the current ECal design
3676 of ND-GAr has two very different types of scintillator layers. The inner layers are made
3677 out of tiles, which provide excellent angular and timing resolutions. On the other hand,
3678 the outer layers are cross scintillator strips. That way, an algorithm that treats hits
3679 from both kinds of layers differently may be able to improve the current performance.

3680 Inspired by the reconstruction of T2K’s ND280 downstream ECal [146], the idea
3681 was to put together a clustering module that first builds clusters for the different ECal
3682 views (tiles, strips segmented in the X direction and strips segmented in Y direction),
3683 and then tries to match them together to form the final clusters.

3684 Working on a module-by-module basis, the algorithm first separates the hits depending
3685 on the layer type they come from. Then, it performs a NN clustering for the 3 sets of
3686 hits separately. For the tile hits it clusters together all the hits which are in nearest-
3687 neighbouring tiles and nearest-neighbouring layers, for strip hits it looks at nearest-
3688 neighbouring strips and next-to-nearest-neighbouring layers (as the layers with strips
3689 along the two directions are alternated). For strip clusters an additional cut in the
3690 direction along the strip length is needed.

3691 After this first clustering I then apply a recursive re-clustering for each collection
3692 of strip clusters based on a PCA method. In each case, we loop over the clusters with
3693 $N_{hits} \geq 2$, computing the centre of mass and three principal components. Propagating
3694 these axes up to the layers of the rest of the clusters, we check if the propagated point

CHAPTER 6. PARTICLE ID IN GARSOFT

3695 and the centre of mass of the second cluster are within next-to-nearest-neighbouring
3696 strips. An additional cut in the direction along the strip length is also needed. Moreover,
3697 I require that the two closest hits across the two clusters are at most in next-to-nearest-
3698 neighbouring strips. I merge the clusters if these three conditions are satisfied. The
3699 re-clustering is repeated until no more cluster pairs pass the cuts.

3700 The clusters in each strip view are combined if their centres of mass are close enough
3701 and they point in the same direction. An alternative approach for the strip cluster
3702 merging could be to compute the overlap between the ellipsoids defined by the principal
3703 axes of the clusters, and then merge the pair if the overlap exceeds some threshold.
3704 Further study is needed to understand if this change would have an impact in the overall
3705 clustering performance.

3706 To merge the tile clusters to the combined strip clusters I propagate the principal
3707 axis of the strip cluster towards the inner layers, up to the centre of mass layer of the
3708 tile cluster. I merge the clusters if the distance between the propagated point and the
3709 centre of mass is below a certain cut.

3710 The last step is to check if clusters in neighbouring modules should be merged
3711 together, both across two barrel modules, across end cap modules and between barrel
3712 end cap modules. I check the distance between the two closest hits in the pair of clusters
3713 and merge them if it passes this and an additional direction cut.

3714 Figure ?? presents an example of the clustering steps relevant for strip layer hits, from
3715 the input hits (top left panel) to the NN clustering (top right panel) and re-clustering
3716 (bottom left panel) for each strip view and the final merging strip clusters (bottom
3717 right panel). It shows the hits from a single ECal barrel module in a ν_μ CC interaction
3718 event with a neutral pion and a proton in the final state. The two clusters on the left
3719 correspond to the photon pair from the π^0 decay and the one on the upper right corner
3720 is associated to the proton.

3721 This algorithm has a total number of eight free parameters that need to be optimised.
3722 I used a sample of 1000 ν_μ CC interactions in order to obtain the optimal configuration of
3723 clustering parameters. This sample was generated up to the default ECal hit clustering

6.6. NEUTRAL PARTICLE IDENTIFICATION

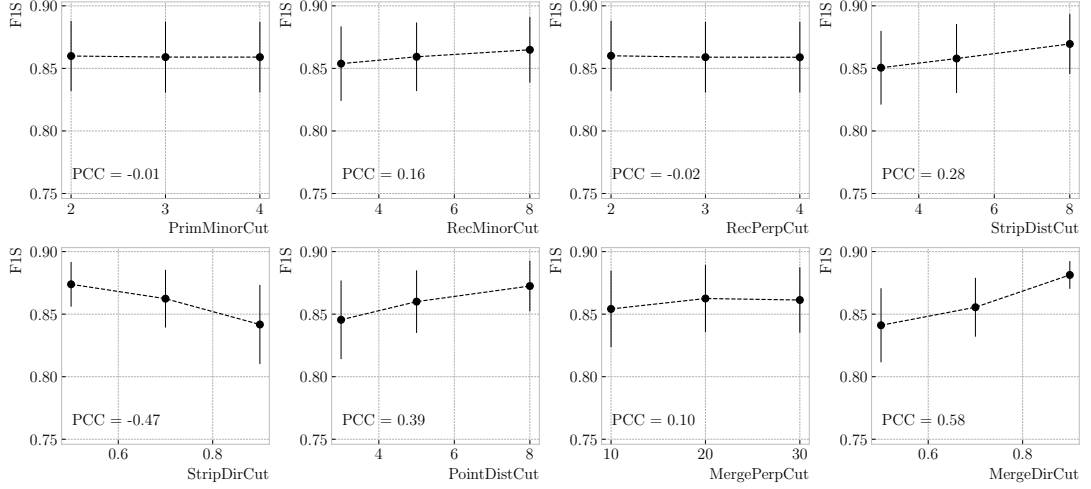


Figure 6.40: Mean values of the F_1 -score marginal distributions for the different free parameters of the new clustering algorithm, with the error bars representing one standard deviation around the mean. The F_1 -score values were computed for the 6561 possible parameter configurations using 1000 ν_μ CC interaction events.

Table 6.5: Summary of parameters and sampled values used in the optimisation of the clustering algorithm.

Name	Units	Sampled values	Description
PrimMinorCut	strips	2, 3, 4	Distance along strip length in NN clustering
RecMinorCut	strips	3, 5, 8	Distance between propagated point and CM along strip length in re-clustering
RecPerpCut	strips	2, 3, 4	Closest hit pair distance in re-clustering
StripDistCut	strips	3, 5, 8	Distance between CMs in strip cluster merging
StripDirCut	cos	0.5, 0.7, 0.9	Main axes direction cut in strip cluster merging
PointDistCut	tiles	3, 5, 8	Distance between propagated point and CM in strip-tile matching
MergePerpCut	cm	10, 20, 30	Closest hit pair distance in module merging
MergeDirCut	cos	0.5, 0.7, 0.9	Main axes direction cut in module merging

3724 level, so then I could run the new clustering algorithm each time with a different
 3725 configuration of parameters. As the number of parameters is relatively large, I only
 3726 performed a coarse-grained scan of the parameter space. Sampling each of the eight
 3727 parameters at three different points each I obtain 6561 different configurations. These
 3728 parameters, together with the used values, are summarised in Tab. 6.5.

3729 In order to measure the performance of the clustering, I use a binary classification
 3730 approach. For each formed cluster, I identify the Geant4 Track ID of the matching MC

CHAPTER 6. PARTICLE ID IN GARSOFT

3731 particle and the energy fraction of each hit. Then, I assign to each cluster the Track ID
3732 with the highest total energy fraction. For each of the different Track IDs associated to
3733 the clusters, I select the cluster with the highest energy (only from the hits with the
3734 same Track ID). I identify such a cluster as the main cluster for that Track ID. I count
3735 as true positives (TPs) the hits with the correct Track ID in each main cluster. False
3736 positives (FPs) are the hits with the incorrect Track ID for the cluster they are in, not
3737 only main clusters. The false negatives (FNs) are the hits with the correct Track ID in
3738 clusters other than the main.

3739 Figure 6.40 shows the computed F_1 -score values for the different cuts. In each case,
3740 the central value represents the mean of the F_1 -score distribution for the specified value
3741 of the corresponding variable and the vertical error bar represents one standard deviation
3742 around the mean. Also shown are the Pearson correlation coefficients of these central
3743 values. We can see that five of the variables have a sizeable effect on the F_1 -score, with
3744 an absolute difference between the last and first values as big as 4%.

3745 The working configuration is obtained as follows. I first select all configurations
3746 with purity $\geq 90\%$. Among those, I choose the combinations that yield the maximum
3747 F_1 -score. If more than one configuration remains I select the one with the highest
3748 sensitivity. Doing so, I end up with a parameter configuration with an efficiency of 88%
3749 and a 90% purity. Compared with the default algorithm, which gives an efficiency of
3750 76% and a purity of 91% for the same sample, I have managed to improve the efficiency
3751 by a factor of 1.16.

3752 6.6.2 π^0 reconstruction

3753 One of the potential applications of the new ECal hit clustering is the reconstruction of
3754 neutral particles, in particular pions. Neutral pions decay promptly after being produced,
3755 through the $\pi^0 \rightarrow \gamma\gamma$ channel ($98.823 \pm 0.034\%$) of the time. The photon pair does
3756 not leave any traces in the HPgTPC (unless one or both of them converts into an
3757 electron-positron pair), but each of them will produce an electromagnetic shower in
3758 the ECal.

6.6. NEUTRAL PARTICLE IDENTIFICATION

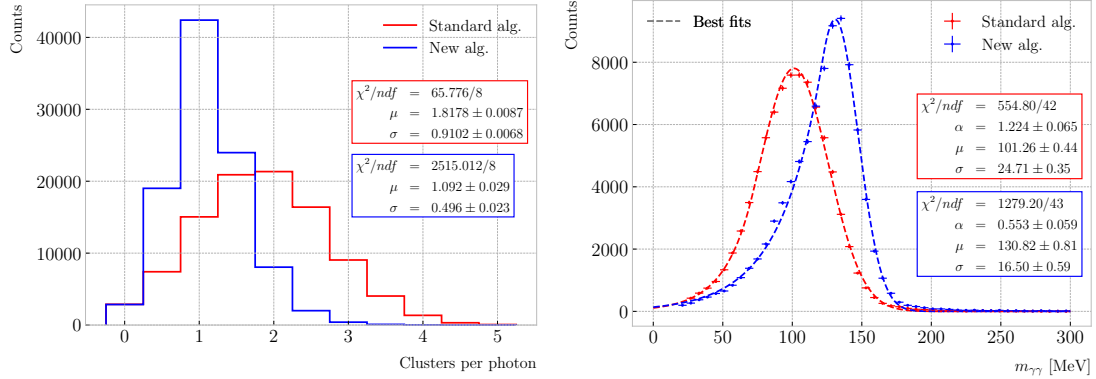


Figure 6.41: Left panel: distributions of the number of ECal clusters per photon from π^0 decays for the standard (red) and new (blue) clustering algorithms. Right panel: reconstructed invariant mass distributions for photon pairs from single π^0 events using the standard (red) and new (blue) ECal clustering algorithms.

3759 To test the potential impact of the new algorithm in π^0 reconstruction, I generated
 3760 a MC sample of single, isotropic neutral pions inside the HPgTPC. All pions were
 3761 generated with a momentum $p = 500$ MeV and their initial positions were uniformly
 3762 sampled inside a $2 \times 2 \times 2$ m box aligned with the centre of the TPC. I ran both the
 3763 default and the new clustering algorithms, using for the latter the optimised configuration
 3764 discussed above.

3765 The first thing to notice is that the number of clusters produced per photon has
 3766 decreased. Figure 6.41 (left panel) shows these distributions for the default (red) and
 3767 new (blue) algorithms. Using a simple Gaussian fit, we see that the mean number of
 3768 ECal clusters per photon went from 1.82 ± 0.01 to 1.09 ± 0.03 . This effectively means that
 3769 with the new algorithm the ECal activity of one true particle is typically reconstructed
 3770 as a single object. From the reconstruction point of view this can be an advantage. As
 3771 now most of the photon energy ends up in a single ECal cluster, I can simply use cluster
 3772 pairs to identify the π^0 decay.

3773 In general, one calculates the invariant mass of the photon pair as:

$$m_{\gamma\gamma} = \sqrt{2E_1E_2(1 - \cos \theta)}, \quad (6.33)$$

3774 where E_i are the energies of the photons and θ the opening angle between them. In this

CHAPTER 6. PARTICLE ID IN GARSOFT

3775 case I can use the energies deposited in the ECal and their incident directions. This
 3776 quantity is computed for all possible pairs of clusters, using their position together with
 3777 the true decay point. In a more realistic scenario, e.g. ν_μ CC interaction, one could use
 3778 the position of the reconstructed primary vertex instead. I also tried to use the principal
 3779 direction of the clusters, but that approach gave considerably worse results. For each
 3780 event I only keep the pair with an invariant mass closer to the true π^0 mass value.

3781 Figure 6.41 (right panel) shows the invariant mass distributions for the photon pairs
 3782 we get using the default (red) and the new (blue) ECal clustering algorithms. For the fit
 3783 I used a modified version of the Crystal Ball function [147], obtained by taking the limit
 3784 where the parameter controlling the power-law tail goes to infinity:

$$f(x; N, \mu, \sigma, \alpha) = N \cdot \begin{cases} e^{\frac{\alpha(2x-2\mu+\alpha\sigma)}{2\sigma}}; & x \leq \mu - \alpha\sigma, \\ e^{-\frac{(x-\mu)^2}{2\sigma^2}}; & x > \mu - \alpha\sigma. \end{cases} \quad (6.34)$$

3785 Comparing the fitted mean and standard deviation values for the Gaussian cores, we
 3786 see that the distribution for the new algorithm is a 67% narrower and also peaks much
 3787 closer to the true m_{π^0} value, going from 101.3 ± 0.4 MeV to 130.8 ± 0.6 MeV.

7

3788

3789

Event selection in ND-GAr

3790 **7.1 CAFs and CAFAna**

3791 **7.2 Event selection**

3792 **7.2.1 ν_μ CC selection**

3793 **7.2.2 Charged pion multiplicity**

8

3794

Conclusions

3795

3796

A [REDACTED]

3797

An appendix

Bibliography

- 3799 [1] J.N. Bahcall, A.M. Serenelli and S. Basu, *New solar opacities, abundances,*
 3800 *helioseismology, and neutrino fluxes, Astrophys. J. Lett.* **621** (2005) L85
 3801 [[astro-ph/0412440](#)]. 22, 42, 122, 123, 124
- 3802 [2] R. Garani and S. Palomares-Ruiz, *Dark matter in the Sun: scattering off electrons*
 3803 *vs nucleons, JCAP* **05** (2017) 007 [[1702.02768](#)]. 22, 120, 121, 124, 125, 126, 148
- 3804 [3] M. Honda, M. Sajjad Athar, T. Kajita, K. Kasahara and S. Midorikawa,
 3805 *Atmospheric neutrino flux calculation using the NRLMSISE-00 atmospheric model,*
 3806 *Phys. Rev. D* **92** (2015) 023004 [[1502.03916](#)]. 22, 129, 130
- 3807 [4] M. Colom i Bernadich and C. Pérez de los Heros, *Limits on Kaluza-Klein dark*
 3808 *matter annihilation in the Sun from recent IceCube results, Eur. Phys. J. C,* **80** 2
 3809 (2020) 129 **80** (2019) [[1912.04585](#)]. 23, 133, 134
- 3810 [5] ANTARES collaboration, *Search for Dark Matter in the Sun with the ANTARES*
 3811 *Neutrino Telescope in the CMSSM and mUED frameworks, Nucl. Instrum. Meth.*
 3812 *A* **725** (2013) 76 [[1204.5290](#)]. 23, 133, 134
- 3813 [6] N. Deutschmann, T. Flacke and J.S. Kim, *Current LHC Constraints on Minimal*
 3814 *Universal Extra Dimensions, Phys. Lett. B* **771** (2017) 515 [[1702.00410](#)]. 23, 133,
 3815 134
- 3816 [7] ICECUBE collaboration, *Search for GeV-scale dark matter annihilation in the Sun*
 3817 *with IceCube DeepCore, Phys. Rev. D* **105** (2022) 062004 [[2111.09970](#)]. 24, 145,
 3818 146

BIBLIOGRAPHY

- 3819 [8] C.-S. Chen, F.-F. Lee, G.-L. Lin and Y.-H. Lin, *Probing Dark Matter*
3820 *Self-Interaction in the Sun with IceCube-PINGU*, *JCAP* **10** (2014) 049
3821 [1408.5471]. 24, 145, 146
- 3822 [9] N.F. Bell, M.J. Dolan and S. Robles, *Searching for dark matter in the Sun using*
3823 *Hyper-Kamiokande*, *JCAP* **11** (2021) 004 [2107.04216]. 24, 145, 146
- 3824 [10] E. Behnke et al., *Final Results of the PICASSO Dark Matter Search Experiment*,
3825 *Astropart. Phys.* **90** (2017) 85 [1611.01499]. 24, 145, 146
- 3826 [11] PICO collaboration, *Dark Matter Search Results from the Complete Exposure of*
3827 *the PICO-60 C₃F₈ Bubble Chamber*, *Phys. Rev. D* **100** (2019) 022001
3828 [1902.04031]. 24, 145, 146
- 3829 [12] DARKSIDE collaboration, *Constraints on Sub-GeV Dark-Matter–Electron*
3830 *Scattering from the DarkSide-50 Experiment*, *Phys. Rev. Lett.* **121** (2018) 111303
3831 [1802.06998]. 24, 150, 151
- 3832 [13] XENON collaboration, *Light Dark Matter Search with Ionization Signals in*
3833 *XENON1T*, *Phys. Rev. Lett.* **123** (2019) 251801 [1907.11485]. 24, 150, 151
- 3834 [14] P.F. de Salas, D.V. Forero, S. Gariazzo, P. Martínez-Miravé, O. Mena,
3835 C.A. Ternes et al., *2020 global reassessment of the neutrino oscillation picture*,
3836 *JHEP* **02** (2021) 071 [2006.11237]. 31, 55, 61
- 3837 [15] W. Pauli, *Dear radioactive ladies and gentlemen*, *Phys. Today* **31N9** (1978) 27. 37
- 3838 [16] F. Reines and C.L. Cowan, *Detection of the free neutrino*, *Phys. Rev.* **92** (1953)
3839 830. 37
- 3840 [17] S.L. Glashow, *Partial-symmetries of weak interactions*, *Nuclear Physics* **22** 579. 37
- 3841 [18] S. Weinberg, *A model of leptons*, *Physical Review Letters* **19** 1264. 37
- 3842 [19] A. Salam, *Weak and Electromagnetic Interactions*, *Conf. Proc. C* **680519** (1968)
3843 367. 37

BIBLIOGRAPHY

- 3844 [20] A. Pich, *The Standard Model of Electroweak Interactions*, in *2010 European
3845 School of High Energy Physics*, pp. 1–50, 1, 2012 [[1201.0537](#)]. 38
- 3846 [21] ALEPH, DELPHI, L3, OPAL, SLD, LEP ELECTROWEAK WORKING GROUP,
3847 SLD ELECTROWEAK GROUP, SLD HEAVY FLAVOUR GROUP collaboration,
3848 *Precision electroweak measurements on the Z resonance*, *Phys. Rept.* **427** (2006)
3849 257 [[hep-ex/0509008](#)]. 41
- 3850 [22] R. Davis, D.S. Harmer and K.C. Hoffman, *Search for neutrinos from the sun*,
3851 *Physical Review Letters* **20** 1205. 42
- 3852 [23] J.N. Bahcall, N.A. Bahcall and G. Shaviv, *Present Status of the Theoretical
3853 Predictions for the ^{37}Cl Solar-Neutrino Experiment*, . 42
- 3854 [24] B.T. Cleveland, T. Daily, R. Davis, Jr., J.R. Distel, K. Lande, C.K. Lee et al.,
3855 *Measurement of the solar electron neutrino flux with the Homestake chlorine
3856 detector*, *Astrophys. J.* **496** (1998) 505. 42
- 3857 [25] SAGE collaboration, *Measurement of the solar neutrino capture rate with gallium
3858 metal. III: Results for the 2002–2007 data-taking period*, *Phys. Rev. C* **80** (2009)
3859 015807 [[0901.2200](#)]. 42, 54
- 3860 [26] F. Kaether, W. Hampel, G. Heusser, J. Kiko and T. Kirsten, *Reanalysis of the
3861 GALLEX solar neutrino flux and source experiments*, *Phys. Lett. B* **685** (2010) 47
3862 [[1001.2731](#)]. 42, 54
- 3863 [27] Q.R. Ahmad, R.C. Allen, T.C. Andersen, J.D. Anglin, G. Bühler, J.C. Barton
3864 et al., *Measurement of the Rate of $\nu_e + d \rightarrow p + p + e^-$ Interactions Produced by
3865 ^8B Solar Neutrinos at the Sudbury Neutrino Observatory*, . 43
- 3866 [28] Q.R. Ahmad, R.C. Allen, T.C. Andersen, J. D. Anglin, J.C. Barton, E.W. Beier
3867 et al., *Direct Evidence for Neutrino Flavor Transformation from Neutral-Current
3868 Interactions in the Sudbury Neutrino Observatory*, . 43
- 3869 [29] T.K. Gaisser and M. Honda, *Flux of atmospheric neutrinos*, . 43

BIBLIOGRAPHY

- 3870 [30] K. Hirata, T. Kajita, M. Koshiba, M. Nakahata, S. Ohara, Y. Oyama et al.,
3871 *Experimental study of the atmospheric neutrino flux*, . 44
- 3872 [31] D. Casper, R. Becker-Szendy, C.B. Bratton, D.R. Cady, R. Claus, S.T. Dye et al.,
3873 *Measurement of atmospheric neutrino composition with the imb-3 detector*, . 44
- 3874 [32] M. Ambrosio, R. Antolini, C. Aramo, G. Auriemma, A. Baldini, G. C. Barbarino
3875 et al., *Measurement of the atmospheric neutrino-induced upgoing muon flux using*
3876 *macro*, . 44
- 3877 [33] W. Allison, G. Alner, D. Ayres, W. Barrett, C. Bode, P. Border et al.,
3878 *Measurement of the atmospheric neutrino flavour composition in soudan 2*, . 44
- 3879 [34] SUPER-KAMIOKANDE collaboration, *Evidence for oscillation of atmospheric*
3880 *neutrinos*, *Phys. Rev. Lett.* **81** (1998) 1562 [[hep-ex/9807003](#)]. 44
- 3881 [35] P. Minkowski, $\mu \rightarrow e\gamma$ at a Rate of One Out of 10^9 Muon Decays?, *Phys. Lett. B*
3882 **67** (1977) 421. 47
- 3883 [36] M. Gell-Mann, P. Ramond and R. Slansky, *Complex Spinors and Unified Theories*,
3884 *Conf. Proc. C* **790927** (1979) 315 [[1306.4669](#)]. 47
- 3885 [37] T. Yanagida, *Horizontal gauge symmetry and masses of neutrinos*, *Conf. Proc. C*
3886 **7902131** (1979) 95. 47
- 3887 [38] R.N. Mohapatra and G. Senjanovic, *Neutrino Mass and Spontaneous Parity*
3888 *Nonconservation*, *Phys. Rev. Lett.* **44** (1980) 912. 47
- 3889 [39] J. Schechter and J.W.F. Valle, *Neutrino Masses in $SU(2) \times U(1)$ Theories*, *Phys.*
3890 *Rev. D* **22** (1980) 2227. 47
- 3891 [40] B. Pontecorvo, *Mesonium and anti-mesonium*, *Sov. Phys. JETP* **6** (1957) 429. 47
- 3892 [41] M. Gell-Mann and A. Pais, *Behavior of neutral particles under charge conjugation*,
3893 . 47

BIBLIOGRAPHY

- 3894 [42] B. Pontecorvo, *Neutrino Experiments and the Problem of Conservation of
Leptonic Charge*, *Zh. Eksp. Teor. Fiz.* **53** (1967) 1717. 48
- 3895
- 3896 [43] B. Pontecorvo, *Inverse beta processes and nonconservation of lepton charge*, *Zh.
Eksp. Teor. Fiz.* **34** (1957) 247. 49
- 3897
- 3898 [44] Z. Maki, M. Nakagawa and S. Sakata, *Remarks on the unified model of elementary
particles*, *Prog. Theor. Phys.* **28** (1962) 870. 49
- 3899
- 3900 [45] PARTICLE DATA GROUP collaboration, *Review of particle physics*, *Phys. Rev. D*
110 (2024) 030001. 51
- 3901
- 3902 [46] L. Wolfenstein, *Neutrino Oscillations in Matter*, *Phys. Rev. D* **17** (1978) 2369. 52
- 3903
- 3904 [47] B.T. Cleveland, T. Daily, R. Davis, Jr., J.R. Distel, K. Lande, C.K. Lee et al.,
*Measurement of the solar electron neutrino flux with the Homestake chlorine
detector*, *Astrophys. J.* **496** (1998) 505. 54
- 3905
- 3906 [48] G. Bellini et al., *Precision measurement of the ^{7}Be solar neutrino interaction rate
in Borexino*, *Phys. Rev. Lett.* **107** (2011) 141302 [[1104.1816](#)]. 54
- 3907
- 3908 [49] SUPER-KAMIOKANDE collaboration, *Solar neutrino measurements in
super-Kamiokande-I*, *Phys. Rev. D* **73** (2006) 112001 [[hep-ex/0508053](#)]. 54
- 3909
- 3910 [50] SNO collaboration, *Combined Analysis of all Three Phases of Solar Neutrino
Data from the Sudbury Neutrino Observatory*, *Phys. Rev. C* **88** (2013) 025501
[[1109.0763](#)]. 54
- 3911
- 3912
- 3913 [51] SUPER-KAMIOKANDE collaboration, *Atmospheric neutrino oscillation analysis
with external constraints in Super-Kamiokande I-IV*, *Phys. Rev. D* **97** (2018)
072001 [[1710.09126](#)]. 54
- 3914
- 3915
- 3916 [52] ICECUBE collaboration, *Measurement of Atmospheric Neutrino Oscillations at
6–56 GeV with IceCube DeepCore*, *Phys. Rev. Lett.* **120** (2018) 071801
[[1707.07081](#)]. 54
- 3917
- 3918

BIBLIOGRAPHY

- 3919 [53] KamLAND collaboration, *Reactor On-Off Antineutrino Measurement with
3920 KamLAND*, *Phys. Rev. D* **88** (2013) 033001 [[1303.4667](#)]. 55
- 3921 [54] RENO collaboration, *Measurement of Reactor Antineutrino Oscillation Amplitude
3922 and Frequency at RENO*, *Phys. Rev. Lett.* **121** (2018) 201801 [[1806.00248](#)]. 55
- 3923 [55] DAYA BAY collaboration, *Measurement of the Electron Antineutrino Oscillation
3924 with 1958 Days of Operation at Daya Bay*, *Phys. Rev. Lett.* **121** (2018) 241805
3925 [[1809.02261](#)]. 55
- 3926 [56] K.J. Kelly, P.A.N. Machado, S.J. Parke, Y.F. Perez-Gonzalez and R.Z. Funchal,
3927 *Neutrino mass ordering in light of recent data*, *Phys. Rev. D* **103** (2021) 013004.
3928 55
- 3929 [57] P. Dunne, “Latest Neutrino Oscillation Results from T2K.” Jul, 2020. 55
- 3930 [58] MINOS collaboration, *Combined analysis of ν_μ disappearance and $\nu_\mu \rightarrow \nu_e$
3931 appearance in MINOS using accelerator and atmospheric neutrinos*, *Phys. Rev.
3932 Lett.* **112** (2014) 191801 [[1403.0867](#)]. 55
- 3933 [59] OPERA collaboration, *Final Results of the OPERA Experiment on ν_τ
3934 Appearance in the CNGS Neutrino Beam*, *Phys. Rev. Lett.* **120** (2018) 211801
3935 [[1804.04912](#)]. 55
- 3936 [60] K2K collaboration, *Measurement of Neutrino Oscillation by the K2K Experiment*,
3937 *Phys. Rev. D* **74** (2006) 072003 [[hep-ex/0606032](#)]. 55
- 3938 [61] DUNE collaboration, *Long-baseline neutrino oscillation physics potential of the
3939 DUNE experiment*, *Eur. Phys. J. C* **80** (2020) 978 [[2006.16043](#)]. 55
- 3940 [62] HYPER-KAMIOKANDE collaboration, *Physics potential of Hyper-Kamiokande for
3941 neutrino oscillation measurements*, *PoS NuFact2019* (2019) 040. 55
- 3942 [63] SUPERNEMO collaboration, *Probing New Physics Models of Neutrinoless Double
3943 Beta Decay with SuperNEMO*, *Eur. Phys. J. C* **70** (2010) 927 [[1005.1241](#)]. 56

BIBLIOGRAPHY

- 3944 [64] SNO+ collaboration, *Current Status and Future Prospects of the SNO+*
 3945 *Experiment, Adv. High Energy Phys.* **2016** (2016) 6194250 [[1508.05759](#)]. 56
- 3946 [65] NEXT collaboration, *Sensitivity of a tonne-scale NEXT detector for neutrinoless*
 3947 *double beta decay searches, JHEP* **2021** (2021) 164 [[2005.06467](#)]. 56
- 3948 [66] P. Coloma and P. Huber, *Impact of nuclear effects on the extraction of neutrino*
 3949 *oscillation parameters, Phys. Rev. Lett.* **111** (2013) 221802 [[1307.1243](#)]. 57
- 3950 [67] P. Coloma, P. Huber, C.-M. Jen and C. Mariani, *Neutrino-nucleus interaction*
 3951 *models and their impact on oscillation analyses, Phys. Rev. D* **89** (2014) 073015
 3952 [[1311.4506](#)]. 57
- 3953 [68] U. Mosel, *Neutrino Interactions with Nucleons and Nuclei: Importance for*
 3954 *Long-Baseline Experiments, Ann. Rev. Nucl. Part. Sci.* **66** (2016) 171
 3955 [[1602.00696](#)]. 57
- 3956 [69] L. Bathe-Peters, S. Gardiner and R. Guenette, *Comparing generator predictions*
 3957 *of transverse kinematic imbalance in neutrino-argon scattering,* [2201.04664](#). 58
- 3958 [70] DUNE collaboration, *Deep Underground Neutrino Experiment (DUNE), Far*
 3959 *Detector Technical Design Report, Volume I Introduction to DUNE, JINST* **15**
 3960 (2020) T08008 [[2002.02967](#)]. 59, 60, 61, 66, 67, 77, 78, 79, 80
- 3961 [71] DUNE collaboration, *Snowmass Neutrino Frontier: DUNE Physics Summary,*
 3962 [2203.06100](#). 61
- 3963 [72] DUNE collaboration, *Deep Underground Neutrino Experiment (DUNE), Far*
 3964 *Detector Technical Design Report, Volume II: DUNE Physics,* [2002.03005](#). 62, 63,
 3965 64, 71, 129, 138, 142
- 3966 [73] SUPER-KAMIOKANDE collaboration, *Search for Proton Decay via $p \rightarrow e^+ \pi_0$ and*
 3967 *$p \rightarrow \mu^+ \pi_0$ in a Large Water Cherenkov Detector, Phys. Rev. Lett.* **102** (2009)
 3968 141801 [[0903.0676](#)]. 62

BIBLIOGRAPHY

- 3969 [74] S. Raby, *Grand Unified Theories*, in *2nd World Summit: Physics Beyond the*
3970 *Standard Model*, 8, 2006 [[hep-ph/0608183](#)]. 62
- 3971 [75] KAMIOKANDE-II collaboration, *Observation of a Neutrino Burst from the*
3972 *Supernova SN 1987a*, *Phys. Rev. Lett.* **58** (1987) 1490. 62
- 3973 [76] R.M. Bionta et al., *Observation of a Neutrino Burst in Coincidence with*
3974 *Supernova SN 1987a in the Large Magellanic Cloud*, *Phys. Rev. Lett.* **58** (1987)
3975 1494. 62
- 3976 [77] J. Strait, E. McCluskey, T. Lundin, J. Willhite, T. Hamernik, V. Papadimitriou
3977 et al., *Long-baseline neutrino facility (lbnf) and deep underground neutrino*
3978 *experiment (dune) conceptual design report volume 3: Long-baseline neutrino*
3979 *facility for dune june 24, 2015*, [1601.05823](#). 63
- 3980 [78] DUNE collaboration, *Deep Underground Neutrino Experiment (DUNE) Near*
3981 *Detector Conceptual Design Report, Instruments* **5** (2021) 31 [[2103.13910](#)]. 65,
3982 66, 69, 70, 72, 73, 153
- 3983 [79] DUNE collaboration, *DUNE Phase II: Scientific Opportunities, Detector*
3984 *Concepts, Technological Solutions*, [2408.12725](#). 68, 74
- 3985 [80] DUNE collaboration, *A Gaseous Argon-Based Near Detector to Enhance the*
3986 *Physics Capabilities of DUNE*, [2203.06281](#). 70
- 3987 [81] F. Sauli, *Gem: A new concept for electron amplification in gas detectors*, *Nuclear*
3988 *Instruments and Methods in Physics Research Section A: Accelerators,*
3989 *Spectrometers, Detectors and Associated Equipment* **386** 531. 72, 76
- 3990 [82] A. Ritchie-Yates et al., *First operation of an ALICE OROC operated in high*
3991 *pressure Ar-CO₂ and Ar-CH₄*, *Eur. Phys. J. C* **83** (2023) 1139 [[2305.08822](#)]. 75
- 3992 [83] ALICE TPC collaboration, *The upgrade of the ALICE TPC with GEMs and*
3993 *continuous readout*, *JINST* **16** (2021) P03022 [[2012.09518](#)]. 75

BIBLIOGRAPHY

- 3994 [84] F. Sauli, *The gas electron multiplier (gem): Operating principles and applications*,
 3995 *Nuclear Instruments and Methods in Physics Research Section A: Accelerators,*
 3996 *Spectrometers, Detectors and Associated Equipment* **805** 2. 76
- 3997 [85] C. Lippmann, *A continuous read-out tpc for the alice upgrade*, *Nuclear*
 3998 *Instruments and Methods in Physics Research Section A: Accelerators,*
 3999 *Spectrometers, Detectors and Associated Equipment* **824** 543. 76
- 4000 [86] C. Calabria, *Large-size triple gem detectors for the cms forward muon upgrade*,
 4001 *Nuclear and Particle Physics Proceedings* **273–275** 1042. 76
- 4002 [87] DUNE collaboration, *The DUNE Far Detector Vertical Drift Technology*,
 4003 *Technical Design Report*, 2312.03130. 81, 82
- 4004 [88] DUNE collaboration, *Deep Underground Neutrino Experiment (DUNE)*, *Far*
 4005 *Detector Technical Design Report, Volume IV: Far Detector Single-phase*
 4006 *Technology*, *JINST* **15** (2020) T08010 [2002.03010]. 83
- 4007 [89] DUNE DAQ, “dtp-firmware.”
 4008 <https://gitlab.cern.ch/dune-daq/readout/dtp-firmware>, 2020. 85
- 4009 [90] DUNE DAQ, “dtp-simulation.”
 4010 <https://gitlab.cern.ch/dune-daq/readout/dtp-simulation>, 2020. 88
- 4011 [91] DUNE DAQ, “dtpe emulator.”
 4012 https://github.com/DUNE-DAQ/dtpe_emulator/tree/fmlopez/filter_ana,
 4013 2022. 88
- 4014 [92] J. McClellan and T. Parks, *A personal history of the Parks-McClellan algorithm*,
 4015 *IEEE Signal Processing Magazine* **22** (2005) 82. 89
- 4016 [93] G. Turin, *An introduction to matched filters*, *IEEE Transactions on Information*
 4017 *Theory* **6** (1960) 311. 92
- 4018 [94] J.W. Goodman, *Statistical Optics*, Wiley (1985). 94

BIBLIOGRAPHY

- 4019 [95] B. Dwork, *Detection of a pulse superimposed on fluctuation noise*, *Proceedings of*
4020 *the IRE* **38** (1950) 771. 95
- 4021 [96] L. Wainstein and V. Zubakov, *Extraction of Signals from Noise*, Prentice-Hall
4022 (1962). 95
- 4023 [97] E.D. Church, *Larsoft: A software package for liquid argon time projection drift*
4024 *chambers*, **1311.6774**. 98, 99
- 4025 [98] S.V. Stehman, *Selecting and interpreting measures of thematic classification*
4026 *accuracy*, *Remote Sensing of Environment* **62** (1997) 77. 112
- 4027 [99] A.A. Taha and A. Hanbury, *Metrics for evaluating 3d medical image*
4028 *segmentation: analysis, selection, and tool*, *BMC Medical Imaging* **15** (2015) . 113
- 4029 [100] J. Silk, K.A. Olive and M. Srednicki, *The Photino, the Sun and High-Energy*
4030 *Neutrinos*, *Phys. Rev. Lett.* **55** (1985) 257. 119
- 4031 [101] M. Srednicki, K.A. Olive and J. Silk, *High-Energy Neutrinos from the Sun and*
4032 *Cold Dark Matter*, *Nucl. Phys. B* **279** (1987) 804. 119
- 4033 [102] J.S. Hagelin, K.W. Ng and K.A. Olive, *A High-energy Neutrino Signature From*
4034 *Supersymmetric Relics*, *Phys. Lett. B* **180** (1986) 375. 119
- 4035 [103] T.K. Gaisser, G. Steigman and S. Tilav, *Limits on Cold Dark Matter Candidates*
4036 *from Deep Underground Detectors*, *Phys. Rev. D* **34** (1986) 2206. 119
- 4037 [104] N. Bernal, J. Martín-Albo and S. Palomares-Ruiz, *A novel way of constraining*
4038 *WIMPs annihilations in the Sun: MeV neutrinos*, *JCAP* **08** (2013) 011
4039 [1208.0834]. 119, 120, 126
- 4040 [105] C. Rott, J. Siegal-Gaskins and J.F. Beacom, *New Sensitivity to Solar WIMP*
4041 *Annihilation using Low-Energy Neutrinos*, *Phys. Rev. D* **88** (2013) 055005
4042 [1208.0827]. 119, 126

BIBLIOGRAPHY

- 4043 [106] C. Rott, S. In, J. Kumar and D. Yayınlı, *Dark Matter Searches for Monoenergetic
4044 Neutrinos Arising from Stopped Meson Decay in the Sun*, *JCAP* **11** (2015) 039
4045 [1510.00170]. 119
- 4046 [107] DUNE collaboration, *Searching for solar KDAR with DUNE*, *JCAP* **10** (2021)
4047 065 [2107.09109]. 119
- 4048 [108] G. Busoni, A. De Simone and W.-C. Huang, *On the Minimum Dark Matter Mass
4049 Testable by Neutrinos from the Sun*, *JCAP* **07** (2013) 010 [1305.1817]. 120
- 4050 [109] V.A. Bednyakov and F. Simkovic, *Nuclear spin structure in dark matter search:
4051 The Zero momentum transfer limit*, *Phys. Part. Nucl.* **36** (2005) 131
4052 [hep-ph/0406218]. 121
- 4053 [110] A. Gould, *WIMP Distribution in and Evaporation From the Sun*, *Astrophys. J.*
4054 **321** (1987) 560. 121
- 4055 [111] J.N. Bahcall, M.H. Pinsonneault and S. Basu, *Solar models: Current epoch and
4056 time dependences, neutrinos, and helioseismological properties*, *Astrophys. J.* **555**
4057 (2001) 990 [astro-ph/0010346]. 124
- 4058 [112] T. Golan, J.T. Sobczyk and J. Zmuda, *NuWro: the Wroclaw Monte Carlo
4059 Generator of Neutrino Interactions*, *Nucl. Phys. B Proc. Suppl.* **229-232** (2012)
4060 499. 128
- 4061 [113] G. Cowan, K. Cranmer, E. Gross and O. Vitells, *Asymptotic formulae for
4062 likelihood-based tests of new physics*, *Eur. Phys. J. C* **71** (2011) 1554 [1007.1727].
4063 129
- 4064 [114] T. Kaluza, *Zum Unitätsproblem der Physik, Sitzungsber. Preuss. Akad. Wiss.
4065 Berlin (Math. Phys.)* **1921** (1921) 966 [1803.08616]. 131
- 4066 [115] O. Klein, *Quantum Theory and Five-Dimensional Theory of Relativity. (In
4067 German and English)*, *Z. Phys.* **37** (1926) 895. 131

BIBLIOGRAPHY

- 4068 [116] T. Appelquist, H.-C. Cheng and B.A. Dobrescu, *Bounds on universal extra*
4069 *dimensions*, *Phys. Rev. D* **64** (2001) 035002 [[hep-ph/0012100](#)]. 131
- 4070 [117] N. Arkani-Hamed, S. Dimopoulos and G.R. Dvali, *The Hierarchy problem and new*
4071 *dimensions at a millimeter*, *Phys. Lett. B* **429** (1998) 263 [[hep-ph/9803315](#)]. 131
- 4072 [118] L. Randall and R. Sundrum, *A Large mass hierarchy from a small extra*
4073 *dimension*, *Phys. Rev. Lett.* **83** (1999) 3370 [[hep-ph/9905221](#)]. 131
- 4074 [119] G. Servant and T.M.P. Tait, *Is the lightest Kaluza-Klein particle a viable dark*
4075 *matter candidate?*, *Nucl. Phys. B* **650** (2003) 391 [[hep-ph/0206071](#)]. 132
- 4076 [120] H.-C. Cheng, K.T. Matchev and M. Schmaltz, *Radiative corrections to*
4077 *Kaluza-Klein masses*, *Phys. Rev. D* **66** (2002) 036005 [[hep-ph/0204342](#)]. 132
- 4078 [121] M. Blennow, J. Edsjö and T. Ohlsson, *Neutrinos from WIMP annihilations using*
4079 *a full three-flavor Monte Carlo*, *JCAP* **01** (2008) 021 [[0709.3898](#)]. 132, 135
- 4080 [122] J. Edsjö, J. Elevant and C. Niblaeus, *WimpSim Neutrino Monte Carlo*. 132, 135
- 4081 [123] U. Haisch and A. Weiler, *Bound on minimal universal extra dimensions from*
4082 *anti-B → X(s)gamma*, *Phys. Rev. D* **76** (2007) 034014 [[hep-ph/0703064](#)]. 134
- 4083 [124] A. Freitas and U. Haisch, *Anti-B → X(s) gamma in two universal extra*
4084 *dimensions*, *Phys. Rev. D* **77** (2008) 093008 [[0801.4346](#)]. 134
- 4085 [125] C. Rott, D. Jeong, J. Kumar and D. Yaylali, *Neutrino Topology Reconstruction at*
4086 *DUNE and Applications to Searches for Dark Matter Annihilation in the Sun*,
4087 *JCAP* **07** (2019) 006 [[1903.04175](#)]. 137
- 4088 [126] F. Pedregosa, G. Varoquaux, A. Gramfort, V. Michel, B. Thirion, O. Grisel et al.,
4089 *Scikit-learn: Machine learning in Python*, *Journal of Machine Learning Research*
4090 **12** (2011) 2825. 143
- 4091 [127] J. Kopp, V. Niro, T. Schwetz and J. Zupan, *DAMA/LIBRA and leptонically*
4092 *interacting Dark Matter*, *Phys. Rev. D* **80** (2009) 083502 [[0907.3159](#)]. 147

BIBLIOGRAPHY

- 4093 [128] PARTICLE DATA GROUP collaboration, *Review of Particle Physics*, *PTEP* **2020**
4094 (2020) 083C01. 148
- 4095 [129] M. Beltran, D. Hooper, E.W. Kolb and Z.C. Krusberg, *Deducing the nature of
4096 dark matter from direct and indirect detection experiments in the absence of
4097 collider signatures of new physics*, *Phys. Rev. D* **80** (2009) 043509 [[0808.3384](#)].
4098 149
- 4099 [130] PLANCK collaboration, *Planck 2018 results. VI. Cosmological parameters*, *Astron.
4100 Astrophys.* **641** (2020) A6 [[1807.06209](#)]. 149
- 4101 [131] C. Green, J. Kowalkowski, M. Paterno, M. Fischler, L. Garren and Q. Lu, *The
4102 Art Framework*, *J. Phys. Conf. Ser.* **396** (2012) 022020. 154
- 4103 [132] H. Bethe, *Zur theorie des durchgangs schneller korpuskularstrahlen durch materie*,
4104 *Annalen der Physik* **397** (1930) 325. 159
- 4105 [133] E. Fermi, *The ionization loss of energy in gases and in condensed materials*,
4106 *Physical Review* **57** (1940) 485. 159
- 4107 [134] R. Sternheimer, M. Berger and S. Seltzer, *Density effect for the ionization loss of
4108 charged particles in various substances*, *Atomic Data and Nuclear Data Tables* **30**
4109 (1984) 261. 159
- 4110 [135] W.W.M. Allison and J.H. Cobb, *Relativistic Charged Particle Identification by
4111 Energy Loss*, *Ann. Rev. Nucl. Part. Sci.* **30** (1980) 253. 160
- 4112 [136] W. Blum, L. Rolandi and W. Riegler, *Particle detection with drift chambers*,
4113 *Particle Acceleration and Detection* (2008), [10.1007/978-3-540-76684-1](https://doi.org/10.1007/978-3-540-76684-1). 160
- 4114 [137] ALICE TPC collaboration, *Particle identification of the ALICE TPC via dE/dx*,
4115 *Nucl. Instrum. Meth. A* **706** (2013) 55. 160
- 4116 [138] L. Landau, *On the energy loss of fast particles by ionization*, *J. Phys. (USSR)* **8**
4117 (1944) 201. 163

BIBLIOGRAPHY

- 4118 [139] W. Ulmer and E. Matsinos, *Theoretical methods for the calculation of Bragg
4119 curves and 3D distributions of proton beams*, *The European Physical Journal
4120 Special Topics* **190** (2010) 1. 165
- 4121 [140] E. Aprile, A.E. Bolotnikov, A.L. Bolozdynya and T. Doke, *Noble Gas Detectors*,
4122 Wiley (Oct., 2008), 10.1002/9783527610020. 166
- 4123 [141] D.S. Wilks, *Statistical Methods in the Atmospheric Sciences*, Academic Press. 203
- 4124 [142] ALICE collaboration, *Production of pions, kaons and protons in pp collisions at
4125 $\sqrt{s} = 900 \text{ gev with alice at the lhc}$* , 1101.4110. 205
- 4126 [143] U. Einhaus, *Charged hadron identification with de/dx and time-of-flight at future
4127 higgs factories*, 2110.15115. 205
- 4128 [144] R. Frühwirth, *Application of filter methods to the reconstruction of tracks and
4129 vertices in events of experimental high energy physics*, Ph.D. thesis, Technischen
4130 Universität Wien, 1988. 211
- 4131 [145] P. Astier, A. Cardini, R.D. Cousins, A. Letessier-Selvon, B.A. Popov and
4132 T. Vinogradova, *Kalman filter track fits and track breakpoint analysis*, *Nuclear
4133 Instruments and Methods in Physics Research Section A: Accelerators,
4134 Spectrometers, Detectors and Associated Equipment* **450** (2000) 138. 211
- 4135 [146] T2K UK collaboration, *The Electromagnetic Calorimeter for the T2K Near
4136 Detector ND280*, *JINST* **8** (2013) P10019 [1308.3445]. 219
- 4137 [147] J.E. Gaiser, *Charmonium Spectroscopy From Radiative Decays of the J/ψ and ψ'* ,
4138 Ph.D. thesis, Stanford University, 1982. 224